Moment-induced block shear failure in bolted flange plate connections

Keith Janghyun Lee

Department of Civil Engineering and Applied Mechanics
McGill University, Montreal

July 2020

A thesis submitted to McGill University in partial fulfillment of the requirements of the degree of Master of Engineering

Abstract

Block shear in bolted steel connections has been widely recognized and studied as a possible failure path for steel members under tension. However, despite their ubiquity in modern steel structures, the block shear failure mode has not been explicitly studied for W-sections with bolted flange plate connections. Further, the block shear failure mode has not been verified for flange-connected W-Sections under *flexure*, where the force developed in the tension flange could theoretically create the conditions necessary for a block shear failure mode. A recent study confirmed the existence of the block shear failure mode in bolted flange plate W-sections under pure tension; this thesis acts as a continuation of that study by investigating the block shear failure mode in W-sections under flexure.

A total of 17 finite element models were developed to perform a parametric study on the possibility of a moment-induced block shear failure mode. Of the 17 section-connection configurations, 6 were fabricated for full-scale laboratory testing to verify the results of the finite element models. The results of the study showed that the block shear failure mode is a possible failure path in the tension flange of bolted moment connections, and should be explicitly considered during design. However, the possibility of the block shear failure mode is limited to a narrow combination of section depths, flange thicknesses, and overall connection geometry. In general, the CSA S16-19 design equation was found to provide good predictive capacity for the

block shear failure mode, with its assumption of a gross shear area and a higher-than-yield stress state at failure accurately reflecting the observed stresses in the finite element models.

In addition, an analytic study on the relation between the local block shear failure mode and the various net section flexural resistance reduction requirements was performed. These requirements, known as the *15% Rule* in the CSA S16 standard, reduce the overall allowable flexural capacity of W-sections when holes are present in the flanges. A significant portion of typical section-connection detail combinations trigger these clauses, which then significantly reduce the allowable capacity of a flexural member. The analytic study, along with the results from the finite element study, showed that the newly revised CSA S16-19 method for the 15% Rule provides a significant increase in allowable flexural capacity as compared to previous methods in the CSA S16 standard as well as similar reduction methods in the AISC 360-16 standard.

Résumé

La rupture par bloc de cisaillement dans les connexions boulonnées en acier a étée largement reconnue et étudiée comme mode de défaillance possible pour les éléments en tension. Cependant, malgré leur omniprésence dans les structures en acier modernes, le bloc de cisaillement n'a pas étée explicitement étudié pour les profilés à ailes larges (section W) avec des connexions de plaques de recouvrement. En plus, ce mode de défaillance n'a pas été vérifié pour les sections W chargées sous un moment de flexion, où la force dans l'aile de tension pourrait théoriquement créer les conditions nécessaires pour une défaillance par bloc de cisaillement. Une étude récente a confirmé l'existence du bloc de cisaillement dans les W-sections de plaques de recouvrement boulonnées sous tension pure. Cette thèse s'inscrit dans la continuité de cette étude en étudiant le mode de rupture par bloc de cisaillement dans les W-sections sous un moment de flexion.

Au total, 17 modèles d'éléments finis ont été développés pour effectuer une étude paramétrique visant à déterminer la possibilité du bloc de cisaillement de l'aile en tension dans les sections W, sous un moment de flexion. Parmi ces 17 modèles, 6 ont été aussi fabriqués pour être essayés en laboratoire afin de vérifier les résultats des modèles d'éléments finis. Les résultats de l'étude ont montré que la rupture par bloc de cisaillement sous moment de flexion est un mode de défaillance possible pour les sections W avec des connexions à plaques de recouvrement, et doit donc être explicitement prise en compte lors de la

conception. Cependant, la possibilité de ce mode de défaillance est limitée à un rang étroit de combinaisons de profondeurs de section, d'épaisseurs d'aile et de géométrie globale de la connexion. En général, l'équation de conception de la norme CSA S16-19 réussit à prédire ce mode de défaillance avec ses hypothèses uniques d'aire de cisaillement sans réduction et de niveau de contrainte supérieur à la limite élastique au moment de la défaillance, d'après les résultats observés dans les modèles d'éléments finis.

En plus, une étude analytique sur la relation entre le mode local de défaillance par bloc de cisaillement, et les exigences de réduction de la résistance à la flexion pour des sections d'aire réduite, a été réalisée. Ces exigences, connues sous la "Règle de 15%", réduisent la capacité de flexion admissible des sections W lorsque des trous pour boulons sont présents dans les ailes. Une grande proportion des détails de connexion entre sections typiques sont concernés par ces clauses, ce qui réduit ainsi la capacité admissible en flexion de l'élément. L'étude analytique, en utilisant les résultats de l'étude par éléments finis, a montré que la méthode de la norme CSA S16-19 récemment révisée pour la "Règle de 15%" fournit une amélioration significative de la capacité en flexion admissible par rapport aux méthodes précédemment adoptée par la norme CSA S16, ainsi que pour des méthodes de réduction similaires de la norme AISC 360-16.

Acknowledgements

My gratitude first to my supervisor, Professor Colin Rogers, who I have had the privilege of working with for four years. His intelligence, quiet support, and guidance has helped me develop as an academic more than anyone else.

Second, to the laboratory staff and senior researchers that keep the department running smoothly: John, Damon, William, Jorge, and Dr. Bill Cook. Nothing in the lab could be possible without their hard work, ingenuity, and good humour.

Third, my colleagues: Andrés González Ureña, Andrea Iachetta, and Jason Wu especially for the many shared laughs, ice creams, and knowledge-sharing over the years; Dr. Mohammad Motallebi, who first introduced me to structural engineering research in 2016; Dr. Sarven Akçelyan, one of the most brilliant people I have ever had the privilege of learning from; Majed Karam, MASc, at the University of Toronto, who I admire greatly as an equally young researcher.

Fourth, I am grateful to the industry partners, federal research councils, and the local academic coalitions that made this research project possible: ADF, CEISCE, NSERC, Métal Perreault, and Denis D'Aranco & Martin Frappier at DPHV.

Last, my mother in BC and my sister in Nova Scotia, my small family, who never falter in their belief in and support of me.

This thesis is dedicated to all the brilliant, beautiful, kind, funny, and inspiring people that I have met during my time in Montreal. There is an enormous breadth of knowledge, experience, and unique brilliance spread across this group of people. Our many shared late nights, early mornings, and bad decisions contextualize *why* anything we do is worth doing in the first place. If I am truly thankful for anything, it's my sheer luck of running into the most incredible people at just the right time. I am forever indebted to those who have shared and taught their patience, kindness, genius, and love. I will hold this city and the people in it dearly in my heart for the rest of my life.

Contents

1 Introduction **1**

1.1 Context 1

1.2 Motivation and Objectives 3

1.3 Scope of Work 4

1.4 Thesis Outline 5

2 Literature Review **6**

2.1 Block shear failure 8

2.1.1 Section efficiency: the effect of load eccentricity 12

2.1.2 Comprehensive equations for block shear 15

2.1.3 W-section block shear failure 18

2.2 Flange section reductions: The 15% Rule 20

2.2.1 Lilly and Carpenter (1939) 21

2.2.2 Recent findings on the 15% rule 23

2.3 Contemporary design procedures for Block Shear 30

2.3.1 Canadian design procedure (CSA S16-19) 30

2.3.2 American design procedure (AISC 360-16) 31

2.3.3 European design procedure (Eurocode 3-2005) 31

2.4 Finite Element Modelling 32

2.4.1 Initial methods of finite element analysis 33

2.4.2 Modelling of fracture in block shear failure 36

2.5 Summary 38

3 Preliminary verification of moment-induced block shear and selection of laboratory test specimens 41

3.1 Selection of initial test specimens 42

3.1.1 Effect of section geometry on moment block shear failure potential 44

3.1.2 Section selection and connection detailing 47

3.1.3 Sample design methodology for M5: W610X101 48

3.1.4 Initial test specimens 63

3.2 Preliminary finite element models 66

3.2.1 Physical representation of test conditions 67

3.2.1.1 Load/Support boundary conditions 68

3.2.1.2 Connection symmetry 69

3.2.1.3 Cross section symmetry 69

3.2.2 Model development and procedure 74

3.2.2.1 Material properties 78

3.2.2.2 Mesh element selection 80

3.2.2.3 Mesh sensitivity analysis 83

3.2.2.4 Contact properties 90

3.2.2.5 Loading procedure 90

3.3 Results of preliminary finite element models 92

3.4 Summary 96

4 Laboratory test preparation 98

4.1 Detailing of specimens 98

4.2 Design of loading beam 102

4.3 Instrumentation and data acquisition 106

4.4 Test assembly and loading method 109

4.5 Summary 112

5 Expanded FE study and results **114**

5.1 Expanded finite element analysis 115

5.1.1 Initial observations 116

5.1.2 Extracting data from finite element models 118

5.1.3 Data parsing, preparation, and analysis 119

5.2 Results and Observations 123

5.2.1 Effect of section geometry 123

5.2.2 Distribution of stress 127

5.2.3 Effect of connection length 133

5.3 Predictive capacities of design equations 138

5.3.1 CSA S16-19 139

5.3.2 AISC 360-16 142

5.3.3 Eurocode 3-2005 145

5.3.4 Summary of block shear predictive capacities 147

5.4 15% Rule 150

5.4.1 Analytic review 150

5.4.1.1 AISC 360-16: Equation F13 151

5.4.1.2 CSA S16: Clause 14.1 152

5.4.1.3 Swanson Equation (2016) 156

5.4.2 Comparison of design methods 157

5.5 Conclusion 162

6 Conclusions **164**

6.1 Overview 164

6.2 Future work 165

References 167

References **170**

Appendices **171**

A Net section flexural resistance **172**

B Code **178**

List of Figures

1.1 Possible loading scenarios for block shear failure in W-sections. . . 2

2.1 Typical block shear failure scenarios. 7
2.2 W-section block shear failure modes as observed by Pizzuto (2019). 19
2.3 All W-sections affected by the 15% rule for 2 bolts per flange as a function of the bolt diameter, d_b, and the beam depth, d. 23
2.4 Potential moment-induced failure modes for W-sections under flexure. 39

3.1 Translation of laboratory test conditions into modelled region. . . 43
3.2 Comparison of thick vs. thin flanges for block shear sensitivity. . . 45
3.3 Comparison of deep vs. shallow sections for block shear sensitivity. 46
3.4 Comparison of wide vs. narrow flanges for block shear sensitivity. 46
3.5 Specimen detailing methodology 49
3.6 Final designed M5 test specimen. 50
3.7 Definition of Pitch, Gauge, and End distances 51
3.8 W610X101 W-Section properties 51
3.9 Design space for W610X101 section. 56
3.10 Possible moment block shear failure modes. 57
3.11 Target moment capacity M_{des} in red against the M5 design space. 58
3.12 Sample of possible connection geometry combinations for a block shear critical failure mode. 59

3.13 Overview of theoretical probable and unfactored moment resistances. 61
3.14 Width, depth, and linear mass of all standard W-Sections (selected specimens highlighted in red) 64
3.15 Theoretical unfactored and probable moment capacities of selected specimens 65
3.16 Translation of test conditions to FE conditions. 67
3.17 Constraint/Displacement method on loading plate. support. . . . 70
3.18 ZSYMM Boundary condition on the M3 pFEM in *Abaqus/CAE* . 71
3.19 XSYMM Boundary condition on the M4 pFEM in *Abaqus/CAE* . 72
3.20 Connection displacement comparison of M2 Full/Half models . . . 73
3.21 End moment comparison of M2 Full/Half models 74
3.22 Edge block shear component comparison of M2 Full/Half models . 75
3.23 Complete block shear component comparison of M2 Full/Half models 75
3.24 Specimen drawing program in Grasshopper 77
3.25 Rhino/Grasshopper output components. 78
3.26 Analysis comparison of Full vs. Reduced C3D8 elements of the M4 pFEM 82
3.27 Comparison of Coarse, Medium, and Fine meshes 84
3.28 Comparison of Coarse, Medium, and Fine meshes 85
3.29 Comparison of Coarse, Medium, and Fine deformed meshes at 100mm load displacement 86
3.30 EBS: Shear Component Comparison 87
3.31 EBS: Tension Component Comparison 88
3.32 Meshed bolt and exterior splice plate. 89
3.33 Relative deformation comparison of M1-M5 pFEMs. 93
3.34 Von Mises Stress comparison of M1-M5 pFEMs. 94
3.35 CSA S16-19 predictive capacity for the EBS failure mode. 95
3.36 CSA S16-19 predictive capacity for the CBS failure mode. 95

4.1 Overview of complete test assembly. 99

4.2 Test assembly overview. 100
4.3 Approximate location of coupon blanks. 101
4.4 Finite element model of loading beam. 105
4.5 Instrumentation for global deformation capture. 107
4.6 Strain gauges for local deformation capture. 107
4.7 Render of loading frame assembly. 110
4.8 Exploded view of test specimen assembly. 111
4.9 Positioning of lateral support clamps. Dimensions in mm. 112

5.1 Complete range of available W-sections. Tested and modelled specimens in red. 116
5.2 Axial displacement contours of tested specimens. Units in mm. . . 118
5.3 Von Mises stress contours of tested specimens. Units in MPa. . . 119
5.4 Load displacement vs. induced moment from M5 FE model. . . . 121
5.5 Von Mises stresses along major failure planes for M5 specimen. Elements highlighted in red. 122
5.6 Block shear failure moments normalized to M_y 124
5.7 Section depth vs. block shear failure moments. 124
5.8 Flange width vs. block shear failure moments. 125
5.9 Net flange area ratio vs. block shear failure moments. 125
5.10 Block shear failure moments compared to gross section capacities. 126
5.11 Average Von Mises stress in each failure plane. 128
5.12 Tension plane stress distribution for M3 specimen. 129
5.13 Shear plane stress distribution for M3 specimen. 130
5.14 Comparison of complete block shear fracture plane Von Mises stress distribution between M3 and M5 specimens. 132
5.15 Comparison of `SPEC` vs. `TYP` series of specimens M1-M5. 134
5.16 Comparison of overall displacement-moment behaviour of M2SPEC and M2TYP specimens. 136

5.17 Comparison of average failure plane stresses of M2SPEC and M2TYP specimens. 137
5.18 CSA S16-19 EBS predictive capacity. 140
5.19 CSA S16-19 CBS predictive capacity. 141
5.20 AISC 360-16 EBS predictive capacity. 143
5.21 AISC 360-16 CBS predictive capacity. 144
5.22 Eurocode 3-2005 EBS predictive capacity. 145
5.23 Eurocode 3-2005 CBS predictive capacity. 146
5.24 Comparison of block shear Professional Factors. 149
5.25 AISC 360-16: Net flexural resistance. 152
5.26 CSA S16-14: Net flexural resistance. 153
5.27 CSA S16-19: Net flexural resistance. 155
5.28 Swanson Equation 3: Net flexural resistance. 157
5.29 Comparison of net flexural resistance methods. 159
5.30 FE results compared to net flexural resistance predictions. 161
5.31 Reduced flexural capacities for common beam sections only. . . . 162

A.1 Simplified boundary condition for web splice. 173
A.2 Comparison of Von Mises stress distributions for the M5S series. . 174
A.3 Comparison of Von Mises stress distributions for the M5S series. . 175
A.4 Location of critical section. 175
A.5 Axial stress distribution across critical net section. 176

List of Tables

2.1 Correlation factors for Equation 2.6 (Driver et al., 2016) 17

3.1 Selected section overview. Critical moment capacities are in **bold.** 66
3.2 True material property sections 79
3.3 Run time comparison of Full vs. Reduced elements of the M4 pFEM 82
3.4 Mesh overview 83
3.5 CPU Time comparison for Coarse, Medium, and Fine meshes . . . 85
3.6 Step definition for *Abaqus* pFEMs 91

5.1 Connection geometry overview for M1-M12 specimens. 117
5.2 Overview of Professional Factors. 148

A.1 W610X101 M5S series overview 173

Chapter 1

Introduction

1.1 Context

W-section steel members are ubiquitous in modern steel structures, where the efficient cross section shape allows for their use in all load-bearing applications. For moment frame connections and beam splices, bolted flange plate connections are necessary to transfer the bending moment between members. *Block shear* of the tension flange is a possible failure mode for such connections. Block shear is a combined tension/shear failure mode, where a block of the flange is torn from the member along the bolt hole line(s); two possible loading scenarios for block shear in W-sections are shown in Figure 1.1. Although block shear failure has been explicitly studied for various structural steel sections, current Canadian design standards (CSA S16-19) for flange-connected W-sections are based on proxy results from tee sections (WT) in pure tension only (Epstein & Stamberg, 2002; Canadian Standards Association, 2019). Until recently, it was not verified that W-sections can be effectively modelled as two connected WT sections; further, it is unclear whether current design equations capture the effect of *moment*-induced block shear failure, where the more complex stress distribution may affect failure behaviour.

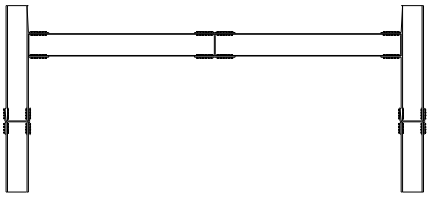

Steel Moment Frame

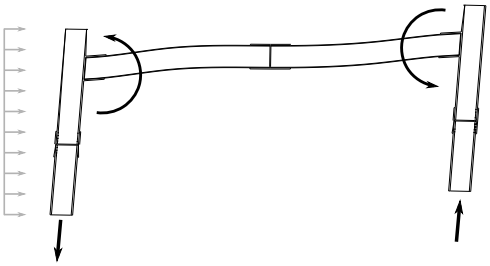

Lateral Load

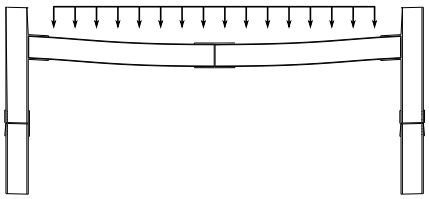

Uniformly Distributed Load

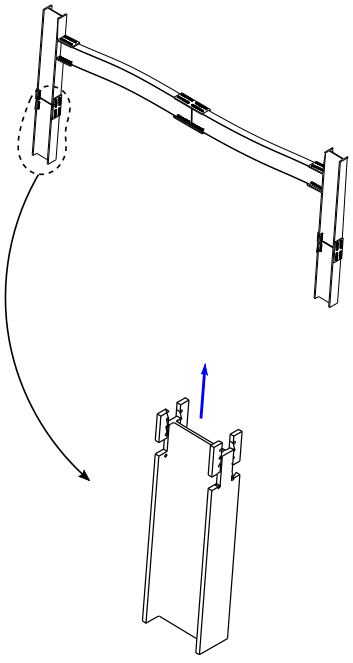

Pure Tension Block Shear

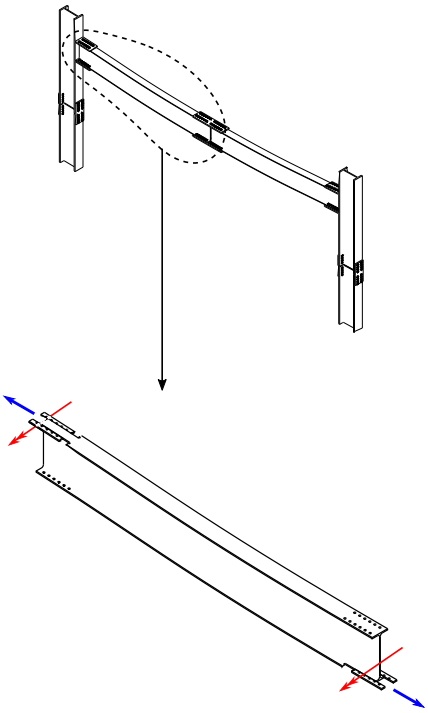

Moment-Induced Block Shear

Figure 1.1: Possible loading scenarios for block shear failure in W-sections.

In addition to block shear considerations, the CSA S16-19 standard calls for moment resistance reductions for W-sections with net flange areas less than 85% of the gross area. Since its introduction in 1954, the reduction equation, known as the 15% Rule, has long been considered overly punitive, with significant flexural capacity still available in the member (Canadian Standards Association, 1954). As moment connections require significant removal of the flange area for bolt holes, many connection details trigger this clause and force a reduction in the overall capacity of the beam. Further, it is also possible that an alternative interpretation of this clause may be used: if the connection detailing does *not* trigger the 15% Rule, a structural designer may assume that the capacity of the member is simply that of its gross section, and bypass the resistance of the connection geometry, namely the potential for the block shear failure mode in the tension flange.

1.2 Motivation and Objectives

The intent of this research project was to provide clarity on the existence of the block shear failure mode for bolted flange plate W-section connections, as well as to evaluate the current predictive capacity of common design equations. First, the possibility of a moment-induced block shear failure should be verified, both analytically and through finite element analysis. Then, the predictive capacity of existing design methodologies should be assessed. Should a block-shear critical connection detail exist, it would confirm that moment-induced block shear failure is both a possible failure mode, and that it should always be explicitly considered when designing connections.

Further, since all studied section-connection details would naturally have reduced flange areas while undergoing flexure, additional insight should be possible on the 15% Rule. The theoretical reduced capacity from the 15% Rule could be compared to the observed flexural capacity of the finite element models to

evaluate the applicability of such strength reduction equations. A block shear failure that occurs below the expected reduced flexural capacity would further confirm that block shear should be independently considered as a failure mode for all bolted W-sections under flexure; a block shear failure that occurs above the expected reduced flexural capacity would suggest that the 15% Rule is in fact overly punitive, and should be revised or removed.

1.3 Scope of Work

This project was the second phase of a two phase project investigating the block shear failure mode in W-section bolted flange plate connections. The work done by Pizzuto (2019) confirmed the existence of block shear failure in flange-connected W-sections in pure tension, and evaluated the predictive capacity of current Canadian, American, and European design procedures. This project investigated the scenario the possibility of a moment-induced block shear failure for bolted W-sections under flexure, where the force developed in the tension flange could potentially induce a block shear failure mode.

The project was carried out in three steps. First, an analytic design methodology was developed to detail pure moment splice connections for a block shear critical failure mode. This methodology was used to detail a series of section-connection combinations that would theoretically fail in moment-induced block shear. Second, six preliminary finite element models were developed and analysed to evaluate the analytic design method, and to provide initial confirmation that the block shear failure mode would occur. These preliminary finite element models were fabricated in full-scale for eventual testing in the structural laboratory at McGill University; a design of the loading beam, as well as the selection and location of laboratory instrumentation was also performed. Third, an expanded finite element model catalogue was created, with 17 total section-connection details designed to fail in block shear. The results of these finite element models

were aggregated, and a review of the predictive capacities of the CSA S16-19, AISC 360=16, and the Eurocode 3-2005 block shear design equations was performed. Further, key observations on the actual failure mechanism of the block shear failure mode were made. Finally, the results of the finite element models was compared against an analytic review of varying flexural resistance reduction equations for further insight on the applicability of the 15% Rule.

1.4 Thesis Outline

Chapter 2 provides an overview of the existing literature on the block shear failure mode, including the results of laboratory tests, methods and improvements in finite element modelling techniques, and the background of the block shear design equations as used by the CSA S16-19, AISC 360-16, and the Eurocode 3-2005 design standards. It also provides the background and current interpretations of net section flexural resistance design equations.

Chapter 3 presents the development and formalized procedure for designing a block shear failure critical moment connection. It also provides an overview on the development and detailing of the first six finite element models, and presents the initial findings.

Chapter 4 covers the design and detailing of support components and instrumentation in preparation for laboratory testing. This includes the design and detailing of the loading assembly, an overview of the overall testing protocol, and the positioning and type of the instrumentation during testing.

Chapter 5 discusses the overall findings of the research objectives after an additional 11 block shear failure critical moment connections were modelled. Further, an analytic study is performed to evaluate the performance of existing and proposed methods for net section flexural reductions.

Chapter 6 summarizes the overall scope and findings of this research project, and provides recommendations for future research.

Chapter 2

Literature Review

Block shear failure has been recognized as a potential failure path for bolted steel connections since the late 1970s. Since then, much research has been performed to determine the mechanics of the failure mode, as well as a suitable equation for design standards that could cover the wide range of potential block shear failure scenarios, some of which are shown in Figure 2.1. Analytical, physical, and finite-element testing has been performed to varying degrees of complexity since the first instance of block shear failure was observed by Birkemoe and Gilmor (1978). The general findings of the decades of research are:

1. The block shear failure mode consists of a rupture plane and a yield plane.
2. The block shear failure mode consists of a tension plane and a shear plane.
3. The effective resistance/sensitivity to the block shear failure mode depends on the cross-section geometry of the loaded member.

In general, the CSA S16-19 (Canadian Standards Association, 2019) design equation for block shear seems to provide accurate predictive capacities for steel sections under pure axial tension, including flange-connected W-sections, while the AISC 360-16 (American Institute of Steel Construction, 2016) design standard tends to underestimate the true capacity of a block section critical member.

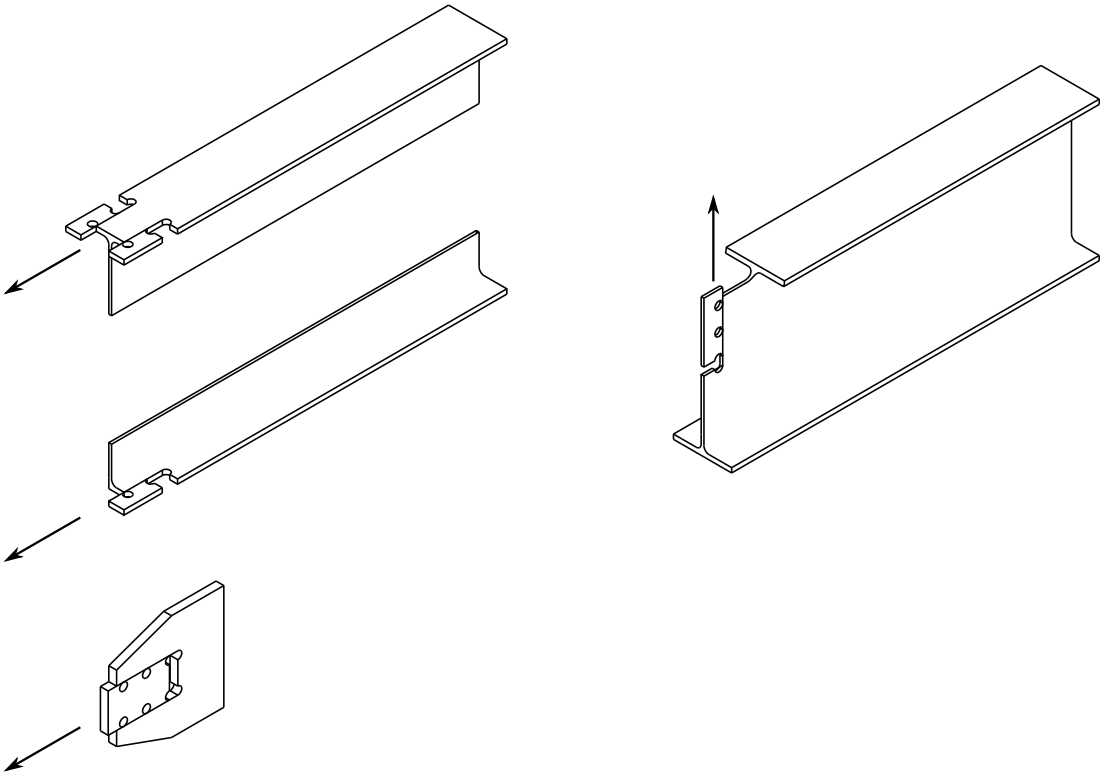

Figure 2.1: Typical block shear failure scenarios.

However, the attempt to develop a truly generalized block shear failure equation that reflects the true observed failure mechanisms is still the subject of ongoing research, with improved design equations suggested by researchers as late as 2016. This chapter provides a summary of the cumulative research on block shear failure, including developments in finite element modelling techniques, up to the current state-of-the-art.

In addition, this chapter provides the background on the recently revised Clause 14.1 in the CSA S16-19 standard, otherwise known as the *15% Rule*. Although it mostly affects how Canadian designers determine the effective flexural capacity of beam members, it is possible that this clause may also affect how structural designers approach the block shear failure mode for W-sections under flexure.

2.1 Block shear failure

The block shear failure mode was first observed by Birkemoe and Gilmor (1978) while investigating beam end double angle connections. While loading a CSA G40.21 44W grade uncoped beam connection, a tension rupture at the free edge of the last bolt row prematurely caused a drop in the connection capacity. Severe rotational deformation was observed, centered around a hinge formed in the upper flange-web interface. To investigate this unexpected failure mode, the researchers performed the same test on a coped beam to eliminate the potential flexural hinge support. The coped beam showed a significant reduction in connection capacity, with the entire block of the web section detaching from the main section. Birkemoe and Gilmor (1978) suggested the following predictive equation for the block shear failure mode:

$$P_{ult} = A_{nt}F_u + 0.6A_{nv}Fu \tag{2.1}$$

Where:
A_{nt} = Net tension area
F_u = Ultimate engineering tensile strength
A_{nv} = Net shear area

The findings of this research were incorporated into the revised *AISC Specification for the Design, Fabrication and Erection of Structural Steel for Buildings* for the same year (American Institute of Steel Construction, 1978). However, it was not introduced as a unique failure mode to be considered via Equation 2.1, but rather as a set of revised edge and end distance limits to prevent tensile rupture on free edges for bolted bearing-type connections.

Ricles and Yura (1983) expanded the work of Birkemoe and Gilmor by testing a series of *double row* bolted beam end connections to evaluate the effect of end and edge distances, as well as the effect of standard and slotted holes on the

overall capacity of the connection. Tests were based on W18X60 sections of ASTM A36 grade steel. The results of their tests showed a block shear failure mode as seen by Birkemoe and Gilmor (1978), but at an ultimate capacity that was significantly lower than predicted by Equation 2.1. It was noted that the capacity of the connection was more sensitive to the edge distance (the *tensile* area near the free edge perpendicular to the force) than the end distance, suggesting that the distribution of stress in the tensile plane played a significant role in the overall capacity of the connection. A finite-element analysis was performed on the connections to investigate the behaviour of both the tensile and shear stress distributions. It was determined that the distribution of stress along the tensile plane was non-uniform, with certain regions unable to reach the material ultimate strength, F_u, before failure. The finite-element analysis showed that short edge distances had a triangular stress distribution, with peak stresses at the free edge where rupture initiates, while larger edge distances resulted in a bi-linear tensile stress distributions, with peak stresses near the bolt holes. The analysis also showed that for the shear planes, the *average* shear stress was relatively stable, with longer connections showing less variance of the shear stress along the gross plane. It was also noted that the shear plane does *not* reach the rupture stress limits at the time of tensile rupture, contrary to Equation 2.1.

Based on these findings, Ricles and Yura (1983) concluded that the block shear capacity is highly dependent on connection geometry, and that further research must be performed to fully understand the failure path. To conclude, they suggested a revised equation to predict the block shear failure mode:

$$P_{ult} = 0.6F_yA_{vg} + 0.5F_uA_{nt} \tag{2.2}$$

Where:
F_y = Yield tensile strength
A_{vg} = Gross shear area

Ricles and Yura reduced the tensile contribution of block shear by half in Equation 2.2, reflecting the significantly lower stresses observed in their double-row connection tests, and changed the shear rupture component to a gross shear yield component to better reflect their test results.

Hardash and Bjorhovde (1985) focussed on evaluating and developing predictive models for block shear in bolted gusset plate connections. A common practice at the time was the use of the *Whitmore Effective Section* method, which simply provided the allowable 'net' section area for tensile rupture based on a 30 degree sweep of stress emanating from the lead row of bolts (Whitmore, 1952). A total of 28 gusset plate connections of steel plates with varying bolt pitches, gauges, and number of bolts were tested. Further, both hot and cold rolled steel plates were tested to investigate the effect of varying F_y/F_u ratios. Hardash and Bjorhovde reinforced the idea that the *net* tensile rupture strength should be used for block shear failure equations, but noted that the shear component remained sensitive to the overall connection length as well as the material yield-to-ultimate strength ratio. Due to some specimens showing shear rupture at failure, it was suggested that the behaviour of the shear plane depends on the F_y/F_u ratio, where higher values result in shear rupture at failure. In other words, since significant deformation is required for the tensile plane to rupture, steel materials with insufficient ductility would rupture along their shear plane before or concurrent with rupture of the tensile plane. Hardash and Bjorhovde concluded with a suggested predictive equation that considered connection lengths, net gauge distances, and 'effective' shear stresses, which provided accurate representation of the test results.

The findings of Hardash and Bjorhovde (1985) and Ricles and Yura (1983) were incorporated into a revised set of design equations in the 1986 AISC LRFD specification (American Institute of Steel Construction, 1986), where the block shear capacity is taken as the *greater* of:

$$R_n = 0.6F_yA_{vg} + F_uA_{nt} \tag{2.3}$$

$$R_n = 0.6F_uA_{ns} + F_yA_{gv} \tag{2.4}$$

The justification for the use of the greater of either Equation 2.3 or 2.4 was based on the observation that block shear failure occurred at the *fracture* point of a failure plane, meaning it should be classified as a brittle failure mode. Whether it was the shear or tensile plane that ruptured, it should be assumed that the yield stress is reached in the opposing plane.

Orbison et al. (1999) tested 12 different configurations of angles and WT sections made from ASTM A36 steel in direct tension. The connections were detailed to investigate the effect of connection lengths and load eccentricities on the tension stress distribution and the overall capacity of the block shear failure mode. Angles were tested with a single colinear row of two bolts with varying edge distances; The WT sections had varying numbers of bolts connected to the web, along with varying edge distances. An additional series of W sections was also tested with two bolt row connections in the web only.

All specimens failed in the typical block shear manner, with a net tension rupture plane, and severe shear deformation, indicating gross yielding of the shear plane. Like other researchers, the authors noted that the edge distance played a critical role in the capacity and stress distribution of the net tension plane. Shorter edge distances had higher peak stress concentrations that initiated rupture, while larger edge distances allowed for a more uniform stress distribution and higher overall tensile capacity. It was noted, however, that the shorter edge distances had the effect of increasing the in-plane eccentricity of the connection to the section centroid; it was possible that the increased shear lag effect on the short edge distance connection was the cause of the higher stress distribution, rather than the edge distance itself. The authors concluded that the 1993 AISC LRFD equation at the time could not account for varying connection configurations, and that further research was necessary to isolate the effect of varying connection parameters.

Topkaya (2004) performed a parametric finite element study of over 1000 connection configurations to better understand the failure mechanism of block shear. It was observed that the failure mechanism at ultimate capacity consisted of a net tensile fracture plane and a gross shear plane with significant yielding and deformation. It was noted that the average stress on the gross shear plane was sensitive to the overall connection length, as well as the F_y/F_u ratio of the material. Longer connection lengths had a lower average stress at failure, but with less variation of stress; shorter connection lengths had a higher average stress at failure, but with greater likelihood of stress concentrations. The study also found that in-plane load eccentricities could affect the connection capacity by up to 10% for longer connections, but out-of-plane eccentricities had little to no affect on the connection capacity.

2.1.1 Section efficiency: the effect of load eccentricity

As research continued on the block shear failure mode, it was clear that load eccentricities, whether in-plane or out-of-plane, played a fundamental role in the overall capacity of a block shear critical connection. Naturally, researchers looked for methods to account for these eccentricities, and their relation to the *shear lag factor* already present in net section fracture calculations.

The net section fracture failure mode consists entirely of tension planes simultaneously reaching their ultimate capacity, f_u, resulting in a complete rupture of the tension member. When a bolted connection has a centroid that is offset from the gross section centroid (typically occurring when only some legs of a non-rectangular section are bolted), a *shear lag* factor, U, is applied to the theoretical net section capacity to reflect the reduction in strength as stresses in unconnected regions must flow into connected regions. The shear lag factor is used to determine an *effective net area*, $A_{ne} = UA_n$, to be used for the net fracture strength

equation.

$$U = 1 - \frac{\bar{x}}{l} \leq 0.90 \tag{2.5}$$

Where:

$\bar{x}$ = connection eccentricity

l = connection length

Equation 2.5 resulted from the work by Munse and Chesson (1963), who investigated the effect of different cross section geometries, connection geometries, and fabrication methods on the overall capacity of bolted and riveted joints. Their work concluded with an empirical design rule that included, in addition to the shear lag coefficient, factors that accounted for material ductility, fabrication methods, and bearing effects on the fasteners. Although only the shear lag factor was adopted by North American design standards, the work by Munse and Chesson showed that connection strengths are dependent on a variety of design decisions.

This equation provided a simplified analytical method for determining the effective resistance of a tensile bolted connection, and remains the basis of the effective net section calculation method in both the AISC 360-16 and CSA S16-19 design equations. However, with the use of Equation 2.5 as presented, three issues are prone to occur. First, since the shear lag efficiency factor is a function of the connection length, a connection must first be designed before its design capacity is calculated. This results in an iterative and inefficient design methodology. Second, as no formal bounds were set by Munse and Chesson (1963), short connection lengths and/or large eccentricities could result in shear lag factors that approach 0, or even negative values. Third, the shear lag factor is unable to account for tensile connections with unconnected regions, where shear lag must occur, but without any connection eccentricities. For example, a W-section tensile member connected only by the flanges would not experience any shear lag reduction. More recent research has suggested simple tabulated values for U based on the

section type and number of bolts present (Kulak & Wu, 1997), while others have provided a more robust analytical method of connection analysis based on the induced moments on the connection (Epstein & D'Aiuto, 2002). The latest CSA S16-19 design standard removes the use of equation 2.5 completely for bolted tensile connections, while the AISC 360-16 design standard maintains the use of equation 2.5 with tabulated lower bounds for different bolt configurations.

Epstein (1992), while testing a series of double-rowed, staggered angle connections, noted that the predictive block shear equations of the AISC 360 provisions of the time were improved by the use of the shear lag factor (Equation 2.5) on the fracture component of resistance. From a test of 38 single-leg bolted angles in tension, the inclusion of the U factor improved the professional factor (PF) of the AISC 360 LRFD design equation from 0.901 to 1.008. Epstein concluded that the shear lag factor inclusion on the tension term was an appropriate method of improving the predictive capacity of the block shear failure mode.

Epstein continued to investigate the effect of shear lag on the block shear failure mode, focussing on structural tees. Epstein and D'Aiuto (2002) developed an analytical method for tensile connection efficiencies based on the induced moments and rotational capacities of connected structural tees. The method provided accurate calculations of the induced tensile forces and moments in each member, and it was suggested that the existing axial-moment interaction equations could then be used to limit the capacity of the connection. The authors concluded, however, that the existing shear lag factor U provided similar results, and sometimes provided a better professional factor than their proposed method. Epstein and D'Aiuto affirmed the use of the shear lag factor as an appropriate inclusion in both net section fracture and block shear fracture calculations.

Epstein and Stamberg (2002) investigated the effect of connection length and web depth on 50 flange-connected structural tees. The web depth was varied by cutting the base W-sections at different points along the depth of the section. A variety of failure modes were observed: a transition from block shear failure to net

section failure as the eccentricity decreased; a transition from block shear failure to net section failure as the connection length increased; premature buckling of the unconnected stem for significantly deep tees. The researchers again affirmed their suggestion that the shear lag factor was an appropriate addition to the tension term in block shear equations. However, as the authors noted that Equation 2.5 as-is would determine values of U that were unrealistically low or even negative, they provided lower and upper bounds of 0.65 and 0.90.

In rebuttal of these recommendations, Grondin (2005) discussed concerns in the methodology and assumptions in Epstein's work. Grondin noted that the use of the shear lag factor was mechanically incorrect when investigating block shear failure, even if it provided statistically accurate results. The shear lag factor developed by Munse and Chesson (1963) and adopted by North American design standards was explicitly meant to address the reduction in the active net tension plane area during a net section fracture failure. Grondin noted that since the block shear failure mode only considered the local geometry of the fracture block, the use of a net area reduction factor made no sense, as the stress distribution of the entire cross section is irrelevant to the stress distribution in the local block tension plane. Previous research on the block shear failure mode suggested that it was rather the *in-plane* eccentricity and corresponding non-uniform stress distribution that affected the ultimate capacity of the connection (Ricles & Yura, 1983; Hardash & Bjorhovde, 1985). It was possible then, that a reduction in the fracture component for block shear equations was appropriate, but that the shear lag factor used by Epstein provided a false positive improvement in predictive capacity.

2.1.2 Comprehensive equations for block shear

The need for an appropriate 'efficiency factor' that accounted for the effect of *in-plane* stress distributions during block shear failure was evident. Driver et al. (2006) proposed the *Unified Block Shear* equation, based on a statistical review

of previous testing on 205 block shear failure specimens of gusset plates, angles, tees, and coped beams.

$$P_u = R_t A_{nt} F_u + R_v A_{gv} \left(\frac{F_y + F_u}{2\sqrt{3}} \right) \tag{2.6}$$

Where:

R_t = Tensile component efficiency factor

R_v = Shear component efficiency factor

The unified equation (Equation 2.6) differed from previous predictive equations for three reasons. First, the components of the equation reflected the typical observed failure mode of net tensile fracture and gross shear yield. Second, based on consistent test results showing that the shear plane reached a stress much higher than the shear yield stress, but lower than the fracture stress, the average of the yield and ultimate shear stresses were taken for the gross shear component of the equation. These tensile stresses are divided by $\sqrt{3}$ to reflect the equivalent shear capacity using the Von Mises yield criterion. Third, the correction factors for the tensile stress, R_t, and the shear stress, R_v, were introduced. These correction factors were empirically based on the results of the aggregate study. Tabulated values were provided depending on the section and connection geometries. The unified equation by Driver et al. (2006) remains the basis for the most current design provisions in both the AISC 360-16 and CSA S16-19 steel design standards, although both design standards only use reduction factors for the tension plane, with the shear plane remaining at full capacity.

However, the most recent AISC 360 standard (AISC 360-16) still uses the original equation for U, but with lower and upper bounds for select connection scenarios. The bounds eliminate the second issue mentioned above, while explicit clauses prevent the third issue from presenting itself; W sections connected only by their flanges are to be treated as WT sections when determining the value for U. For bolted connections, the Canadian design provisions (CSA S16-19) have

Table 2.1: Correlation factors for Equation 2.6 (Driver et al., 2016)

Connection Type	R_t	R_v
Gusset Plates	1	1
Angles and Tees	0.9	0.9
Coped Beams: one bolt line	0.9	0.1
Coped beams: two bolt lines	0.3	1

simplified the effective area calculations into tabulated values of U for the tension plane, depending on the section type and number of bolts present. The CSA S16 method eliminates the need for Equation 2.5, as well as the need to know the connection length before determining the overall capacity.

Recent advancements in finite element modelling techniques have been used to perform a more detailed evaluation of the stress distribution and failure mechanisms for block shear failure. Clements and Teh (2013) performed finite element analysis on bolted plate connections, and concluded that the true critical shear plane lies between the net and gross shear sections. The authors named this critical plane the *active shear plane*, which was a function of the connection geometry and the hole diameter. Based on a series of nineteen finite element models, the authors demonstrated that the use of the active shear plane had the greatest predictive accuracy, with a mean Professional Factor of 1.02, compared to the AISC 360-10 (PF = 0.88) and the Eurocode 3-2005 (PF = 1.04), whose block shear design method is presented in Section 2.3. Further their proposed equation correctly predicted the critical failure mode between the block shear failure and net section fracture for all nineteen block shear connection models, something that the AISC 360-10 design equations could not do.

$$P_p = F_u \sum A_{nt} \left(0.9 + 0.1\frac{d}{p_2}\right) + 0.6F_y A_{av} \tag{2.7}$$

Equation 2.7 shows the proposed block shear failure equation as a function of the hole diameter, d, the bolt gauge, p_2, as well as the average shear area, A_{av}.

The average shear area is in turn a function of the hole diameter and the connection length. Although more involved than existing design equations from the AISC 360 and the CSA S16 standards, the proposed *active shear plane* model provides a user-friendly, analytical approach to determining the block shear capacity of a connection, rather than the empirical best-fit equations provided by other laboratory-based studies. Further research and finite element verifications have shown that this proposed equation performs well for a wide range of block shear failure scenarios (Elliott et al., 2019; Elliott & Teh, 2019). Despite favourable results, the AISC 360 and the CSA S16 standards continue to use more simplified design equations to calculate the block shear resistance.

2.1.3 W-section block shear failure

Despite their ubiquity in modern structural steel design, block shear failure has not been widely studied or verified in the context of W-sections. However, there are numerous possibilities for a tensile failure to occur in W-sections, such as W-sections used as brace members, W-section columns during uplift scenarios from wind/seismic loading, as well as the tension half of W-sections under flexural capacity. When the block shear failure mode is checked for W-sections, the efficiency factor, U, is borrowed from the varying suggested factors for strutural tees in direct tension, something that has not been explicitly verified.

To provide this explicit verification on the block shear failure mode for W-sections under pure tension, Pizzuto (2019) tested a series of full-scale flange-only bolted splice connections of W-sections, and performed subsequent FE analysis on the expected failure mechanism. Pizzuto performed ten laboratory tests on flange-only bolted splice plate W-section connections under pure tension, with section sizes ranging from a W250X73 section to a W690X152 section, and evaluated the predictive capacity of both the CSA S16-14 and the AISC 360-16 design standards. Two potential block shear failure modes were identified, and are shown in Figure 2.2:

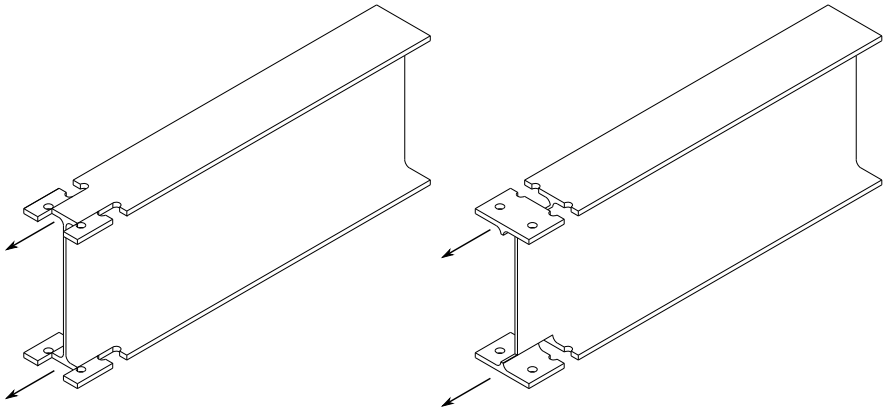

Figure 2.2: W-section block shear failure modes as observed by Pizzuto (2019).

1. The *Edge Block Shear* (EBS[1]) Failure mode, where the corners of the flanges are removed, and the entire failure block remains in the flanges

2. The *Complete Block Shear* (CBS) Failure mode, where the entire flange is removed, with the shear plane lying in the web/K-area interface along the connection length

The test specimens were detailed using the CSA S16-14 design equations to force a theoretical block shear critical failure mode. Three of the ten specimens were detailed to fail in Complete Block Shear, while the remaining were detailed with a critical Edge Block Shear resistance. The results of the tests provided key insight on block shear failure for W-sections: first, that block shear was a very possible failure mode for flange-connected W-sections, and must be considered during design. Second, the CSA S16-14 design equations have a good predictive capacity for block shear failure in W-sections, as indicated by Professional Factors, the test-to-predicted resistance ratios, that were close to 1.0.

The average professional factor for the CSA S16-14 design method was 1.03, compared to the AISC 360-16 professional factor of 1.16. This reaffirmed the

[1]It is noted that Pizzuto referred to the EBS failure mode as *Corner Block Shear*. The name has been changed to *Edge Block Shear* to easily distinguish from the Complete Block Shear failure mode when using their respective acronyms.

observations made by numerous other block shear researchers, in that the true reflective failure mechanism is a net section fracture and a gross shear yield plane. The significant underestimation of block shear capacity provided by the AISC 360-16 lies in the fact that the assumed failure mode includes a *net shear fracture*. The work by Pizzuto (2019) laid the foundation for the research presented in this thesis: since block shear failure is a confirmed critical failure mode in W-sections, with good predictive capacity from current design standards, do these conclusions still hold for a W-section under flexure?

2.2 Flange section reductions: The 15% Rule

The CSA S16-14 standard states, in Cl.14.1 (Canadian Standards Association, 2014), Proportioning of Beams and Girders:

> Beams and girders consisting of rolled shapes...shall be proportioned on the basis of the properties of the gross section...No deduction need be made for fastener holes in webs or flanges unless the reduction of flange area by such holes exceed 15% of the gross flange area, in which case the excess shall be deducted.

This clause, known as the *15% Rule*, which has remained in the CSA S16 standard since its introduction in 1954, has had a significant impact on the way Canadian steel designers detail their flexural members and connections (Canadian Standards Association, 1954). Only with the recent release of the 2019 version of the CSA S16 standard has this clause been revisited to reflect the advances in structural steel materials, connection methods, and understanding of ductile steel behaviour. This section provides an overview of the background of the 15% Rule as well as its effect on structural steel design.

2.2.1 Lilly and Carpenter (1939)

The basis of the 15% rule lies in a study performed by Lilly and Carpenter (1939) on the effect of holes in built-up riveted plate girders on the flange stresses experienced during load. A series of built-up plate girders under four-point loading was tested to evaluate the effect of open holes, bolted holes, and riveted holes on the effective moment of inertia, as well as the stresses at the flange extremities. Engineers of this era had multiple options when determining the moment of inertia for the design of built-up plate girders. Typically, the 'net moment of inertia' of the girder was calculated, which was determined by deducting the effect of the *tension flange* holes from the gross moment of inertia. This effectively shifted the neutral axis of the member away from the gross section centroid. The use of this 'net moment of inertia' also relied on two unsubstantiated assumptions: first, it assumed the section behaviour of the plate girder through its entire length is based on the net section with tension flange hole reductions. Since it is clear that tension flange holes are intermittently spaced, with full gross section properties between holes, it should be expected that this 'net moment of inertia' calculation was inherently conservative. Second, it assumed that the net compression flange effectively acted as the gross flange section; the assumption was ostensibly based on the fact that fasteners in the compression flange holes would sufficiently transfer forces across the hole by contact bearing. It was noted that the gross moment of inertia, however, was used by at least some engineers for deflection calculations of the girder.

The results of their test program shed light on the two assumptions stated above. Test specimens were loaded to the same peak deflection within the elastic range. By comparing the observed strains in the tension and compression flange extremities, it was possible to evaluate the effect of holes and fasteners on the moment of inertia, as well as to determine the working neutral axis of the test specimen. First, it was observed that the neutral axis deviated only slightly from the gross section neutral axis, even for the worst-case scenario open hole

sections. Previous calculations of the 'net moment of inertia' provided a significantly shifted neutral axis. This suggested that compression flange deformation was as significant as that of the tension flange, and that compression flange holes should be considered if net moment of inertia calculations are performed.

Second, the observed stresses in the extreme tension flanges were lower than the predictions based on both a traditional net moment of inertia (with an offset neutral axis) as well as a modified net moment of inertia calculation (that assumed the neutral axis remained at the gross centroid). This confirmed the belief that assuming net section properties continuously extend along the length of the member resulted in significant underestimations of flexural capacity. It was also observed that the hole spacings affected the magnitude of this underestimation, with closer spaced holes showing a better correlation between predicted net section behaviour and observed stresses. However, the measured flange stresses were somewhat higher than the calculated values using the gross moment of inertia, suggesting that flange area reductions did have some effect on the overall section properties.

Overall, Lilly and Carpenter concluded that the working moment of inertia approached that of the gross moment of inertia, and that the neutral axis effectively remained at the gross centroid, contrary to the practice at the time. In recognition that the observed moment of inertia lay somewhere between the typical net moment of inertia and gross moment of inertia, Lilly and Carpenter provided an analytical equation for an 'effective moment of inertia' that correlated well with their experimental data, and was influenced by the hole pitch and diameter. However, they concluded that the difference was negligible, and that the gross section area was acceptable for use with most strength and deflection calculations.

These tests were performed on steel grades vastly different than what is typically used in modern construction, with an average yield strength of 265 MPa and an average ultimate strength of 443 MPa. Further, the test specimens were

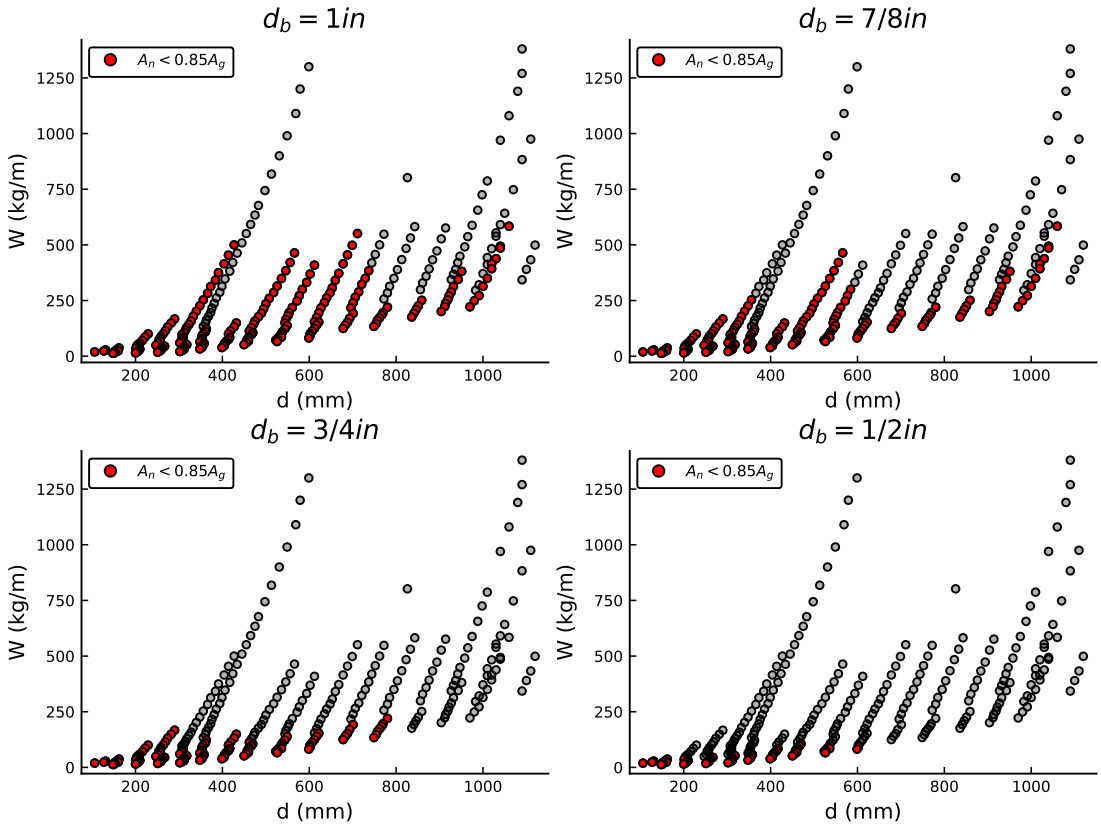

Figure 2.3: All W-sections affected by the 15% rule for 2 bolts per flange as a function of the bolt diameter, d_b, and the beam depth, d.

not loaded to their ultimate capacity. Still, despite the differences in material strengths as well as the limited testing, the findings of this study were adopted into the 15% rule as observed up until the CSA S16-14 standard, where the gross section properties may be used *up to* an A_{fn}/A_{fg} of 85%, past which the net section properties must be used.

2.2.2 Recent findings on the 15% rule

The 15% rule has had a profound impact on the design of steel flexural members for over 50 years. Figure 2.3 shows the significant number of W-sections that trigger this clause when a typical arrangement of two bolt rows per flange is used for a bolted connected. Almost all W-sections used as primarily flexural

members are affected when using 7/8" bolts or larger, reducing the allowable flexural capacity to as much as 75% of the gross capacity. This limitation has left structural designers with two options: design flexural members with significant reduced capacities to account for bolted connections, or specify more expensive welded connections and/or flange reinforcement to allow for full flexural capacity to develop. Research has developed over the past fifteen years to scrutinize the 15% rule and its relevancy with respect to modern materials and design methods.

Sivakumaran et al. (2010), based on the doctoral thesis of Arasaratnam (2008), reviewed the results of 25 tests on ASTM A992 steel W-sections under flexure with varying configurations of holes and fasteners in both tension and compression flanges. The objective of their study was to verify the applicability of the 15% rule on modern steel materials, and to observe the true effect of net flange areas on the ductility and ultimate capacity of flexural members. Twenty-five W200X42 sections were tested under 4-point loading, with a single set of holes in the constant moment region in four general configurations:

1. No holes in flanges
2. Tension flange holes only, up to 50% of gross area removed
3. Holes in both flanges, up to 60% of gross area removed
4. Holes in both flanges, up to 60% removed, with fasteners in holes

Specimens were loaded to the post-ultimate strength range, typically until the load-deflection curve returned to the initial yield load limit. All specimens, without exception, surpassed the gross plastic moment at ultimate capacity regardless of the hole/fastener configuration. The ratio of peak experienced moment, M_m, to the theoretical gross plastic moment, M_p, ranged from 1.07 (63% of gross flange area, both flanges) to 1.23 (85% of gross flange area, tension flange only). Sivakumaran et al. (2010) observed that even for specimens with net flange areas nearing 50% of the gross area, the rotational stiffness in the elastic range changed

very little, and that the reduced flange areas only affected the *peak* rotational capacity of the beam well past the ultimate moment. Almost all test specimens failed in eventual net section fracture of the tension flange, except those with holes in the compression flange *without* fasteners. Some specimens with unfilled compression flange holes experienced local compression flange buckling due to the reduced area, which limited the peak moment capacity of the specimen. With the compression flange holes filled with fasteners, the failure mode returned to a tension net fracture as the fasteners provided an adequate bearing force transfer mechanism. The authors concluded that flexural members of typical modern steel materials that greatly exceed the 15% net flange area rule can reach the ultimate gross section capacity, and that current design methodology was overly punitive. Additionally, the authors noted that although the ultimate flexural capacity is not affected by moderate to significant flange area removal, the available rotational ductility is. For flexural members with a net flange area ratio $A_{fn}F_u/A_{fg}F_y < 0.95$, the rotational ductility of the section may be reduced. However, it was noted that this rotational capacity is dependent on numerous other factors unrelated to the section geometry, such as stability constraints and the rotation capacity and stiffness of the connecting member. The authors concluded with a suggested alternative design method that assumes the complete fracture of the tensile region of the flexural member as the ultimate failure mode:

$$M_{fnf} = 0.85 Z_n F_u \leq M_p \tag{2.8}$$

While the CSA S16 standard for net section flexural capacities remained unchanged since the inclusion of the 15% rule until the S16-2019 edition, the American AISC 360 standard had modified their equivalent rule to the following equation in the AISC 360-05 and onwards (American Institute of Steel Construction, 2005), based on the findings by Geschwindner (2010):

$$F_u A_{fn} \geq Y_T F_y A_{fg} \tag{2.9}$$

$$M_n = \frac{F_u A_{fn}}{A_{fg}} S_x \tag{2.10}$$

Where: $Y_T = 1.0$ if $F_y/F_u \leq 0.80$, $Y_T = 1.1$ otherwise.

This design method assumes the failure mode to be the onset of rupture of the extreme tensile fibre of the *net* flange area. It is noted that this method is valid only if Equation 2.9 does not hold; otherwise, the full gross section moment capacity may be used. Although Equation 2.10 is more involved and provides higher flexural resistances than the 15% rule of the CSA S16-14 standard, its assumed failure mode and reduced overall resistance is still not consistent with those observed by Arasaratnam (2008) and Geschwindner (2010).

For these reasons, Swanson (2016) performed an aggregate review of bolted W-section flexural capacity tests from five different universities (Larson, 1996; Swanson & Leon, 2000; Schneider & Teeraparbwong, 2002; Altstadt, 2004; Sato et al., 2007) to evaluate the true observed failure mechanisms, as well as the predictive capacity of the AISC 360 design equation. Like the results observed by Sivakumaran et al. (2010), an average ultimate flexural capacity of $1.06M_{p,gross}$ was observed across all test specimens, with A_{fn}/A_{fg} ratios reaching as low as 70%.

Swanson (2016) made two conclusions on the state of current design methods for flexural W-sections with reduced flange areas that complemented the conclusions of Sivakumaran et al. (2010): first, current design methods for net flexural capacities are overly conservative, with almost all observed test specimens reaching the full gross plastic moment capacity before ultimate failure. Second, the current design methodology is removed from the actual observed failure mechanisms for these flexural members. Both the simplified 15% rule of the CSA S16-14 and the revised method in the AISC 360-16 are only triggered by strict clauses; in other words, for the CSA S16-14 method, a section with a net flange area ratio of 14.9% would have a significantly different flexural resistance than a section with a ratio of 15.1%. For the AISC 360-16 method, this sudden jump in

section capacity is also met with a sudden change in the assumed failure mode from a gross section plastic moment failure to the fracture of the extreme tensile fibre of the section. Based on these findings, Swanson suggested an improved design equation that better correlated with the observed test results, eliminated the sudden shift in flexural capacity, and was more reflective of the true observed failure mode:

$$M_n = \frac{F_u A_{fn}}{A_{fg}} S_x + F_u Z_{x,web} \leq F_y Z_x \tag{2.11}$$

Equation 2.11 properly reflects the observed failure mode with the onset of flange rupture with the remaining section under complete yielding.

In light of contemporary evidence of the inadequacy of the 15% rule in the CSA S16 design standard, and based on the work of Sivakumaran et al. (2010), the most recent 2019 version of the CSA S16 standard has revised and expanded on Clause 14.1 for the first time since its introduction (Canadian Standards Association, 2019). For steel materials with $F_y \leq 350MPa$, and whose flange area reductions do not exceed 15%, the gross section properties may still be used like in previous iterations of the 15% rule. The major difference is the treatment of flexural members that do not meet either the yield strength requirement ($F_y > 350MPa$), or the 15% maximum flange area reduction, with the introduction of *effective section properties*, S_e and Z_e respectively.

$$S_e = \alpha S + S_n \leq S \tag{2.12}$$

$$Z_e = \alpha Z + Z_n \leq S \tag{2.13}$$

Where S_n and Z_n are the calculated *net* section modulus and plastic modulus, and with values of α varying depending on the material yield strength (above or below $350MPa$), as well as the location of the fastener holes (one flange only vs. both flanges). For values of $F_y \leq 350MPa$, α is a fixed value equal to 0.05

for sections with holes in one flange only, and 0.12 for sections with holes in both flanges. For values of $F_y > 350MPa$, an upper limit for the value of α is introduced:

$$0 \leq \alpha \leq \left[1 - \beta \left(\frac{F_y}{F_u}\right)\right] \tag{2.14}$$

With the value of β based on whether there are holes in one flange ($\beta = 1.24$) or both flanges ($\beta = 1.15$).

The inclusion of Equations 2.12 to 2.14 has provided much needed clarity and improvement on the design of flexural members with fastener holes exceeding 15% of the gross flange area. First, Equations 2.12 and 2.13 imply that the failure mode of W-sections that trigger the 15% rule clause will be identical to that of their equivalent gross section, albeit at a reduced capacity; class 1 and 2 sections will still reach the ultimate flexural capacity at full plasticity of the reduced section, while class 3 sections will reach their capacity at the onset of yielding of the reduced section. This is in contrast to the AISC 360-16 design method (Equation 2.10), which assumes a sudden change to a fracture failure mode should its equivalent net flange area ratio limit be surpassed. Maintaining the assumption of a ductile failure mode is in accordance with the findings of the most current research (Topkaya, 2004; Sivakumaran et al., 2010; Geschwindner, 2010; Swanson, 2016).

Second, the addition of the α parameter significantly increases the allowable flexural capacity of a section triggering the 15% rule clause, and eliminates the sudden drop in flexural capacity as soon as the 15% net flange area ratio threshold is crossed. For a typical steel section with $F_y \leq 350MPa$, and holes in both flanges, an additional 12% of the gross section property (Z, S), is included in the effective section and plastic moduli. This additional 12% increase in the flexural capacity of a reduced-area W-section effectively provides a smooth transition from gross section flexural capacities to a reduced capacity for sections with net flange area ratios of 85% or less.

Third, the use of different α values for higher strength steel sections reflect

the need for a more conservative design approach for steel materials with higher F_y/F_u ratios. As noted by Sivakumaran et al. (2010), flexural sections with higher F_y/F_u ratios are more susceptible to a tensile fracture failure, even if it occurs past the gross plastic moment capacity of the section, and are also more susceptible to a reduced rotational capacity. Providing a lower value of α for these material types provides a level of additional precaution while maintaining the same methodology for calculating effective section properties.

The revised CSA S16-19 Cl.14.1 provides a much needed change to the 15% rule in the context of current knowledge and modern steel materials. As Canadian steel designers transition into the S16-19 standard, the true effect of the improved allowable performance of reduced flange area flexural members can be determined. However, considering the research that this revised method is based on, it should still be expected that the calculated reduced flexural capacity of many W-sections will still be below the true available capacity. Whether this discrepancy remains too punitive for Canadian steel designers, or whether the revised design method provides a sufficient compromise and a real-life benefit is yet to be seen.

With the AISC 360-16 method for net section flexural resistances detached from the true observed mechanisms of net section flexural failure, as well as a new and unproven CSA S16-19 method, it is not clear if there is an overlap or redundancy between the net flexural resistance calculations and other failure modes associated with bolted flexural members. Namely, if the block shear failure exists in bolted flexural W-section members, and if current design equations can accurately predict these failure modes, do they implicitly consider the effect of flange area reductions on the overall flexural capacity of the member? Is the 15% rule relevant if a more low-level analysis of the block shear failure mode is taken? On the contrary, if the 15% rule clause is *not* triggered, does this provide an avenue for designers to not explicitly check the block shear failure mode for flexural members? Further, it is not even clear whether the 15% rule should *ever* be applied in a bolted flexural connection for W-sections, which

naturally must occur at the beam ends, whether it is at a moment splice or a beam-column connection. The intent of the 15% rule was to evaluate the overall flexural capacity of a section with reduced cross-sectional area, and not as a check on a force transfer mechanism.

2.3 Contemporary design procedures for Block Shear

The extensive research on block shear failure has resulted in many suggested design equations to both accurately and safely predict the capacity of a given tensile bolted connection. However, many of these proposed equations are too involved for practical use by designers, and as such, design standards have adopted and maintained calculation approaches that are relatively simple to implement. This section provides an overview of the current design equations used by the CSA S16, AISC 360, and the Eurocode 3 standards.

2.3.1 Canadian design procedure (CSA S16-19)

The Canadian design standard specifies in Cl.13.11, the block shear resistance as:

$$T_r = \phi_u[U_t A_n F_u + 0.6 A_{gv} \frac{F_y + F_u}{2}] \tag{2.15}$$

Where:

ϕ_u = Resistance factor = .075

U_t = Efficiency factor = 1.0 for Flange-connected Tees

And where the $(F_y + F_u)$ term is replaced by F_y for $F_y > 460MPa$.

This equation is based on a modification of the proposed unified equation by (Driver et al., 2006), It is noted that there is no explicit suggested value for the efficiency factor for W-sections, nor are there any suggestions for bending-induced

tensile stresses. However, it is reasonable to assume that the efficiency factors for structural tees would adequately apply to tensile W-sections, given no explicit suggestions are provided.

2.3.2 American design procedure (AISC 360-16)

The current AISC Load and Resistance Factored Design (LRFD) provision for block shear failure is provided in AISC 360-16, equation J4-5:

$$\Phi R_n = \Phi \left[0.60 F_u A_{nv} + U_{bs} F_u A_{nt}\right] \leq \Phi \left[0.60 F_y A_{gv} + U_{bs} F_u A_{nt}\right] \tag{2.16}$$

Where:

$\Phi = 0.75$

$U_{bs} = 1$ (uniform tension stress), 0.5 (nonuniform tension stress)

The AISC specified capacity of the block shear failure mode is the combination of the lower of the net section shear fracture or gross section shear yield along with the net section tensile fracture. The efficiency factor, U_{bs}, is either 1 or 0.5, depending on the tensile stress distribution. It is unclear whether the uniformity of the tension stress distribution is with respect the the fracture plane area only, or across the entire section of the member in question.

2.3.3 European design procedure (Eurocode 3-2005)

The European code specifies separate equations for concentric and eccentric loading. For symmetric bolt groups subject to concentric loading (Eq. 3.9):

$$V_{eff,1,Rd} = \frac{f_u A_{nt}}{\gamma_{M2}} + \frac{f_y A_{nv}}{\gamma_{M0}\sqrt{3}} \tag{2.17}$$

For a bolt group subject to eccentric loading (e.g., coped beams):

$$V_{eff,2,Rd} = \frac{f_u A_{nt}}{2\gamma_{M2}} + \frac{f_y A_{nv}}{\gamma_{M0}\sqrt{3}} \tag{2.18}$$

Where:

A_{nt} = net tension area

A_{nv} = net shear area

$\gamma_{M0} = 1.00$

$\gamma_{M2} = 1.25$

The Eurocode 3-2005 generally follows the same procedure as the AISC 360-16 design method, but without the upper bound in place for the transition into a gross shear yield failure mode. Regardless of material ductility and relative strengths of each failure plane, the assumed failure mode for the Eurocode 3-2005 design method is always a complete fracture of the block. It is also noted that the shear strength of $f_y/\sqrt{3}$ used by the Eurocode 3-2005 is equivalent to the 0.60 factor used by the AISC 360-16 and the CSA S16-19 methods; the use of 0.60 is simply a rounded value of the Von Mises shear yield criterion of $f_y/\sqrt{3}$.

2.4 Finite Element Modelling

To expand beyond time-intensive and expensive laboratory testing, finite element modelling has been extensively used to explore the block shear failure mechanism. The use of finite element modelling software allows researchers to quickly explore the varying parameters that affect the block shear failure mode, allowing for a more complete understanding of the underlying mechanisms. However, there must be careful consideration when developing these models to ensure they are representative of true physical scenarios: the representation of material behaviour in complex stress states; boundary conditions and other simplifications of external factors of loading; proper definition of failure criteria.

Linear elastic two-dimensional finite element models were developed early on

in block shear research, and the methods and technology used have progressed over time. Different element types, material definitions, and boundary conditions have been used to varying degrees of accuracy. An active field of research is the modelling of rupture initiation and the corresponding post-ultimate behaviour of the connection. This section provides an overview of the varying techniques used by researchers to evaluate the block shear failure mode via finite element modelling.

2.4.1 Initial methods of finite element analysis

After the first instance of block shear failure was observed by Birkemoe and Gilmor (1978), Ricles and Yura (1983) set to perform a parametric analysis of coped beams to determine the effects of bolt spacings, edge distances, and single or double row bolt configurations on the block shear failure mode. The objective of the study was to determine how the different parameters affected the stress distribution along the tension and shear planes. The study included a series of finite element models to explore the variation of stresses in the main failure planes. Due to computational limitations of the time, significant simplifications were made on the FE models to represent the true test conditions. First, both the beam and the connecting clip angle were modelled with two-dimensional planar elements, using a combination of four-node quadrilateral and three-node triangular elements. The use of planar stress elements significantly reduce computational time, but are unable to capture any effects of out-of-plane deformations, whether it is the buckling of the web, or the out-of-plane necking of the net tensile region. Second, the connecting clip angles were simplified with spring boundary conditions. Third, bolt holes were not modelled as circular absences in the planar beam model, but rather as square absences to match the element types used for the model. The force transfer from the bolts was modelled as nodal ties between the theoretical connecting surfaces of the square bolt "hole" in both the clip angle and the beam web. This simplified the connection to an infinitely rigid, always-in-contact

transfer of shear between the beam web and the connecting plate. Despite these simplifications, the general results derived from the finite element analyses provided additional insight on the block shear failure mechanism. Namely, that the free edge distance of the tension plane has a great effect on the stress concentration and distribution of the failure plane; that a second row of bolts creates a highly non-uniform stress distribution on the tension plane, which reduces the capacity at failure, and; the most typical stress distribution of the block shear failure path at capacity was a tensile fracture with a shear yielding plane.

Since the first finite element models were performed by Ricles and Yura (1983), many block shear researchers developed their own models for varying section types and loading configurations to further understand the mechanics of the failure mode. Epstein and Thacker (1991) used finite element modelling techniques to investigate the block shear failure mode for single-leg connected angles. They developed FE models to investigate the effect of out-of-plane eccentricities and the corresponding shear lag on the tensile capacity of single-leg bolted steel angles, as well as the possible strengthening effects of bolt stagger. Since single-leg connected angles will experience out of plane as well as torsional deformations, the authors developed a model using four-node quadrilateral shell elements that were unrestrained from out of plane deformations. The models also included realistic circular bolt holes as opposed to the square estimates of Ricles and Yura (1983). However, some simplifications remained: the variation in thickness of the web-heel fillet can not be captured using shell elements; only material non-linearity is modelled, as necking in the out-of-plane direction for shell elements is not captured.

Epstein and Chamarajanagar (1996) improved on these limitations by using three-dimensional 20 node hexahedral elements (C3D20) in their correlation models with previously tested single-leg connected steel angles. The use of 3D elements allowed for geometric non-linearities to be captured as well as the ability to directly correlate FE results to strain gauge readings that are placed on the

exterior surfaces of the test specimens. It also allowed for a better representation of the true geometric properties of the tested specimens. Failure of the tension plane was based on interpolated strain data between two nodes on opposing sides of the expected failure plane; once the interpolated strain reached a predefined failure limit, ranging from $2\epsilon_y$ to $5\epsilon_y$, the ultimate strength of the fracture plane was assumed to be reached. The authors do not mention how or if the strain and stresses of the shear plane were evaluated.

Topkaya (2004) expanded the finite element analyses study of block shear failure in both gusset plates and single-leg connected angles. Over one thousand analyses were performed to evaluate the predictive capacities of the AISC 360 block shear equations at the time. For this study, three-dimensional ten-node tetrahedral elements (C3D10) were used to model the angles, while two-dimension, six-node triangular plane stress elements (CPS6) were used to model the gusset plate. These elements were selected for their ability to handle large in-plane deformations and material non-linearities. The models used a generic true stress-strain response of an elastic perfectly plastic response, and then a linear strain hardening region, with a stress plateau once the ultimate strength was reached. The predictive capacity of these model parameters were tested on previous laboratory test results, showing a professional factor of 0.990, indicating a good representation by the finite element models (Hardash & Bjorhovde, 1985; Gross et al., 1995; Orbison et al., 1999).

Pizzuto (2019) performed FE analysis for the initial confirmation of block shear failure in flange-connected W-sections under pure tension, before performing laboratory tests on full-scale representative sections. FE analysis was also redone using calculated geometric and material measurements to compare and calibrate against the laboratory results. All relevant parts were modelled using solid elements to best capture significant deformations, both in and out of plane. C3D8 brick elements were used for the W-section, splice plates, and bolts. while C3D6 wedge elements were used for the K-area as it better suited the curved and

triangular geometry. The load displacement vs. applied force curves of the FE models had very good correlation to the observed test results up to the ultimate load point. As expected, since no simulation of fracture was implemented, the FE models could not accurately reflect the post-ultimate behaviour of the overall section. However, qualitative observations between the simulated and true deformed shapes of the connection region past the ultimate capacity of the section showed a very reasonable predictive capacity of the FE models. For these reasons, the FE modelling of this thesis is widely based on the methodology used by Pizzuto.

2.4.2 Modelling of fracture in block shear failure

Although the studies discussed in the previous section used a range of finite element modelling techniques to varying degrees of accuracy, none of the mentioned studies modelled the initiation and propagation of fracture in the tensile failure plane. Although these non-fracture models can accurately represent the stress distributions up to the failure point (the initiation of fracture), understanding the complete failure mechanism requires the ability to model the post-ultimate behaviour of a given connection. The different methods used to represent the rupture path of tension and shear planes in block shear tensile failure are explored in this section.

Huns et al. (2006) performed an in-depth finite element study of block shear in gusset plates to investigate the exact failure mechanism and progression of block shear. The models were developed using four-node, reduced-integration shell elements (S4R), which allowed for changes in element thickness. The material true stress-strain behaviour up to the engineering ultimate strength was derived from averaged tensile coupon testing results, with post-ultimate true stress-strain behaviour (up to $\epsilon = 1.2$) based on a previous study on ductile structure steel by Khoo et al. (2000). Fracture was modelled via a *deletion* method, where an element was removed from the analysis model once the major principal strain of the element integration points reached the average tensile rupture strain based on

coupon testing results; in this study, this total (elastic + plastic) strain was $\epsilon = 1.13$. The modelling of the shear plane was slightly more involved: the shear strain at the point of rupture during tensile coupon testing was recorded, and acted as the shear strain corresponding to shear fracture. A similar deletion method was used, where once the integration points of an element reached this maximum shear strain, the element was removed from the analysis. The predictive capacity of these models were tested against eight different laboratory results on gusset plate block shear failure, with a mean professional factor of 1.04.

Wen and Mahmoud (2017) developed a more involved method to represent fracture in FE models of block shear failure in gusset plates. Their work developed an analytical method of approximating the rupture strength of the shear plane based on the inclusion of the *Lode Parameter* in addition to the stress triaxiality used to model tensile fracture. They developed a damage model to represent the plastic strain in a given element as a proportion of the total strain energy capacity. The damage value, D, was checked at each iteration of the finite element analysis, and the elements with $D > 1$ was deleted before the next iteration. The authors used reduced-integration, two-dimensional planar stress elements (CPS4R) for their analysis. Testing the predictive capacity of these models to previously tested laboratory results showed an extremely high degree of accuracy that extended well past the ultimate capacity of the connection. The inclusion of the new damage parameter allowed for an accurate modelling of post-fracture behaviour of the gusset plate.

Elliott and Teh (2019), while evaluating the validity of the *Whitmore Net Section* capacity calculation method, performed finite element models of bolted gusset plate connections that included fracture modelling. For the best representation of out-of-plane element deformation, three-dimension, eight-node hexahedral elements were used (C3D8R). Like previous researchers, fracture was modelled using damage initiation parameters and an element deletion method. A true stress-strain material curve was defined using the Ramberg-Osgood power func-

tion (Ramberg & Osgood, 1943), and the stress triaxiality and strain at fracture were defined based on previous tension coupon testing by Aalberg and Larsen (2000). Once an element reached these limits, it was deleted from subsequent steps in the analysis.

2.5 Summary

Block shear as a failure mode for bolted connections has been observed, studied, and calculated for over 50 years. Through extensive laboratory testing and finite element analysis, the Canadian S16 design standard has provided an accurate and general method of predicting block shear strength capacities. The CSA S16-19 design method for block shear failure assumes a gross shear yielding plane and a net tensile fracture plane for a given block, with an efficiency factor, U, that accounts for non-uniform stress distributions from in-plane eccentricities; while the U factor was initially calculated as a function of the connection length as well as the bolt group eccentricity, it has largely been replaced by tabulated values based on direct tension test results on plates, angles, and structural tees.

Until recently, however, the block shear failure mode had not been explicitly verified for flange-connected W-sections, despite their widespread use in structural steel design. It was generally accepted that the efficiency factor could be borrowed from flange-connected structural tees due to the inherent symmetry of W-sections. This verification was finally performed by Pizzuto (2019), where finite element analyses and full-scale laboratory testing concluded that the CSA S16-14 design method (unchanged in 2019) calculated accurate predicted capacities for flange-connected W-sections under pure tension. The results from Pizzuto also confirmed that the failure mechanism as assumed by the CSA S16 standard, consisting of a gross shear yield plane and a net tension fracture plane, accurately reflected the observed failure mechanism in the laboratory tests.

With this failure mode and corresponding predictive equation verified and

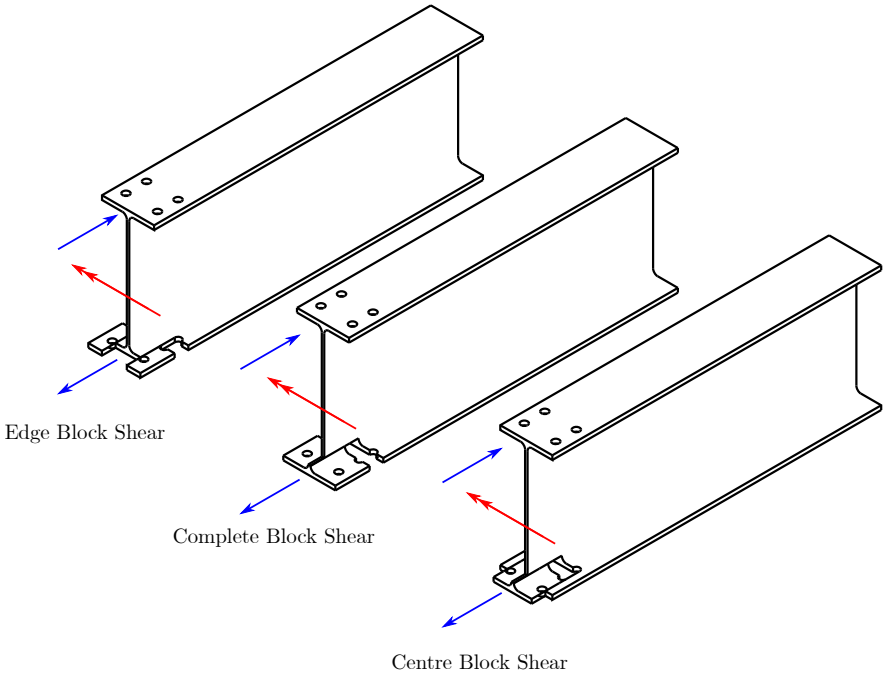

Figure 2.4: Potential moment-induced failure modes for W-sections under flexure.

assessed for W-sections in pure tension, it is natural to consider the same questions for the tension flange of a bolted W-section connection under moment, since W-sections are widely used as flexural members. A potential block shear failure scenario could occur at beam ends for moment-frame bolted connections, as well as mid-span in bolted beam splices; three possible moment-induced block shear failure modes are presented in Figure 2.4. Although the effect of relatively small induced moments due to connection eccentricities have been studied in the context of block shear failure, it is to the author's knowledge that the effect of a directly applied moment on the block shear failure mode and predictive capacity has not yet been performed; this corresponds well to the fact that most studies on the block shear failure mode have been performed on sections that are not used as flexural members, namely gusset plates, angles, and tees.

Further complicating the study of block shear under moment-induced tension is the potential conflict or redundancy with the *15% Rule* found in the CSA S16 design standard, that reduces the allowable flexural capacity of W-sections

with reduced flange areas due to bolt holes. It is unclear whether the flexural capacity corresponding to a potential tension flange block shear failure inherently covers the effect of bolt holes in flexural members, or if the 15% rule must also be considered during design. Further, it is unclear whether the 15% rule is applicable at all in the context of beam ends, since the origins and subsequent research that the rule is based on is with respect to hole along the mid-span of the beam.

Through a series of finite element analyses and corresponding full-scale laboratory tests, this thesis aims to shed light on the following questions. First, is block shear in the tension flange a real possibility for bolted W-section connections under flexure? Second, can the current design equations in the CSA S16, AISC 360, and Eurocode 3 standards accurately predict this failure mode? And third, does the 15% rule play any part in the design and detailing of a flange-connected bolted splice plate W-section under flexure, or should this rule be reserved for bolt holes placed along the mid-span of a beam?

Chapter 3

Preliminary verification of moment-induced block shear and selection of laboratory test specimens

Before the predictive capacities of the current block shear design equations can be evaluated in the context of moment-induced tension in the flange of W-sections under flexure, the *possibility* of this failure mode must first be confirmed. Further, should the moment-induced block shear failure mode be a possibility, the predictive capacity of current design equations should be evaluated. These questions were addressed in three phases. First, a general iterative design methodology was developed for the selection and detailing of a bolted splice plate connection under pure moment that would theoretically fail in moment-induced block shear. Second, the design methodology was used to select five initial section-connection details that would be modelled using finite element analysis, and fabricated to test in the structural laboratory for finite element analysis calibration. Next, the five section-connection details were developed into preliminary finite element

models (pFEMs) to verify the analytic assumptions and expected loads at failure. The configuration of the finite element models were developed to replicate the conditions of the structural laboratory at McGill University, as seen in Figure 3.1, to allow for a direct comparison with laboratory test results. This section provides an overview of the selection of the preliminary test specimens, which include the development of the analytical design, as well as the development and verification of the initial finite element models.

3.1 Selection of initial test specimens

The selection of five initial preliminary models with moment-induced block shear critical connection details required the development of a consistent design methodology. In the early stages of the development of this methodology, it was observed that the theoretical moment-induced failure mode for W-sections was highly sensitive to varying geometric factors of the section itself, as well as the number of bolts that are required to carry the block shear capacity in the flange. However, basic requirements were defined before the completion of the design methodology and specimen selection to guide the process and to reduce the range of viable sections:

1. The section chosen should reflect a typical W-section used for beam elements.

2. The section should be ideally a Class 1 section to avoid premature local buckling of the flange and/or web.

3. The connection should be detailed such that the block shear failure mode is critical.

4. The critical block shear failure strength should ideally occur while the gross section remains elastic.

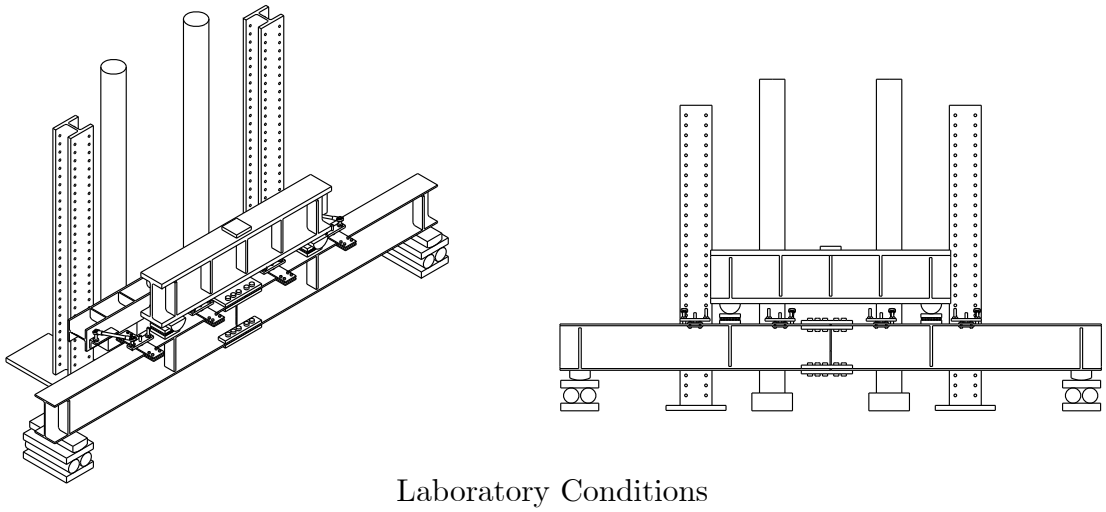

Laboratory Conditions

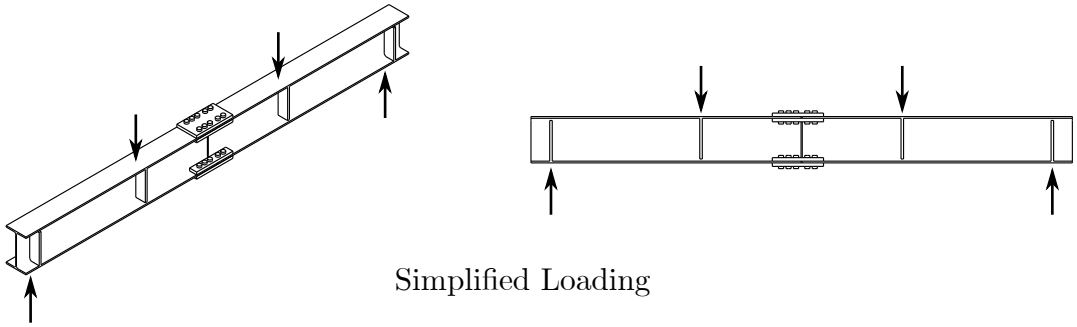

Simplified Loading

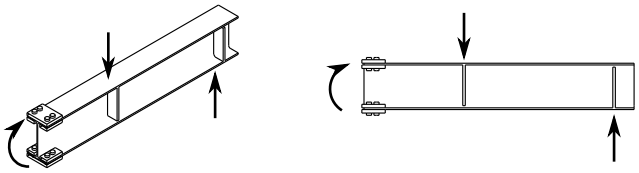

Modelled Region

Figure 3.1: Translation of laboratory test conditions into modelled region.

5. All peripheral elements (bolts, splice plates) should remain well within their elastic range at the point of block shear failure.

6. The critical required load should be below the capacity of the laboratory actuator (11 MN).

This section provides a detailed overview of the geometric constraints for moment-induced block shear, as well as the final design methodology and the selection of the five preliminary test specimens to be numerically modelled as well as fabricated and tested in the structural laboratory.

3.1.1 Effect of section geometry on moment block shear failure potential

Due to the widespread use of W-sections in all load bearing applications, there is an extensive range of available depths, widths, and linear masses. Various geometric properties of a given W-section influence the range of possible failure modes for a bolted moment connection, including the flange thickness, flange width, as well as the depth of the section.

Since the failure plane areas for both the gross shear yield and net tension fracture are proportional to the flange thickness, sections with relatively thick flanges require a greater amount of force to induce the block shear failure mode. A larger force at block shear failure would require additional rows of bolts to carry this force. However, this addition of bolts further increases the block shear resistance due to the increased connection length, and often leads to a required moment-at-failure that is greater than the gross section capacities, namely M_y and M_p. A visual example of this conflicting requirement is shown in Figure 3.2. For heavy flange sections, it was determined to be impossible to detail a connection such that the block shear failure mode was critical *while* maintaining adequate bolt strength and remaining below gross section capacities.

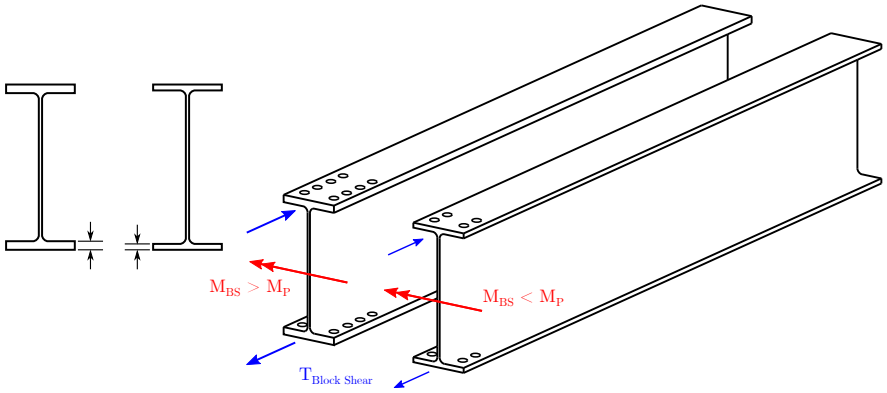

Figure 3.2: Comparison of thick vs. thin flanges for block shear sensitivity.

In a comparison of deep to shallow sections, the induced flange forces for an equivalent moment in deep sections are much lower due to the larger moment arm between the compression and tension flanges. Therefore, for an equivalent moment splice connection detail, a deeper section must be loaded to a greater moment to reach the block shear strength capacity of the connection, as shown in Figure 3.3. It was observed that with bolt spacing details consistent with those used in practice, this required moment often encroached on the gross section moment capacities, and made it difficult to isolate the moment-induced block shear failure mode. However, on the contrary, shallower sections, although they have a greater induced flange force for a given applied moment, also typically have smaller gross section flexural capacities. Therefore, a shallower beam did not immediately allow for a block shear critical connection, because the minimum block shear force may still exceed the gross section capacity due to its inherently lower flexural strength.

Further, sections with narrow flanges caused geometric limitations when detailing the connection and splice plates, as seen in Figure 3.4. The narrow width of the flange compounded by the reduction of usable space in the flange interior due to the fillet region made the detailing of the interior splice plate difficult or impossible to meet CSA S16-19 edge spacing limits (Canadian Standards Association, 2019).

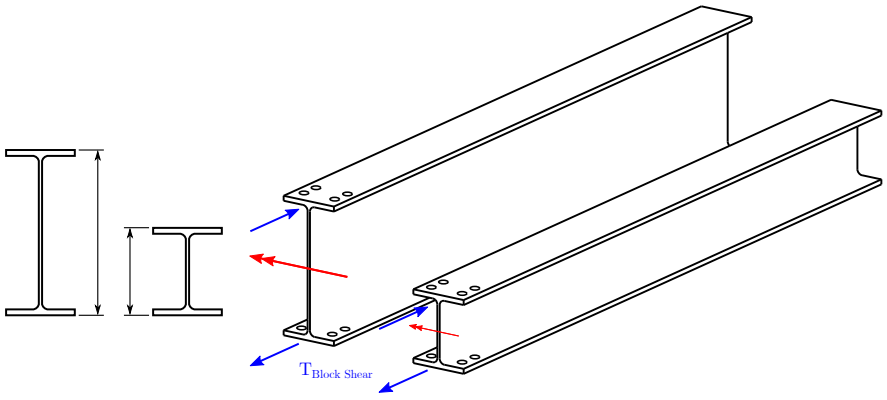

Figure 3.3: Comparison of deep vs. shallow sections for block shear sensitivity.

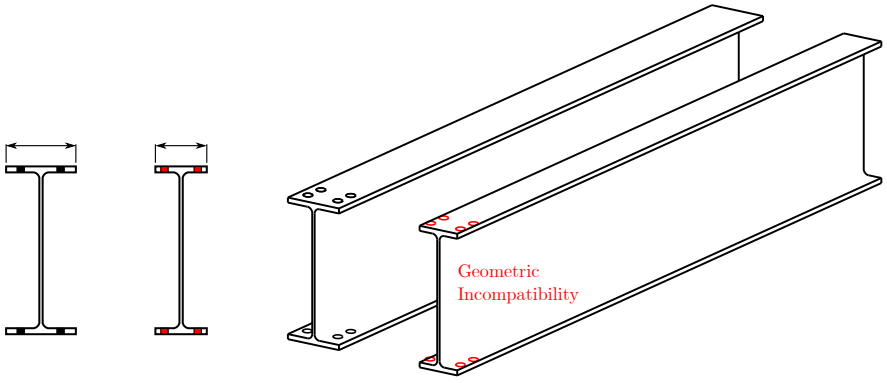

Figure 3.4: Comparison of wide vs. narrow flanges for block shear sensitivity.

In general, it is noted that the potential for a moment-induced block shear failure to occur in a bolted flange splice connection is limited to relatively shallow sections with moderate-to-thin flange thicknesses, with a moderate-to-wide flange width. In addition to these specific section geometry limitations, it is noted that the number of required bolts in each flange greatly affects the possibility of a block shear critical connection detail. For every new row of bolts added to a flange, the connection length increases significantly due to the minimum spacing requirements for fastener holes. This increase in connection length increases the shear component of the block shear failure mode, and often leads to a block shear resistance surpassing the gross section capacity for flexure.

3.1.2 Section selection and connection detailing

With the initial geometric limitations in mind, W-sections were selected by random, and a block shear critical moment splice connection detail was attempted. The detailing of the connections relied on certain base assumptions and requirements:

1. The connection is a bolted moment splice under pure moment only.
2. No web splice is provided – all force transfer occurs through the flanges.
3. Full lateral stability is provided for the beam.
4. Bolts are in double-shear, with both interior and exterior splice plates[1].
5. The induced force in each flange is assumed to be $M_{applied}/(d - t_f)$, i.e. the assumed moment arm of the force couple is between the centroids of the two flanges.

[1] bolts in double-shear were specified to provide the shortest connection length possible for a given bolt diameter. As previously discussed, the moment-induced block shear failure mode was found to be highly sensitive to the overall connection length of the bolt group.

The design methodology (outlined in Figure 3.5) was automated via *Julia* functions in a step-by-step procedure template created in *Jupyter Notebooks* (Kluyver et al., 2016). Using *Jupyter Notebooks* allowed for visual exploration of all possible combinations of bolt diameter, end distance, edge distance (gauge), and pitch, and ensured that all connection details met CSA S16-19 distance requirements at all times. *Jupyter Notebooks* also provided the added benefit of easy annotation and case-by-case notes for each test specimen.

The semi-automation of the preliminary design phase was especially necessary due to its trial-and-error nature. Although general limitations in section geometry were understood before the preliminary design phase, these limitations were only relative measures; it was unclear as to what constituted a "narrow" flange or a "deep" section in absolute value terms.

3.1.3 Sample design methodology for M5: W610X101

This section provides the step-by-step design methodology for one of the six section-connection details that were selected for fabrication for full-scale laboratory testing, detailed in Section 3.1.4; the selected specimen was a W610X101 section, whose geometric properties relative to other W-sections is shown in Figure 3.8. The logic of each step is presented, along with the basic performed calculations. Full design checks and S16-19 spacing limit calculations are not explicitly shown, but are performed when following the workflow in Figure 3.5.

First, basic assumptions of material strengths were defined:

$$F_y = R_y F_{y,nominal} = 1.1 \times 350 = 385MPa \text{ (ASTM A992, probable)}$$
$$F_u = 460MPa \text{ (ASTM A992, nominal)}$$
$$F_{u,bolt} = 1050MPa \text{ (ASTM F3125 Grade A490[1])}$$

Since the objective of this study was to evaluate the predictive capacity of existing block shear design equations, and not to evaluate their statistical level

[1]American Society for Testing and Materials (2019)

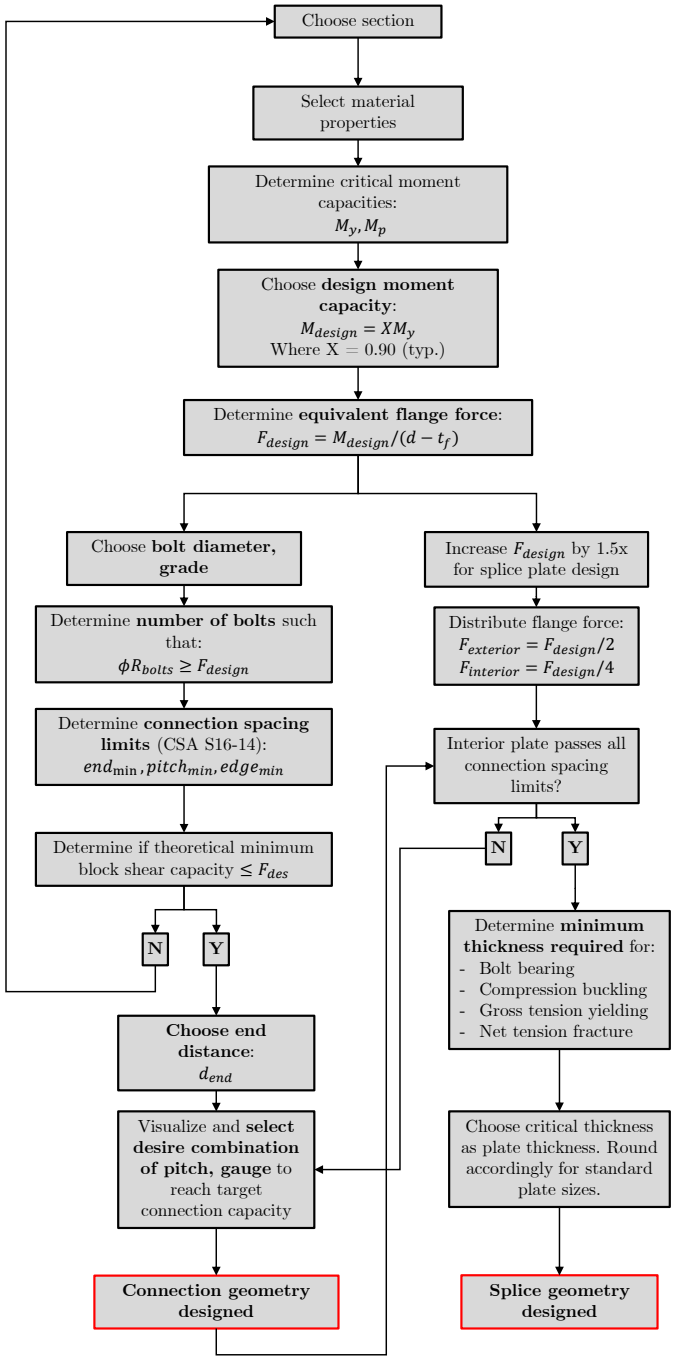

Figure 3.5: Specimen detailing methodology

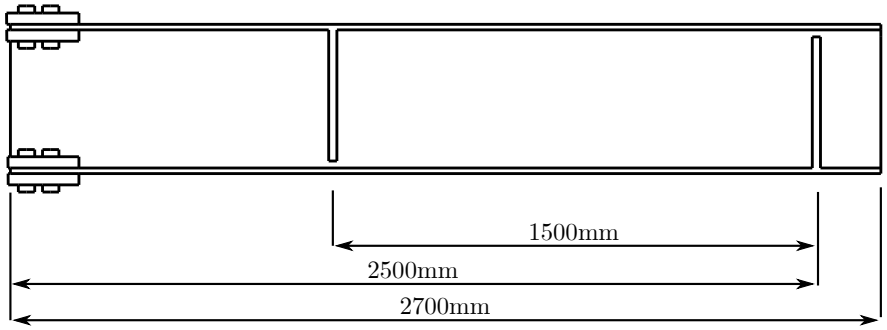

Figure 3.6: Final designed M5 test specimen.

of safety, probable material capacities and unfactored design equations are used. The nominal yield strength, F_y, is multiplied by 1.1 to determine the probable yield strength as per the CSA S16-19 Cl.27.1.7 (2019) for seismic design. It is noted that the ultimate strength, F_u, was left at its nominal value as no direct method for a probable ultimate strength value is provided in the CSA S16-19 standard. During the finite element analysis of these designed specimens, probable material strengths based on the coupon testing results of similar sections performed by Pizzuto (2019) were used.

Second, the basic bolt information was defined:

$$d_b = 7/8\text{”}$$
$$\text{Hole tolerance} = 2mm$$
$$d_h \approx 24mm$$
$$\text{Shear planes} = 2$$

The selection of the initial bolt diameter was arbitrary, but was typically chosen to be either 7/8” (22.2mm) or 1” (25.4mm). This provided an ideal compromise between strength (reducing the number of total bolts required per flange), while minimizing the reduction in flange area as well as minimizing the require bolt spacing limits.

Then, since the ideal critical block shear failure moment occurs *below* the yield moment of the gross section, a target moment value, M_{des}, was determined

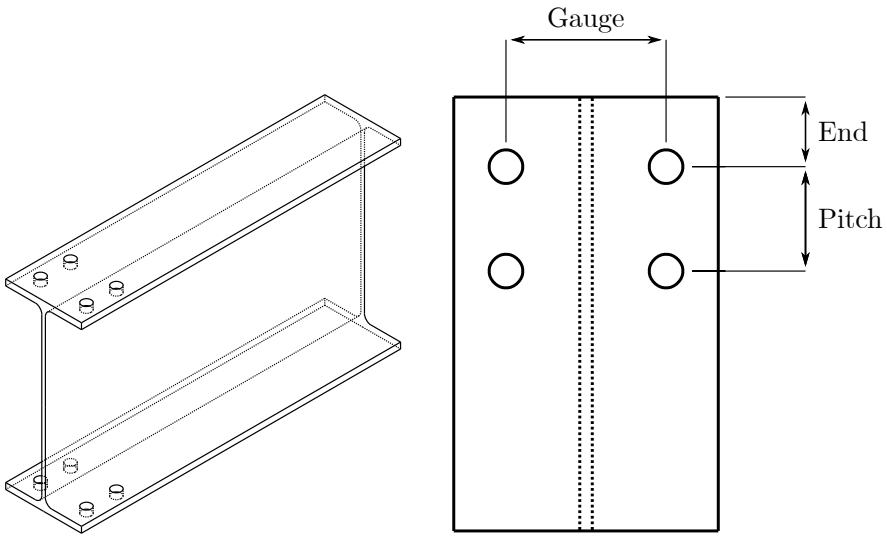

Figure 3.7: Definition of Pitch, Gauge, and End distances

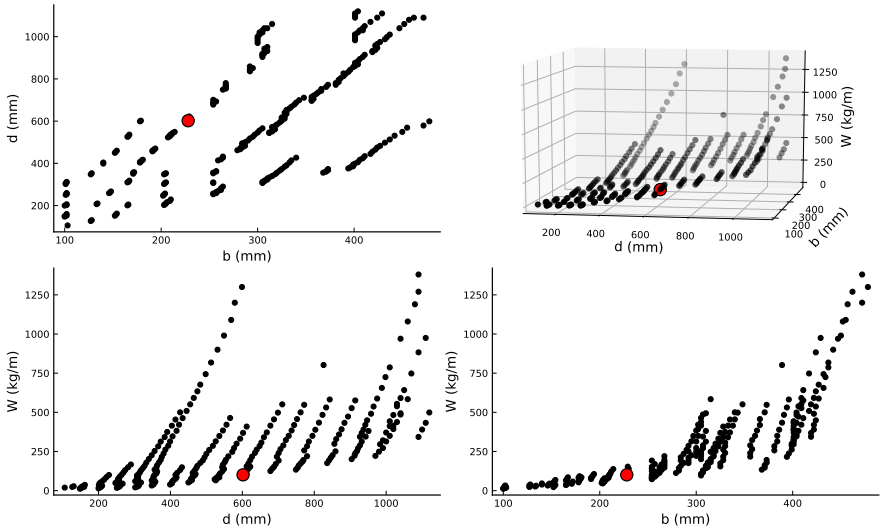

Figure 3.8: W610X101 W-Section properties

as a proportion of the yield moment, M_y. This proportion was typically taken as $0.80M_y$, but was adjusted depending on the section.

$$M_{des} = 0.80M_y = 0.80S_xF_y = 776kNm \tag{3.1}$$

As the moment splices were detailed without any web connections, *the entire moment must transfer through the flanges*. The design moment was then translated into a design *force* by assuming a moment arm between the compression and tension flange centres.

$$F_{des} = \frac{M_{des}}{d - t_f} = 1322kN \tag{3.2}$$

Then, a block shear resistance of the tension flange equal to F_{des} would correspond to a moment design equivalent to $M_{des} = 0.80M_y$, and would be the critical moment resistance of the section. At this stage, a preliminary check on the capacity of the fasteners was performed. To maximize the potential for a block shear critical moment connection, it was important to minimize the overall connection length by minimizing the number of bolts used in each bolt row. To determine this minimum viable number of bolts per flange, the target block shear capacity F_{des} was divided by the shear resistance of an individual bolt. Nominal material strengths and unfactored strength equations were assumed for the bolt, and two shear planes were used, as both interior and exterior splice plates were specified.

$$V_{r,shear} = 0.6F_{u,bolt}nA_b \tag{3.3}$$
$$= 0.6(1050)(2)(\frac{\pi 22.2^2}{4})$$
$$= 489kN$$
$$V_{r,bearing} = 2.4F_{u,beam}d_b t_f \tag{3.4}$$
$$= 2.4(460)(22.2)(14.9)$$
$$= 366kN$$
$$V_r = min\left[V_{r,shear}, V_{r,bearing}\right] \tag{3.5}$$
$$= 366kN$$

Then:

$$n_{b,min} = \frac{F_{des}}{V_r} \tag{3.6}$$
$$= \frac{1322}{366}$$
$$= 3.6 \rightarrow 4$$

A total of 4 bolts was required per flange to adequately resist the specified target moment capacity. At this stage of the design process, some qualitative information was provided on the likelihood of a block shear critical moment connection design. By experience, it was noted that a block shear critical connection geometry was difficult or impossible when *six or more* fasteners were required in the tension flange, assuming the bolts will always be placed in a single line on each side of the flange. Since the shear component of the block shear equation was proportional to the connection length, l_c, adding another bolt to each row on the tension flange had a significant impact on the block shear resistance. If M_{des} was large and required a significant number of bolts to adequately resist its corresponding flange force, the *minimum possible* block shear resistance value

would exceed the target flange resistance, F_{des}. In this case, the target moment could be increased in an attempt to match this minimum block shear resistance, with M_{des} allowed to exceed M_y, but remaining below M_p. However, this could induce a positive feedback loop in which increasing M_{des} would further increase the number of bolts required to resist the target force. An alternative option was to increase the bolt size. However, due to a limited selection of standard bolt diameters, this method was found to be ineffective from the author's experience. Therefore, should the required bolt number per flange for a reasonable value of M_{des} exceed 4 bolts, the design process could either be restarted with a new section size, or continued with the understanding that the critical block shear moment strength would most likely *not* be the critical moment capacity.

Next, the connection spacing limits defined by the CSA S16-19 Cl.22.3 and Table 5 (2019) were determined. The relevant limits were the minimum end distance, the minimum edge distance, and the minimum/maximum bolt pitch. A visual definition of these three values are provided in Figure 3.7. An upper limit of 100mm (4") was set for the maximum end distance. The minimum edge distance was used to determine the minimum and maximum possible bolt gauge, or the centre-to-centre distance between bolt rows on opposing sides of the web. The maximum gauge was the distance where the minimum edge distance was reached on the free end of the flange; the minimum gauge was the distance where the minimum edge distance was reached for the yet-to-be-designed interior splice plate that was placed on either side of the section web. Since the interior splice plate must lie flat on the interior face of the flange, its width was governed by the flange width as well as the k_1 distance from the centre of the section to the toe of the flange-web fillet. For a given combination of pitch, gauge, and end distance, the corresponding block shear resistance of the tension flange and its equivalent

moment resistance was determined by:

$$T_{r,EBS} = 2 \times \left[\frac{b_f - gauge - d_h}{2} t_f F_u + 0.6(end + pitch(n_{bolts} - 1)) t_f \frac{F_y + F_u}{2} \right] \tag{3.7}$$

$$T_{r,CBS} = (b_f - 2d_h) t_f F_u + 0.6(end + pitch(n_{bolts} - 1)) t_w \frac{F_y + F_u}{2} \tag{3.8}$$

And:

$$M_{EBS} = T_{r,EBS} \times (d - t_f) \tag{3.9}$$

$$M_{CBS} = T_{r,CBS} \times (d - t_f) \tag{3.10}$$

Since all connection geometry limits were defined, the entire block shear design space could then be determined and plotted. A plot of all possible combinations of bolt geometry and the corresponding *critical* block shear moment capacity is shown in Figure 3.9. Each vertically stacked surface represented a given end distance, and all combinations of allowable pitch and gauge were represented by the X and Y axes. The two distinct slopes along the pitch axis represented the two different possible block shear failure modes, Edge Block Shear (EBS) for smaller pitches, and the Complete Block Shear (CBS) for larger pitches. The intersection of the two slopes represented the theoretical connection length where the two block shear failure modes would have the same theoretical resistance.

It is noted that there exists a third theoretical block shear failure mode, the Centre Block Shear (CeBS), where a central block is removed from the flange, with shear planes lying in both the flange as well as the web. Due to three simultaneous shear planes for this failure mode, it was found to not govern the connection design for practical connection details. Nevertheless, the CeBS failure mode was considered during the automated calculations. A visual overview of these three moment block shear failure modes is provided in Figure 3.10.

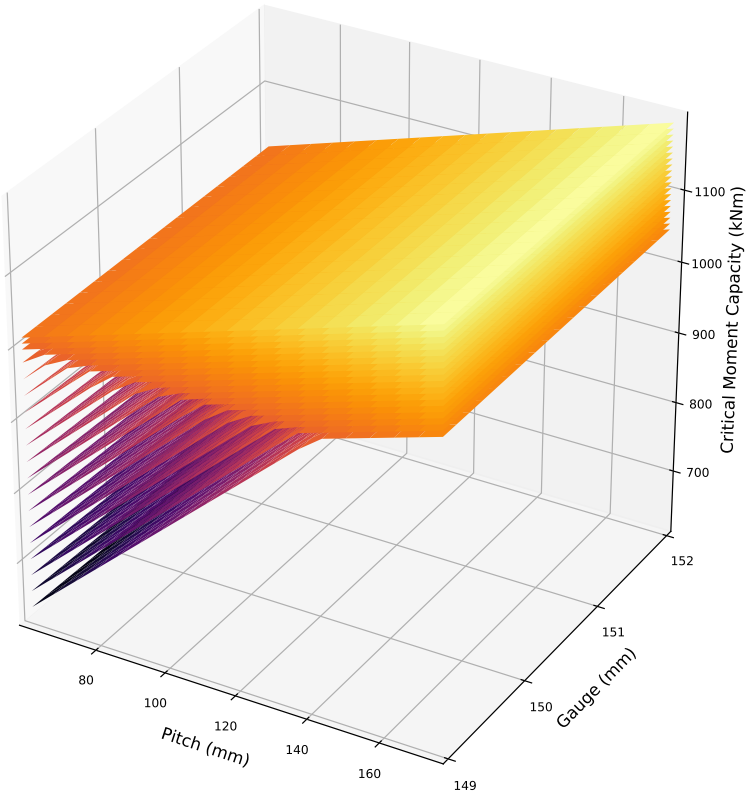

Figure 3.9: Design space for W610X101 section.

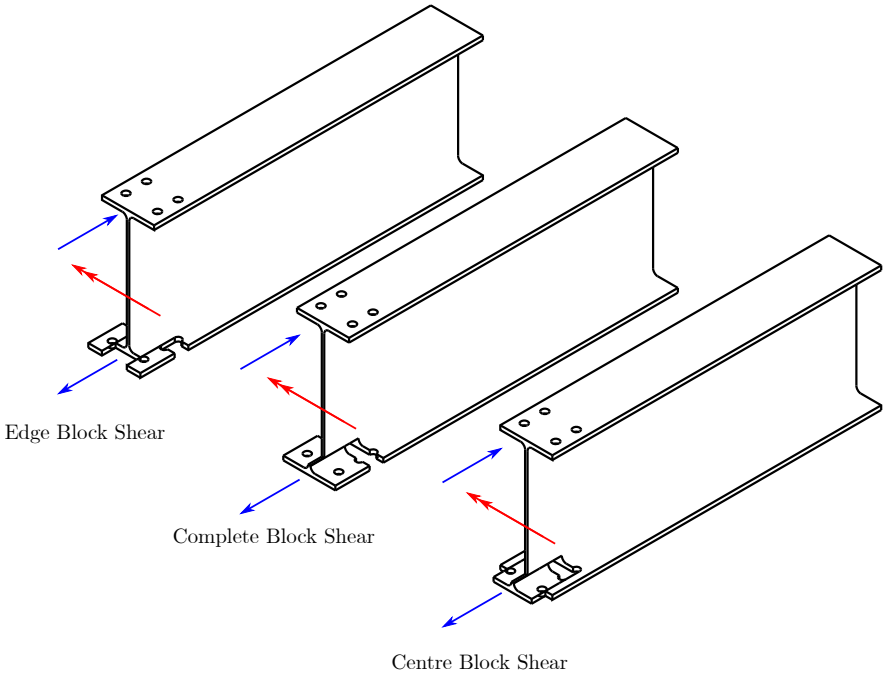

Figure 3.10: Possible moment block shear failure modes.

At this stage, a critical design requirement was evaluated: did there exist a possible combination of end, pitch, and gauge distances that resulted in a theoretical block shear failure resistance that was *equal to or less than* the specified target moment capacity, M_{des}? A plot of M_{des} against the possible design space for the W610X101 section is shown in Figure 3.11; the intersection of the target moment surface with the design space indicated that there was a possible combination of connection geometry such that the critical block shear moment capacity was equal to or less than the target moment capacity, M_{des}. Should the target moment surface not intersect with the connection design space, two options were possible. First, the target design moment could be increased to allow for a possible design space intersection, effectively raising the red surface. Second, the bolt size could be adjusted to change minimum spacing requirements to lower the design space surfaces. From experience, it is noted that the second option had marginal impact on the absolute values of the design space surfaces. The first option was limited by the gross section properties: the target moment

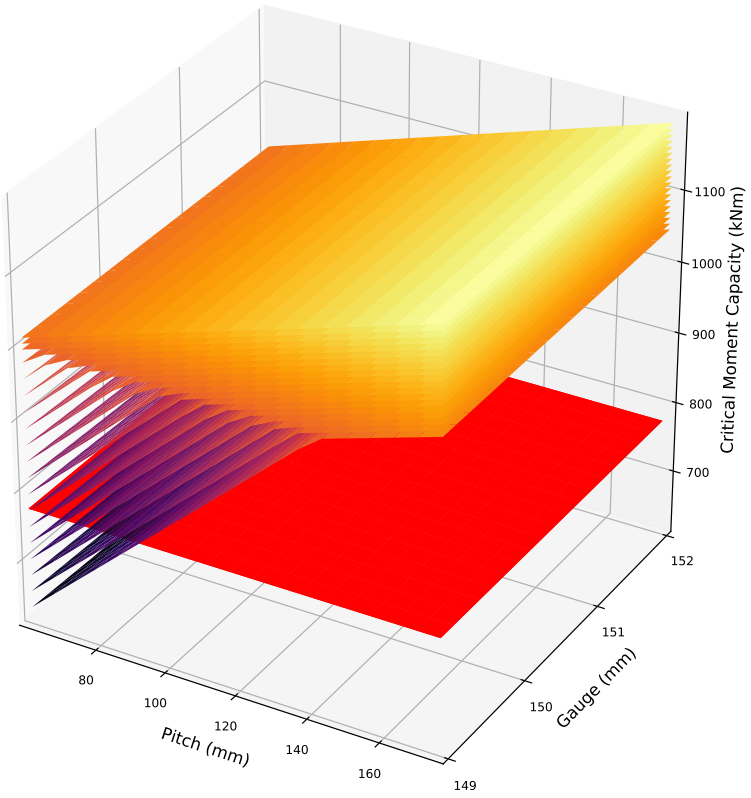

Figure 3.11: Target moment capacity M_{des} in red against the M5 design space.

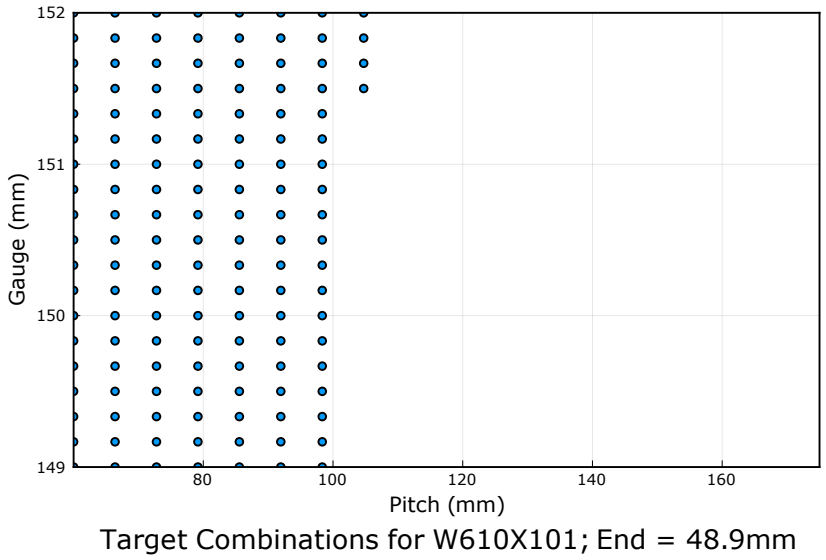

Figure 3.12: Sample of possible connection geometry combinations for a block shear critical failure mode.

may be increased to above the elastic moment, but should remain below the gross plastic moment to create a block shear critical connection. However, since the difference between M_y and M_p is typically small, the actual window of adjustment for M_{des} was also small. It is in the author's experience that should the initial target moment not be met by the selected section and bolt hole size, a block shear critical connection was unlikely to control the design, and a new section should be selected.

Once a possible block shear critical failure mode was confirmed, the geometric combinations that resulted in a block shear moment resistance within a set tolerance (typically 10%) of the target moment was plotted for a final connection geometry design. One possible set of connection geometry with an end distance of 50mm (2") that provided a critical block shear moment capacity within 10% of the target moment capacity is shown in Figure 3.12. When possible, the final connection geometry was chosen to reflect typical spacings used by practising engineers, typically in half-inch increments. These typical spacings are end dis-

tances of approximately 50mm (2"), pitch distance of approximately 75mm (3"), and edge distances greater than 38mm (1.5"). For the M5 specimen, the following connection geometry was selected:

$$\begin{aligned} \text{end} &= 35\text{mm} \\ \text{pitch} &= 75\text{mm} \\ \text{gauge} &= 145\text{mm} \end{aligned}$$

With the final connection geometry, all possible failure modes and their corresponding unfactored, probable moment capacities were calculated. A comparative overview of the moment capacities of all possible failure modes is shown in Figure 3.13. For example, the Edge Block Shear moment, M_{EBS}, was calculated by:

$$\begin{aligned} T_{r,EBS} &= 2 \times \left[\frac{b_f - gauge - d_h}{2} t_f F_u + 0.6(end + pitch(n_{bolts} - 1)) t_f \frac{F_y + F_u}{2} \right] \\ &= 2 \times \left[\frac{228 - 145 - 24}{2} (14.9)(460) + 0.6(35 + 75(2-1))(14.9) \frac{385 + 460}{2} \right] \\ &= 1256kN \end{aligned} \tag{3.11}$$

$$\begin{aligned} M_{EBS} &= T_{r,EBS}(d - t_f) = 1256(602 - 14.9) \\ &= 724kNm \end{aligned} \tag{3.12}$$

With the final connection geometry specified, and critical moment capacities verified, the periphery elements were designed. For the splice plates, one exterior and two interior splice plates were specified for each flange. The flange force was assumed to be transferred approximately proportional to its size, and was increased to 150% of the expected critical failure mode to provide an additional level of safety:

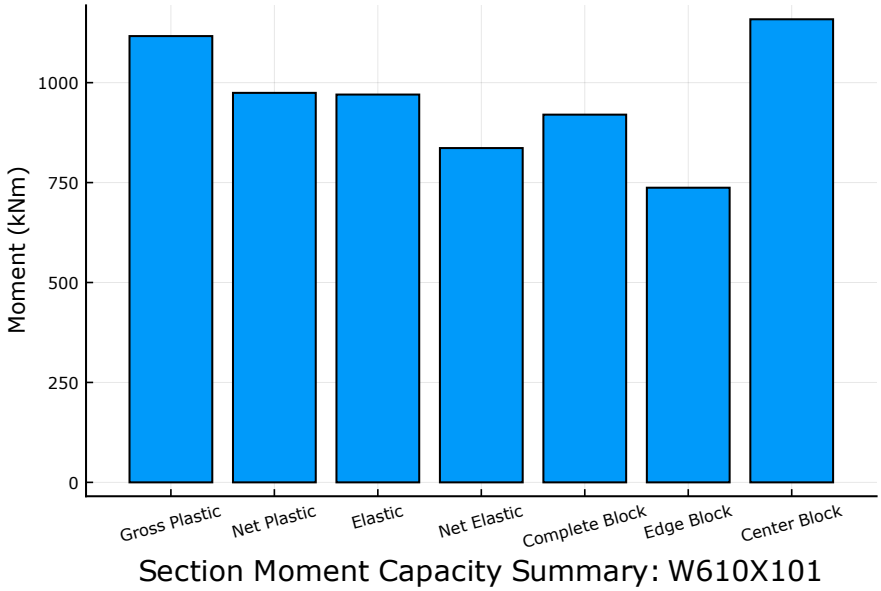

Figure 3.13: Overview of theoretical probable and unfactored moment resistances.

$$F_{ext} = 1.5 \times F_{crit}/2 = 1.5T_{r,EBS}/2 = 942kN \tag{3.13}$$

$$F_{int} = 1.5 \times T_{r,EBS}/4 = 471kN \tag{3.14}$$

The minimum thickness of each plate was determined for each potential failure mode using the CSA S16-19 design standard. The widths of both the interior and exterior splice plates were maximized to the available flat surfaces on both sides of the flange:

$$b_{splice,ext} = b_f \tag{3.15}$$

$$b_{splice,int} = \frac{b_f - 2k_1}{2} \tag{3.16}$$

The design checks included: gross section yielding, net section fracture, plug shear, bearing failure, as well as the buckling compression resistance of the exte-

rior compression flange. For this calculation, the end to end length was taken as the centre-to-centre distance between the nearest bolt holes on opposing sides of the splice. With a typical 12mm (0.5") gap specified between opposing sections, this length was calculated by:

$$L_u = 2 \times end + 12 \tag{3.17}$$

The effective length factor of $k = 0.7$ was chosen for compression buckling design, as the geometry of the splice plates and bolts were assumed to act as fixed boundaries for the free length. Once the critical plate thickness was determined, it was then rounded up to the nearest half-inch increment to reflect common stock plate thicknesses for structural steel fabricators. A standard end distance of 50mm (2") was used for the free ends of each splice plate.

Since the detailed connections were to be modelled using finite element analysis software as well as fabricated and tested in the structural laboratory, the rest of the section outside of the connection region was also designed and detailed. First, as the laboratory test specimens would be loaded under a four-point load configuration, the shear span and total length of the beam were selected. The total length of the beam was chosen to be $l = 2500mm$ with a shear span of $a = 1500m$; a justification of these dimensions are provided in Chapter 4. With the selected shear span, the required applied force in a four-point load configuration was calculated. To be conservative, the expected required force was chosen as the force corresponding to the gross plastic moment:

$$
\begin{aligned}
P_{applied} &= \frac{M_{applied}}{a} \\
&= \frac{M_p}{1.5m} \\
&= \frac{1117kNm}{1.5m} \\
&= 1675kN
\end{aligned}
\tag{3.18}
$$

Next, the bearing capacity of the section was determined for this required force. For most of the sections tested, the bearing capacity of the web alone was sufficient to withstand the expected forces. However, to minimize local deformations during laboratory testing, bearing stiffeners were specified for all test specimens. One inch stiffeners were placed at load and support points that spanned up to the toe of the web fillet in the K-area of the opposing flange from the point of contact. A base size of 8mm E490 electrode fillet welds was initially specified along all contact points between the stiffener and the section, with the size being increased if the welds could not withstand the full expected load on the stiffener. The beam end was extended by 200mm ($l_{total} = 2700mm$) to provide additional bearing support at the end. The effective length and shear span of the beam section remained at $l = 2500mm$ and $a = 1500mm$, as seen in Figure 3.6.

3.1.4 Initial test specimens

The process above was performed over thirty times, with sections selected by trial-and-error, accounting for the general rules for block shear sensitive section geometries as listed previously. From the initially designed section-connection details, five unique sections were selected to be fabricated and tested in the structural laboratory. These sections were chosen to represent the general geometric limits for block shear critical sections in flange width and section depth. The range of geometry in depth, width, and linear mass of the selected five specimens

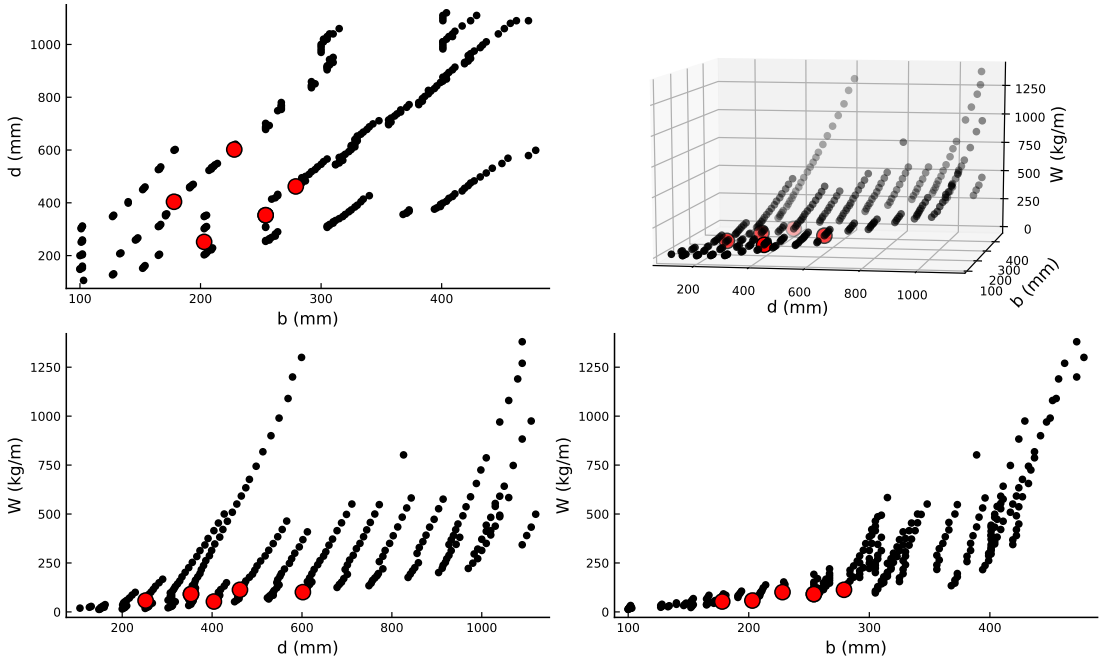

Figure 3.14: Width, depth, and linear mass of all standard W-Sections (selected specimens highlighted in red)

is shown in Figure 3.14. It is noted that although a good range in flange width and section depth was captured in the selected group, the linear masses are all similar in value, with a maximum linear mass of $113kg/m$, and a minimum of $53kg/m$. This is in part due to the fact that the wide range of linear masses available for a W-section with similar section depths come from the large variance in available flange thicknesses. This is best observed by the series of upwards sloping groups of section sizes in the d vs. W graph in Figure 3.14. As previously indicated, since the block shear resistance is highly sensitive to the flange thickness, heavier sections typically could not be detailed such that the block shear moment was the critical resistance.

The expected moment capacities of the two block shear failure modes as well as the two gross section flexural strengths are found in Figure 3.15 and Table 3.1. All specimens were detailed such that the critical moment resistance was tied to the Edge Block Shear failure mode. The isolation of the EBS failure

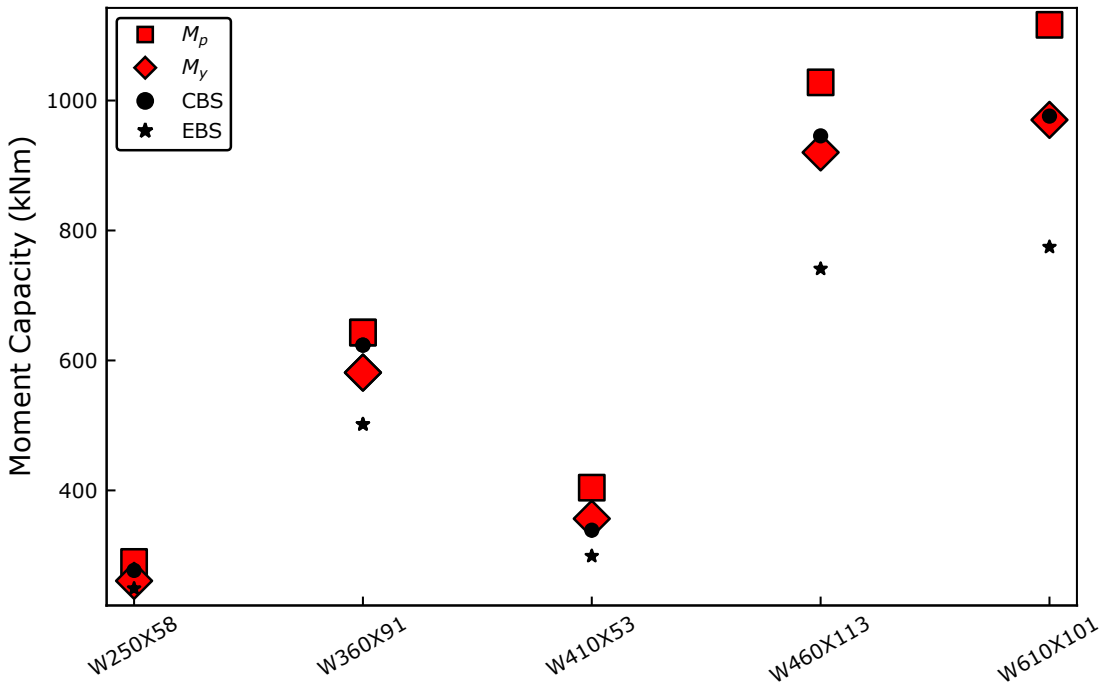

Figure 3.15: Theoretical unfactored and probable moment capacities of selected specimens

Table 3.1: Selected section overview. Critical moment capacities are in **bold.**

Test ID	Section	Bolt Diameter (in)	M_p (kNm)	M_y (kNm)	M_{CBS} (kNm)	M_{EBS} (kNm)
M1	W250X58 (W10X39)	7/8	295	266	277	**250**
M2	W360X91 (W14X61)	7/8	643	581	624	**502**
M3	W410X53 (W16X36)	3/4	404	357	339	**299**
M4/M6	W460X113 (W18X76)	1	1028	920	946	**741**
M5	W610X101 (W24X68)	7/8	1117	970	894	**724**

mode, or the difference in resistance between the critical resistance and the next lowest resistance, varied depending on the section, with the M1:W250X58 section having the smallest difference between the EBS moment failure mode and the Yield Moment. The connection details of the preliminary models M1-M6 are provided in Chapter 5. It is noted that M4 and M6 have the same section size and connection geometry, but M6 has the addition of a typical web splice plate connection with slotted holes to observe the effects of these additional bolts in the block shear failure mechanism.

3.2 Preliminary finite element models

Once specimens M1 to M6 were selected and detailed, preliminary finite element models (pFEMs) of the expected laboratory loading conditions were created to verify the initial analytical calculations on the expected failure mode. Like all finite element analyses, the preliminary set of models require significant iteration and verification to ensure that a suitable compromise was met between proper boundary conditions that reflect true expected loading conditions, the selection of mesh elements and mesh density for analysis resolution, and computational time. For physical representation of the test configuration, a parametric script in

Grasshopper for the Rhinoceros computer aided design program was developed. These files were then imported into Abaqus/CAE for all remaining finite element analysis tasks. This section provides an overview of the development of the preliminary finite element models.

3.2.1 Physical representation of test conditions

As the objective of this project was to investigate the block shear failure mode during *moment-induced tension*, a four-point load, pure bending moment method was chosen for the laboratory testing component. The four-point load method provides the benefits of eliminating shear forces in the mid-span region, controlling the applied moment for a given load by adjusting the distance between load/support points, and allowing for an extended region of constant moment to allow for comparisons of gross/net section behaviours at the same moment value. A more detailed description of the laboratory loading conditions is provided in Chapter 4.

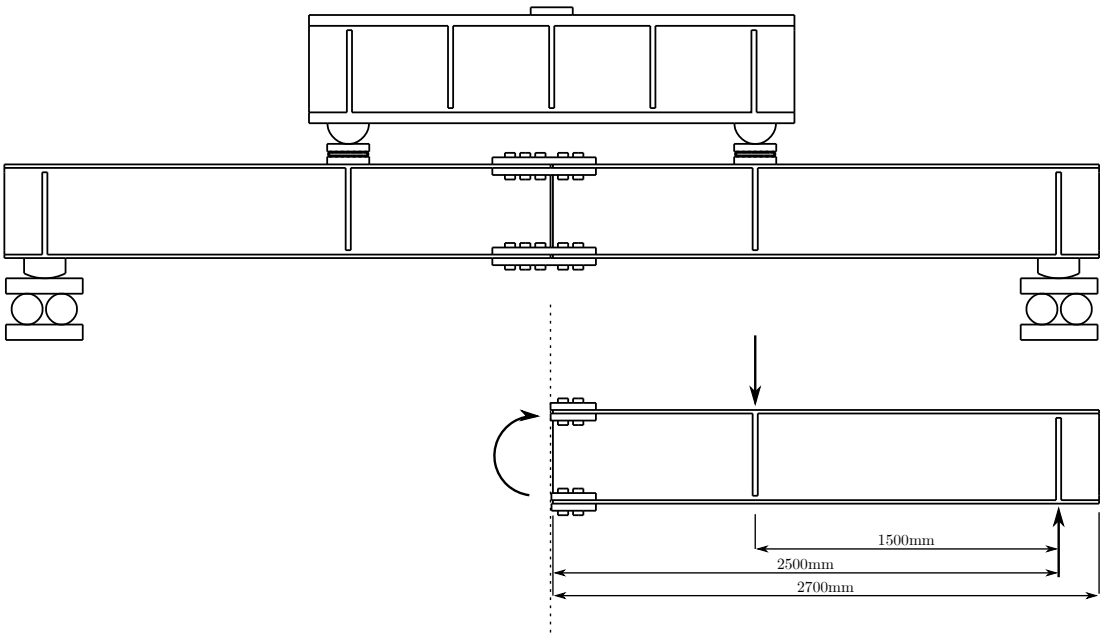

Figure 3.16: Translation of test conditions to FE conditions.

The loading method also provides the added benefit of two planes of symmetry, the first at the centre of the splice plates (see Figure 3.16), and the second being along the weak axis of the cross-section, parallel and centred on the web. These planes of symmetry allow for modelling only one half of each symmetry plane in the pFEMs, significantly reducing the computational time required for analysis.

3.2.1.1 Load/Support boundary conditions

The behaviour of the loading and support points was controlled by displacement/rotation boundary conditions on the exposed face of the loading and support plates (Fig. 3.17). Both plates were tied to the beam, simulating a no-slip condition. The surfaces of these plates were then coupled to a single reference point 100 mm above each plate using the kinematic coupling constraint method. Coupling the face of each plate to a single point allowed for simpler manipulation of the changing displacement/rotation conditions on the plate during the loading process. Figure 3.17 shows the coupling and displacement of the loading plate to simulate the displacement-based loading performed in the structural laboratory. A similar coupling was performed on the support plate to represent that roller support.

During the bolt preloading step of the analysis, both the loading and support reference points were fully restrained from any displacement or rotation. For loading steps, the support reference point was only restrained from lateral/vertical displacement, and was only permitted to rotate in the direction of bending; the loading reference point restrained all rotation in the non-bending direction, and was deflected directly downwards to load the beam. The loading of each specimen occurred in two steps:

1. **LOAD1** displaced the load plate 10mm downwards. This small initial displacement was to allow for all bolt slippage to occur before primary loading. Additionally, the use of Abaqus' *restart requests* allowed for mid-analysis

changes to the FE model without having to restart the computationally expensive initial slippage phase.

2. **LOAD2** displaced the load plate beyond the initial slip point to the point of ultimate connection capacity. After trial and error, a final displacement of 90-120mm at the load point provided the necessary flange force development and deformation. Using *restart requests*, the specimens could be further loaded without restarting the analysis by creating an additional **LOAD3** step when necessary.

3.2.1.2 Connection symmetry

The four-point loading configuration was symmetric about the centre of the loaded member. Applying a symmetry plane boundary condition to the faces of the splice plates cut at the centreline allowed for the modelling of one-half of the loading assembly (Figure 3.18). The rotation at the location of the boundary condition (the mid point of the splice plates) was 0, i.e. parallel to the horizon.

It is noted that this naturally assumed perfect symmetry and positioning of all loading and support plates, as well as perfect symmetry of both beam specimens on either side of the connection. Although these assumed conditions are impossible to replicate in real life, for the preliminary finite element models, these simplifications were acceptable, since only the general behaviour of the tension flange was desired.

3.2.1.3 Cross section symmetry

The second plane of symmetry was in the weak-axis, parallel to the web (Global X axis in *Abaqus/CAE*). Two main points were noted:

1. This boundary condition was applied to all surfaces that have been effectively 'cut' by the symmetry plane, including the exterior splice plates and

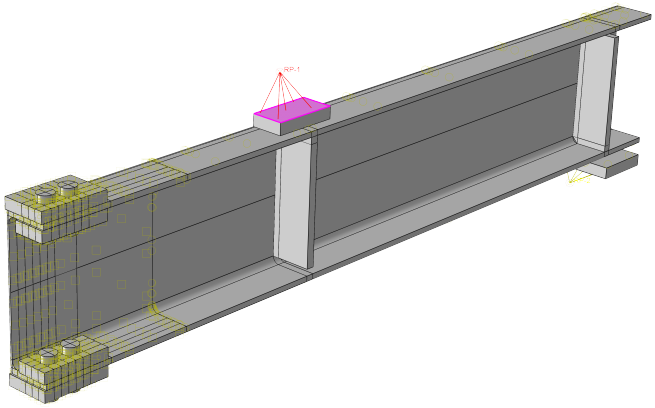

(a) Loading plate constraint.

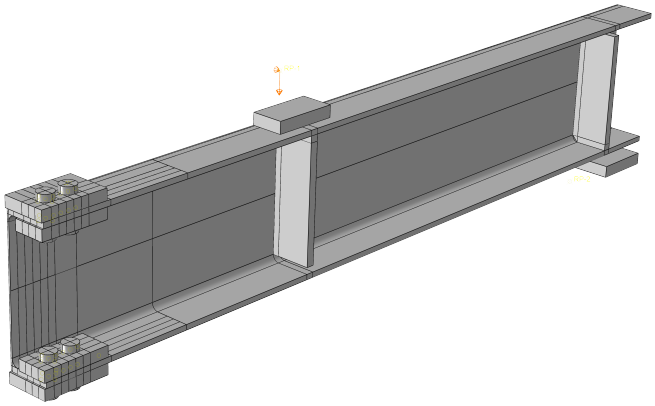

(b) Displacement on reference point.

Figure 3.17: Constraint/Displacement method on loading plate. support.

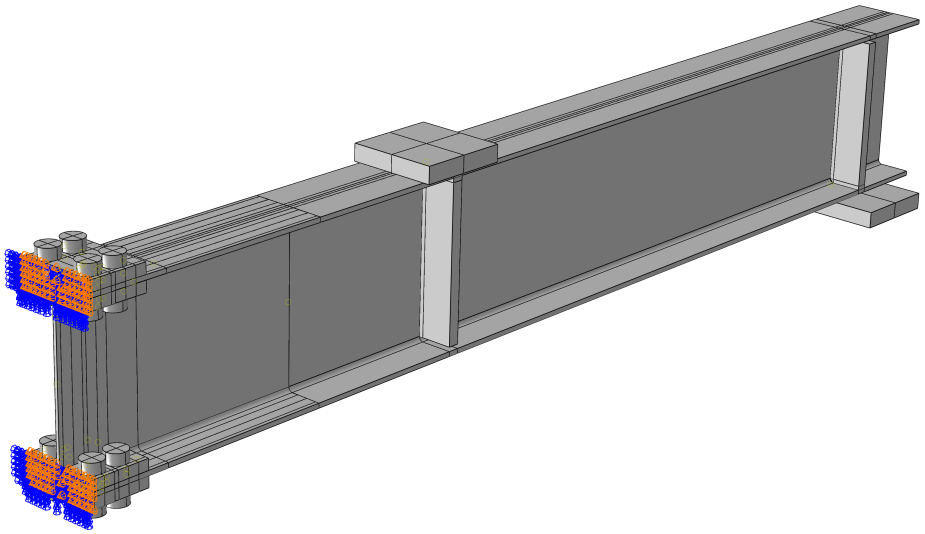

Figure 3.18: ZSYMM Boundary condition on the M3 pFEM in *Abaqus/CAE*

load/support plates. It is noted that this boundary condition does not restrict the *relative displacement between parts*; the slipping/bearing of the splice plates with respect to the beam was still captured. However, this boundary condition would not be able to capture any lateral distortion of the splice plates should it occur during laboratory testing.

2. This boundary condition eliminated the possibility of capturing (in)elastic lateral buckling of the beam section, as it effectively placed a lateral displacement restriction on the entire length of the beam. It was determined that since the real-life laboratory lateral supports would ensure that the test specimen's unbraced length (L) was significantly lower than that of its critical length (L_u), this simplification of the lateral support was adequate for preliminary analysis.

To verify the validity of point 2, two full FE analyses were performed on the

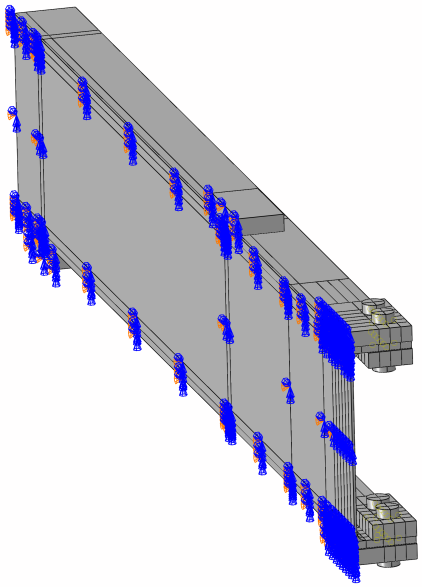

Figure 3.19: XSYMM Boundary condition on the M4 pFEM in *Abaqus/CAE*

M2 (W360X91) specimen: one modelling the full section geometry, with only the splice plate symmetry and realistic lateral restraint points; the other using both the splice and web symmetry planes, effectively providing complete lateral support for the specimen. All other model details (element type and size, loading protocol, interaction properties) remained identical, and the force/moment values from the half model were doubled and compared to the full model results.

A series of comparisons between the full and half finite element models is shown in Figures 3.20 to 3.23. The X, Y, Z displacements of a single node in the centre of the web are compared in Figure 3.20, and shows virtually identical behaviour, indicating that the web splice symmetry boundary condition is a suitable simplification for the behaviour of the connection, and that lateral torsional buckling will not occur.The global behaviour of applied displacement vs. the end moment (Figure 3.21) experienced by the connection is also identical, further confirming that the web symmetry boundary conditions is a valid simplification

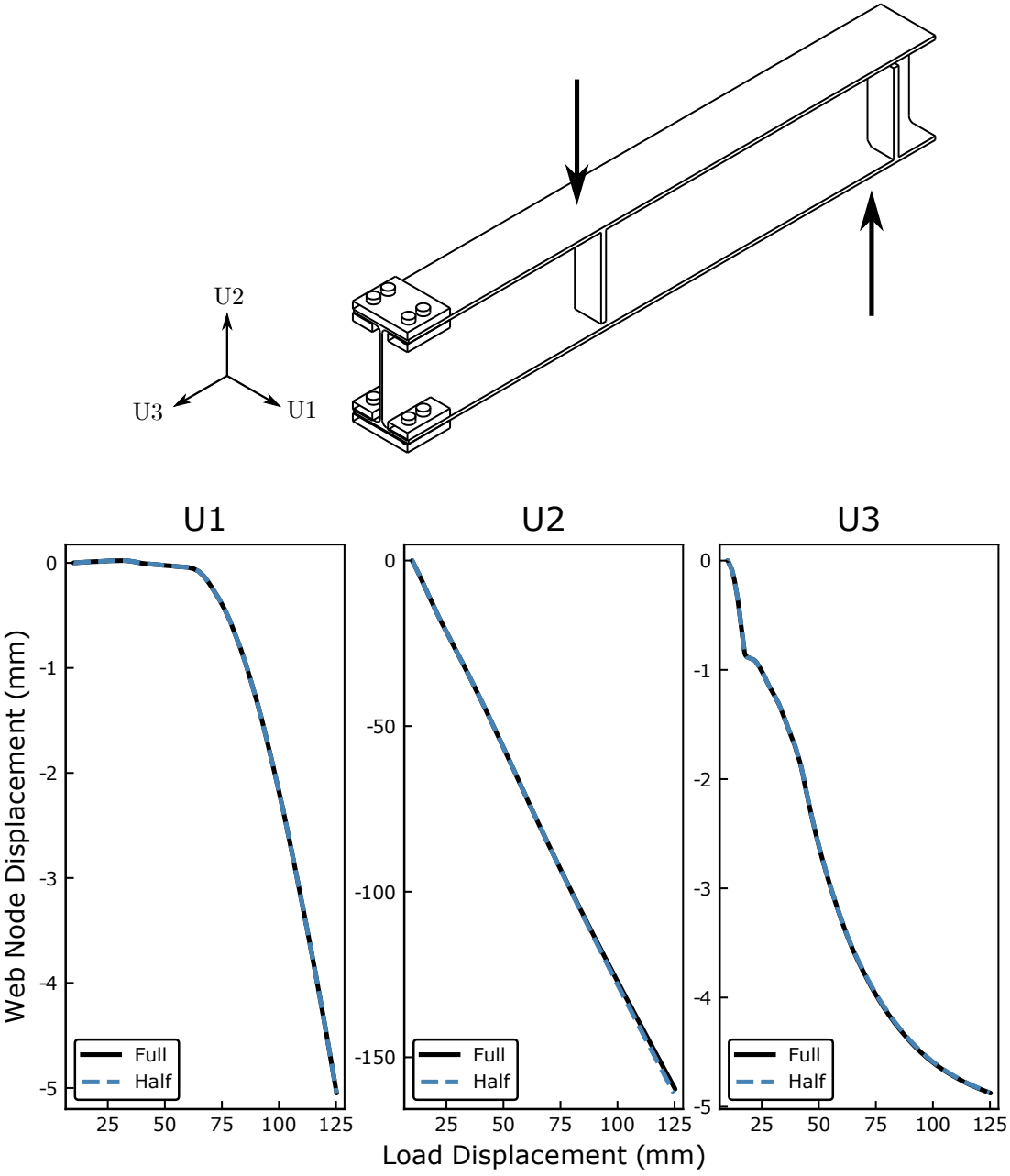

Figure 3.20: Connection displacement comparison of M2 Full/Half models

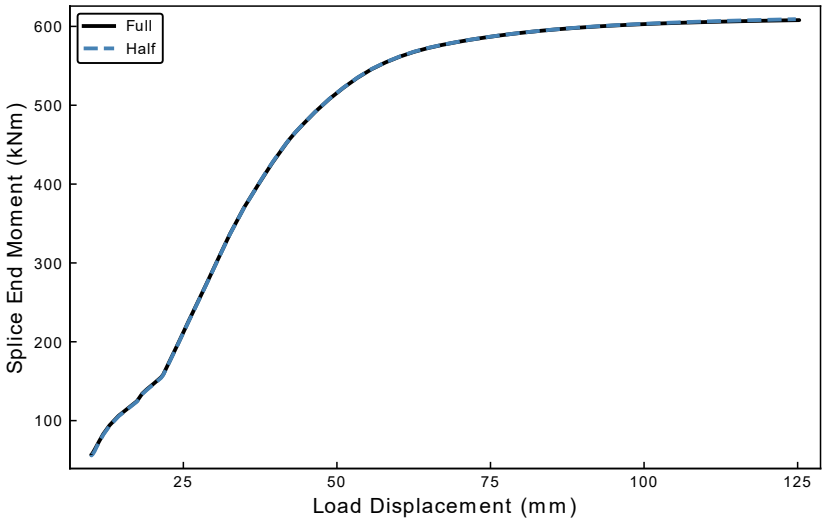

Figure 3.21: End moment comparison of M2 Full/Half models

of the full section model.

In addition, the local failure components for both the Edge Block Shear and Complete Block Shear failure modes were nearly identical for both the full FE model and the simplified half model. The comparison of each failure mode was split into the corresponding shear and tension plane regions. The *free body cut* tool in Abaqus was used to determine the cumulative force vector magnitude in each failure plane to compare between the full and half models. As these local stressed areas were the major concern point for analysis, it was concluded that the double-symmetric, quarter-model representation of the test conditions was suitable for the primary finite-element analysis.

3.2.2 Model development and procedure

The 3D solid models of the test specimens and all supporting pieces were created in a parametrically driven *Grasshopper* file in the *Rhinoceros v6* CAD program (Robert McNeel & Associates, 2018). The use of parameter-based design was chosen to expedite the drawing procedure for future models. Although the pFEMs

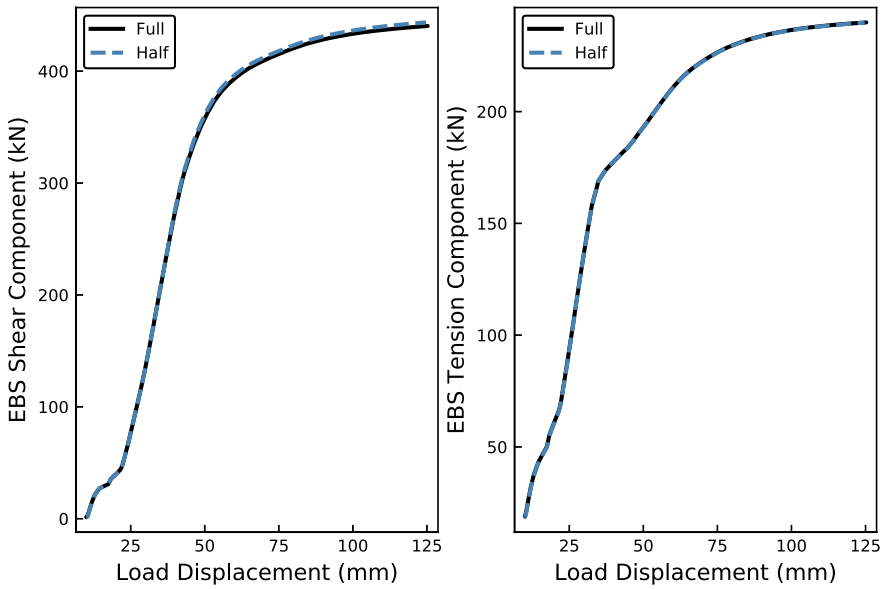

Figure 3.22: Edge block shear component comparison of M2 Full/Half models

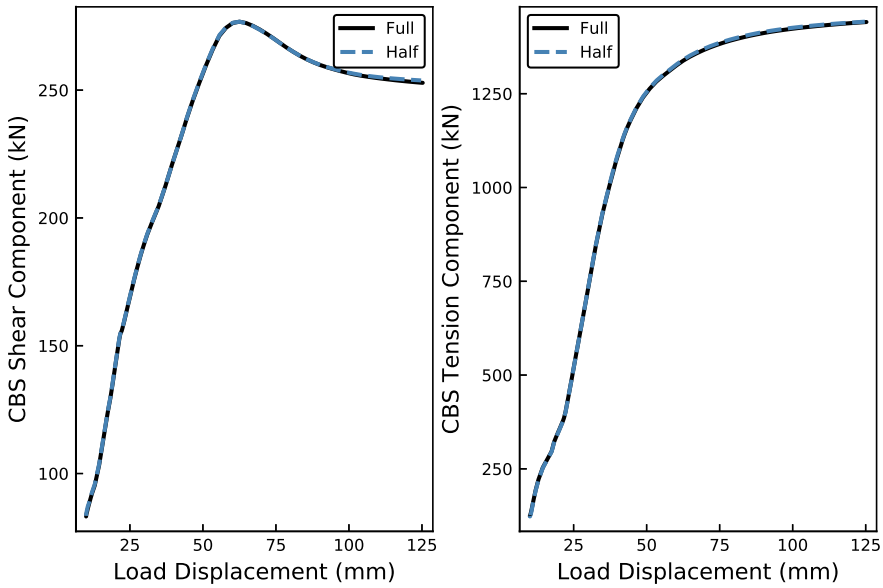

Figure 3.23: Complete block shear component comparison of M2 Full/Half models

are based on nominal section properties, and nominal connection geometries, the post-laboratory phase of modelling would require as-measured section and connection properties. Further, for future parametric studies after the model calibration, the Grasshopper script provides a significant increase in productivity.

A conceptual illustration of the Grasshopper script developed for this project is presented in Figure 3.24. The input parameters were adjusted by the user in the following groups:

1. **Cross Section Details:** d, b_f, t_f, t_w, k, k_1.
2. **Connection Details:** $d_{hole}, n_{rows}, end, gauge, pitch$.
3. **Plate Details:** t_{plate}, d_{end}.
4. **Bolt Details:** d_b, d_{head}, l_b.
5. **Loading Details:** Location and dimension of stiffeners, l_{beam}, l_{shear}

Once the unique parameters were provided, the script outputted five unique 3D parts, some of which were used multiple times. The general part list and their number of use in the FE models are listed below, with a reference image in Figure 3.25:

1. **Fine Mesh Section**: the portion of the beam close to the splice connection. This is defined as the first 500mm of the beam section from the connection end. (1)
2. **Coarse Mesh Section**: the remaining portion of the beam. (1)
3. **Exterior Plates**: The splice plates touching the outer faces of both the compression and tension flanges. (2)
4. **Interior Plates**: The splice plates touching the inner faces of the tension/-compression flanges. (4)

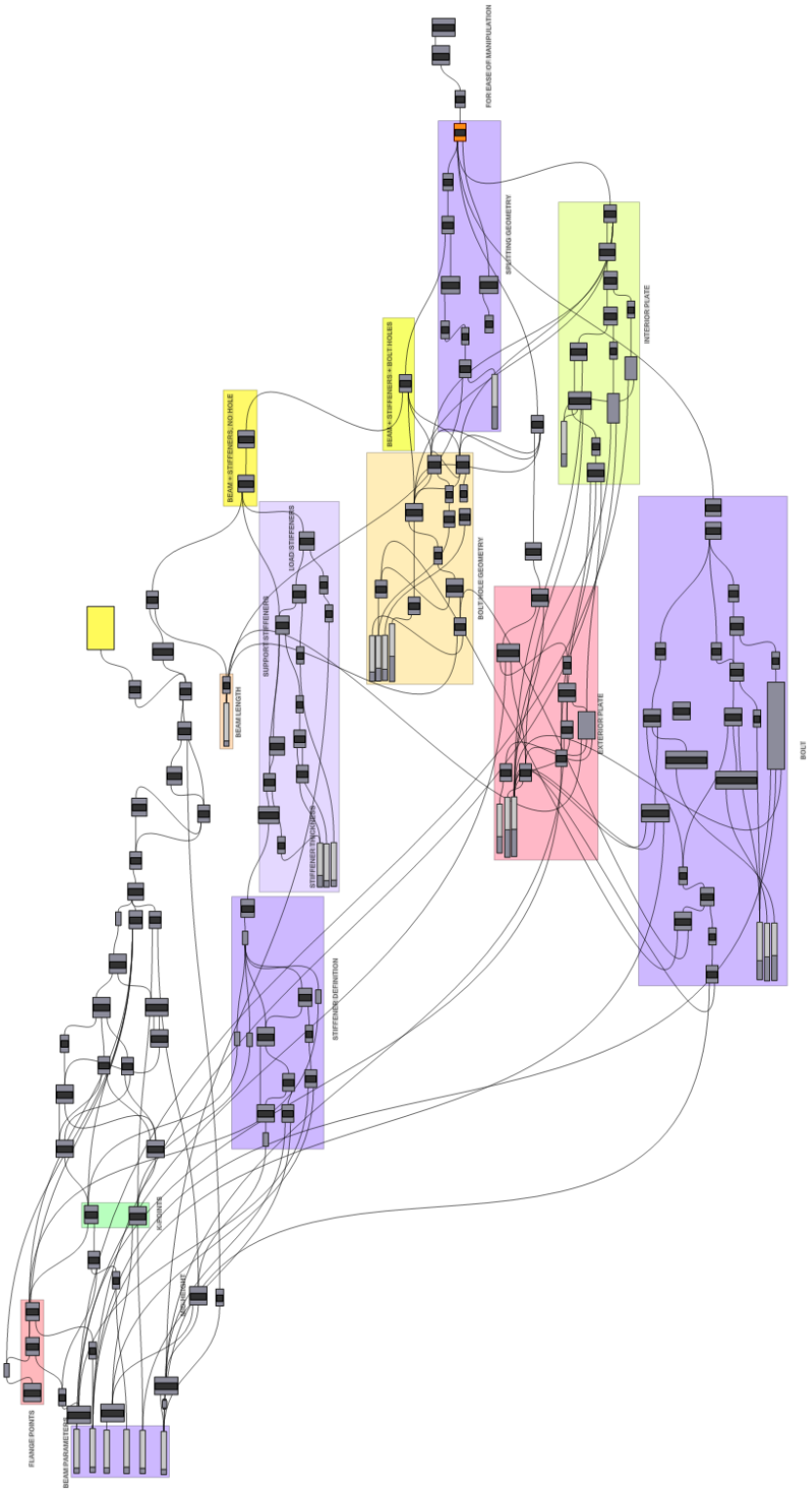

Figure 3.24: Specimen drawing program in Grasshopper

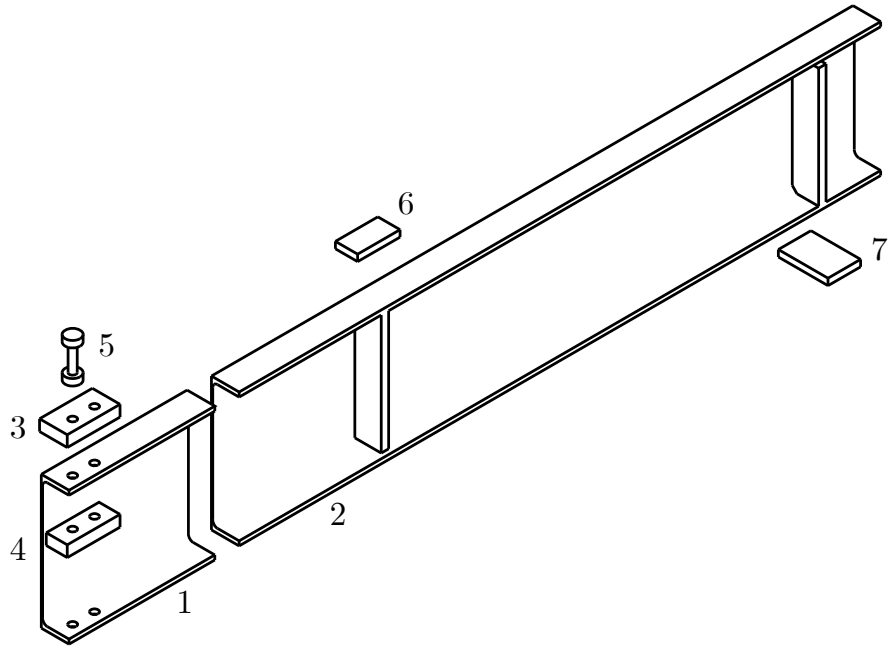

Figure 3.25: Rhino/Grasshopper output components.

5. **Bolt**: A simplified bolt model of both cylindrical shank and head. The shank length is specified as the exact grip length between the flange thickness and the plate thicknesses. (8-12)

6. **Loading Plate**: the 8"×8"×1.5" hardened plate used to load the beam.

7. **Support Plate**: the 8" wide steel plate at the supports.

These parts were exported as *.sat* files and imported separately into *Abaqus/-CAE* and re-assembled. In addition to the section-specific parts outputted by the CAD program, two additional section-independent parts were defined once and reused for each model: the loading plate and support plate representing the two contact points on the beam section to the applied loads.

3.2.2.1 Material properties

Early-stage models to test part interactions and analysis methods used fully elastic steel material properties with a Young's Modulus of 200 GPa and a Poisson's

ratio of 0.3. As the pFEM analysis developed, representative material properties were required to reach the high strain, non-linear stress state that was required to develop the expected block shear failure mode.

Since the laboratory test specimens were not fabricated during the pFEM portion of this study, the coupon testing data from the work of (Pizzuto, 2019) was used as surrogate true material properties for the pFEMs. For each unique section, four flange and three web coupons were taken from the same fabrication heat. Testing results provided the local Young's Modulus, and the engineering stress-strain curve until rupture. The Poisson's ratio was assumed to be constant at 0.3. The engineering stress-strain curves were converted to the true stress-strain values, and were used for the plastic material properties in the FE models.

The coupon testing results for Pizzuto had values of the Young's Modulus ranging from 199 GPa to 226 GPa, and yield stresses ranging from 342 MPa to 444 MPa. As there was a significant spread in the true material properties of the available coupon data, the properties of the section closest to the FE model section was used to represent the probable material property. The comparison is show in Table 3.2.

Table 3.2: True material property sections

Test ID	**Section Size**	**Closest Coupon Section**
M1	W250X58	W360X64
M2	W360X91	W360X64
M3	W410X53	W410X85
M4/M6	W460X113	W460X113
M5	W610X101	W530X138

Abaqus requires the use of *sections* to define material properties for different regions on the same mass. This resulted in separate section definitions for the beam flange and web. Following the procedure of (Pizzuto, 2019), the 'flange' section included the entire K-area fillet region of the flange/web interface, as well as the portion of the web that is enclosed within the fillet depth. This was

considered a suitable replacement to having additional coupon data for the K-area alone as the region represents a very small portion of the overall cross-section area, and was assumed to have a negligible effect on the global behaviour of the section.

Bolts, splice plates, and loading plates, which were conservatively detailed to remain elastic under load, were modelled as perfectly elastic materials with E = 200 GPa. In case of unexpected yielding/failure during laboratory testing, coupons were specified for the fabrication of the splice plates for eventual testing.

3.2.2.2 Mesh element selection

The selection of elements was based on previous successful element choices made by past studies on structural steel connections at McGill University (Pizzuto, 2019; Moreau, 2014). Meshing was performed entirely with solid elements. Initially, the "Coarse" section of the beam was planned to be represented by planar shell elements as high localized strain and plastic behaviour was not expected in the gross section, and shell elements could greatly reduce the computational time. However, it was determined that the added complexity of adequately representing the flange/web fillet interface, the bearing stiffeners, and the tie constraint to the solid "Fine Mesh" section was not worth the computational time that could potentially be saved.

The majority of the mesh was based on hexahedral, first-order reduced integration C3D8R 'brick' elements. Hexahedral elements were chosen to represent the section as the base shape resembled the major section geometries of rectangular flanges, webs, and stiffeners, allowing for elements to naturally fill most of the base geometry with limited distortion. The combination of the first-order analysis and the reduced-integration scheme provides a single integration point for each element, rather than upwards of 27 for the same base element shape (Dassault Systèmes, 2018). In addition to the C3D8R elements, C3D6 'wedge' elements were also used for the flange/web fillet area, as well as in the central

portion of the bolts. The wedge elements were suitable for approximating the curved and axisymmetric regions.

Although second-order elements provide more integration points and thus more accurate and 'smoother' results, they are ideal only for problems that do not involve severe element distortions (Dassault Systèmes, 2018). Since the region of interest at the tension connection was expected to undergo significant deformation at the bolt holes, and for the added benefit of reduced computational demand, first-order elements were selected for analysis.

The selection of reduced-integration elements over full-integration elements was initially based on expected computational efficiency. However, in a reduced vs. full integration comparative trial on the M4 pFEM, it was observed that CPU time required for either integration scheme was virtually identical (Table 3.3). A comparison of local and global behaviour of the output models of both the full and reduced integration methods showed equally similar results, even when loaded well beyond the critical failure point of the connection (Figure 3.26). However, even though both the computational resources required and the analysis results were similar, it was decided that reduced-integration elements would be used for the remaining pFEMs, and to re-evaluate the procedure during the post-laboratory calibration phase of the project. Reduced-integration elements was selected for two reasons: first, since only the M4 pFEM was used to compare the results between the integration schemes, it was possible that a reduced computational time could still be achieved with other geometries for the remaining models; second, reduced-integration elements are often preferred for high-strain and bending scenarios, where shear locking is not possible (Dassault Systèmes, 2018; Sun, 2006).

One potential issue with the use of first-order reduced-integration hex elements was the possibility of *hourglassing*, where the strain at the single integration point is calculated to be zero, resulting in a false zero-energy scenario and erroneous results. However, there are many safeguards that can prevent hourglassing:

Table 3.3: Run time comparison of Full vs. Reduced elements of the M4 pFEM

Integration Type	CPU Time (s)
Full	27091
Reduced	27094

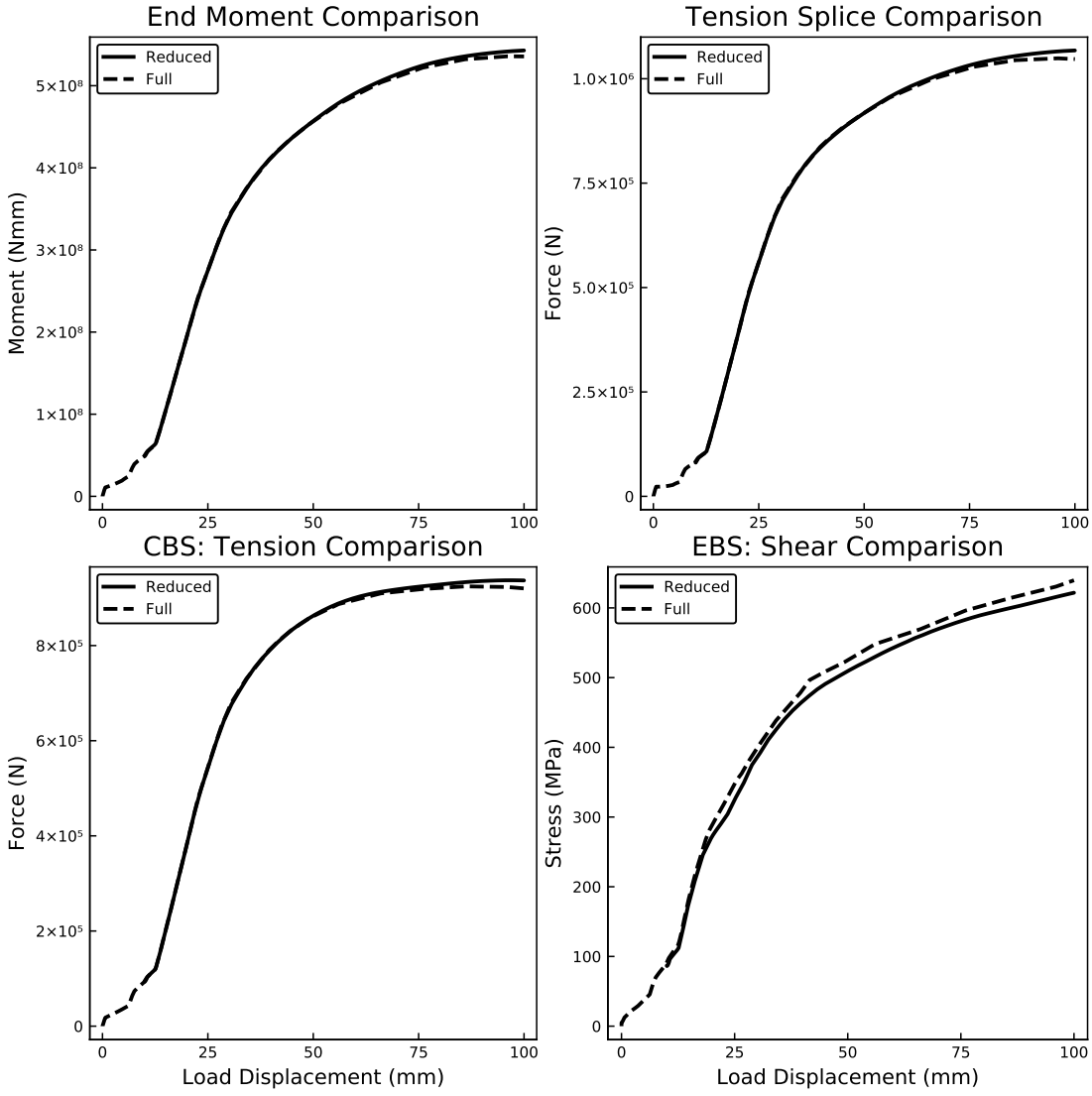

Figure 3.26: Analysis comparison of Full vs. Reduced C3D8 elements of the M4 pFEM

Table 3.4: Mesh overview

Mesh	No. Edge Elements and Approx. Size (mm)		Total no. Elements
	Bolt Hole	Flange Thickness	
Coarse	5 (3)	4 (4)	19080
Medium	8 (2)	6 (3)	41508
Fine	10 (1.5)	8 (2)	101040

Abaqus provides a built-in hourglass control method where an artificial stiffness is introduced to limit any propagation of zero-strain elements, and; increasing the number of elements through the thickness of a member and/or increasing the mesh density of a high-strain region limits the possibility of an hourglass effect failure (Sun, 2006; Rao, 2011; Dassault Systèmes, 2018). The mesh sensitivity analysis in the following section ensured that the risks for the hourglass effect were minimized.

3.2.2.3 Mesh sensitivity analysis

To ensure both analytic accuracy and computational efficiency, a mesh sensitivity analysis was performed on the M4:W460X113 pFEM. Starting with an initial 'Coarse' mesh density based on previous FE work and recommendations by Pizzuto (2019), the mesh size was subsequently reduced for two additional models; the mesh sensitivity analysis was only performed on the expected high-deformation end connection region, while the remaining parts did not change in mesh size. Table 3.4 provides an overview of the changes in the approximate mesh size and number of elements in the bolt hole edge region and flange thickness for each trial model. With each change in mesh density, both local and global behaviour was observed and compared to the previously completed models.

A major point of concern was the ability of the mesh to capture the high strains expected from bolt hole deformation at the gross shear plane. The deformed meshes from all three mesh density trials are shown in Figure 3.29; of note is the

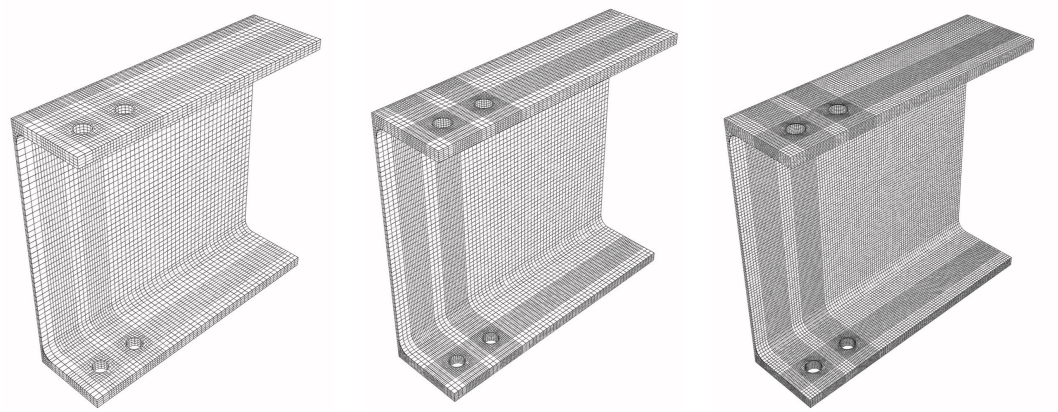

Figure 3.27: Comparison of Coarse, Medium, and Fine meshes

significant single-element distortion for the coarse mesh at the bolt hole along the gross shear plane, and the smoother and more distinct 'teardrop' deformation in the fine mesh.

Since it is the local stress/strain behaviour that is of major importance, two stress regions were used to compare the results of the three mesh densities. First, the Von Mises stress along the gross shear plane for the edge block shear failure mode was compared from a load displacement of 0 to 50mm; second, the Von Mises stress in the net tension plane for the edge block shear failure mode near the end of loading (100mm load displacement) was compared. Since the location and configuration of the elements change with each new mesh density, it was impossible to compare a single element's or node's response. For the purpose of the mesh sensitivity analysis, the nodal output response of all nodes along either the gross shear plane or the net tension plane was extracted from Abaqus and the mean value was determined. The averaged stresses from each mesh density and the comparison between the average values are shown in Figures 3.30 and 3.31.

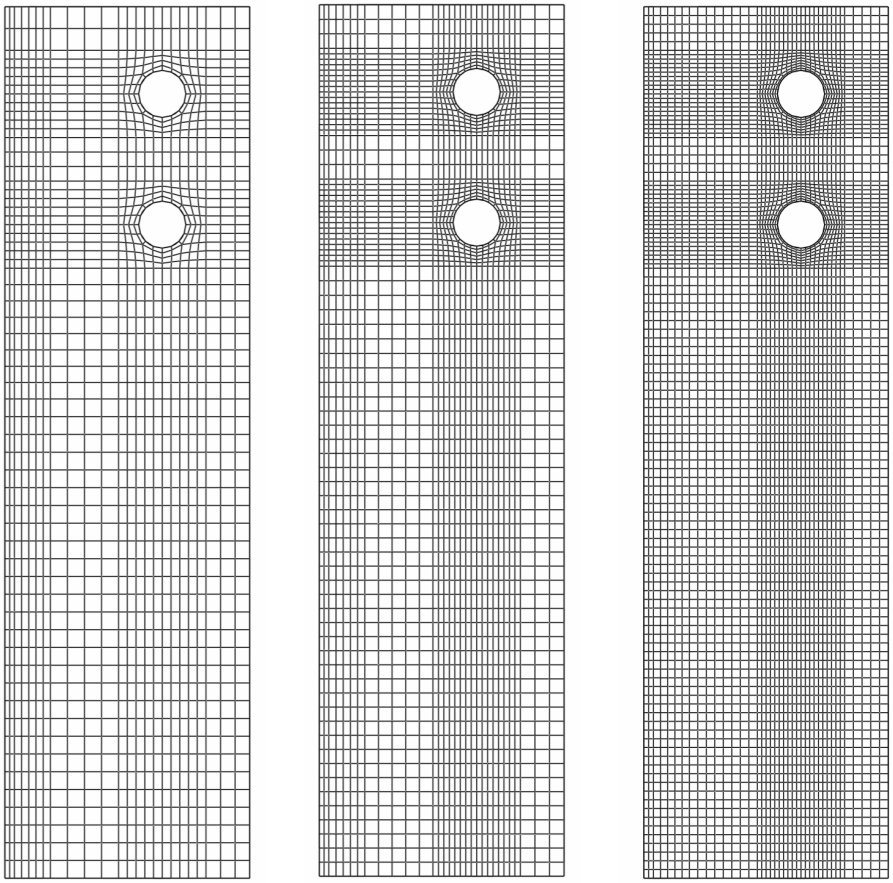

Figure 3.28: Comparison of Coarse, Medium, and Fine meshes

Table 3.5: CPU Time comparison for Coarse, Medium, and Fine meshes

Mesh Density	**CPU Time (s)**
Coarse	13146
Medium	27094
Fine	53226

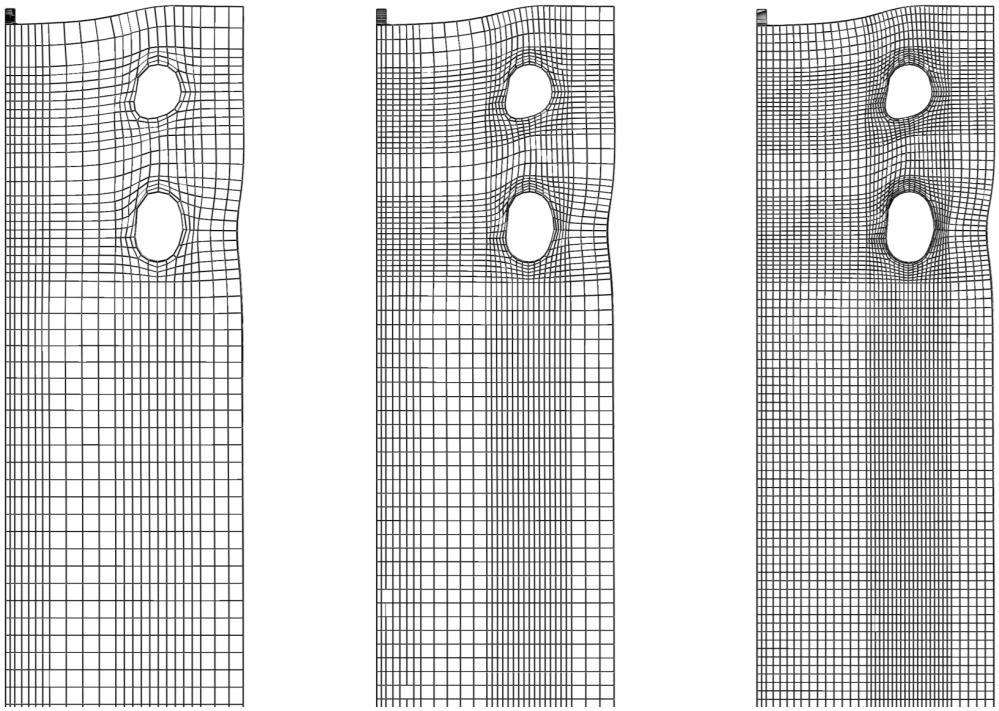

Figure 3.29: Comparison of Coarse, Medium, and Fine deformed meshes at 100mm load displacement

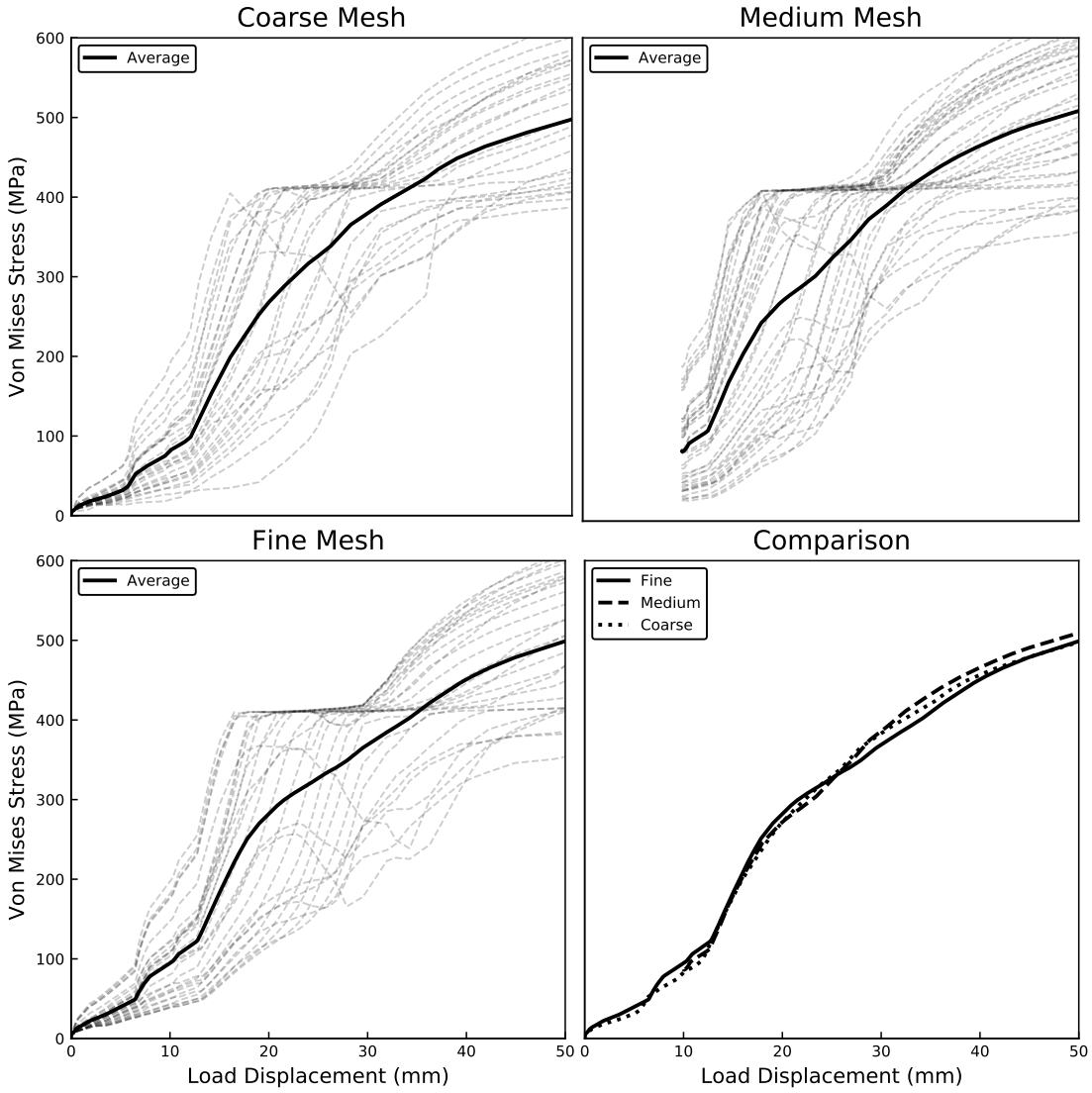

Figure 3.30: EBS: Shear Component Comparison

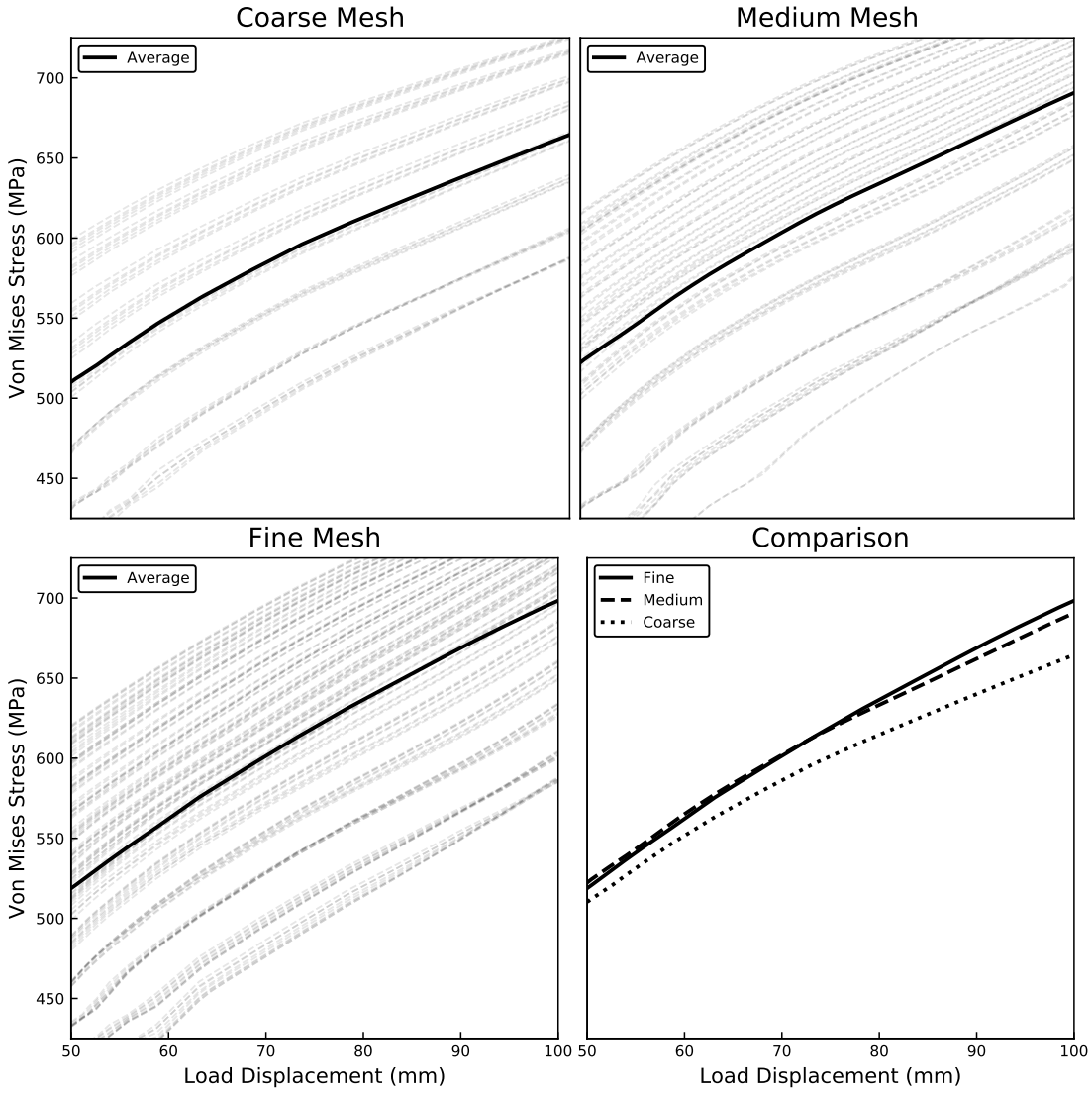

Figure 3.31: EBS: Tension Component Comparison

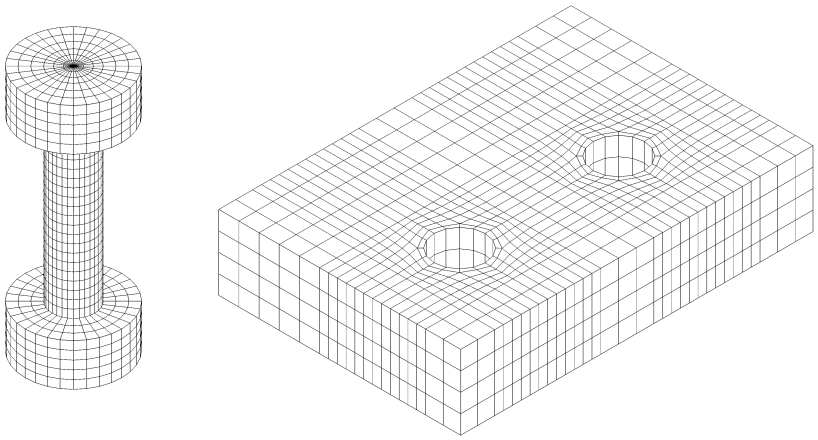

Figure 3.32: Meshed bolt and exterior splice plate.

There was no significant difference between all three mesh densities for the stresses in the shear region. However, for the tension stress response, the coarse mesh increasingly underestimated the average stress compared to the other two densities as the loading increased, while the fine and medium meshes showed a similar response. Based on the comparison of these two local responses, as well as complete correlation of global responses (such as the total splice end moment and tension splice force), it was determined that the medium mesh density was suitable for the preliminary finite element models. Computation time (Table 3.5) scaled approximately linearly with the total number of elements, allowing for the medium mesh to provide a suitable compromise between accuracy and resources required.

With the mesh sensitivity analysis performed and a comparison between the reduced and full-integration schemes evaluated, a general method for the finite element model meshing was completed. The coarse mesh section of the model followed the general element sizing principles as the Coarse Mesh values in table 3.4, while the splice plates were detailed with a mesh similar to that of the fine mesh section. The bolts were meshed using a Hex-Dominated Sweep mesh of approximately 4mm to symmetrically fill the cylindrical shank and bolt head; the use of this mesh type and size was based on its successful use by Pizzuto

(2019).

3.2.2.4 Contact properties

Contact between parts were simplified with a single friction coefficient of 0.30, corresponding to a contact surface Class A in the CSA S16-19 standard, with default *Abaqus* normal contact properties. While first developing the pFEMs, contact instabilities were the major cause of diverging analyses and solver errors. Errors in CAD precision from the imported parts caused plates in contact with the flanges to have a non-flat surface, resulting in the lack of a proper initial contact interface, resulting in instability issues. Additionally, without the initial snug contact interface, the sudden preloading of the bolts caused the static solution procedure to diverge, as Abaqus attempted to resolve contact overclosures between parts. The improvement of input CAD file tolerances, as well as the use of the automatic stabilization feature for the bolt pretension step resolved this issue. The automatic stabilization provides damping to the model proportional to the total strain energy of the system, preventing any sudden shifts in adjacent model components that would cause solution convergence stability issues.

3.2.2.5 Loading procedure

The analysis was split into four distinct steps in Abaqus to allow for changes in loading procedures without having to completely restart the analysis. The steps are described in Table 3.6. Each step started with an initial increment size of $1E^{-4}s$, with an automatically adjusted minimum increment size of $1E^{-8}s$, and a maximum increment size of $0.05s$. Typically, the smaller increment sizes were necessary during the bolt slipping and first contact of the bolt shank to the flanges in the LOAD1 step. Once all parts were in solid contact with each other, the step sizes increased.

Determining the total displacement for the LOAD2 step was an iterative process. Since the FE models did not consider fracture of the tension (or shear)

Table 3.6: Step definition for *Abaqus* pFEMs

Step	Time	Description
INITIAL	N/A	Defining all boundary conditions.
PRETENSION	0.1	Pretensioning of bolts while supports are fixed in place.
LOAD1	0.5	Load until all slipping has occurred.
LOAD2	1	Load until failure.

plane, the stress in the tensile plane followed the true stress-strain path as determined by previous coupon test data. As no fracture stress/strain was defined, the tensile stress continually increased until the material definition reached its limit.

Failure for a given block shear mode could then be defined as the point where both the shear and tension planes reach their nominal stress capacity, or $0.6\frac{F_y+F_u}{2}$ for the shear plane and F_u for the tension plane when using the CSA S16-19 design equations. The stress from the finite element models could be determined in two ways: first, the free body cut resultant force magnitude of each failure plane region can be divided by the initial, undeformed failure plane area to determine the engineering stress of each plane. Second, the Von Mises stress of all the elements in each failure plane can be extracted from each failure plane, with the mean value compared to the failure criteria. The second method has proved to be more meaningful, as it inherently considers the often significant deformation of each failure plane at failure, and better considers the complex stress distributions by using the Von Mises yield criterion rather than engineering stress values. Chapter 5 provides greater detail in the definition, calculation, and use of this failure criteria.

3.3 Results of preliminary finite element models

Once the first five finite element models were completed, an initial evaluation of the expected failure modes compared to the observed failure mechanism was performed. First, a qualitative evaluation of the tension flange at maximum load was performed; the relative deformation and the Von Mises stress contours are shown in Figures 3.33 and 3.34.

It is immediately evident that the Edge Block Shear failure mode has occurred due to the significant displacement of the corner blocks relative to the rest of the flange section, as well as the distribution of higher stresses around the last row of bolts that propagate towards the free edge and along the gross shear plane. For specimens M3-M5, significant necking can be observed along at the net tension failure region, suggesting an imminent fracture of the plane.

Second, the predictive capacity of the CSA S16-19 block shear equation and the assumed conversion between the block shear resistance and the equivalent moment resistance was evaluated. The block shear failure of the pFEM was defined as the point where the average Von Mises stresses on both the tension and shear planes reached their nominal capacities, F_y and F_u. The total moment at the splice face at this point of failure was then defined as the corresponding moment capacity of the given failure mode.

These resistances were then compared to the theoretical moment resistance calculated in the process described in Section 3.1.3, where the unfactored, probable CSA S16-19 block shear resistance of the tension flange was multiplied by the assumed moment arm between the flange centroids to determine the corresponding moment resistance of the block shear failure mode.

The true observed moment resistance was divided by the theoretical moment resistance to obtain the Professional Factor for the CSA S16-19 design equation and the methodology used in Section 3.1.3, the results of which are shown in Figures 3.35 and 3.36. A Professional Factor of 1.0 would indicate a perfect predictive design equation; a Professional Factor greater than 1.0 would indicate a predic-

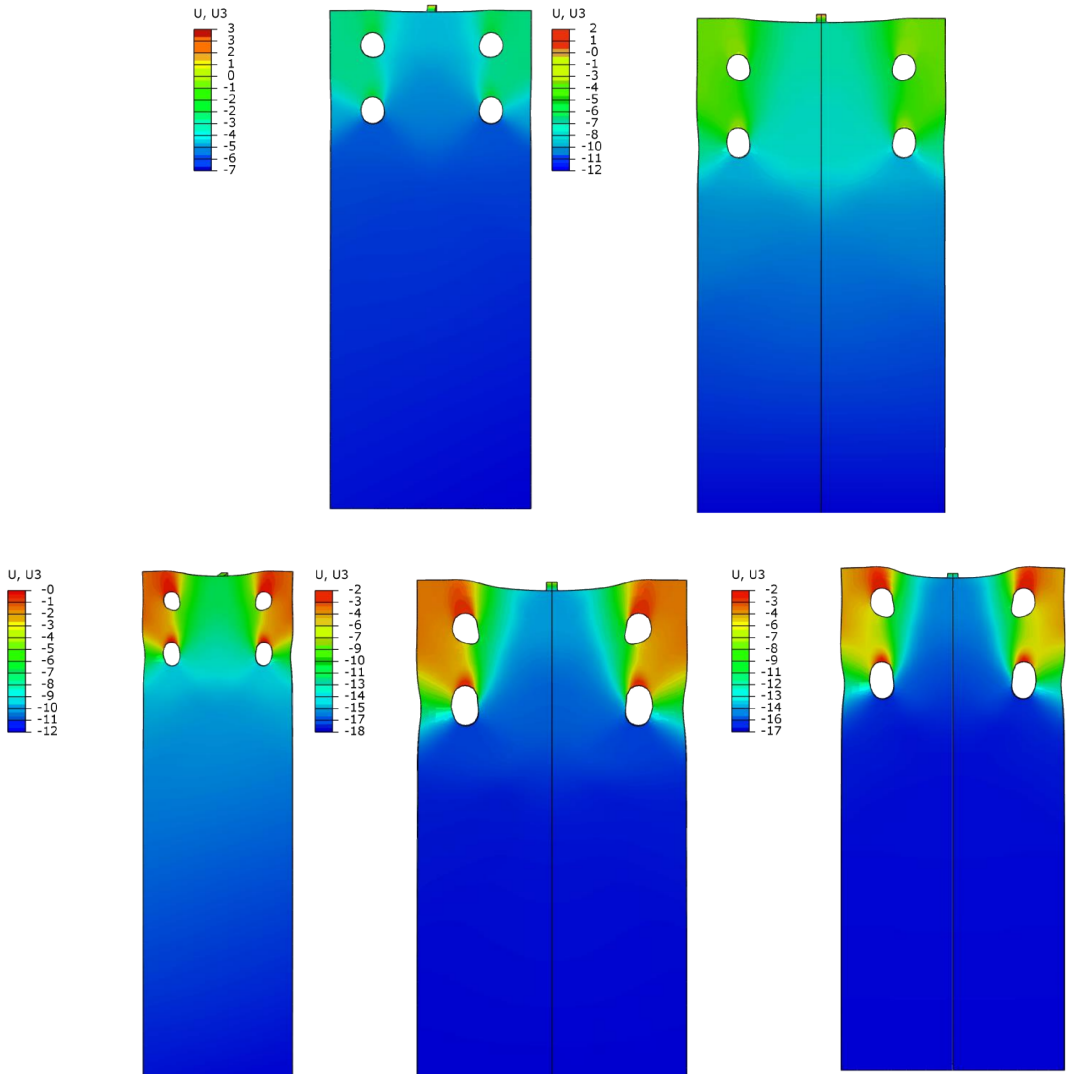

Figure 3.33: Relative deformation comparison of M1-M5 pFEMs.

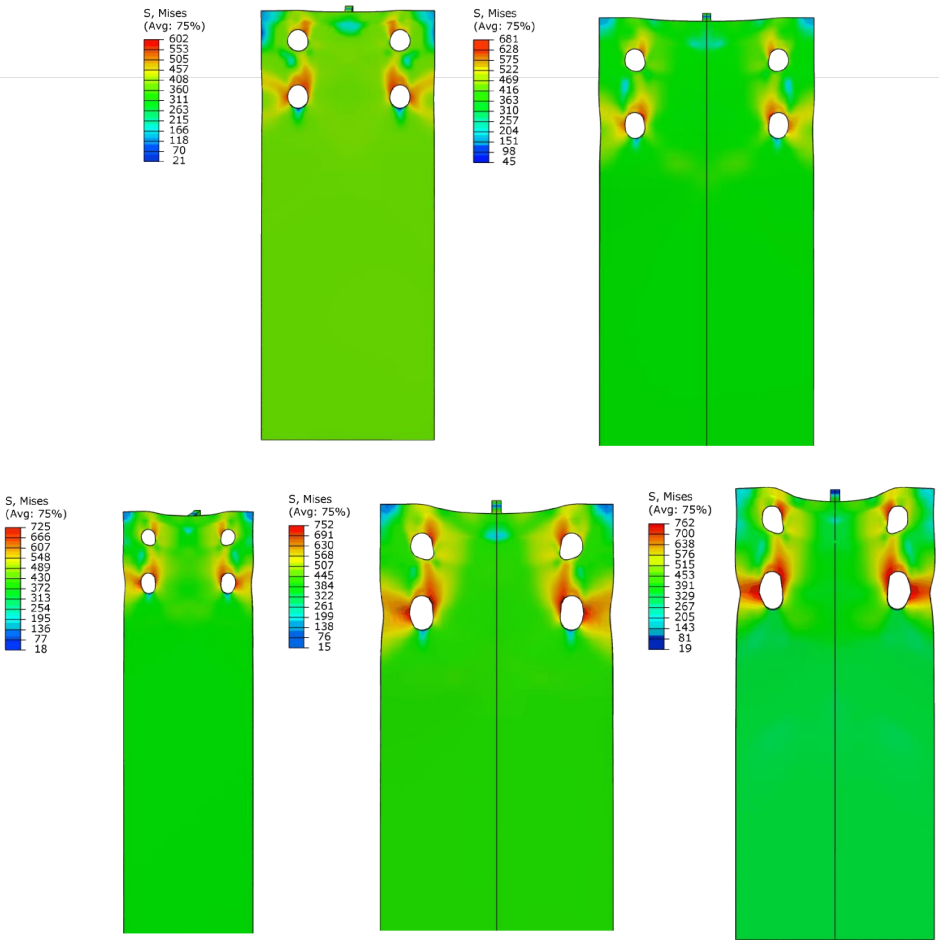

Figure 3.34: Von Mises Stress comparison of M1-M5 pFEMs.

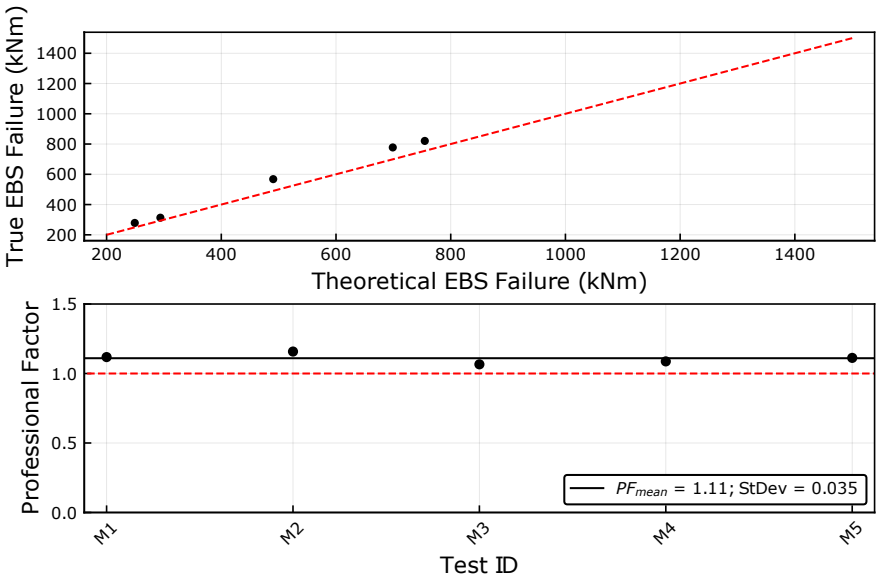

Figure 3.35: CSA S16-19 predictive capacity for the EBS failure mode.

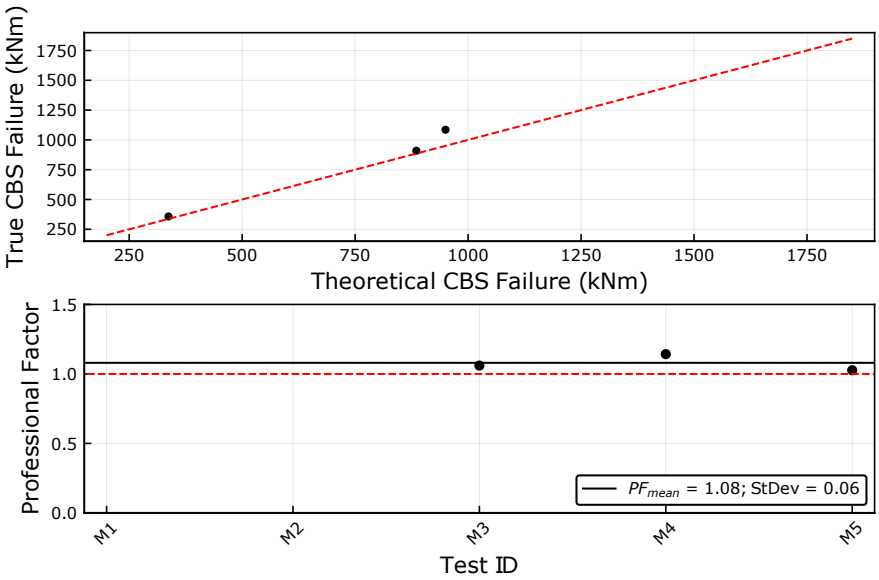

Figure 3.36: CSA S16-19 predictive capacity for the CBS failure mode.

tive design equation that underestimates the true capacity of the section, and conversely, a Professional Factor less than 1.0 would indicate a predictive design equation that overestimates the true capacity. Since the ultimate displacement of the load point in the pFEMs were a rough estimate of the critical displacement at ultimate load, some specimens were loaded to a point where the Complete Block Shear failure planes also reached their respective limits. These values were compared to the theoretical resistances in Figure 3.36 as an additional point of evaluation for the CSA S16-19 block shear design equations, but it is noted that the EBS failure mode still governed the overall capacity as expected.

The Professional Factors for the EBS and CBS failure modes were 1.11 and 1.08 respectively, suggesting that the design methodology could reasonably predict for the moment-induced block shear failure mode. Further, little scatter of the data points in Figure 3.35 indicated that any deviation from perfect predictive capacity was from smaller systematic errors of the design equation and not a complete dissociation between predicted and true failure behaviour.

Based on the qualitative confirmation of the Edge Block Shear failure mode, as well as reasonable Professional Factor values of both the failure modes, the final detailing of the pFEM specimens for fabrication could be performed with confidence. Further, the good correlation of both qualitative and quantitative data of the pFEMs confirmed that the assumptions and methodology for calculating moment-induced block shear resistances was reasonable, and that further finite element modelling could be performed for additional data and insight on the moment-induced block shear failure mode.

3.4 Summary

Insight on two key components of the research project was provided in this section. First, the analytic methodology for the selection and detailing of a W-section moment splice connection with a block shear critical failure mode was presented.

From numerous trial and error attempts to detail a block shear critical moment splice connection, a general set of observations on what section geometry parameters could allow for a block shear critical connection was determined. In general, a block shear critical moment splice connection is expected to be possible in a limited subset of available W-sections due to the conflicting limitations between bolt shear strengths, connection lengths, and gross section flexural capacities. This analytic design procedure was also expanded to design the bolts, splice plates, and bearing stiffeners should the section-connection detail be fabricated and tested in a structural laboratory.

Second, once a set of potential moment block shear failure section-connection details were determined, preliminary finite element analyses were performed to provide initial verification that the analytic methods were accurate. The development of these models required multiple iterations to verify the validity of boundary condition assumptions as well as a mesh sensitivity analysis to determine a reasonable mesh density to reflect true deformation and stress distributions at failure. The preliminary finite element analysis results showed that the moment-induced block shear was a possible failure mode for bolted moment connections, and that the proposed design methodology and assumptions were reasonable for predicting the capacity of a moment-induced block shear failure.

With the base methodology for both the analytic design and finite element modelling of a moment block shear connection completed, the laboratory testing phase of the project could be developed. This required the analysis and design of additional components for laboratory testing such as the loading beam and bearing plates, as well as the selection and detailing of the required instrumentation. Chapter 4 provides an overview of the laboratory testing preparation performed for this research project.

Chapter 4

Laboratory test preparation

For the calibration and verification of the preliminary finite element models, full scale testing of the six test specimens was planned in the Jamieson Structural Laboratory at McGill University. The overall footprint of the test configuration as well as the detailing of the loading beam were based on the capacity of the available loading apparatus, the spatial limitations of the structural laboratory, and the geometric and strength limitations of existing test apparatuses. The type, quantity, and location of a series of instruments to record strain, force, and displacement during testing were also determined. Due to fabrication delays and the disruption of in-person research work due to COVID-19 during the Spring of 2020, the laboratory phase was not completed within the time frame of this thesis. This section provides an overview of the preparation and detailing of the laboratory testing phase, but does not provide the results of these tests.

4.1 Detailing of specimens

With the connection geometry finalized for the M1-M6 test specimens, additional design decisions were required before fabrication and laboratory testing. First, the length of the test specimens was chosen to be 2700mm, with an effective support-to-connection end length of 2500mm, based on the spatial constraints

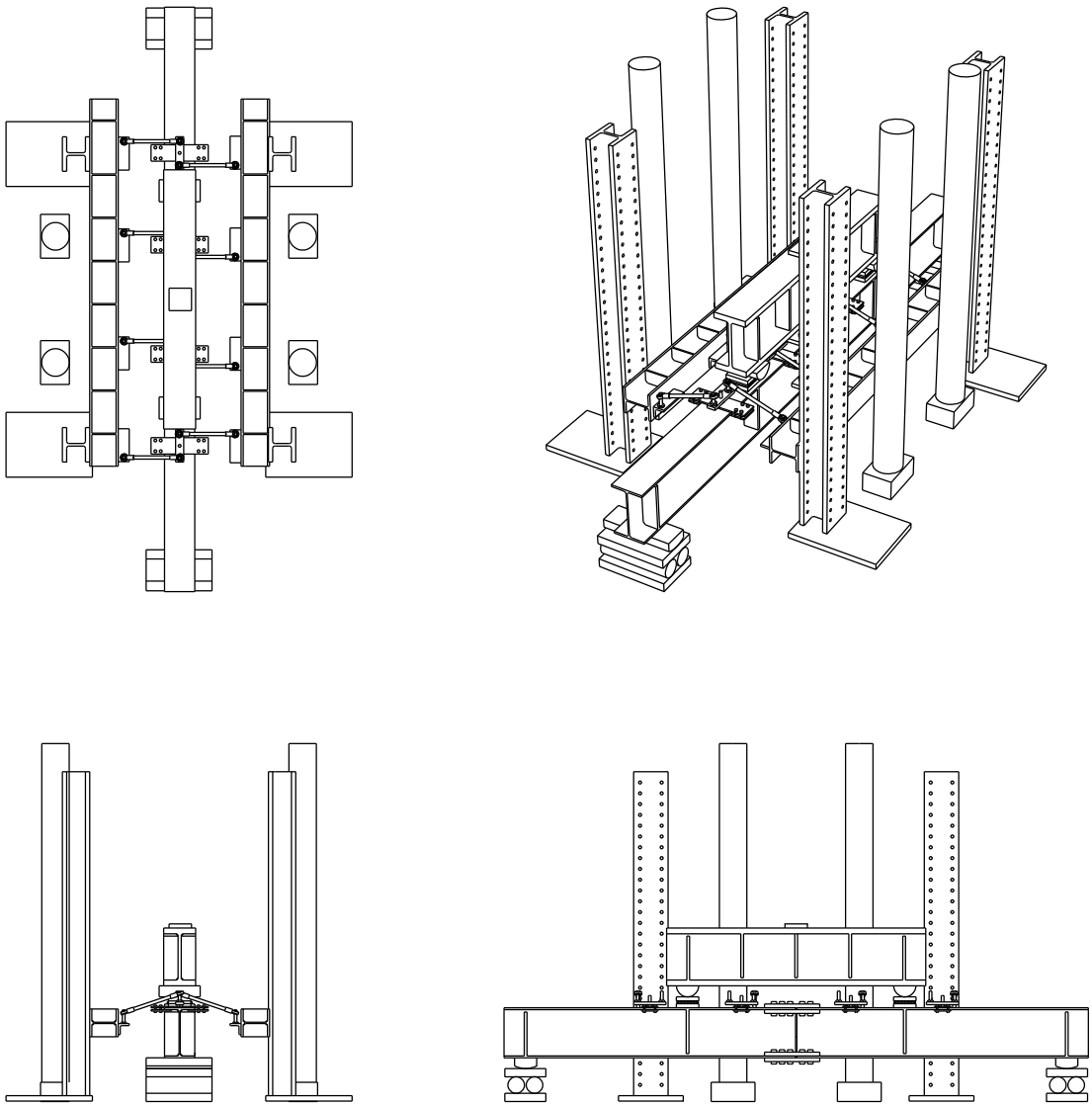

Figure 4.1: Overview of complete test assembly.

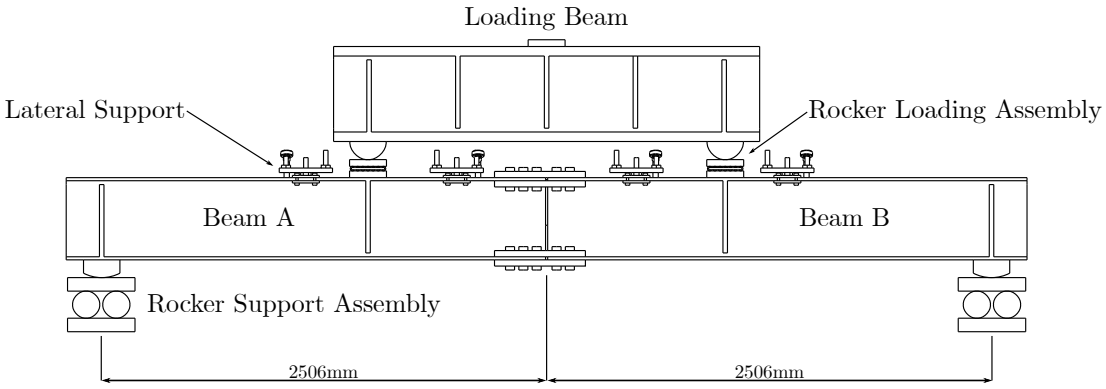

Figure 4.2: Test assembly overview.

of the structural laboratory. The total test length of 5400mm allowed for the majority of the testing assembly to remain within the footprint of the loading frame assembly surrounding the main hydraulic actuator, as shown in Figure 4.1. The individual specimen lengths of 2700mm allowed for efficient storage and transportation within the structural laboratory, as the total weight of each specimen remained below the lifting capacity of the magnetic lift attachment used when transporting the beams.

The selection of a 1500mm shear length combined with the total 2500mm effective length of the beam was based on two factors. First, it minimized the required effective length of the loading beam to 2000mm; this allowed for a reasonably sized W-section to be used as the loading beam, while providing adequate strength and stiffness throughout the test series. Second, it provided suitable clearance for the lateral support clamp plates on either side of the loading plate assembly. This was critical, as the available positions for the lateral support assemblies were limited by the existing longitudinal running beams on the test frame. The 1500mm shear span also provided a suitable distance to develop the required moment in the splice connection without exceeding the capacity of the 11MN actuator. As determined in Section 3.1.3 Equation 3.18, the absolute peak expected force at each load point was 1675kN; this would then require a load at the hydraulic actuator of 3350kN, well below the 11MN capacity of the machine.

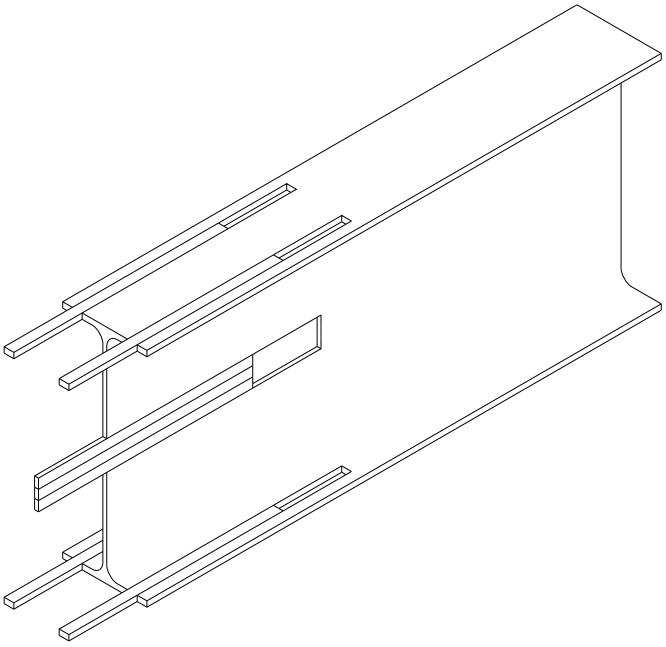

Figure 4.3: Approximate location of coupon blanks.

Since the laboratory testing configuration consisted of a symmetric moment splice connection, two beams were required for each test. However, to reduce the amount of instrumentation required for each test, and to allow for certainty in the failure behaviour of the overall splice connection, it was desirable to force the expected block shear failure mode on one side of the moment splice. This was achieved by adding an additional row of bolts for one of the two beams, Beam A, to increase the connection strength of one side of the moment splice. Instrumentation could then be installed on Beam B alone, as failure would localise in the Beam B connection region. This asymmetry would also provide the benefit of requiring a lower total displacement of the loading beam to reach the expected block shear failure mode, as severe tension flange deformation would concentrate on one half of the moment splice. In the structural laboratory, Beam B was always specified on the South side of the testing frame, as the Data Acquisition System and hydraulic actuator controllers were closer to that end, allowing for shorter lead wires and connections from the instrumentation to the recording system.

For capturing the true material properties of each test specimen, 60mmx600mm blanks were cut from the web and flanges of the parent W-section; the approximate locations of these blanks are shown in Figure 4.3. The blanks were then specified to be milled to shape and tested for tensile properties as per the ASTM A370-05 standard (American Society for Testing and Materials, 2005). The results of the coupon testing will allow for more accurate finite element models to be created.

4.2 Design of loading beam

Since a four point loading configuration was specified for the laboratory tests, a suitable load spreading member was required to transfer the single point load from the hydraulic actuator to the two sides of the moment splice. The design of the loading beam required that it was well within its elastic range for the expected flexural, shear, and bearing loads during all six of the laboratory tests. As the shear span of the four point load configuration was set as $1500mm$, and the total effective length of each specimen was $2500mm$, the loading beam would have a total effective length of $2000mm$, excluding any additional extension at each end to provide improved bearing resistance. The loading beam would then have to adequately withstand an effective three point loading configuration with a distance between points of $1000mm$.

The design load was selected to be two times the expected load to reach gross plastic moment capacity on the M5:W610X101 test specimen, which had the highest theoretical value of M_P from all selected specimens. The equivalent load applied at the two ends of the loading beam was determined by dividing the expected unfactored gross plastic moment using probable material properties by the shear span, $a = 1500mm$:

$$
\begin{aligned}
M_{max,M5} &= 2 \times M_P && (4.1)\\
&= 2 \times (1.1 \times 350MPa)(Z_x)\\
&= 2233kNm\\
P_{max} &= M_{max}/a && (4.2)\\
&= \frac{2233kNm}{1.5m}\\
&= 1488kN \rightarrow 1500kN
\end{aligned}
$$

Then the expected shear, moment, and bearing load was determined for the loading beam:

$$
\begin{aligned}
V_f &= 1500kN && (4.3)\\
M_f &= 1500kN \times 1m\\
&= 1500kNm\\
B_f &= 1500kN \times 2 && (4.4)\\
&= 3000kN
\end{aligned}
$$

Tabulated values for flexural and shear resistances in the CISC Handbook, based on the CSA S16-14 standard, were used as starting points for the selection of a suitable W-section loading beam. A heavy-flange W-section was chosen to maximize the flexural stiffness of the loading beam while maintaining a reasonable weight. As many W-sections fit the calculated strength requirements, a 2400mm long W460X349 section was chosen based on the available stock of the steel fabricator. The additional 400mm is due to an extension of 200mm on either end of the loading beam to provide sufficient bearing area for the half-round contact assembly between the loading beam and the test specimens. The expected

strengths of the loading beam were calculated using nominal material strengths for ASTM A992 steel (American Society for Testing and Materials, 2019) as well as factored design equations from the CSA S16-19 standard:

$$M_r = M_y = 2407kNm > M_f$$
$$V_r = 3287kN > V_f$$
$$B_r = 6945kN > B_f$$
$$\Delta_{max} = 1.2mm = \frac{L}{1665}$$

As with specimens M1-M6, 25mm (1") bearing stiffeners were specified at all contact points. The stiffeners were not necessary for strength requirements, but were included to provide additional torsional stability to account for possible load eccentricities during testing. Further, due to the heavy beam section and relatively short length, additional shear stiffeners were included between load points to prevent any onset of shear buckling. These stiffeners also provided additional torsional stiffness along the length of the loading beam. The elastic deflection of the loading beam at midpoint from the peak expected load was also calculated; this deflection of 0.06% of the load beam length was determined to be suitable for testing.

Further verification of the loading beam design was performed by an elastic finite element analysis, as shown in Figure 4.4. The loading beam model was placed in representative boundary conditions, and the central loading plate was displaced downwards until the onset of yielding of the beam. The finite element analysis verification of the loading beam was necessary since the CSA S16-19 design methodology used to determine the shear and bearing resistances allow for yielding of the section before reaching the ultimate capacity state. Since any yielding in the loading beam would provide measured displacement errors during testing, and would result in progressive deformation of the loading beam

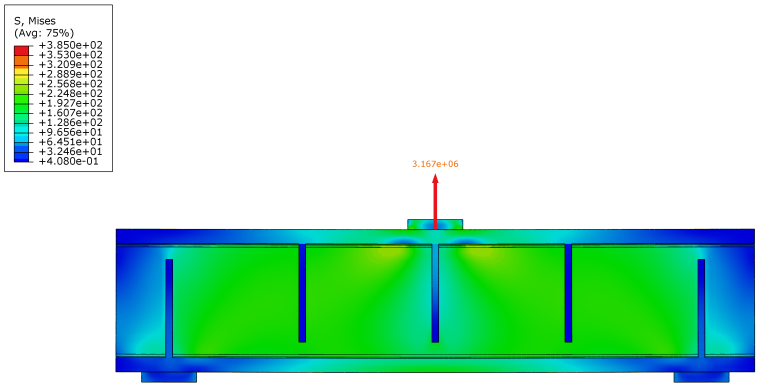

(a) General overview.

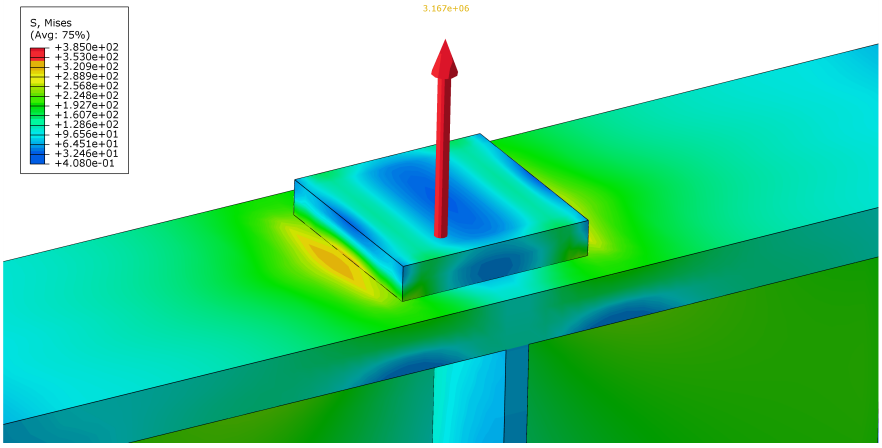

(b) Loading region.

Figure 4.4: Finite element model of loading beam.

for subsequent tests, preventing yielding of the loading beam was critical. A visual inspection of the finite element model showed the onset of yielding at the compression flange near the central loading plate. This yielding onset occurred at a load of 3167kN, which surpassed the design peak bearing load on the beam during testing. The conservative analytical and finite element analysis verification of the loading beam design provided confidence that the W460X349 section was a suitable member to load the test specimens.

4.3 Instrumentation and data acquisition

Since the objective of the laboratory tests was to verify the validity of the finite element models, instrumentation to capture accurate strains and deformations was specified at critical locations along the test specimen. A series of strain gauges, linear variable differential transformers (LVDTs), and string potentiometers were specified for each test to capture strains in local failure plane regions as well as global displacements and induced forces.

Spring potentiometers, LVDTs, and load cells were specified along the test assembly to capture global values of displacement and force, as shown in Figure 4.5. Three string potentiometers were specified on the ground of the test configuration at the precise location of the loading points on each half of the connection. The string potentiometers were secured to wood plates that could be weighed downed during testing to keep the position stable. The total force at the load point was determined by the internal load cell of the loading head of the 11MN hydraulic actuator. An internal LVDT also provided the displacement of the actuator head on the loading beam. Not shown in Figure 4.5 are two additional LVDTs magnetically attached to each side of the tension flange, that would capture the displacement of the edge 'block' for the EBS failure mode.

For local observations of strain at the expected failure planes, as well as precise measurements of strain across the gross section, a series of strain gauges were

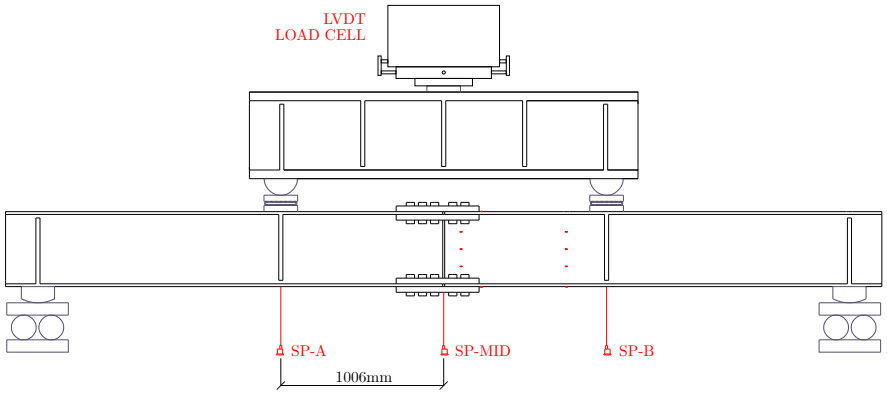

Figure 4.5: Instrumentation for global deformation capture.

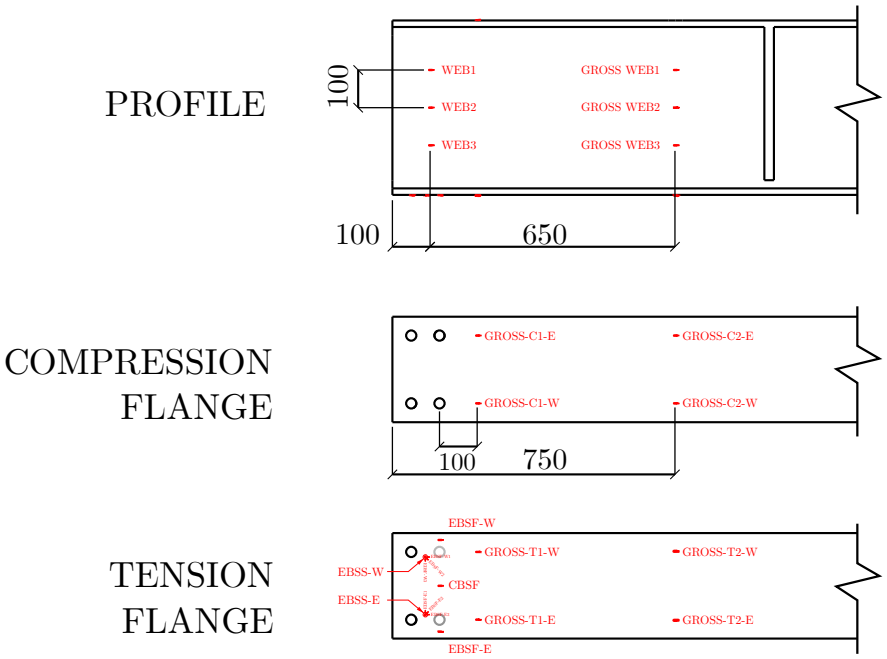

Figure 4.6: Strain gauges for local deformation capture.

specified for each test specimen, as shown in Figure 4.6. First, to determine the overall moment experienced at the moment splice, linear strain gauges were specified along the gross section of the web as well as at the extreme edges of both flanges. The positioning of the gross section strain gauges was based on remaining in the constant moment region of four-point load configuration, as well as avoiding the location of the lateral support clamp plates. In general, the gross section strain gauges were placed 100mm behind the centreline of the last row of bolts in a given connection. Providing a series of strain gauges at the gross section allowed for an accurate measurement of the induced moment on the section, as well as the stress profile along the depth of the member.

At the tension flange near the connection region, additional strain gauges were specified to measure the local strain in three of the four expected failure planes of block shear: the shear plane for the EBS failure mode (EBSS), the fracture plane for the EBS failure mode (EBSF), and the fracture plane for the CBS failure mode (CBSF). The stress at the failure plane could then be determined once the true material properties of the section were determined. Strain gauges were not appropriate for the shear plane for the complete block shear failure mode (CBSS) as the failure plane is located at the curved intersection of the web/K-area interface, and were not installed. Since the controlling failure mode for all six laboratory test specimens was expected to be in Edge Block Shear, the omission of strain gauges in the CBSS plane was determined to be acceptable; a post-test visual analysis of the deformation of the CBSS area was planned by drawing a series of equidistant grid lines alone the entire connection region for the beam, where the change in distance between grid points could then be measured by hand. For the two fracture planes, EBSF and CBSF, linear strain gauges were placed at the centreline of each expected failure plane. For the CBSF plane, the strain gauge was centred between the two bolt hole centres; for the EBSF plane, the strain gauge was placed halfway between the free edge of the flange and the closest edge of the neighbouring bolt hole. The expected shear yielding failure

mode for the EBSS failure plane was captured by rectangular stacked strain gauge rosettes. Since the stress pattern of the shear plane near the bolt holes were expected to be significantly more complex than that of the tension planes, a rosette was specified for the EBSS failure plane. The rosette allowed for the calculation of all principal stress values, which could then be used to determine the Von Mises stress at the EBSS failure plane, allowing for a direct comparison to the average Von Mises stress extracted from the finite element models.

The specified strain gauges were capable of accurately measuring up to $\epsilon = 0.014$ of total strain. From experience with testing steel coupons of ASTM A992 steel, the strain gauges were expected to provide usable results up to approximately the initial strain hardening region of the stress-strain curve. Although this limitation of the strain gauges would not allow for a complete capture of the local strain profile up to fracture, their use was justified since the onset of fracture would be visually evident from extensive deformation, as well as from the change in the applied load vs. deformation curve that is constantly monitored during testing.

4.4 Test assembly and loading method

The full testing assembly, as seen in Figures 4.7 and 4.8, consisted of the moment splice connection assembly, the loading beam, and contact points. The contact points provided proper bearing surfaces for loading, support, and lateral restraint, and came from existing components from the structural laboratory at McGill University.

The support assembly consisted of a rocker element providing 200mm of bearing length on each end of the moment connection, that rested on a series of 3" (75mm) thick plates and two 6" (150mm) diameter steel cylinders that allowed free displacement in the axial direction, as well as rotational freedom at the support locations. The loading assembly contact point provided an equivalent degree

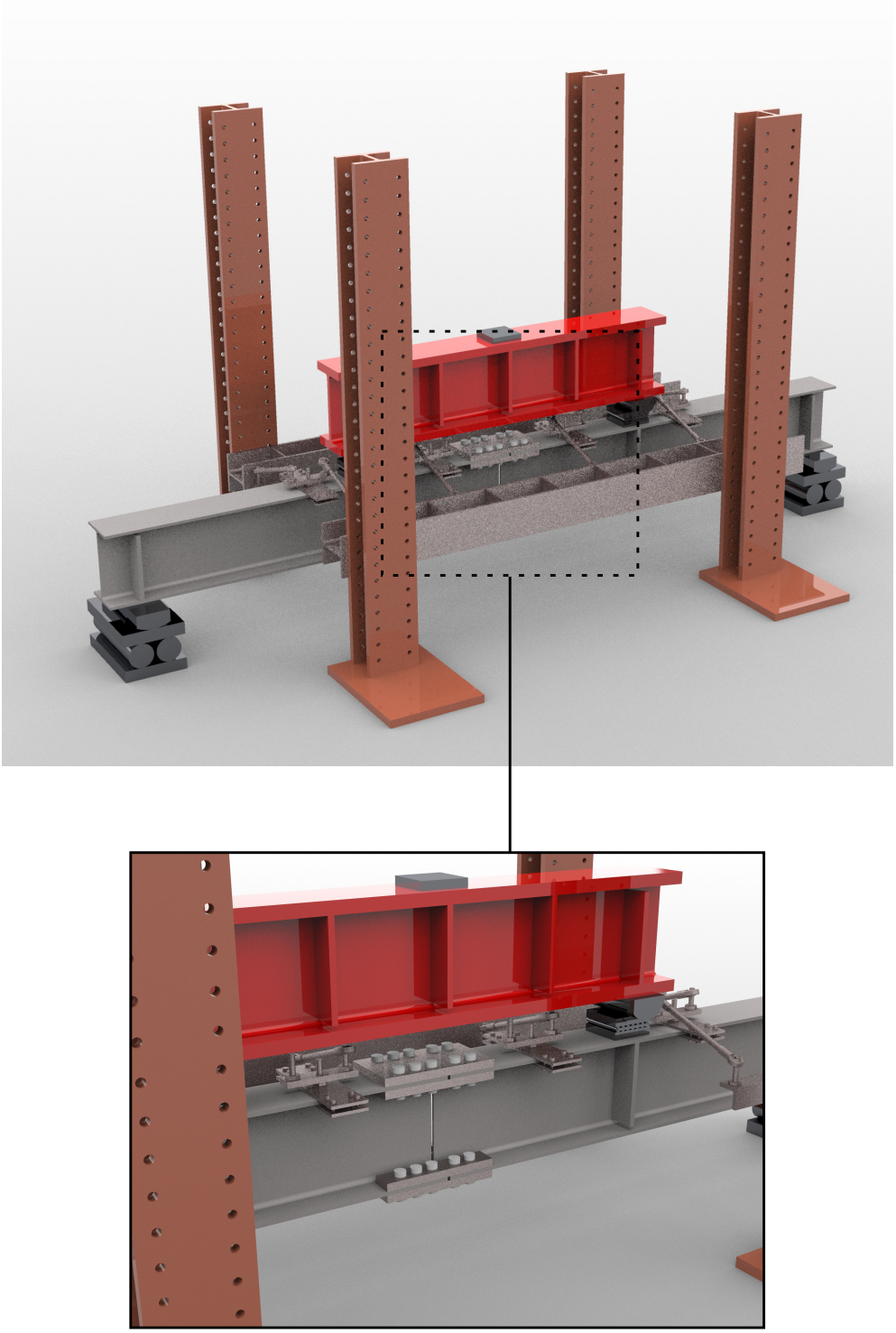

Figure 4.7: Render of loading frame assembly.

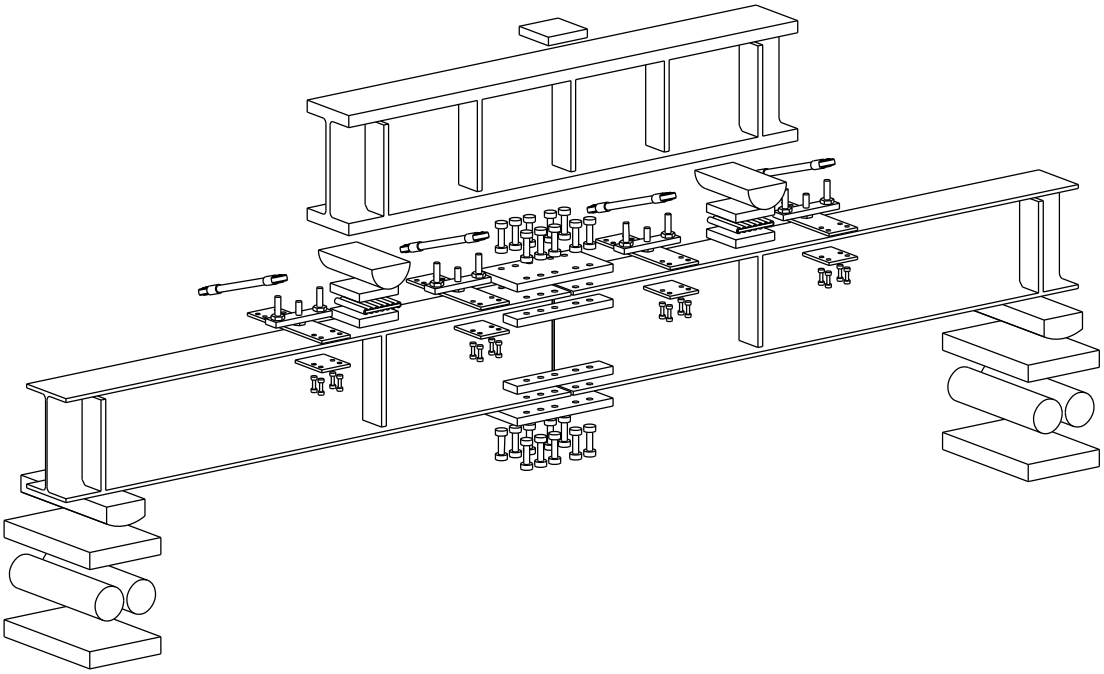

Figure 4.8: Exploded view of test specimen assembly.

of freedom at the load points, with an 8" (200mm) half-cylinder providing the rocking surface on a series of 1.5" (38mm) thick steel plates and a series of 1" (25mm) cylinder rollers.

To restrain any lateral torsional buckling of the beams during testing, lateral support was provide by four clamp plate assemblies that were bolted to the compression flanges of the beams. These clamp plates were restrained from lateral displacement by a series of tie rods and ball joints that were fixed along two existing running beams on the test frame. As existing holes in the running beams governed the location of the lateral support anchor points, the position of the clamp plate assemblies on the two test beams were not perfectly symmetric; the exact positions are shown in Figure 4.9. The tie rod support system allowed for vertical displacement by means of a freely spinning upper plate on each of the clamp assemblies. The limited vertical stroke of this lateral support configuration (100mm), as well as the existing holes in the test frame columns to mount the running beams, required that the vertical position of the running

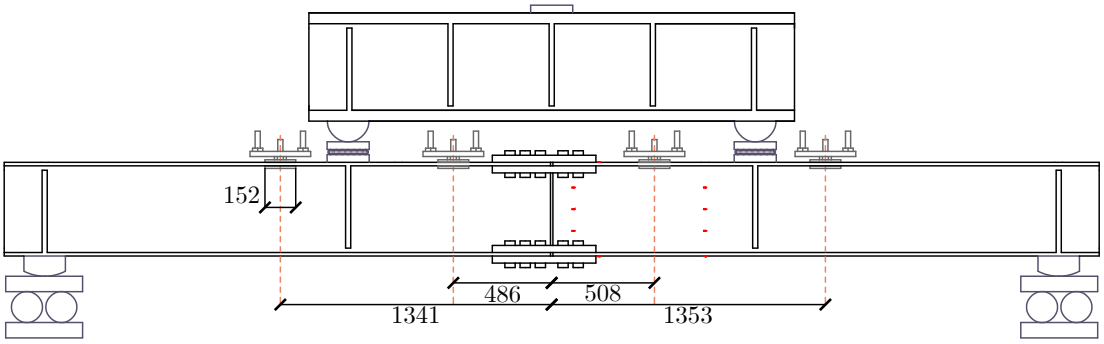

Figure 4.9: Positioning of lateral support clamps. Dimensions in mm.

beams be changed depending on the section depth being tested. This allowed for the maximum possible amount of vertical displacement while maintaining lateral support.

A fixed-rate, displacement-based loading protocol was specified for the laboratory tests, with a 1mm/minute loading rate determined to be a suitable compromise between test duration, safety, and resolution in the captured data.

4.5 Summary

To calibrate and verify the preliminary finite element models, a full-scale laboratory test procedure was developed, and six representative moment splice connections were detailed and fabricated for testing at the structural laboratory at McGill University. The test configuration consisted of new and existing components to support, load, and stabilize the specimens during testing. Existing assemblies were used to provide load, support, and lateral restraint contact points, while a new loading beam was design and verified using finite element analysis to adequately load the beams on either end of the moment splice connection. The loading beam was designed to remain well within the elastic range when under the theoretical maximum required load for the entire test program. This design was based on factored design equations in the CSA S16-19 standard using nominal ASTM A992 steel properties, and was verified using finite element analysis.

String pontentiometers, LVDTs, and load cells were specified to capture global values of displacement and force during testing, while linear and rosette strain gauges were specified at critical points to accurately measure strain and stress in local failure regions. Due to fabrication delays as well as the disruption of in-person research work due to COVID-19, testing was not completed within the time frame of the author's program, and is thus not discussed in this chapter.

Chapter 5

Expanded FE study and results

From the preliminary models `M1-M5`, 12 additional finite element models under the same loading conditions were created and evaluated. These additional models served to explore a wide range of section sizes and connection geometry to provide a reasonable level of certainty on the evaluation of the predictive capacity of the current block shear design equations. As the preliminary models included non-standard connection geometry to isolate the block shear failure mode as much as possible, they were given the `SPEC` suffix in the test ID. Five additional models with the same section sizes as the `SPEC` series, but with more typical bolt spacing details were modelled to observe the minor changes in the connection capacities; these specimens were given the ID suffix `TYP` to represent *Typical Connection*. The remaining FE models `M7-M12` were of varying section sizes and connection geometries. In addition to a review of the performance of the current block shear design equations, an analytic investigation on the 15% rule was performed. The results from the block shear finite element study provided further insight on the validity of current and proposed design methods for reduced flexural capacities for reduced flange areas of W-sections.

5.1 Expanded finite element analysis

With the completion of the preliminary finite element models and their fabrication for laboratory testing, the catalogue of block shear critical finite element section-connection details was expanded to provide additional insight on the moment-induced block shear failure mode. The finite element model procedure, including the selection and density of mesh elements as well as the loading protocol, followed the procedure used to develop the initial five models.

Five additional finite element models, M1TYP to M5TYP, were based on the same section sizes as M1-M5, but with connection spacing details more commonly used in practice. The initial M1-M5 primary finite element models were renamed M1SPEC to M5SPEC to indicate that the connection details were specified by the author, while M1TYP to M5TYP indicated that the connection details had 'typical' bolt spacings. *Typical* in this context meant bolt pitches of 3" (75mm), end distances of 2" (50mm), and edge distances no less than 1.5" (38mm). For specimens in M1SPEC to M5SPEC that already met the requirements of 'typical' connection details, an additional row of bolts was added for the equivalent TYP model. In addition to the five models based on the initial section sizes, six new section-connection details, M7 to M12, were designed and modelled. The methodology used in the detailing of the initial M5-M6 models was retained, with sections being selected at the discretion of the author to span as much of the available W-section geometric parameters as possible. An overview of all modelled specimens and connection details are provided in Figure 5.1 and Table 5.1. The three main parameters were the section width (b_f), the section depth (d), and the linear mass (W). The relative geometries of the entire tested catalogue of sections is shown in Figure 5.1. As discussed in Chapter 4, although a suitable range of beam depths (d) and flange widths (b_f) were covered by the test catalogue, the linear masses (W) of the tested sections remained relatively low ($W \leq 170kg/m$) due to the limitation on block shear critical failure modes. With a total of 17 section-connection details, all relevant information on stresses,

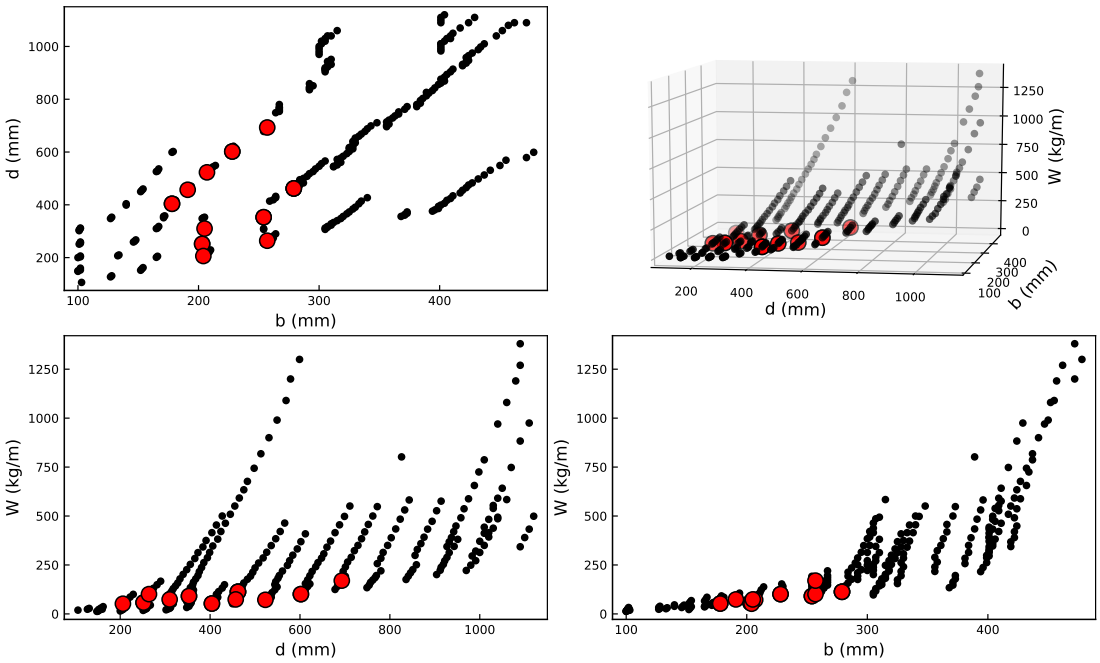

Figure 5.1: Complete range of available W-sections. Tested and modelled specimens in red.

forces, and displacements of the loaded models was extracted for an aggregated review.

5.1.1 Initial observations

Before numerical data were extracted from the finite element analysis models, an initial visual evaluation of the deformed shapes of the loaded connection as well as the colour-graded contour plots of stress and displacement was performed. For most sections, the isolated deformation of the edge block was evident, and was clearly demarcated by the displacement contours as shown in Figure 5.2; the necking of the tensile plane was also visually evident for most sections. The Von Mises stress contours also provided initial confirmation that the block shear failure occurred, with most of the gross shear plane reaching the yield stress, while the net tensile plane typically showed stresses approaching or surpassing the expected ultimate strength of the material, indicating the onset of rupture.

Table 5.1: Connection geometry overview for M1-M12 specimens.

ID	SECTION	d_h (mm)	n_{rows}	End (mm)	Pitch (mm)	Gauge (mm)
M1SPEC	W250X58	24	2	35	65	120
M1TYP	W250X58	24	2	50	75	126
M2SPEC	W360X91	24	2	50	75	170
M2TYP	W360X91	24	3	50	75	170
M3SPEC	W410X53	21	2	35	60	110
M3TYP	W410X53	21	2	50	75	107
M4SPEC	W460X113	27	2	50	75	180
M4TYP	W460X113	27	3	50	75	180
M5SPEC	W610X101	24	2	35	75	145
M5TYP	W610X101	24	2	50	75	145
M6	W460X113	27	2	50	75	180
M7	W530X72	24	2	50	75	130
M8	W200X52	21	2	38	65	125
M9	W250X101	24	2	50	75	170
M10	W310X74	24	2	50	75	128
M11	W460X74	24	2	50	75	115
M12	W690X170	27	2	50	75	165

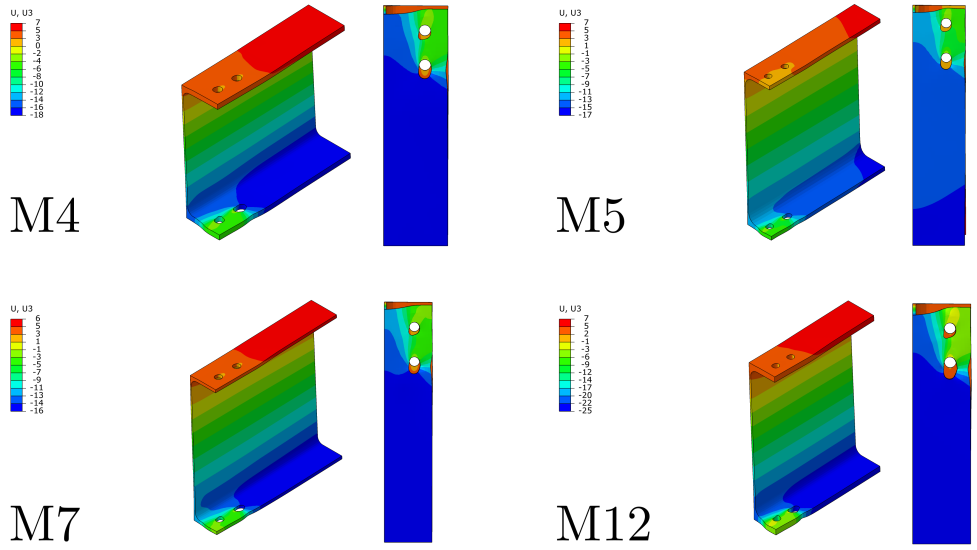

Figure 5.2: Axial displacement contours of tested specimens. Units in mm.

The Von Mises stress contours for a subset of specimens are shown in Figure 5.3.

The initial visual observations of the deformed section allowed for confidence in both the assumed simplifications used for the finite element modelling, as well as the general accuracy of the design methodology in developing a block shear critical connection detail. Once these initial observations were made, a more quantitative analysis of the data was performed.

5.1.2 Extracting data from finite element models

All relevant data after the completion of a finite element model run in Abaqus is contained in its Output Database, or .odb, file. From this .odb file, two levels of data were extracted. First, global values of force (N), moment (Nmm), and displacement (mm) were extracted using the *Free Body Cut* tool in Abaqus. These values captured the vertical displacement of the load point, the induced moment at the centreline of the splice plates, as well as the total force in each of the four block shear failure planes, the compression and tension splice plate groups, as well as the loading plate; these data sets were exported into a .csv file using the Excel

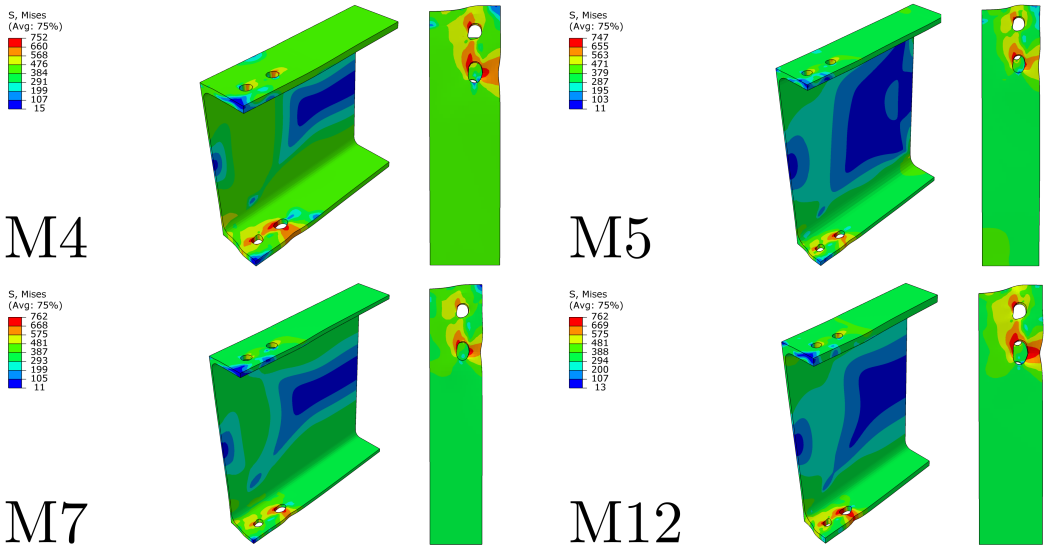

Figure 5.3: Von Mises stress contours of tested specimens. Units in MPa.

plugin in Abaqus. Second, local Von Mises stress data from the integration point of each element along the four major block shear failure planes were extracted using the *Report* tool in Abaqus. Depending on the connection geometry, a given failure plane could have over 150 individual elements that each output a unique time history report of the stress states; these individual datasets were automatically merged into a single .rpt file when exported using Abaqus, which could be parsed using a custom Julia function.

5.1.3 Data parsing, preparation, and analysis

The data extracted above was then parsed, modified, and analyzed in an automated *Jupyter Notebook* in the *Julia* programming language. The objectives of the Jupyter Notebook were:

1. Converting .csv and .rpt data into easily manipulable vectors and matrices
2. Converting units of *N, mm* to *kN, m* for global data
3. Determining failure plane areas from connection and section geometry

4. Doubling force/moment units to account for symmetric modelling of one half of the specimen

5. Determining average stress values for each failure plane

6. Determining the index at failure for each failure mode

7. Exporting the cleaned data into a single .csv file

Once the results of the finite element model were parsed and analysed, relevant information could be plotted, compared, and exported for future use. Two major visualizations are the total splice moment of the section detail, shown in Figure 5.4, and the stresses along each individual block shear failure plane, shown in Figure 5.5. Although the global splice moment graph provided a qualitative understanding of the overall behaviour of a given section-connection detail, it did not provide any information on the local block shear failure region. To evaluate the true failure mechanisms, the aggregated elemental stress data were used instead. The Von Mises stress in each of the four failure planes were plotted (Figure 5.5) along with the average value across each plane. The failure plane was assumed to reach its capacity once the average value reached the theoretical material capacity for the given plane and load type, meaning the yield strength, f_y, for the shear failure planes, and the ultimate tensile strength, f_u, for the tensile fracture planes. The use of the Von Mises stress was appropriate for both failure planes, since it is equal to the maximum principal tensile stress when under pure tension, and would not provide erroneous results when estimating the point of failure of the fracture plane. This was further verified early in the analysis procedure by extracting both the Von Mises stress and pure axial stress data from the fracture plane of the EBS failure mode and comparing the two data sets. The comparison confirmed that the purely tensile loading of the EBS fracture plane provided equivalent stress values when using either the Von Mises stress or the axial stress of each element.

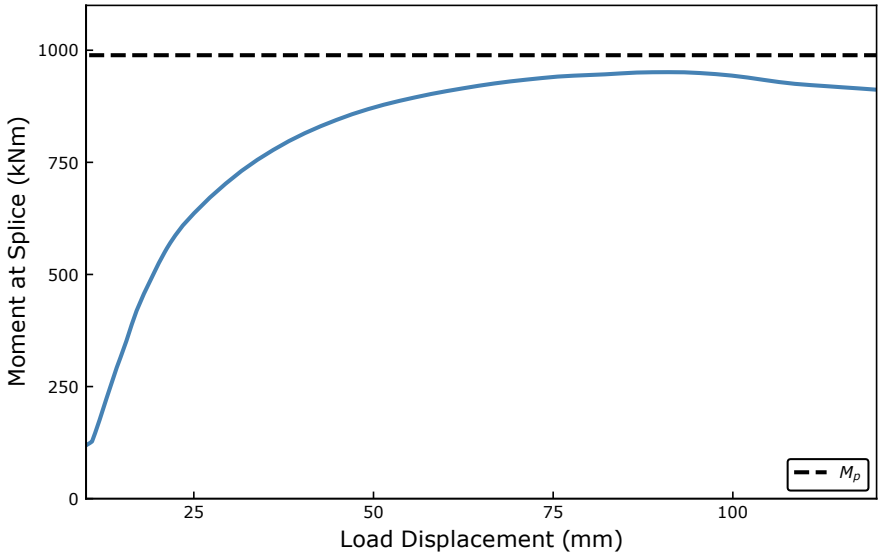

Figure 5.4: Load displacement vs. induced moment from M5 FE model.

A given block shear failure was assumed to occur at the moment when both planes for a given failure mode reached their respective stress limits: the shear plane reaching a Von Mises stress of f_y, and the tension plane reaching a Von Mises stress of f_u. The index of the overall data set at this failure point was recorded, and the relevant global data at the moment of failure was extracted. The moment developed in the splice connection at the failure index was taken as the moment capacity of the given block shear failure mode. For most specimens, the load point was displaced significantly past the Edge Block Shear failure mode such that the Complete Block Shear failure planes also eventually reached their respective capacities. For example, for the M5 specimen shown in Figure 5.5, the average Von Mises stress, shown as the blue curves, of all four block shear failure planes eventually reached their respective strength limits during the loading procedure.

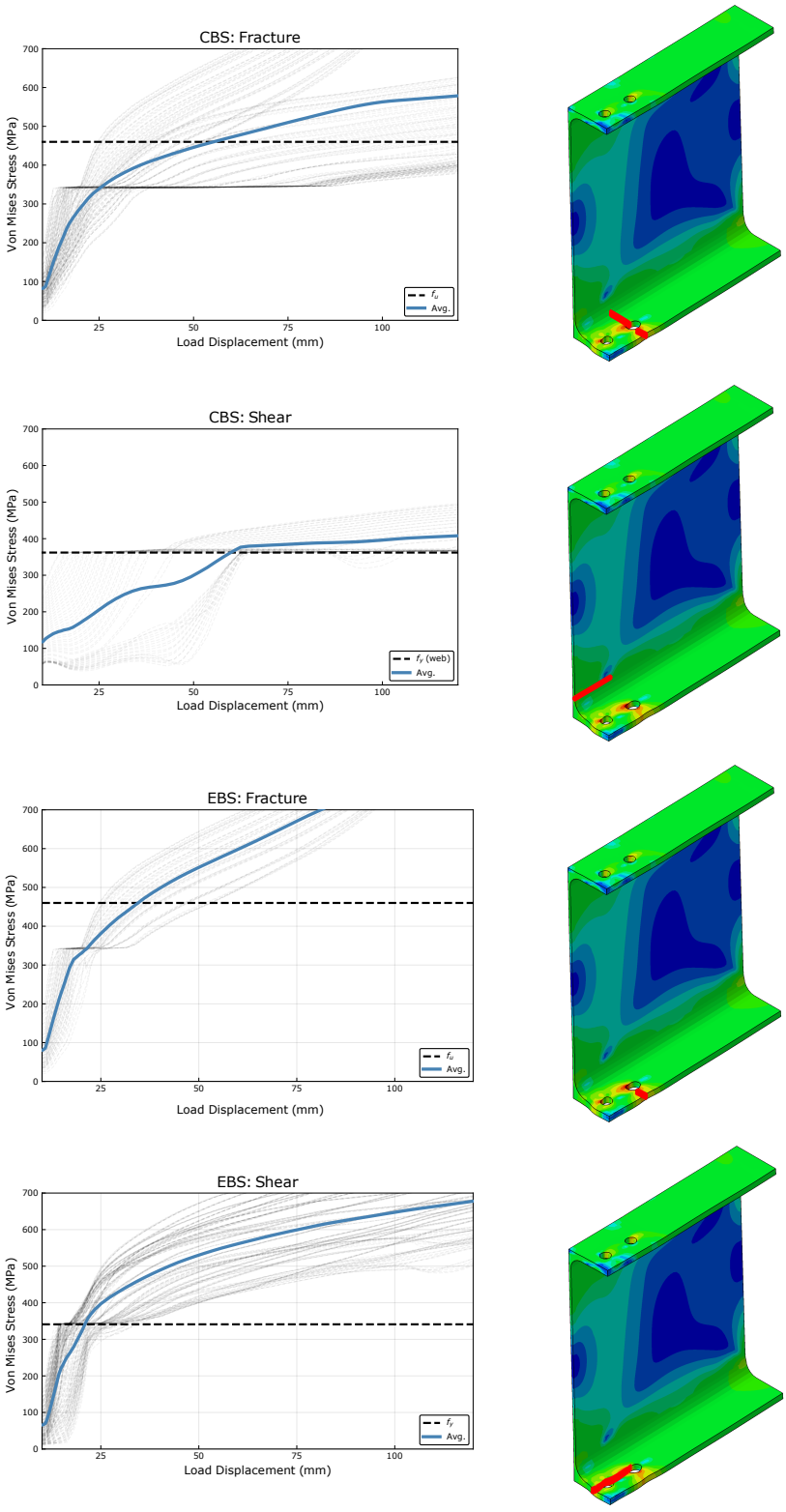

Figure 5.5: Von Mises stresses along major failure planes for M5 specimen. Elements highlighted in red.

5.2 Results and Observations

5.2.1 Effect of section geometry

With the analysis of each individual specimen completed, and clear metrics for failure defined, an overall comparison of all 17 models was performed using normalized data. First, the moment capacities of all observed failure modes were plotted against the major geometric properties of the W-sections, namely the section depth (d), the flange width (b_f), and the net flange area ratio (b_n/b_g), to determine if any clear trends were visible. To provide moment resistance values that could be compared against other modelled sections, all resistance values were normalized to the theoretical gross yield moment capacity, M_y, which was calculated using the engineering yield strength associated with the true material stress-strain function defined in each model. The blue circles represent the moment-at-failure for the Edge Block Shear failure mode, while the orange squares show the moment-at-failure for the Complete Block Shear failure mode, should it have occurred; the gross plastic moment resistance, M_p, for each section is also plotted as a dashed line. These initial comparisons of moment block shear failure resistances are presented in Figures 5.6 to 5.9.

From the initial observations on geometric properties vs. the block shear failure moment, no clear relationship between the variables was evident. One minor exception was the effect of the section depth to the ability to achieve the Edge Block Shear moment before the gross yield moment. From the available data, sections below $d = 400mm$ did not reach the critical EBS moment until after the gross yield moment. However, this limitation was not taken as a fundamental change to the failure mechanism of the block shear failure mode, but was simply a physical limitation and conflict between a shallow section's limited gross section flexural capacity and the required moment to induce the necessary forces to cause block shear failure in the tension flange. A more in-depth discussion on this geometric conflict was provided in Chapter 3.

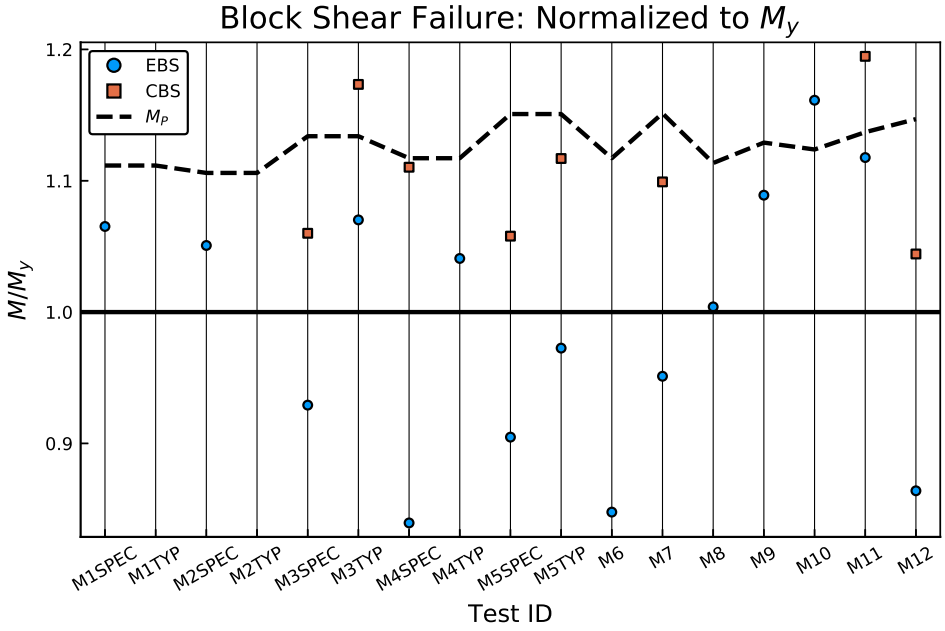

Figure 5.6: Block shear failure moments normalized to M_y

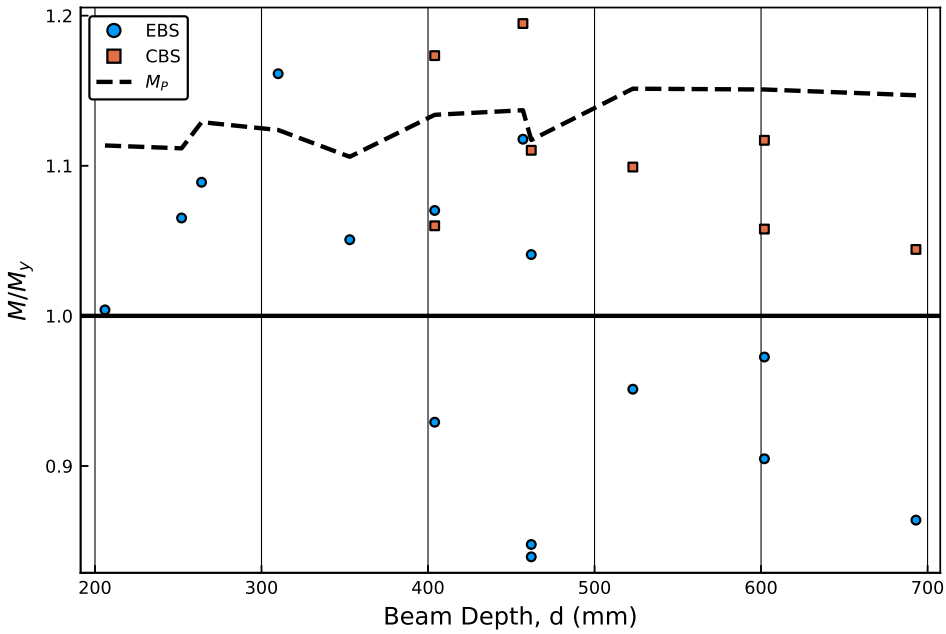

Figure 5.7: Section depth vs. block shear failure moments.

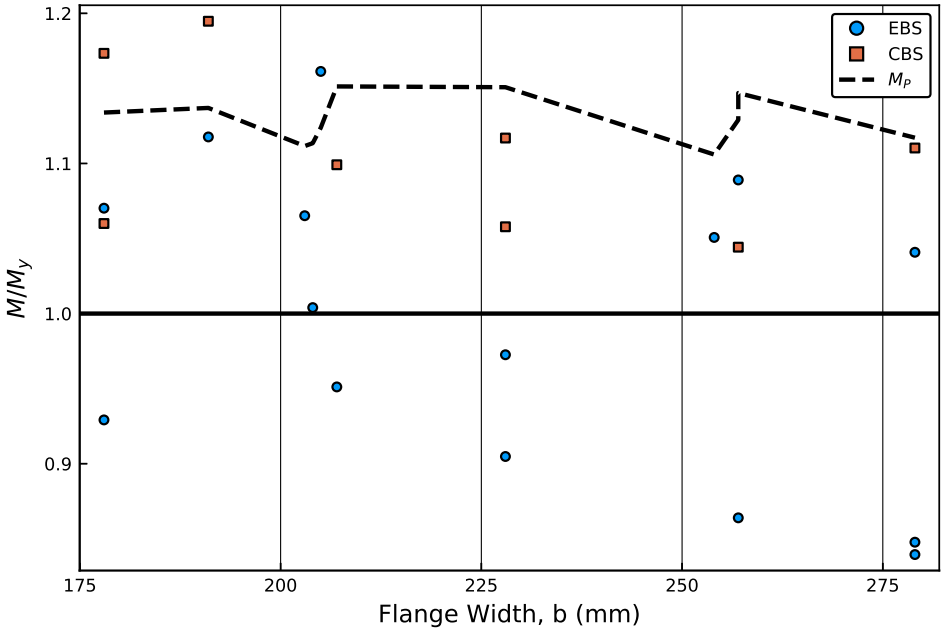

Figure 5.8: Flange width vs. block shear failure moments.

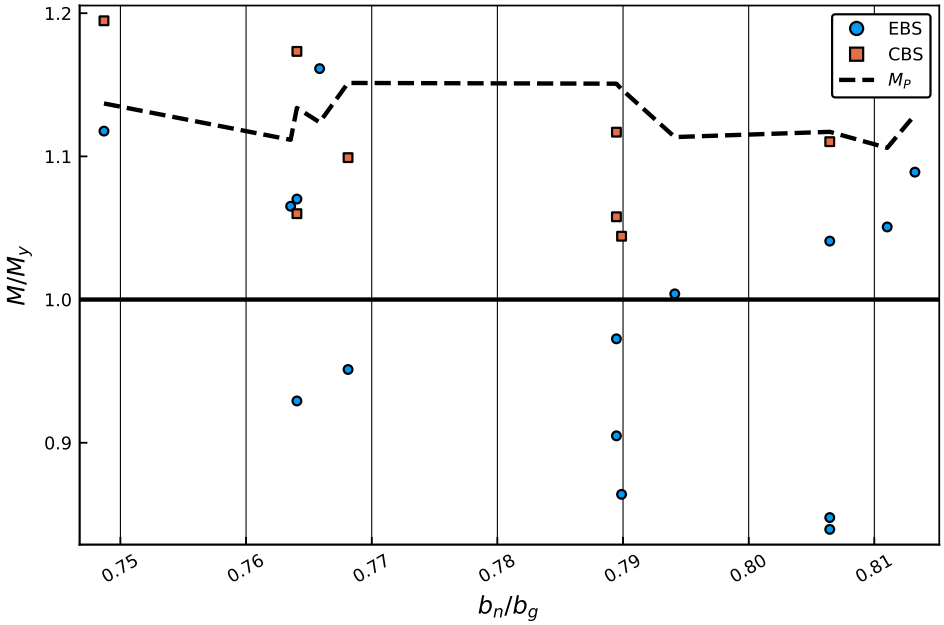

Figure 5.9: Net flange area ratio vs. block shear failure moments.

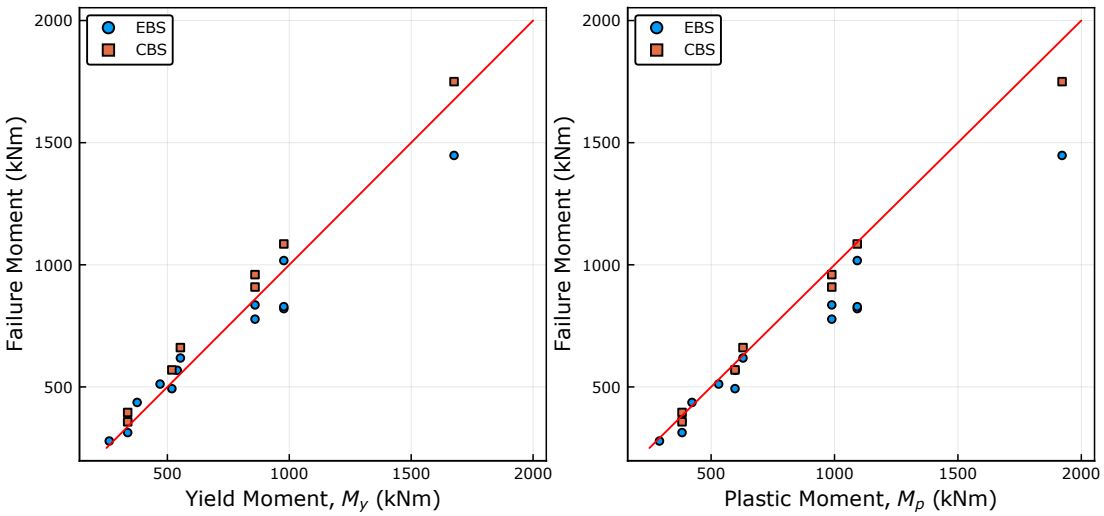

Figure 5.10: Block shear failure moments compared to gross section capacities.

An alternative comparison of the block shear failure moments relative to the gross section capacities is provided in Figure 5.10. With all else held equal, the gross section capacity of a flexural W-section would increase with the increase in depth of the member; then, for an equivalent connection detail, there would be a greater likelihood that the required moment to induce a block shear failure would remain below either M_y or M_p of the gross section. It is noted, however, that this may not always be the case, since the increase in depth would also require an increase in applied moment to reach an equivalent force in the two flanges as a shallower section. This conflict between the section depth, the gross section properties, and the induced flange forces was discussed in detail in Chapter 3. However, for the modelled set of specimens shown in Figure 5.10, the increase in flexural capacity of a deeper section provided a net difference in favour of isolating the block shear failure mode.

5.2.2 Distribution of stress

A comparison of the average Von Mises stress in each of the four block shear failure planes for all modelled specimens is shown in Figure 5.11; an overview of the location of each shear plane was provided in Figure 5.5. The total splice end moment normalized to the gross section yield moment was taken as the independent variable, while the average Von Mises stress in each failure plane was normalized to the theoretical stress capacity of the given section and failure type. The point at which a given stress line crossed the theoretical capacity (shown as a red line) would represent the moment-at-failure for the given failure plane. In general, both the EBS and CBS fracture planes had similar moment vs. stress behaviour, with a generally linear relationship. The EBS and CBS shear planes, however, had a significantly greater spread in their path towards failure, with the CBS shear plane in the web exhibiting a highly non-linear and random relationship to the total applied moment. What was consistent for both failure modes was that fracture plane failure was preceded by the shear plane failure, affirming that the failure mechanism as assumed by the CSA S16-19 standard, where ultimate failure of the block shear mode occurs with a shear plane yield and eventual tension plane fracture.

When observing the stress distribution along each failure plane for a single specimen, further clarity on the assumed failure mechanism for block shear failure was provided. A typical stress distribution in the shear and tension planes as observed in the M3:W410X53 model is shown in Figures 5.12 and 5.13.

For the fracture plane, a common observation from all models was that the entire net flange area participated to a high degree of stress, whether or not the EBS failure mode governed over the CBS failure mode. As observed in Figure 5.12, a significant portion of the entire net flange area (the CBS Fracture plot) is near its ultimate tensile strength at the point of EBS Fracture failure. This suggested that the EBS and CBS fracture planes are highly related, and that the isolation of one failure mode over the other is more dependent on the behaviour

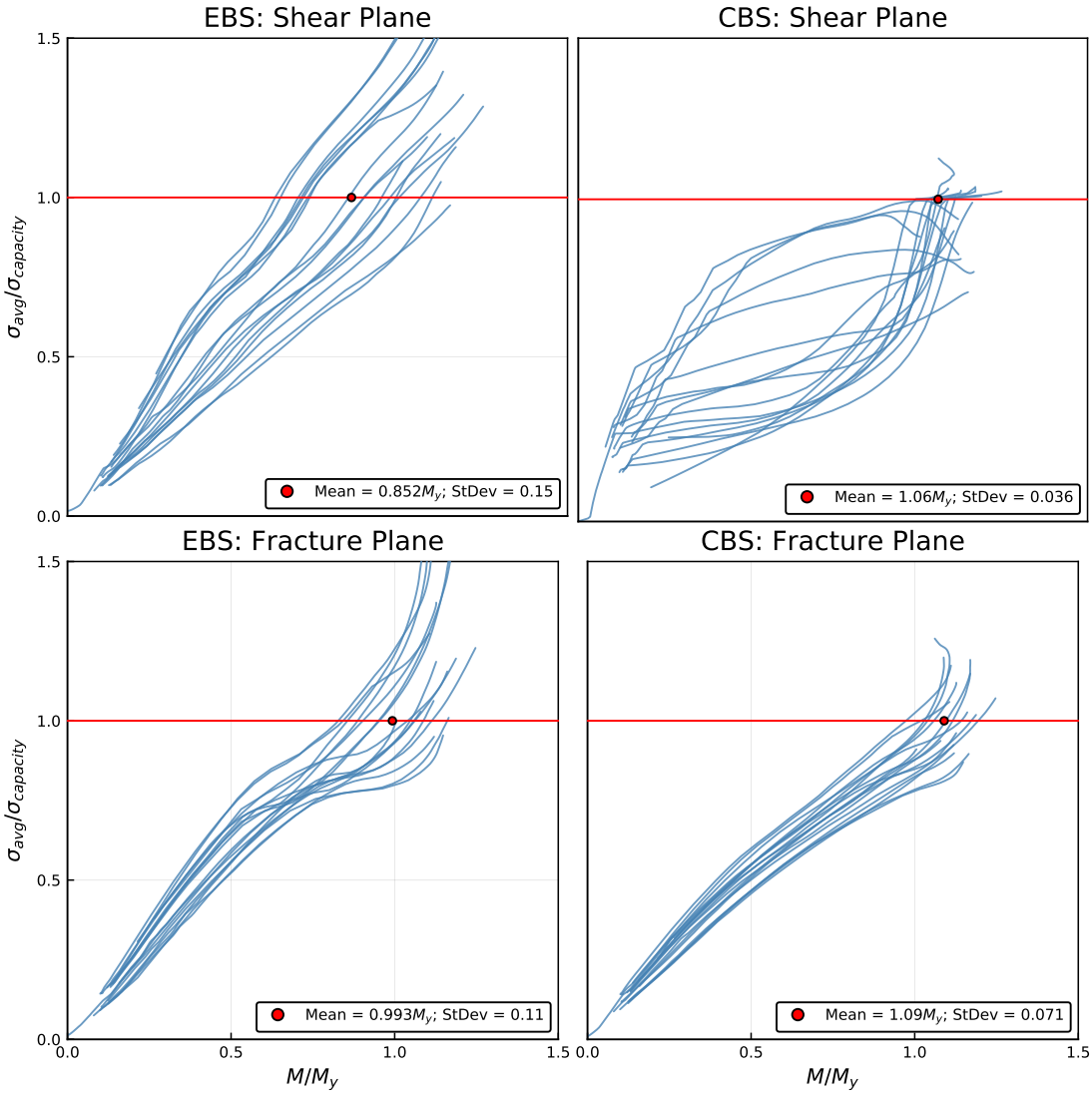

Figure 5.11: Average Von Mises stress in each failure plane.

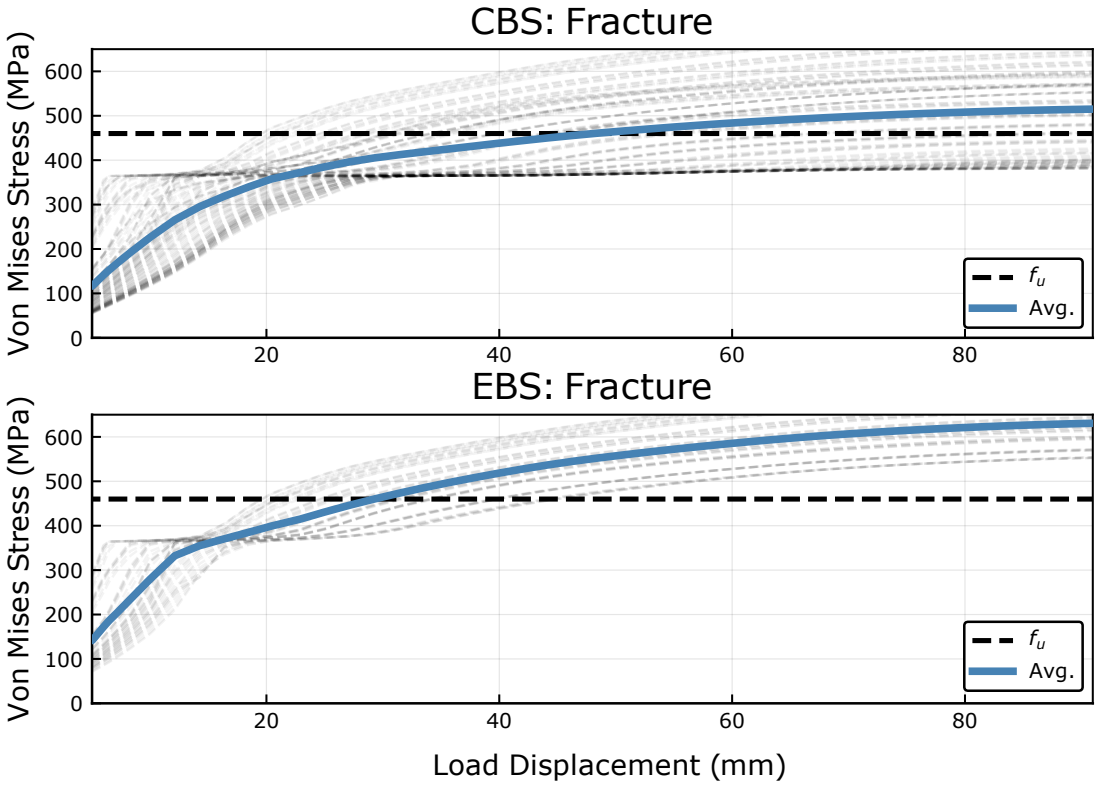

Figure 5.12: Tension plane stress distribution for M3 specimen.

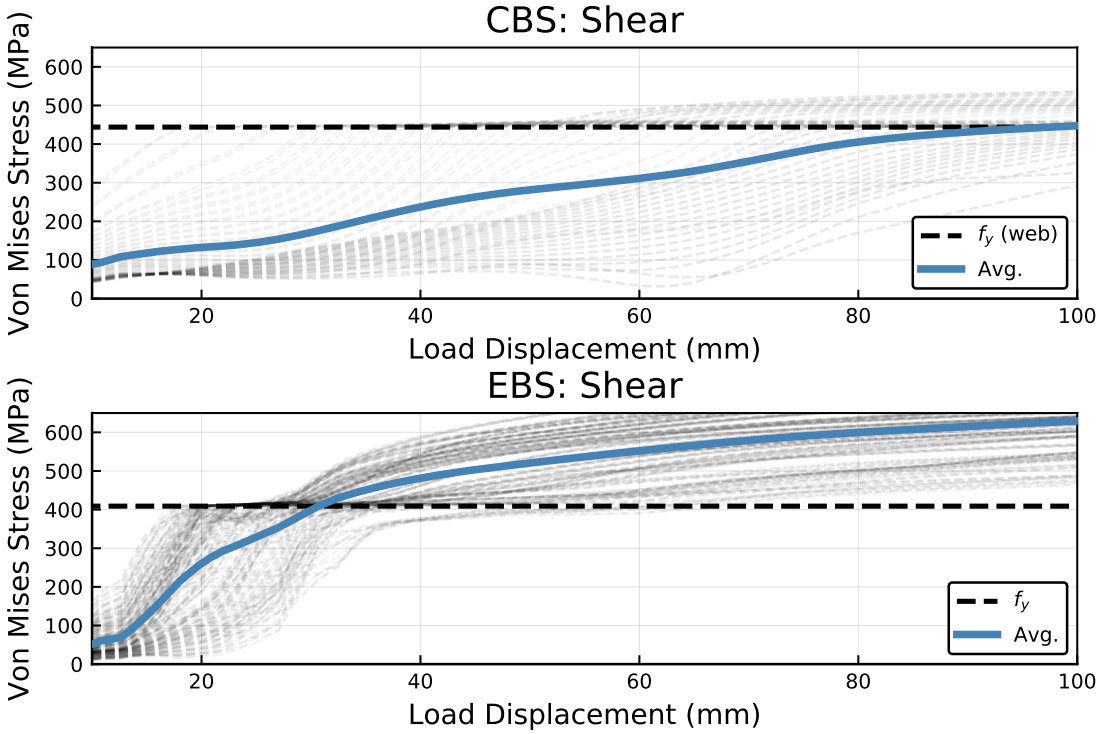

Figure 5.13: Shear plane stress distribution for M3 specimen.

of the respective shear planes rather than a clear stress concentration on one of the two fracture planes. It is noted, however, that as the connection is loaded beyond the point of initial EBS failure, the concentration of stress in the EBS fracture failure plane becomes evident. A comparison of the distribution of stress across the net flange area for the M3 and M5 specimens is provided in Figure 5.14. The M5 specimen, which had a greater flexural stiffness than the M3 specimen, reached its block shear capacity early in the load displacement of the model. As the model was continuously loaded, significant necking occurred in the EBS Fracture plane, which concentrated the stresses at that location. The CBS Fracture plane plot for the M5 model in Figure 5.14 shows a clear divergence of two groups of stress as the loading increased. The upper block shows the concentration of stress in the EBS Fracture plane as necking increases.

For the shear planes, the distribution of stresses was less uniform, and highly dependent on the failure mode in question. The EBS shear planes, which are directly adjacent to the bearing surfaces of the bolts, showed a uniform increase in stress during loading, similar to the EBS and CBS fracture planes. However, the CBS shear plane, located at the Web/K-Area interface, showed a highly non-uniform stress distribution throughout the loading of the connection. At the point where the average stress along each plane reached its yield strength, a significant portion of the CBS shear plane remained below its capacity. Two key observations were made on the shear planes of the block shear failure modes. First, for the EBS shear plane, the highly uniform increase in stress indicated that the assumption of the gross section for the shear plane, as used in the design methodology of the CSA S16-19 standard, was correct, since a net section shear failure would plot low stress values for elements that are exclusively in the gross section. Second, for the CBS shear plane, it was clear that the true distribution of stress along the failure plane did not match the assumed failure mechanism; a significant portion of the assumed failure plane did not participate in any load resistance. Although the connections were not detailed such that the CBS failure

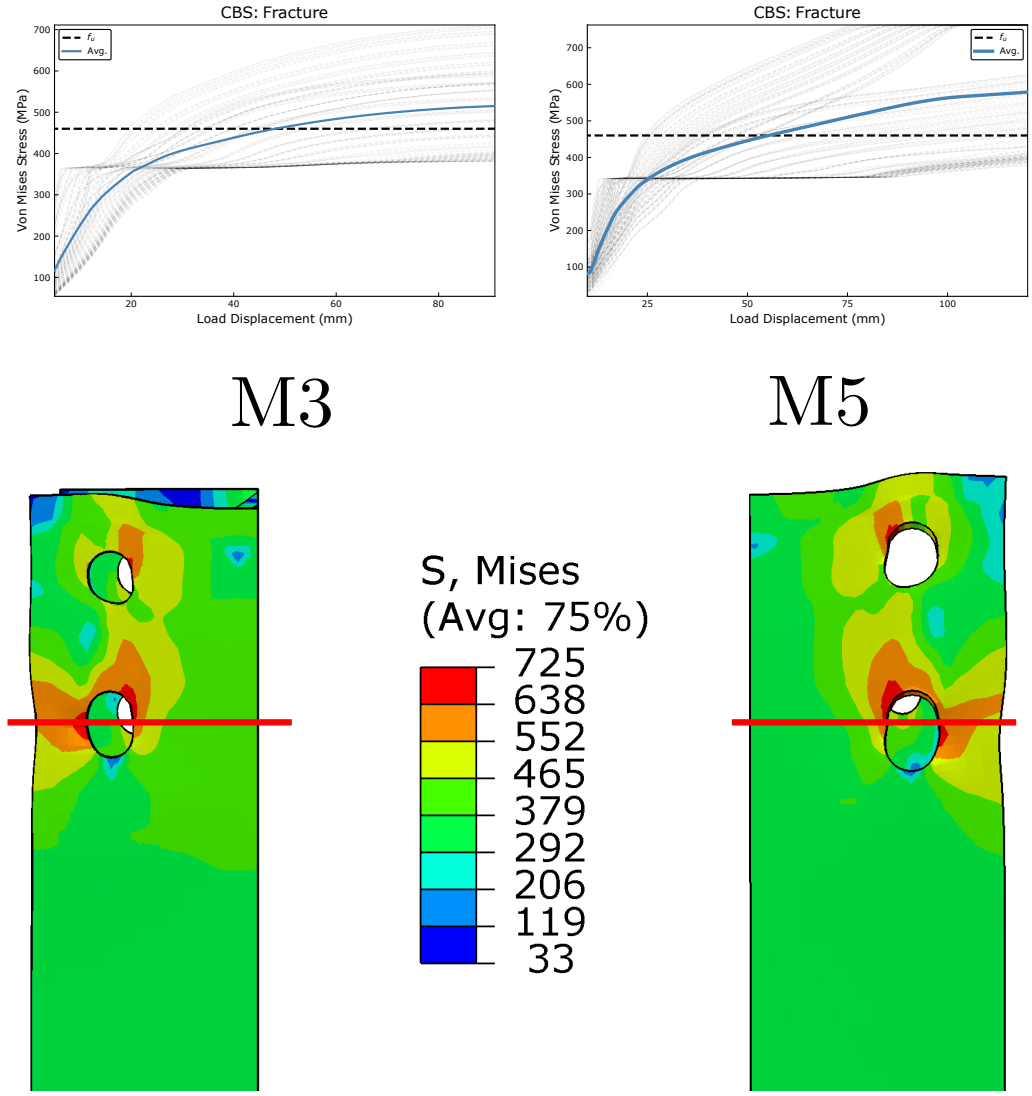

Figure 5.14: Comparison of complete block shear fracture plane Von Mises stress distribution between M3 and M5 specimens.

mode was critical, it would be likely that the progression of stress would behave similarly should a CBS critical connection be loaded.

Based on these observations, two outcomes on the current predictive capacity of block shear design equations were expected. First, for the Edge Block Shear failure mode, the CSA S16-19 design methodology, which assumes a gross shear plane and a net tension plane, should provide a more accurate prediction of the EBS resistance compared to the AISC 360-16 and Eurocode 3-2005 methods, which assume both net shear and tension planes. Second, since the distribution of stress along the Complete Block Shear failure plane did not match the assumed stress state for any block shear design equation, the predictive capacity for the CBS failure mode was expected to be worse than that of the EBS failure mode for any given design equation.

5.2.3 Effect of connection length

As discussed in Chapter 3, the moment-induced block shear failure mode was determined to be highly sensitive to the overall connection length of the bolt group, as the shear plane component of the block shear resistance equation is proportional to this length. As previously noted, the connection geometry of all specimens were selected to be as representative of typical bolt spacings as possible; these typical spacings were end distances of 2" (50mm), and bolt pitches of 3" (75mm). However, for the initial 5 specimens, M1-M5, some deviations from typical bolt spacings were made to isolate the block shear failure mode as much as possible. For example, specimen M1 was specified with an end distance of 35mm and a bolt pitch of 65mm, and specimen M5 was specified with an end distance of 35mm. Further, all bolts were detailed with both inner and outer splice plates, allowing for a double shear configuration. For more typical moment splice scenarios where only the outer splice plate would be specified, a minimum of double the amount of bolt rows would be necessary to carry the equivalent force in a single shear configuration. This doubling of rows would have a significant

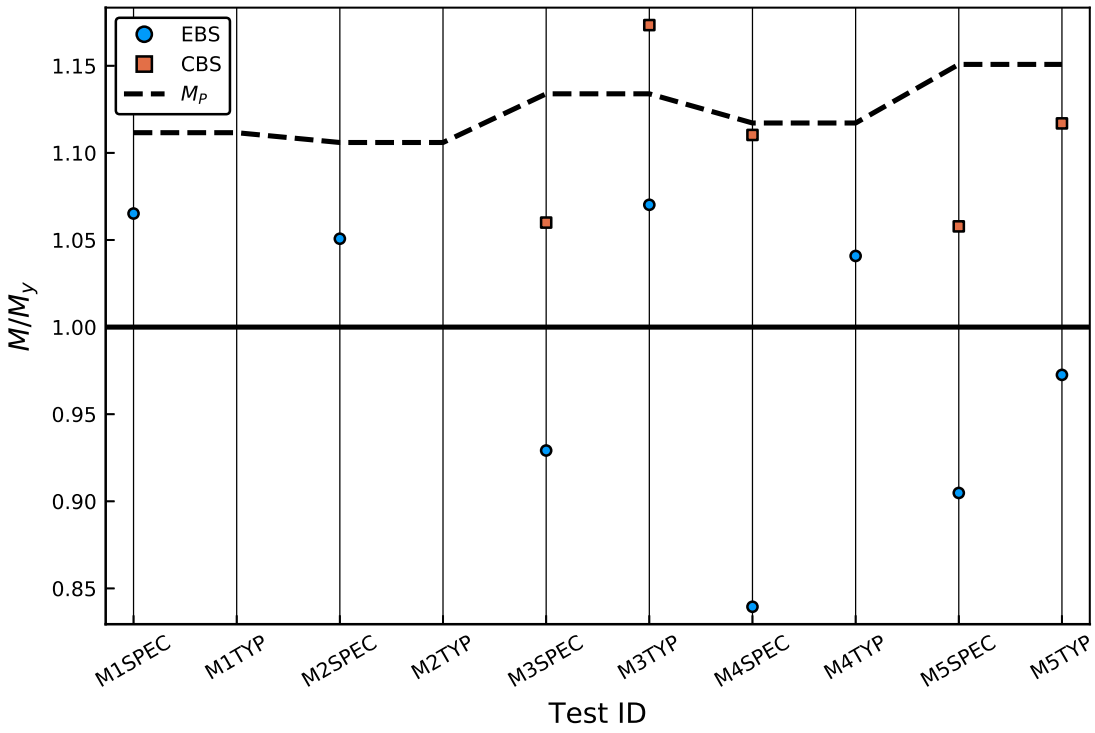

Figure 5.15: Comparison of `SPEC` vs. `TYP` series of specimens M1-M5.

impact on the overall connection length of the bolt group, as well as the ability to force a block shear critical connection.

To observe the effect of the connection length on the overall behaviour of the moment splice connection, an additional 5 specimens, M1TYP to M5TYP, were modelled to compare to the initial M1-M5 series, renamed M1SPEC to M5SPEC. For specimens with atypical bolt spacings, such as M1 and M5, the bolt geometry was reconfigured to meet typical spacing values; for specimens that were already specified with typical spacing values, an additional row of bolts was added using the same bolt pitch. The values of these distances was provided in Table 5.1.

The overall critical moment resistances of the SPEC and TYP specimens is shown in Figure 5.15. As expected, the slight to moderate increase in connection length corresponded to a significant increase in the overall block shear failure resistance. For specimens M1TYP and M2TYP, this increase in connection length

resulted in a change from a block shear critical connection to a gross section failure, as seen by the absence of block shear failure moments in the figure. For specimens M3TYP and M4TYP, the increase in connection length resulted in the Edge Block Shear moment resistance to exceed the gross yield moment resistance.

A more detailed comparison of the global and local effects of the connection length for the M2 specimen is shown in Figures 5.16 and 5.17. The M2TYP specimen is equal to the M2SPEC specimen, albeit with an additional row of bolts at the same pitch, resulting in an overall connection length of 200mm compared to 125mm for the M2SPEC specimen. Observing the global load displacement vs. total splice moment in Figure 5.16, a significantly stiffer connection behaviour was evident for the M2TYP specimen. This was expected, since the individual force transferred at each bolt region is reduced, minimizing the local deformation. When comparing the average Von Mises stress in each of the four block shear failure planes, shown in Figure 5.17, the effect of the increased connection length was more evident. A general reduction in the overall stress in each failure plane was observed for the M2TYP series, with no failure plane reaching its strength capacity. The increased capacity of the M2TYP block shear failure planes allowed for more of the gross section to participate in the induced moment, reaching the gross plastic moment before any local failure modes occurred.

As expected analytically, and verified with the M1TYP-M5TYP specimens, the overall connection length of the bolt group played a significant role in the block shear failure capacity of a bolted moment connection, as well as the overall stress distribution in the connection region. Increasing the connection length was observed to stiffen the overall flexural response of the beam, reduce the average stress in the shear plane for a given load, and allow for greater participation by the gross section to change the overall failure mode from a local block shear to a gross plastic moment. For a typical moment splice connection for W-sections, practising engineers would most likely specify single shear bolts to the capacity of the gross plastic moment of the section, rather than the double shear bolts

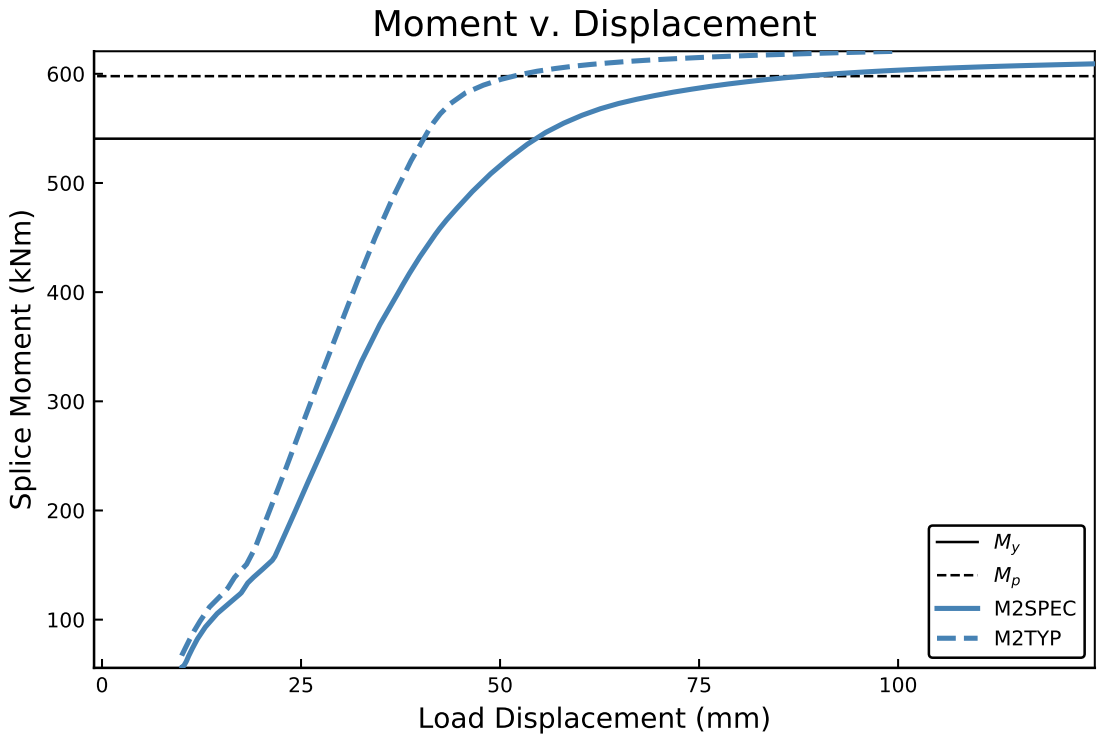

Figure 5.16: Comparison of overall displacement-moment behaviour of M2SPEC and M2TYP specimens.

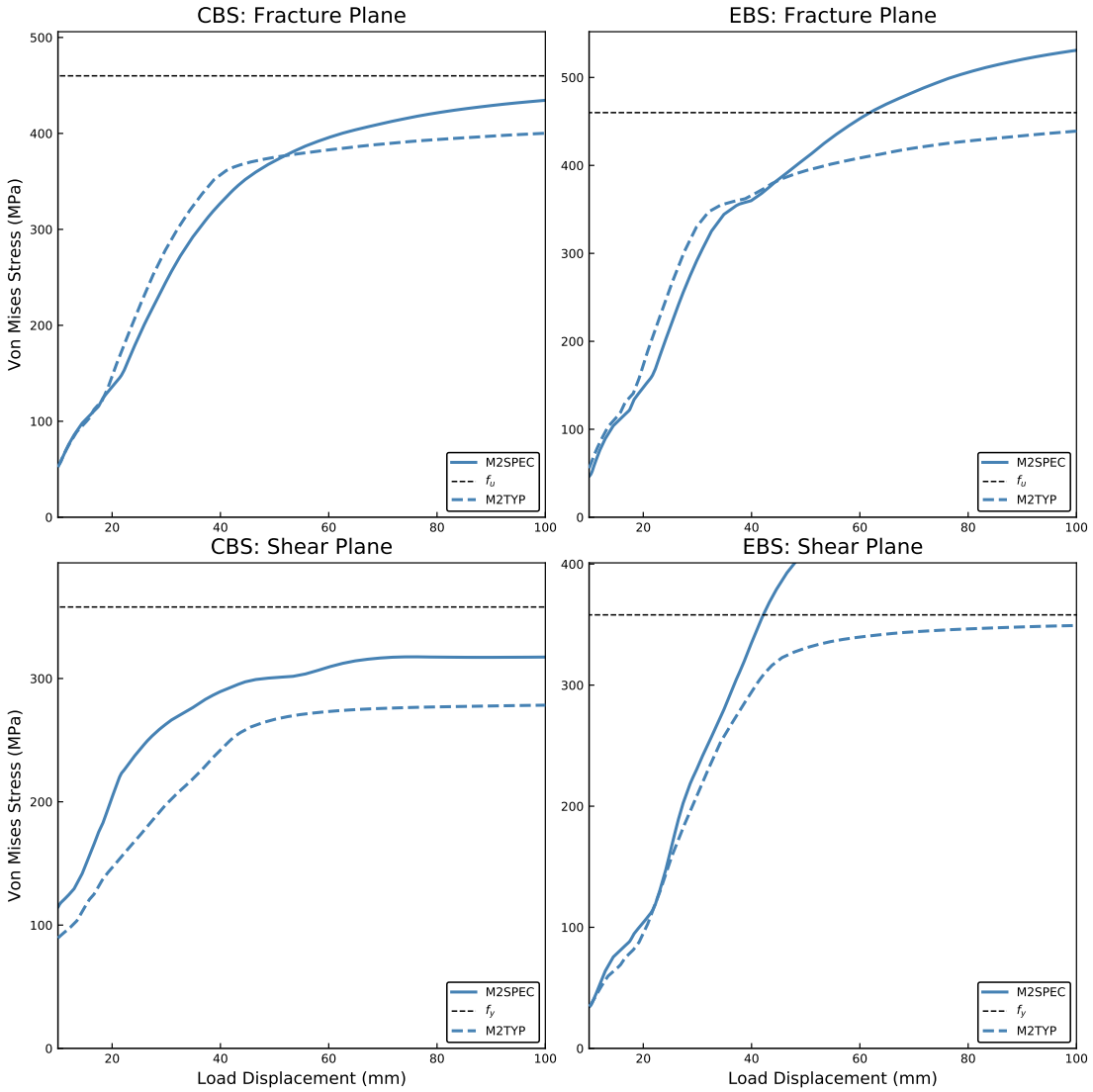

Figure 5.17: Comparison of average failure plane stresses of M2SPEC and M2TYP specimens.

designed to the capacity of the expected block shear resistance as performed during this study. The increased number of bolt rows would almost certainly increase the connection length to the point where the block shear failure mode would not govern the overall resistance of the section-connection detail.

5.3 Predictive capacities of design equations

The predictive capacities of the CSA S16-19, AISC 360-16, and Eurocode 3-2005 design methods were evaluated for both the EBS and CBS failure modes. Although the detailing of the connections never provided for a CBS critical failure, some specimens reached the theoretical CBS failure state as the specimen was loaded beyond the EBS failure point; for these specimens, the predictive capacity of the CBS failure mode was also evaluated. Further, some specimens did not reach either block shear failure mode; these specimens were generally from the `TYP` series of specimens that did not explicitly detail the connection geometry for a block shear failure mode, but rather to reflect more industry-standard bolt spacing distances.

The moment value at which both failure planes of a given block shear failure mode reached their respective capacities was taken as the failure mode's moment capacity, which was then compared to the calculated, theoretical moment capacities of the three listed design methods. The metric used for determining the accuracy of a given design equation was the Professional Factor (PF), taken as the true observed moment-at-failure divided by the expected moment-at-failure as calculated by the design equation. A Professional Factor greater than 1 would indicate that the given equation had underestimated the true available capacity of a given failure mode; a Professional Factor less than 1 would indicate that the true capacity of a given failure mode was below the expected value. Since probable material properties and unfactored design equations were used when determining the predictive capacity of an equation, a PF greater than 1 did not

suggest an increased level of safety, nor was it a desirable outcome. Rather, it suggested that the predictive design equation could not accurately represent the true failure mechanism.

5.3.1 CSA S16-19

The CSA S16-19 block shear resistance equation is unique from both the AISC 360-16 and Eurocode 3-2005 design equations in that the shear failure plane is strictly defined as the *gross* shear area yielding at a stress averaged between the tensile yield and ultimate strengths. The efficiency factor, U_t, is a tabulated value used to account for the reduced capacity of the tension plane when in-plane eccentricities exist. For the moment-induced block shear failure modes, the value of U_t was taken as 1.0, which is the tabulated value for flange-connected structural tees in direct tension.

$$T_r = \phi_u[U_t A_n F_u + 0.6 A_{gv} \frac{F_y + F_u}{2}] \tag{5.1}$$

An overview of the predictive capacity of the CSA S16-19 design equation for the EBS and CBS failure modes is presented in Figures 5.18 and 5.19. As expected from visualizing the distribution of stresses in the failure planes, the CSA S16-19 design equation accurately predicted the EBS failure mode, with a mean Professional Factor of 1.08. This further suggested that the use of the gross shear area was appropriate for the block shear failure mode. What was not expected was the equally high predictive capacity for the CBS failure mode, as the assumed stress distribution of the CBS Shear failure plane did not reflect the observed stresses in the finite element model. It was possible that although a uniform stress level was not present along the CBS Shear plane, highly stressed regions of the failure plane made up the difference of lower stressed regions and provided an effective stress across the entire plane that could be predicted by the simplified CSA S16-19 equation.

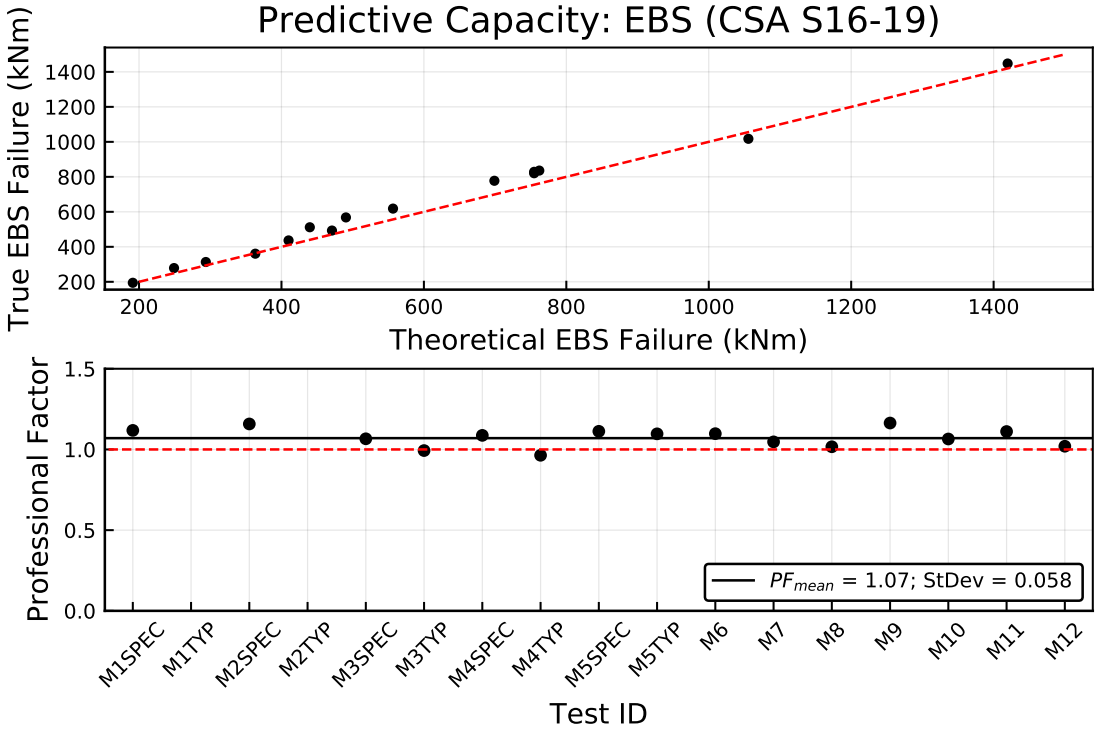

Figure 5.18: CSA S16-19 EBS predictive capacity.

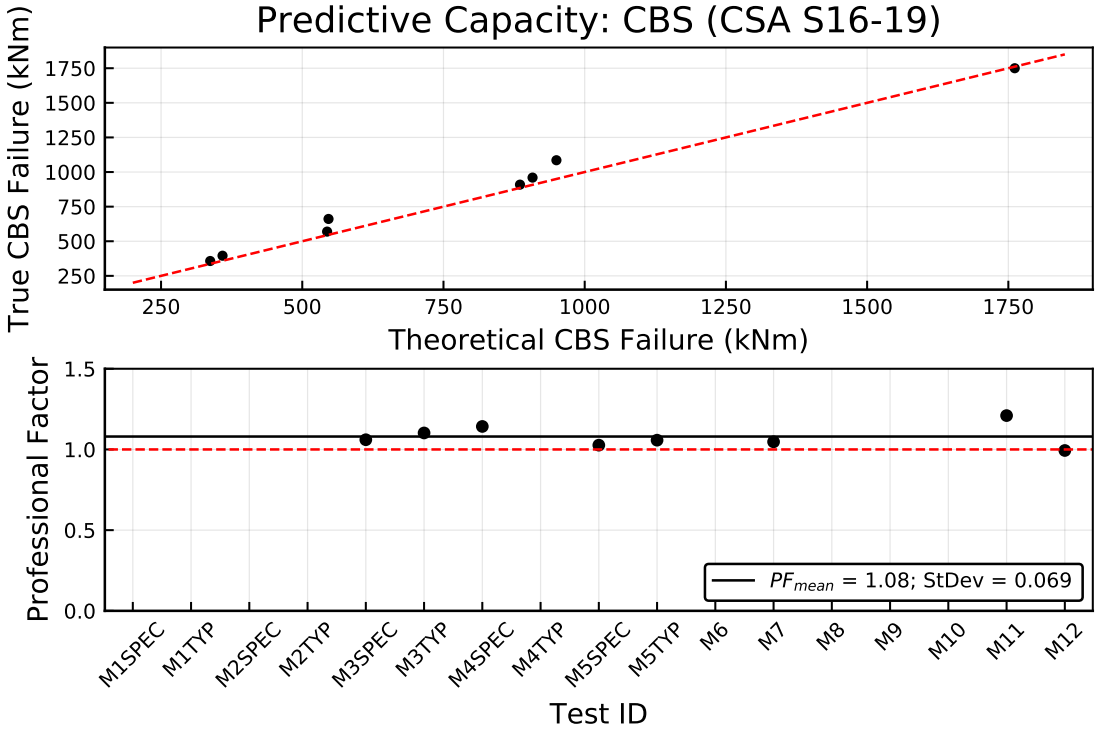

Figure 5.19: CSA S16-19 CBS predictive capacity.

5.3.2 AISC 360-16

Two key differences exist in the AISC 360-16 design equation compared to the CSA S16-19:

$$R_n = 0.60F_uA_{nv} + U_{bs}F_uA_{nt} \leq 0.60F_yA_{gv} + U_{bs}F_uA_{nt} \tag{5.2}$$

1. The assumed failure mode is the simultaneous rupture of the net tension plane and the net fracture plane, with a shear fracture strength taken to be $0.6f_u$.

2. However, if the net shear fracture term exceeds the gross shear yield capacity, the gross shear yield strength is taken instead. The shear yield strength is taken to be $0.6f_y$, whereas the shear yield strength for the CSA S16-19 equation takes into consideration significant strain hardening, and is higher.

From the observed stress distributions for the EBS Shear failure planes, it was evident that the assumed failure mechanism of the AISC 360-16 design equation was not reflective of the true load path. This was further confirmed by the significantly poorer Professional Factor of 1.28 for the EBS failure mode. It is noted that although the AISC 360-16 design method *reduces* the active shear area of the failure plane, the higher professional factor compared to the CSA S16-19 design equation arises from the fact that the AISC 360-16 assumes a shear fracture, rather than shear yielding. However, like the CSA S16-19 design equation, the AISC 360-16 provided a reasonable mean Professional Factor of 1.09 for the CBS failure mode, a significant improvement compared to the EBS failure mode. The improvement of the Professional Factor for the CBS failure mode was attributed to the fact that the assumption of the net shear area fracture does not hold for the CBS Failure mode, where $0.6F_uA_{nv}$ must be greater than $0.6F_yA_{gv}$, and would thus require the use of the more reflective assumption of a gross area shear yield.

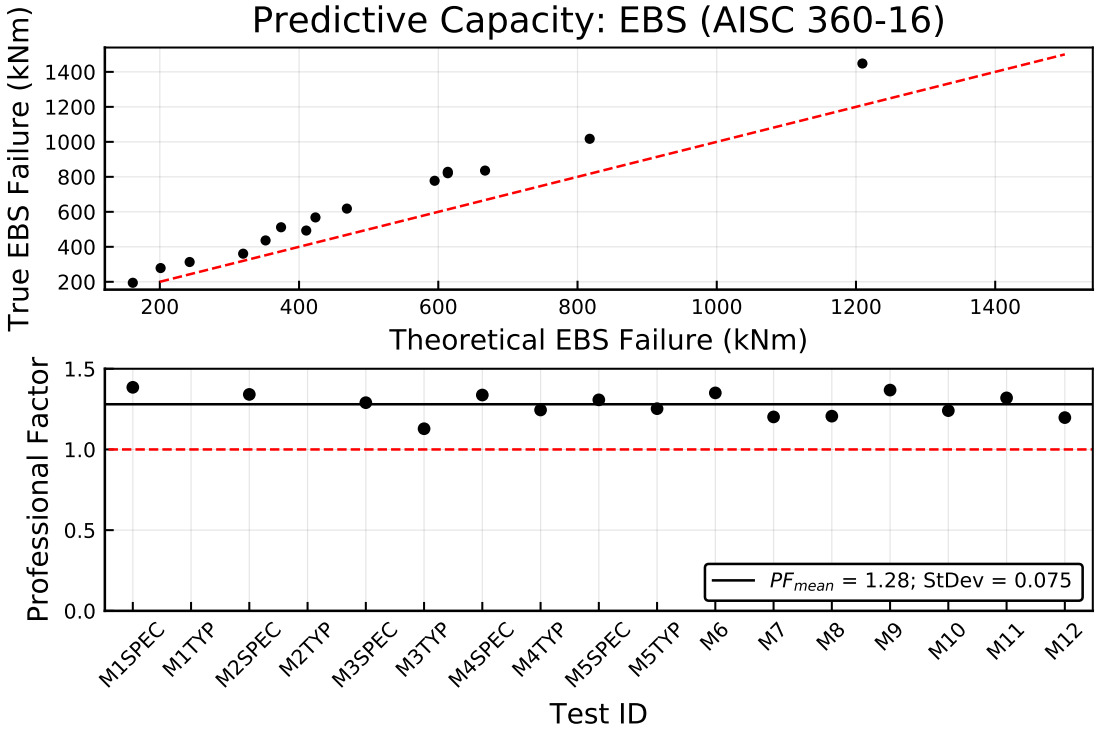

Figure 5.20: AISC 360-16 EBS predictive capacity.

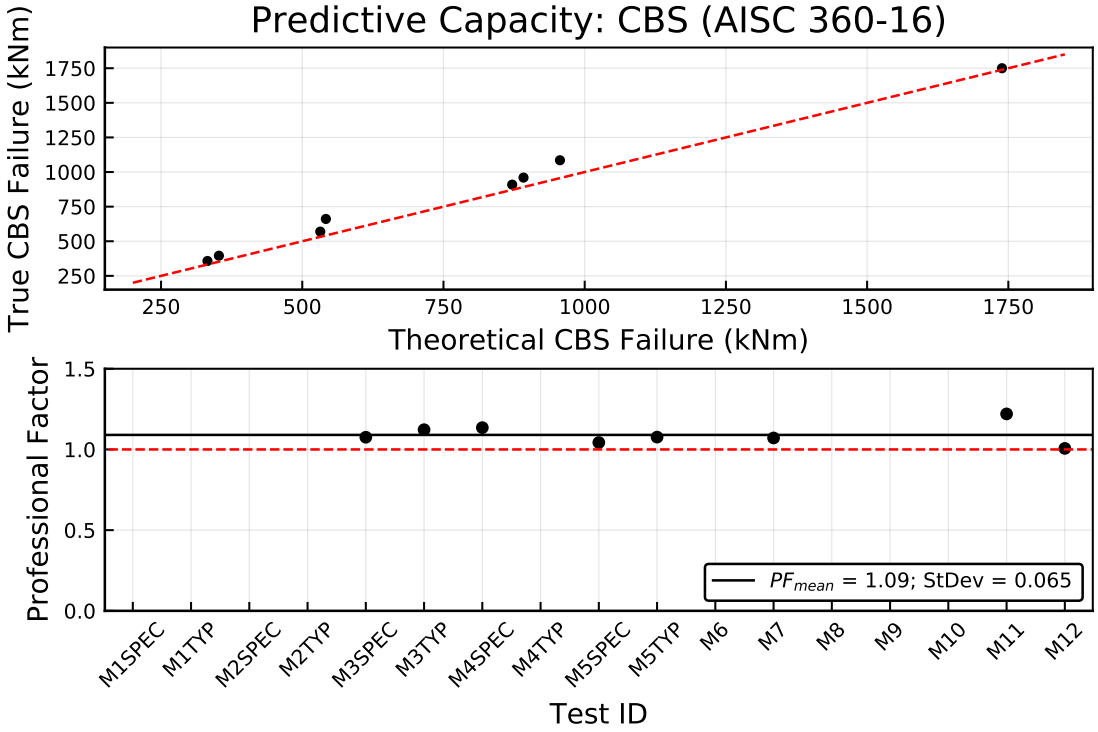

Figure 5.21: AISC 360-16 CBS predictive capacity.

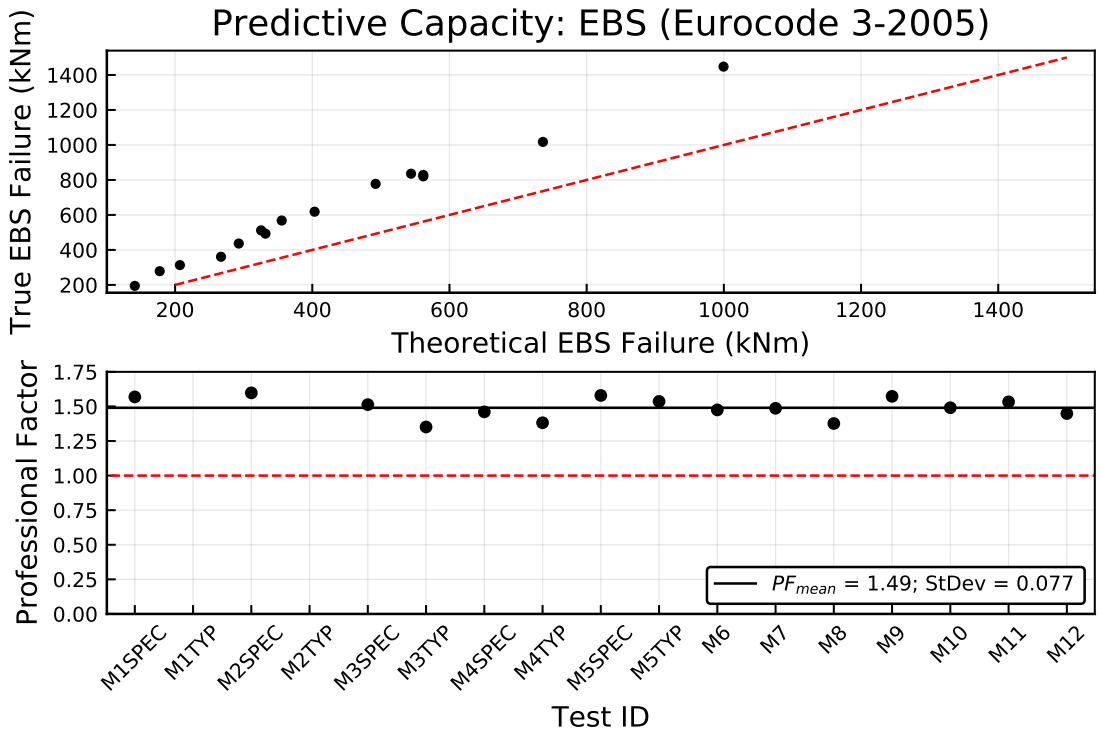

Figure 5.22: Eurocode 3-2005 EBS predictive capacity.

5.3.3 Eurocode 3-2005

The Eurocode 3-2005 design equation was expected to provide the greatest underestimation block shear resistance due to the assumption of a net area yield contribution of the shear plane. This was confirmed by the Professional Factor of 1.5 for the EBS failure mode, meaning the true resistance of this failure mode was 150% of the predicted value. Like the AISC 360-16 design method, the Eurocode 3-2005 equation showed an improvement in the Professional Factor for the CBS failure mode, with PF=1.1, since the net shear area is equal to the gross shear area along the web/K-area interface.

$$V_{eff,2,Rd} = \frac{f_u A_{nt}}{\gamma_{M2}} + \frac{f_y A_{nv}}{\gamma_{M0}\sqrt{3}} \tag{5.3}$$

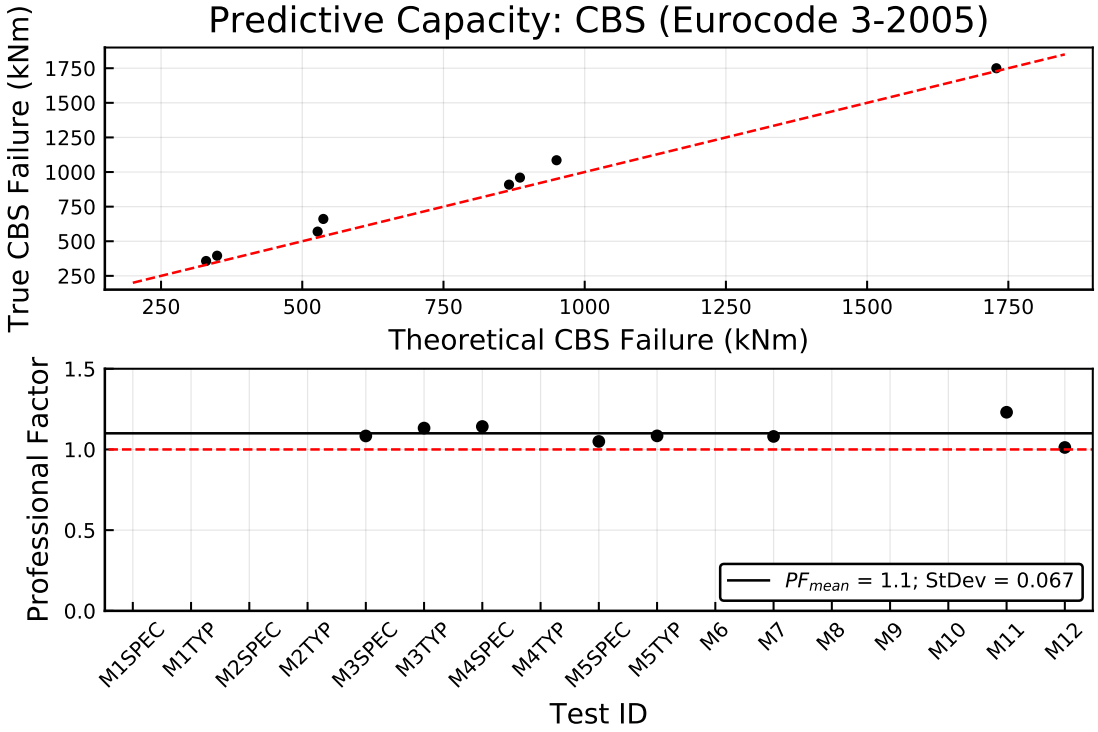

Figure 5.23: Eurocode 3-2005 CBS predictive capacity.

5.3.4 Summary of block shear predictive capacities

Comparisons of the predictive capacities of the three equations are shown in Table 5.2 and Figure 5.24. Empty values for the Professional Factor in Table 5.2 reflect specimens that did not reach the given block shear failure mode. The CSA S16-19 design equation provided the best predictive capacity out of the three design standards, especially for the prediction of the EBS failure mode. Further, the AISC 360-16 and Eurocode 3-2005 equations appeared to provide increasing Professional Factors (increasing underestimation of strength) as the overall capacity of the EBS failure mode increased. The high predictive capacity of the CSA S16-19 design equation supported the use of the gross area for the shear plane, as well as using an intermediate strength value between the yield and ultimate strengths, as determined by (Driver et al., 2006). For the AISC 360-16 and the Eurocode 3-2005, the use of the net shear area at either a yield or fracture strength state significantly underestimated the resistance of the EBS failure mode. The use of the gross shear area was further supported by the fact that both the AISC 360-16 and Eurocode 3-2005 design equations performed better when predicting the CBS failure mode, where the net shear area was equivalent to the gross shear area. One unexpected outcome of all three design equations was the relatively good predictive capacity for the CBS failure mode, as observations on the stress distribution along the CBS Shear plane suggested that significant regions of the plane did not reach strength limits throughout the entire loading of the connection. Although the simplified shear resistance components of all three design equations do not reflect the true mechanism of failure for the CBS plane, it is probable that it provides a reasonable estimation of the average stress state along the plane, with certain regions of the shear area participating with a higher degree of stress that offsets the lower stressed regions.

Table 5.2: Overview of Professional Factors.

		CSA S16-19		AISC 360-16		Eurocode 3-2005	
ID	Section	EBS	CBS	EBS	CBS	EBS	CBS
M1SPEC	W250X58	1.12		1.38		1.57	
M1TYP	W250X58						
M2SPEC	W360X91	1.16		1.34		1.60	
M2TYP	W360X91						
M3SPEC	W410X53	1.07	1.06	1.29	1.08	1.51	1.08
M3TYP	W410X53	0.99	1.10	1.13	1.12	1.35	1.13
M4SPEC	W460X113	1.09	1.14	1.34	1.14	1.46	1.14
M4TYP	W460X113	0.96		1.24		1.38	
M5SPEC	W610X101	1.11	1.03	1.31	1.04	1.58	1.05
M5TYP	W610X101	1.10	1.06	1.25	1.08	1.54	1.08
M6	W460X113	1.10		1.35		1.47	
M7	W530X72	1.05	1.05	1.20	1.07	1.49	1.08
M8	W200X52	1.02		1.21		1.38	
M9	W250X101	1.16		1.37		1.57	
M10	W310X74	1.06		1.24		1.49	
M11	W460X74	1.11	1.21	1.32	1.22	1.53	1.23
M12	W690X170	1.02	0.99	1.20	1.01	1.45	1.01
Mean:		**1.07**	**1.08**	**1.28**	**1.09**	**1.49**	**1.10**
		Combined:	**1.08**	Combined:	**1.21**	Combined:	**1.35**

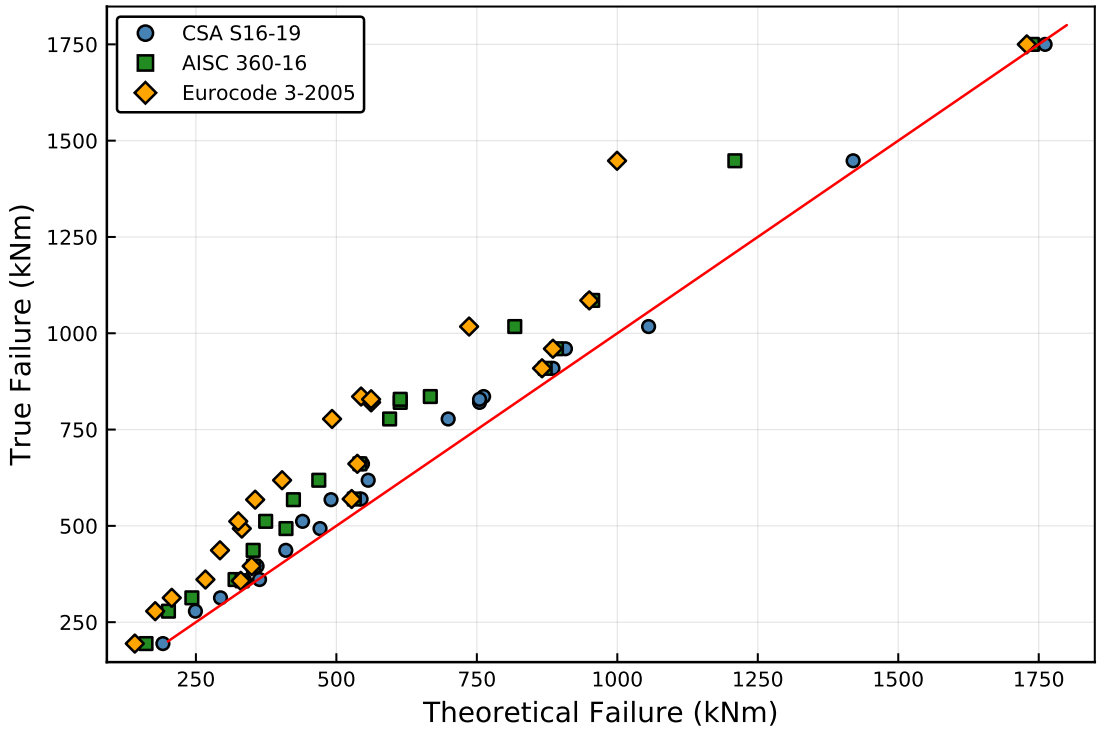

Figure 5.24: Comparison of block shear Professional Factors.

5.4 15% Rule

To investigate the role of the 15% rule on the net section flexural resistance and any relationship to the block shear failure mode, an analytic review of four net section flexural resistance equations was performed and compared against the results from the finite element study.

5.4.1 Analytic review

The reduced capacity of a flexural W-section with holes in the flanges is approached in varying ways, as reviewed in Chapter 2. The AISC 360-16 design method uses a proportional reduction in flexural capacity based on the area removed from the flanges; the CSA S16-14 method simply took the net section properties of S or Z for net flange areas below 85%; the CSA S16-19 method adds a modifier to the S16-14 method depending on geometric and material properties of the section, and; the proposed design method by Swanson (2016) adds a modifier to the AISC 360-16 method to account for the participation of the web at failure. To investigate the significance of the flexural resistance limits that these equations impose, the theoretical reduction in moment capacity as a proportion of the gross plastic moment capacity was calculated for all tabulated W-sections using bolt diameters from a range of 1/2" (13mm) to 1-1/2" (38mm). The following assumptions and simplifications were made for all four analyses:

1. Nominal properties of ASTM A992 steel: $f_y = 345MPa$, $f_u = 450MPa$.
2. Two parallel rows of bolts in each flange, i.e. four bolt holes across the net section.
3. A 2mm hole tolerance for each bolt hole.
4. Full lateral support provided.

For computational efficiency, the reduced section capacity calculations were performed on all W-sections and each of the bolt sizes, regardless of any geometric incompatibility or the section's likelihood of use as a flexural member. Although the figures presented below show net flange area ratios as low as 25%, it should be clear that such a combination of section and bolt size would not exist in practice. However, the inclusion of these theoretical combinations provided additional insight on the general trend of each design equation on its effect on net section flexural members.

5.4.1.1 AISC 360-16: Equation F13

The AISC 360-16 method for net flexural resistances do not have a geometric limit on the net flange area to trigger the reduced capacity equation, but rather considers the capacities for the net flange fracture strength and the gross flange yield strength, as seen in Equation 5.4. Should the inequality in Equation 5.4 not hold, i.e. the net fracture resistance is critical, the section capacity is reduced to the calculated value of Equation 5.5. For ASTM A992 steel sections, this critical point of transfer from the gross section flexural capacity to the reduced flexural capacity occurs at a net flange area ratio of $\sim 76\%$.

$$F_u A_{fn} \geq Y_T F_y A_{fg} \tag{5.4}$$

$$M_n = \frac{F_u A_{fn}}{A_{fg}} S_x \tag{5.5}$$

Where: $Y_T = 1.0$ if $F_y/F_u \leq 0.80$, $Y_T = 1.1$ otherwise.

The effect of the AISC 360-16 design method on all tabulated W-sections and bolt size combinations is shown in Figure 5.25. Two clear issues are evident with the AISC 360-16 design method. First, the sudden reduction of approximate 20% of the gross section flexural capacity at the 76% net flange area limit seems unreasonable, especially along with the assumed change of failure mode from a

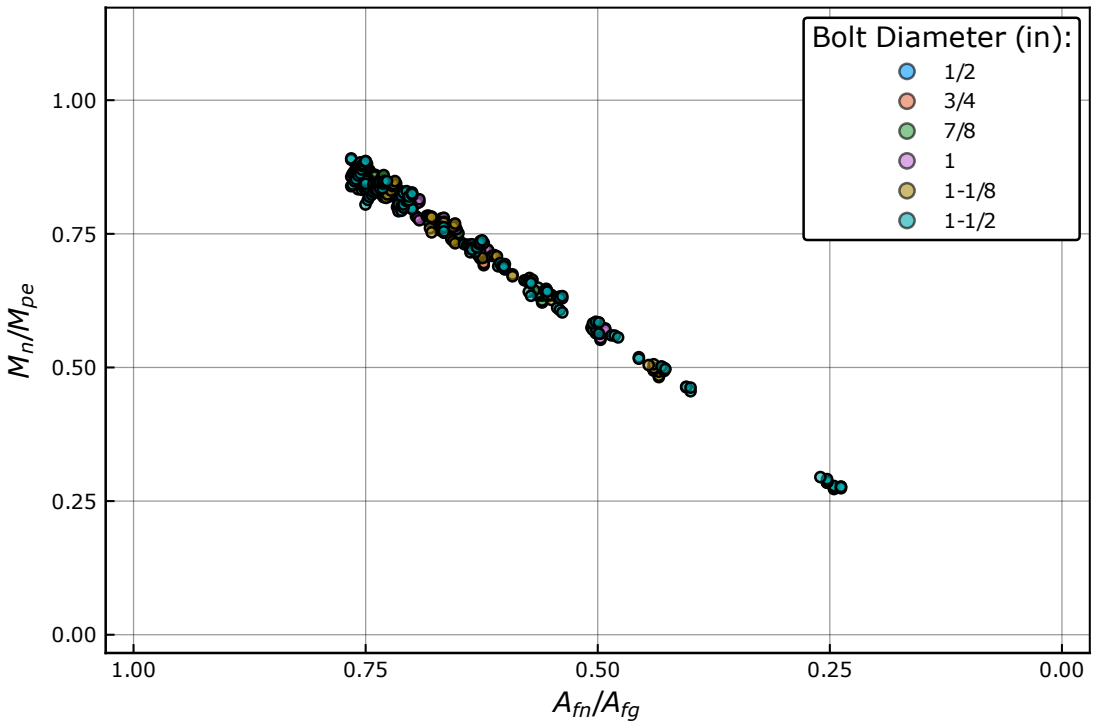

Figure 5.25: AISC 360-16: Net flexural resistance.

yield stress limit state to the sudden fracture of the flange extremity. An equation like this would suggest that a section with a net flange area ratio of 78% would perform and fail in a significantly different way than the same section with a net flange area ratio of 75%. It is noted, however, that the majority of the section-connection details that were modelled for the block shear failure analysis had a net flange area ratio greater than 76%, and would not have had an overall flexural capacity resistance reduced by the AISC 360-16 design method.

5.4.1.2 CSA S16: Clause 14.1

Two methods of the CSA S16 were explored, as the most recent S16-19 standard provided the first revision on net flexural capacity design since its initial adoption in the 1950s. The original method, which was in effect up until the CSA S16-14 standard, simply required that the net section geometric properties should be

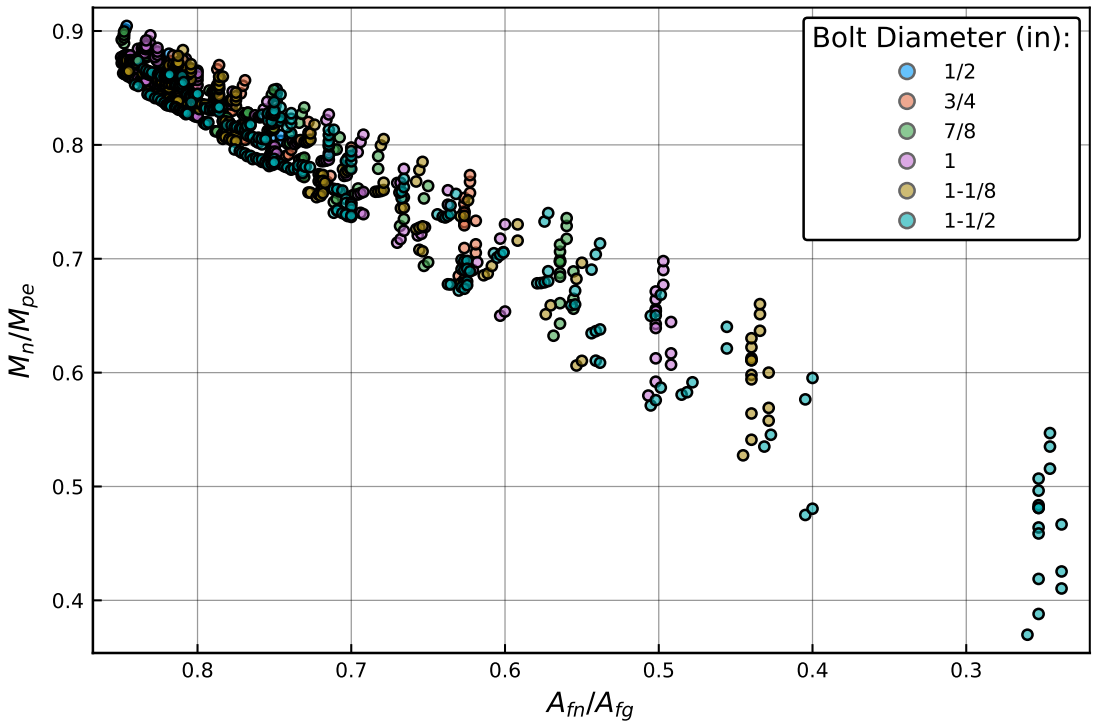

Figure 5.26: CSA S16-14: Net flexural resistance.

used if the reduction in flange area was greater than 15%. Ostensibly, this meant that Class 1 and 2 sections were allowed to reach the plastic moment state, albeit with a reduced value of the plastic section modulus, Z, while Class 3 sections would reach a similarly reduced yield moment state with a lower value of the elastic section modulus, S. This provided a more reasonable assumed ductile failure mode compared to the AISC 360-16 method; however, the sudden drop in capacity from one side of the net area threshold to the other remained. The effect of the CSA S16-14 15% Rule on all tabulated W-sections is shown in Figure 5.26. Since the CSA S16-14 15% rule was tied to a non-linear geometric property (S or Z), the reduction in capacity was no longer proportional to the amount of flange area lost, and as such, there is a greater variation in the proportional loss of available flexural capacity for a given net flange area ratio.

The revised 15% Rule design method introduced in the most current CSA S16-

19 standard added a term to the net section property. This term was a proportion, α, of the gross section property, which would then be added to the net section values of S and Z. The value of α was dependent on the yield strength of the material, as well as the existence of holes in both the tension and compression flanges; a complete explanation was provided in Chapter 2. For the assumed conditions of the analytic study, the value of α was taken as 0.12.

$$S_e = \alpha S + S_n \leq S \tag{5.6}$$

$$Z_e = \alpha Z + Z_n \leq Z \tag{5.7}$$

The effect of the revised 15% rule in the CSA S16-19 standard on the flexural capacity of bolted W-sections is shown in Figure 5.27. The revised method showed the same spread of reduced capacities for a given net flange area ratio as the CSA S16-14 method, but improved on the previous method by shifting the entire reduction capacity upwards by 12% of the gross section property. It is clear that the revised method provided a significant improvement in allowable performance for flexural members. Perhaps more significant, however, is that this upward shift in the allowable capacities has effectively eliminated the sudden discontinuity of flexural strength on either side of the 15% reduction threshold. A flexural member with a net flange area of just below 85% could reach an allowable moment that is close to M_p, rather than a sudden drop in capacity.

The CSA S16-19 in general provided a welcome improvement in allowable flexural strengths for bolted W-sections compared to the previous CSA S16-14 standard. It also reduced the sudden discontinuity of flexural capacity once the 15% rule was first triggered; however, this was at the cost of a slightly more involved design method. Further, one key component was unchanged in the S16-19 design method: the use of a 15% flange area reduction as the threshold for reduced section capacities. Although the tested combinations of section-connection

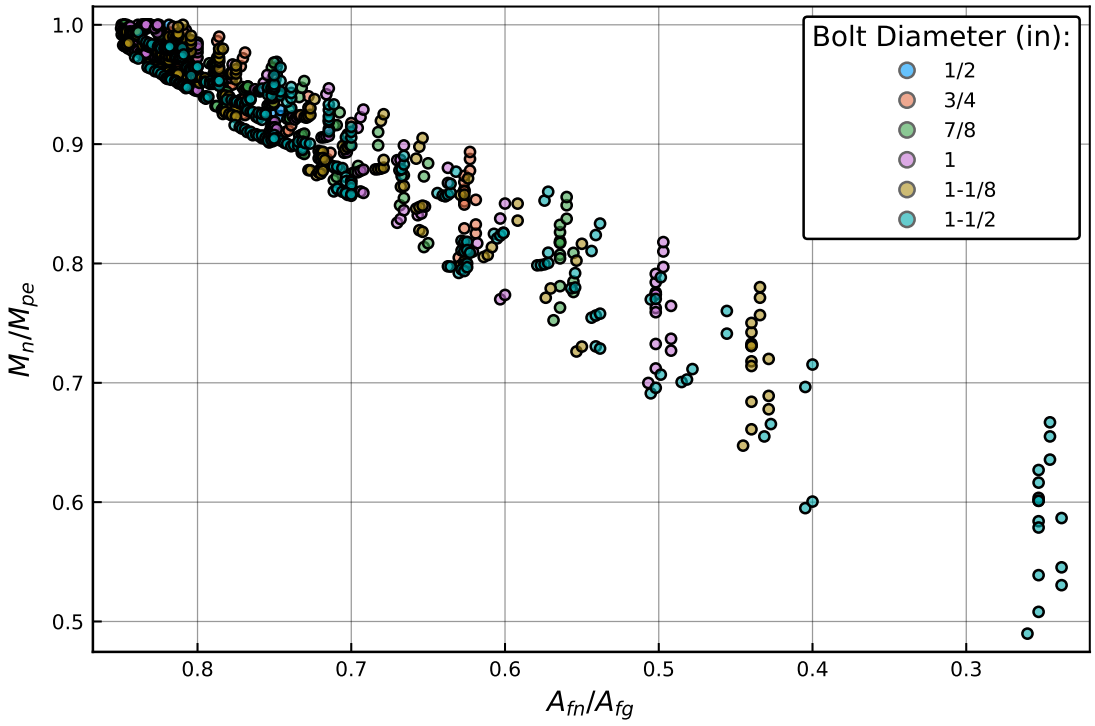

Figure 5.27: CSA S16-19: Net flexural resistance.

details for the block shear finite element study did not trigger the AISC 360-16 equation for flexural capacity reductions, all models *would* trigger the 15% threshold of the S16-19 method, as the specimens had net flange area ratios of 75% to 81%. Therefore, although the S16-19 method would perform better than the AISC 360-16 when both clauses are triggered, the AISC 360-16 had the benefit of an additional reduction in approximately 10% of the net flange area ratio before any decrease in the section capacity is required.

5.4.1.3 Swanson Equation (2016)

After completing a statistical review of previously performed tests on bolted W-section connections, Swanson (2016) suggested an improved design equation that better fit the observed ultimate flexural capacities. The reduced capacity was based on the proportional reduction used by the AISC 360-16 method, but included an additional contribution from the web, which was assumed to reach the ultimate strength limit. It is noted, however, that the use of the ultimate strength across the web region was not based on the observed failure mechanisms of the laboratory tests, but rather because it provided the best statistical fit for the aggregated test results. What was unique with the Swanson equation was that there was no threshold for the net flange area ratio before the equation is triggered. Rather, the equation would be used for any amount of reduced area caused by bolt holes, with an upper limit in place that ensured that flexural capacities did not exceed the gross section capacity.

$$M_n = \frac{F_u A_{fn}}{A_{fg}} S_x + F_u Z_{x,web} \leq F_y Z_x \tag{5.8}$$

The effect of the Swanson equation on reduced flexural capacities is shown in Figure 5.28. The benefit of including the contribution of the web was immediately clear; sections with net flange areas as low as 60% could still theoretically reach the gross plastic moment capacity. It is noted, however, that these section-connection combinations were most likely from sections with extremely thick

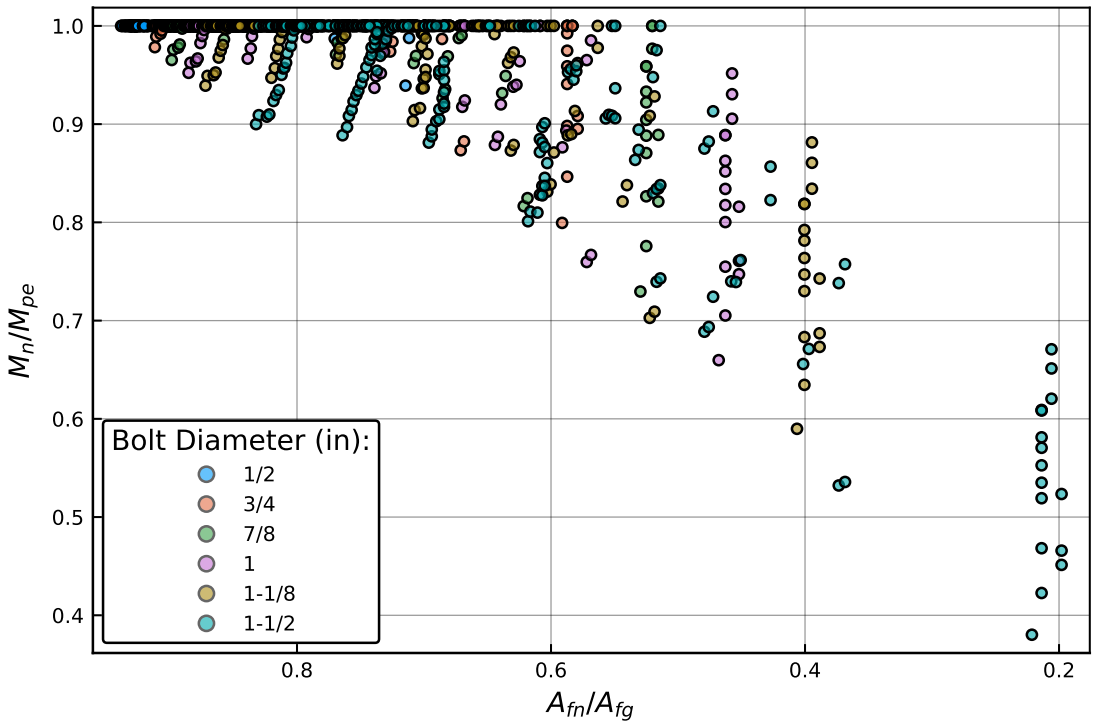

Figure 5.28: Swanson Equation 3: Net flexural resistance.

webs, and would typically not be used in a flexural loading scenario. Another key observation was that some section-connection details that did not trigger either the 15% rule for the CSA S16-19 standard or the approximate 76% threshold for the AISC 360-16 standard still had reduced flexural capacities, since the Swanson method required the reduction equation to apply for all bolted flexural members. In general, however, the Swanson equation allowed for a wide range of net flange area ratio values with little to no reduction in the overall flexural resistance of the section.

5.4.2 Comparison of design methods

A comparison of all four design methods and regression lines is shown in Figure 5.29. The significant improvement of the CSA S16-19 method from the CSA S16-14 method was immediately clear, as well as the smooth transition from reduced

section capacities to full gross section strength. When comparing the AISC 360-16 and the CSA S16-19 methods, the AISC 360-16 provided a better allowable flexural capacity for net flange area ratios greater than 76%, due to the inherently lower threshold before reductions were imposed. However, for sections with net flange area ratios below the threshold of the AISC 360-16 equation, the CSA S16-19 provided consistently higher allowable strengths. The Swanson method typically provided the highest flexural capacity for sections with significant flange area reductions, but also had a significantly larger spread of reduction due to the dependence on the geometry of the web. It would be expected for typical flexural W-sections that the reductions would be on the lower end of the plotted range, since thick web sections are typically restricted to columns. Further, for sections with net flange area ratios greater than 85%, there was a greater possibility that the Swanson equation would provide a lower resistance than the CSA S16-19 method, since the area threshold for CSA S16-19 reduction was not met, and gross section properties could be used.

To evaluate section-connection combinations more reflective of reality, the results of the block shear finite element study were plotted against the four predictive design equations; this plot is shown in Figure 5.30. The Edge Block Shear moment capacities are shown as red circles, while the peak experienced moments are shown as black squares. Since the modelled specimens were specifically detailed to fail in block shear, the plotted capacities do not perfectly reflect a more conventional moment connection with the same bolt diameters, since additional rows of bolts would increase the block shear moment capacity. However, it is clear that some block shear critical connection details still failed at a moment greater than allowed by the CSA S16-19 equation, and even the proposed Swanson equation. Further, all of the peak experienced moments were near, or greater than, the theoretical gross plastic moment capacity, an observation made by previous researchers on net section flexural capacities (Swanson, 2016; Sivakumaran et al., 2010). Since the net flange area ratio would be unaffected with additional rows of

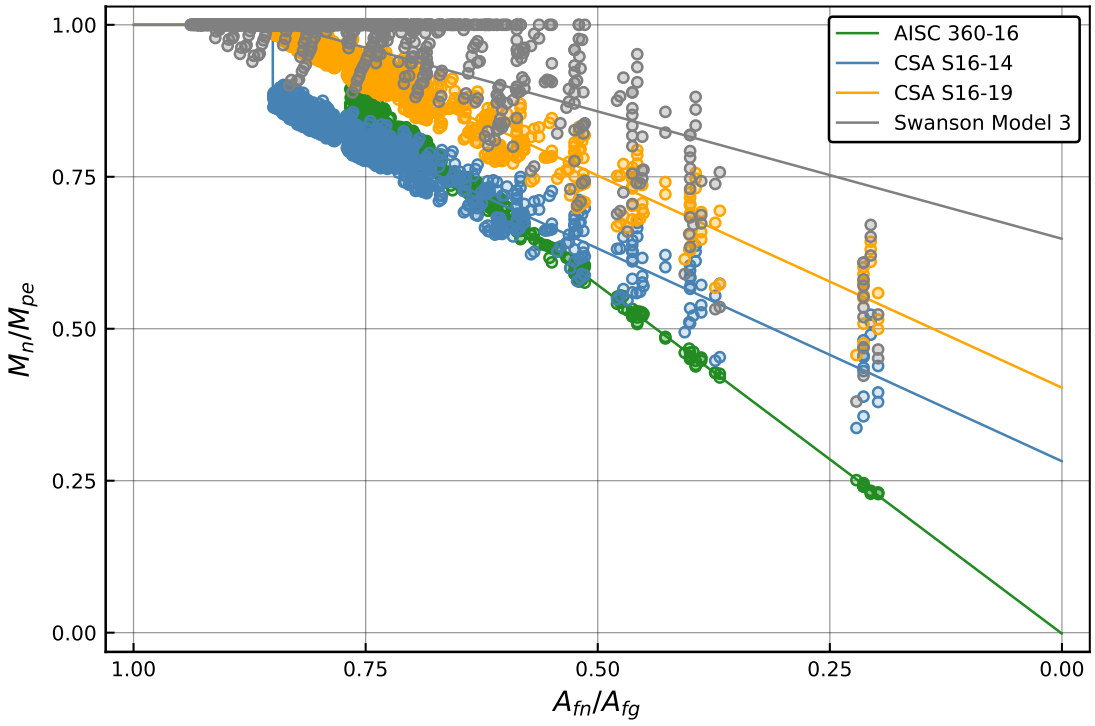

Figure 5.29: Comparison of net flexural resistance methods.

bolts, it would be expected that as the block shear moment resistance increases above the gross section capacities, the overall capacity of the connection would approach the values of M_{PEAK} in Figure 5.30.

In general, the CSA S16-19 design method provided a much needed improvement in allowable flexural capacity for typical flexural section-connection details for bolted W-sections. It also eliminated the sudden loss in flexural capacity once the 15% rule was first triggered, instead providing a smooth and gradual decrease in strength as net flange area ratios decreased. For the range of net flange area ratios observed in the block shear finite element study, the greatest reduction in allowable strength was approximately 95% of the gross plastic moment for a net flange area ratio of 75%. It was clear that even connections detailed to critically fail in block shear could still surpass the theoretical moment capacity of the entire section. Instead of a measure of the actual reduced capacity of the member, these limits on flexural strength could rather be considered as proxy load limitations due to the loss of rotational ductility from the reduced flange areas, as observed by Sivakumaran et al. (2010), where although the strength of the net flexural member is not greatly affected by reduced flange areas, the rotational capacity is. However, the significance of the improved S16-19 method for Canadian structural steel designers is yet to be determined, as the standard has not been widely adopted at the time of this report. It is unclear if the improvement in allowable flexural capacity provides a reasonable compromise for engineers attempting to maximize the performance of structural members, or whether it still causes unacceptable reductions in flexural capacity for net flange area ratios typically encountered by practising engineers. Should it be the latter, the proposed equation by Swanson (2016) could provide the required additional flexural capacity. However, Swanson's equation implied a failure mechanism that was not observed in any of the laboratory tests on which the equation was based; rather, the fracture of the web plane was included as it provided the best statistical fit. Should Swanson's equation be desired as an eventual replacement for the

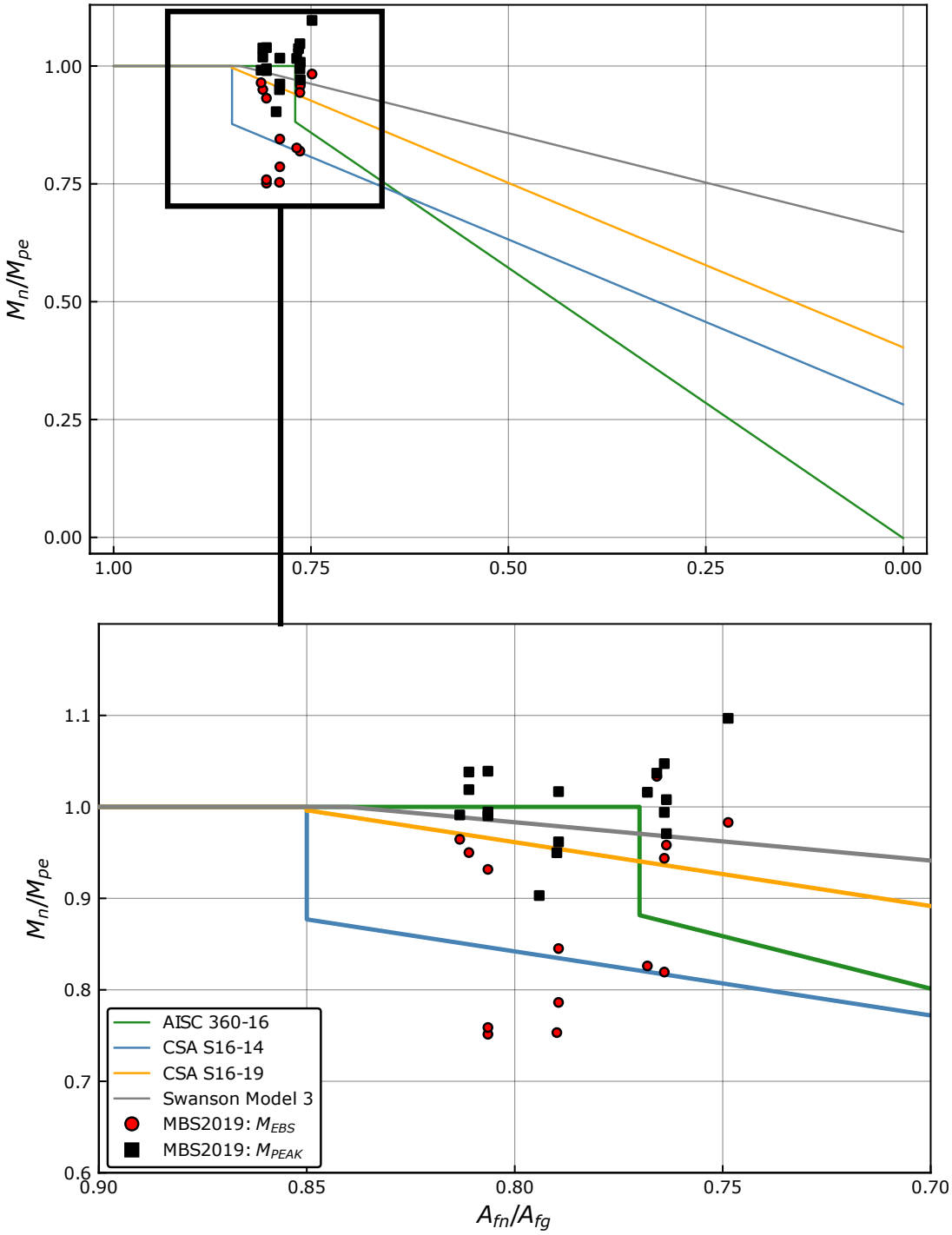

Figure 5.30: FE results compared to net flexural resistance predictions.

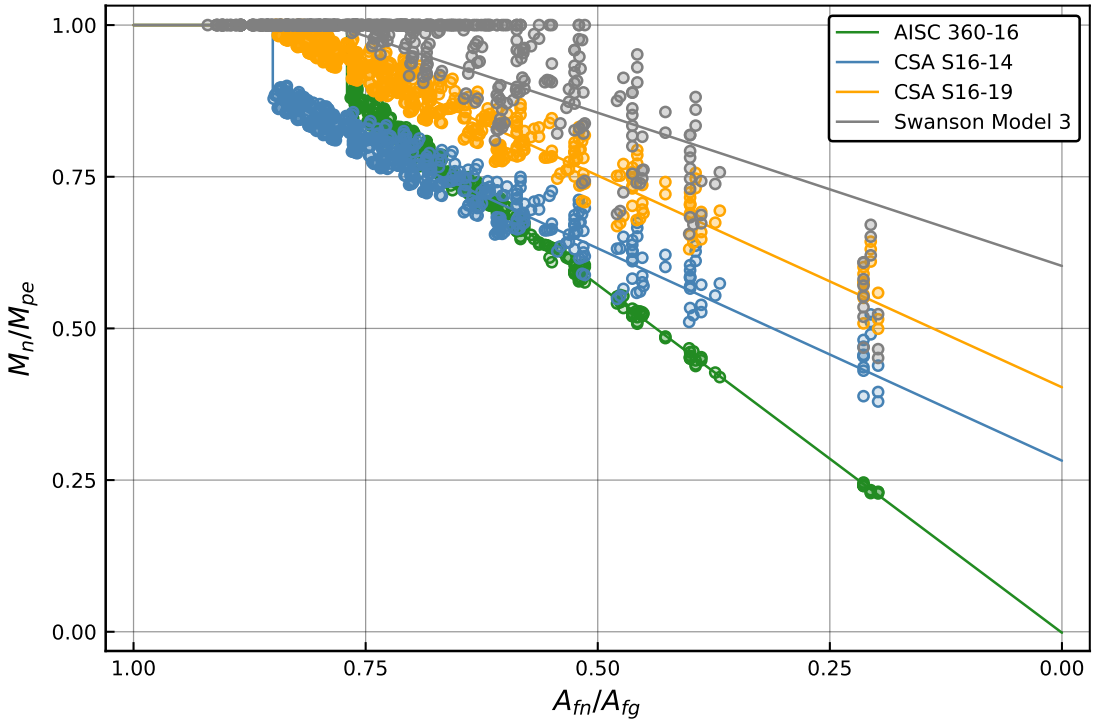

Figure 5.31: Reduced flexural capacities for common beam sections only.

CSA S16-19 design method, significant testing should be done to confirm that the web fracture term in the equation remained appropriate for a wider range of section-connection configurations.

5.5 Conclusion

The finite element study of 17 bolted moment connections provided insight on the existence of, and the current predictive capacity for, moment-induced block shear failure in W-sections. The CSA S16-19 method, which uniquely assumes a gross shear area and a stress-at-failure that is greater than the yield strength, provided the best predictive capacity for both the Edge Block Shear and Complete Block Shear failure modes, with a Professional Factor of 1.08. The importance of using the gross shear area was evident in the fact that the AISC 360-16 and Eurocode 3-

2005 both performed significantly better in predicting the Complete Block Shear failure mode, where the net shear area is equivalent to the gross shear area. It was conclusively determined that the block shear failure was a possible failure mode for the tension flange in bolted W-section moment connections, and should be explicitly considered during the design of steel structures.

In addition to the finite element study for moment-induced block shear failure, an analytic study reviewed the effect of the various net section flexural capacity reduction methods on all tabulated W-sections and for a wide range of typical bolt diameters. It was found that the CSA S16-19 design method for the 15% rule provided a significant improvement on the allowable flexural strength of a bolted W-section compared to the previous method in use up to the CSA S16-14 standard. It also performed significantly better than the AISC 360-16 method, but only when the net flange area ratio limits were met by both design standards. The performance of a proposed equation by Swanson (2016) was also evaluated. Although the proposed equation may provide the highest allowable flexural resistance in certain scenarios, the equation proposed by Swanson is divorced from the true failure mechanism of net section flexural members observed by previous researchers. It is yet to be seen whether the improved method provided by the CSA S16-19 provides a suitable compromise for Canadian structural designers between safe design and maximizing performance, or if a further increase in allowable flexural strengths is required.

Chapter 6

Conclusions

6.1 Overview

An analytic design methodology for block shear critical W-section moment splice connections was developed to investigate the theoretical possibility of the block shear failure mode for W-sections under flexure. Using this methodology, a wide range of W-section moment connections were detailed to theoretically fail in block shear in the tension flange. At this stage, it was observed that a block shear critical moment connection detail was highly dependent on the geometry of the W-section, as well as the overall connection length of the bolt group. To verify the design methodology, 17 representative non-linear finite element models were developed and analysed. Further, 6 of the 17 models were fabricated for eventual full-scale laboratory testing to calibrate the finite element models.

The analysis of the finite element models confirmed that block shear failure in the tension flange was a possible failure mode for bolted W-section moment connections under flexure, and should be explicitly considered when designing steel structures. Further, the block shear failure mode was observed to consist of a gross shear area at a stress state between the yield and ultimate strengths, and a net tension area at the ultimate strength. These two observations were supported when comparing the predictive capacities of the CSA S16-19, AISC 360-16, and the Eurocode 3-2005 design methods for block shear failure. The

CSA S16-19 design equation, which uniquely assumes a gross shear area, as well as a stress-at-failure of the shear plane that is greater than the yield strength, had the greatest predictive performance, with a Professional Factor of 1.08.

In addition to the block shear failure analysis, an analytic study on the existing and proposed design methods for net section flexural resistances of W-sections was performed. The flexural resistances of the 17 finite element models were compared against the theoretical reduced flexural capacities from the equations in the CSA S16-14, CSA S16-19, AISC 360-16, as well as a proposed equation by Swanson (2016). This analytic review showed that the newly revised CSA S16-19 method for net flexural capacity provided a significant increase in performance compared to previous iterations of the standard, as well as the AISC 360-16; however, it was noted that the true flexural capacity of some of the finite element models still exceeded the reduced limit, suggesting the reduction equations are still overly punitive. The proposed equation by Swanson (2016) provided the highest allowable flexural resistance, but assumed a failure mechanism that is divorced from observed laboratory results.

6.2 Future work

With an analytic design methodology, a finite element model catalog, and a review of the finite element analysis results, key insight on moment-induced block shear failure in W-sections was provided. The immediate suggested progression of this study is the laboratory testing of the M1-M6 specimens for calibration of the finite element models. This calibration phase will provide the evaluation metrics for the assumed boundary conditions, loading protocols, and mesh selection and densities for the existing finite element models. The laboratory testing phase is expected to be completed by the end of Summer 2020.

Next, to be further representative of true loading scenarios, the effect of shear across the splice connection on the block shear failure mode should be explored. It is possible that the transfer of shear load across a beam splice could influence

the overall stress distribution across the tension flange such that the block shear failure mode is affected. Further, since a shear splice theoretically contributes some moment transfer across a connection, the global flexural response would also be affected.

Finally, it was noted that the block shear failure mode is highly sensitive to varying section geometry parameters as well as the overall connection length. However, the limits of these section geometry parameters were qualitatively defined, with the overall observation being that *moderate depth, moderate widths,* and *moderate-to-thin flange thicknesses* are required for a block shear critical connection. Since the value of these variables, as well as the typical expected connection lengths, are finite and tabulated, a further analytic study into defining these geometric limits should be possible.

In general, further work for moment-induced block shear failure in W-sections should shift towards practical scenarios of design and analysis. As the main focus of this study was to isolate the moment-induced block shear failure mode as much as possible, many simplifications and deviations from typical design and loading conditions were made, such as the flange-only pure-moment connection, as well as atypical bolt spacings. Further research should consider the effect of shear transfer, and should maintain the use of typical bolt spacings and numbers.

References

Aalberg, A., & Larsen, P. (2000). Strength and ductility of bolted connections in normal and high strength steels. In *Proceedings of the seventh international symposium on structural failure and plasticity.* 38

Altstadt, S. (2004). *Tensile strength and ductility of high performance steel girders* (Unpublished doctoral dissertation). University of Minnesota. 26

American Institute of Steel Construction. (1978). Specification for the Design, Fabrication and Erection of Structural Steel for Buildings. *American Institute of Steel Construction.* 8

American Institute of Steel Construction. (1986). Load and Resistance Factor Design Specification for Structural Steel Buildings. *American Institute of Steel Construction.* 10

American Institute of Steel Construction. (2005). Specification for Structural Steel Buildings (ANSI/AISC 360-05). *American Institute of Steel Construction.* 25

American Institute of Steel Construction. (2016). Specification for Structural Steel Buildings (ANSI/AISC 360-16). *American Institute of Steel Construction, Chicago-Illinois.* 6

American Society for Testing and Materials. (2005). *ASTM A370: standard test methods and definitions for mechanical testing of steel products.* 102

American Society for Testing and Materials. (2019). ASTM F3125/F3125M-19: Standard Specification for High Strength Structural Bolts and Assemblies, Steel and Alloy Steel, Heat Treated, Inch Dimensions 120 ksi and 150 ksi Minimum Tensile Strength, and Metric Dimensions 830 MPa and 1040 MPa Minimum Tensile Strength. *ASTM International, West Conshohocken, PA.* 48

Arasaratnam, P. L. (2008). *Effects of flange holes on flexural behavior of steel beams* (Unpublished doctoral dissertation). 24, 26

Birkemoe, P. C., & Gilmor, M. I. (1978). Behavior of bearing critical double-angle beam connections. *Engineering Journal*, *15*(4). 6, 8, 9, 33

Canadian Standards Association. (1954). CSA-S16-54: design of steel structures. *Canadian Standards Association, Ottawa, Ontario, Canada.* 3, 20

Canadian Standards Association. (2014). CSA-S16-14: design of steel structures. *Canadian Standards Association, Mississauga, Ontario, Canada.* 20

Canadian Standards Association. (2019). CSA-S16-19: design of steel structures. *Canadian Standards Association, Mississauga, Ontario, Canada.* 1, 6, 27, 45

Clements, D. D., & Teh, L. H. (2013). Active shear planes of bolted connections failing in block shear. *Journal of structural engineering*, *139*(3), 320–327. 17

Dassault Systèmes. (2018). *Abaqus fea.* Retrieved from `www.simulia.com` 80, 81, 83

Driver, R. G., Grondin, G. Y., & Kulak, G. L. (2006). Unified block shear equation for achieving consistent reliability. *Journal of Constructional Steel Research*, *62*(3), 210–222. 15, 16, 30, 147

Elliott, M. D., & Teh, L. H. (2019). Whitmore tension section and block shear. *Journal of Structural Engineering*, *145*(2), 04018250. 18, 37

Elliott, M. D., Teh, L. H., & Ahmed, A. (2019). Behaviour and strength of bolted connections failing in shear. *Journal of constructional steel research*, *153*, 320–329. 18

Epstein, H. I. (1992). An experimental study of block shear failure of angles in tension. *Engineering journal, AISC*, *29*(2), 75–84. 14

Epstein, H. I., & Chamarajanagar, R. (1996). Finite element studies for correlation with block shear tests. *Computers & structures*, *61*(5), 967–974. 34

Epstein, H. I., & D'Aiuto, C. (2002). Using moment and axial interaction equations to account for moment and shear lag effects in tension members. *Engineering Journal*, *39*(2), 91–99. 14

Epstein, H. I., & Stamberg, H. (2002). Block shear and net section capacities of structural tees in tension: test results and code implications. *Engineering Journal*, *39*(4), 228–239. 1, 14

Epstein, H. I., & Thacker, B. (1991). The effect of bolt stagger for block shear tension failures in angles. *Computers & structures*, *39*(5), 571–576. 34

Geschwindner, L. F. (2010). Notes on the impact of hole reduction on the flexural strength of rolled beams. *Engineering journal*, *47*(1), 37. 25, 26, 28

Grondin, G. Y. (2005). Discussion: Using moment and axial interaction equations to account for moment and shear lag effects in tension members. *Engineering Journal*, *45*(1), 45-50. 15

Gross, J. M., Orbison, J. G., & Ziemian, R. D. (1995). Block shear tests in high-strength steel angles. *Engineering Journal, AISC*, *32*(3). 35

Hardash, S. G., & Bjorhovde, R. (1985). New design criteria for gusset plates in tension. *Engineering journal*, *22*(2). 10, 15, 35

Huns, B. B., Grondin, G. Y., & Driver, R. G. (2006). Tension and shear block failure of bolted gusset plates. *Canadian Journal of Civil Engineering*, *33*(4), 395–408. 36

Khoo, H., Cheng, R., & Hrudey, T. (2000). Ductile fracture of steel. structural engineering report no. 233. *Report no*. 36

Kluyver, T., Ragan-Kelley, B., Pérez, F., Granger, B., Bussonnier, M., Frederic, J., ... others (2016). Jupyter notebooks. *a publishing format for reproducible computational workflows*, *850*, 87–90. 48

Kulak, G. L., & Wu, E. Y. (1997). Shear lag in bolted angle tension members. *Journal of Structural Engineering*, *123*(9), 1144–1152. 14

Larson, P. C. (1996). *The design and behavior of bolted beam-to-column frame connections under cyclical loading* (Unpublished master's thesis). University of Texas at Austin. 26

Lilly, S. B., & Carpenter, S. T. (1939). Effective moment of inertia of a riveted plate girder. In *Proceedings of the american society of civil engineers* (Vol. 65, pp. 1407–1422). 21

Moreau, R. (2014). *Evaluation of the "Modified-Hidden-Gap" Connection for Square HSS Brace Members* (Unpublished master's thesis). McGill University, Montreal. 80

Munse, W. H., & Chesson, E. (1963). Riveted and bolted joints: net section design. *Journal of the Structural Division*, *89*(1), 107–126. 13, 15

Orbison, J. G., Wagner, M. E., & Fritz, W. P. (1999). Tension plane behavior in single-row bolted connections subject to block shear. *Journal of Constructional Steel Research*, *49*(3), 225–239. 11, 35

Pizzuto, D. (2019). *Block shear failure in W-section tension members connected by bolted flange plates* (Unpublished master's thesis). McGill University, Montreal. 4, 18, 20, 35, 38, 50, 79, 80, 83, 89, 90

Ramberg, W., & Osgood, W. R. (1943). Description of stress-strain curves by three parameters.
38

Rao, S. S. (2011). *The finite element method in engineering* (5th ed.). Elsevier. 83

Ricles, J. M., & Yura, J. A. (1983). Strength of double-row bolted-web connections. *Journal of Structural Engineering*, *109*(1), 126–142. 8, 9, 10, 15, 33, 34

Robert McNeel & Associates. (2018). *Rhinoceros.* Retrieved from `www.rhino3d.com` 74

Sato, A., Newell, J., & Uang, C. (2007). Cyclic testing of bolted flange plate steel moment connections for special moment frames. *Final Rep. to Am. Inst. Steel Constr. Inc.* 26

Schneider, S. P., & Teeraparbwong, I. (2002). Inelastic behavior of bolted flange plate connections. *Journal of Structural Engineering*, *128*(4), 492–500. 26

Sivakumaran, K., Arasaratnam, P., & Tait, M. (2010). Strength and ductility of steel beams with flange holes. In *Sdss rio 2010 stability and ductility of steel structures.* 24, 26, 27, 28, 29, 158, 160

Sun, E. Q. (2006). Shear locking and hourglassing in msc nastran, abaqus, and ansys.. 81, 83

Swanson, J. A. (2016). Strength of beams in beam-to-column connections with holes in the tension flange. *Engineering Journal-American Institute of Steel*

Construction, *53*(3), 159–172. 26, 28, 150, 156, 158, 160, 163, 172

Swanson, J. A., & Leon, R. T. (2000). Bolted steel connections: tests on t-stub components. *Journal of Structural Engineering*, *126*(1), 50–56. 26

Topkaya, C. (2004). A finite element parametric study on block shear failure of steel tension members. *Journal of Constructional Steel Research*, *60*(11), 1615–1635. 12, 28, 35

Wen, H., & Mahmoud, H. (2017). Simulation of block shear fracture in bolted connections. *Journal of Constructional Steel Research*, *134*, 1–16. 37

Whitmore, R. E. (1952). *Experimental investigation of stresses in gusset plates*. Engineering Experiment Station, University of Tennessee, Knoxville. 10

Appendices

Appendix A

Net section flexural resistance

In Section 5.4, varying methods for reduced flexural capacities for W-sections with bolt holes in the flanges were reviewed. Of these methods, the reduction equation developed by Swanson (2016) consistently provided the highest allowable flexural capacity for typical section-bolt diameter combinations for flexural members. However, it was noted that the assumed failure mechanism of the Swanson Equation did not reflect the observed laboratory failure paths that the equation was based on. Specifically, the assumption of the stress-at-failure across the entire web of F_u was disputed.

A supplementary series of finite element models was developed to investigate the true stress distribution along the critical net section for bolted moment connections. The series was based on the M5:W610X101 test specimen, and was noted as M5S to represent the investigation of the Swanson Equation. Based on the initial M5 model, which was renamed as M5S0, two parameters were varied to investigate their effect on the overall stress distribution across the net section. First the number of bolt rows was increased from 2 to 3, to transition the critical failure mode away from block shear failure and towards the theoretical net section flexural capacities; second, the presence of a web splice was also included to investigate how a moment transfer through the web would affect the stress distribution across the critical net section. A total of four specimens were evaluated, and are summarized in Table A.1.

Table A.1: W610X101 M5S series overview

ID	End (mm)	Pitch (mm)	Gauge (mm)	# Rows	Web Splice
M5S0	35	75	145	2	No
M5S1				2	Yes
M5S2				3	No
M5S3				3	Yes

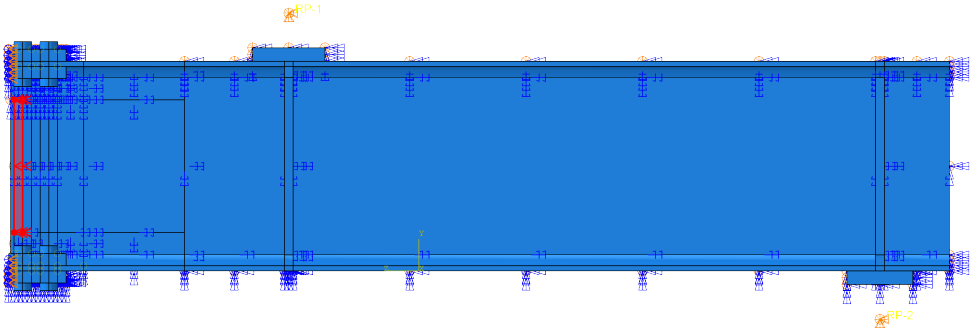

Figure A.1: Simplified boundary condition for web splice.

The web splice was simplified as a rotationally fixed boundary condition across a 1" x 15" (25mm x 375mm) region of the beam end, as seen in Figure A.1. This simplification effectively provided an infinitely stiff web connection; although this simplification would cause an overestimation of the true stress transfer across the web splice, it was deemed acceptable to investigate a 'best case scenario' influence on the stress distribution across the critical net section.

All specimens were loaded to a 90mm displacement at the load point, and the elemental stresses across critical regions of the specimens were compared. First the general visual stress contours shown in Figures A.2 and A.3 were compared. In general, the effect of the web splice on the overall stress distribution was most evident when comparing the 2 bolt row specimens, M5S0 and M5S1. Since the M5S0 specimen was detailed to fail in block shear, the inclusion of the web

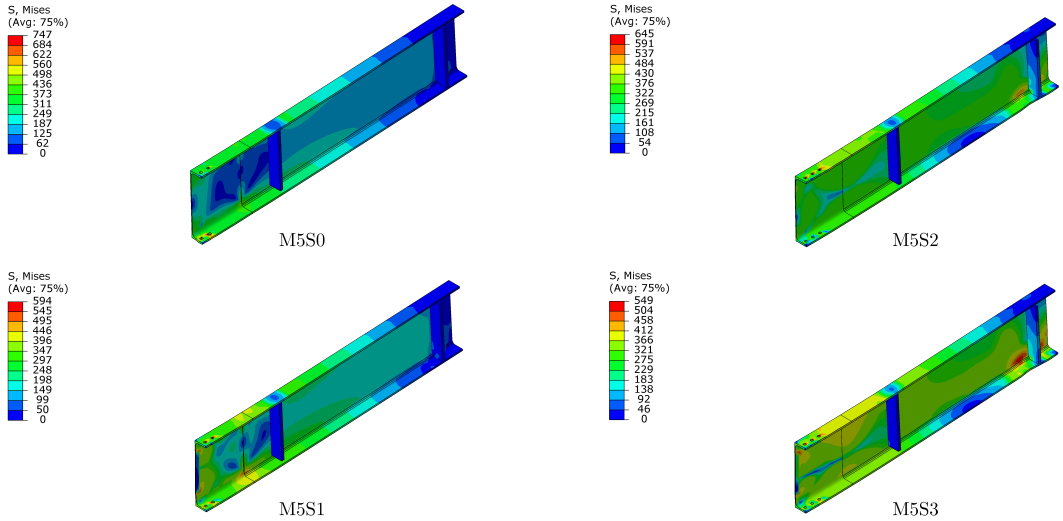

Figure A.2: Comparison of Von Mises stress distributions for the M5S series.

splice had the greatest effect in limiting the extreme local deformations that were present in the tension flange of the M5S0 specimen, and participating in the moment transfer across the connection. For the M5S2 specimen, where the block shear failure mode was no longer critical, the participation of the web splice was less pronounced.

Next, the elemental axial stresses across the critical net section was plotted and compared. The critical net section is the section across the last row of bolts in a given bolted connection, where any theoretical failure would occur; the location of the critical net section is shown in Figure A.4. A comparison of the elemental stresses cross the critical net section is shown in Figure A.5. Elements in the flanges (black) were visually separated from the elements in the web (blue). The red horizontal lines represent the yield strength, and the red vertical line indicates the load displacement at which the overall unfactored gross plastic moment was reached at the splice connection. All specimens eventually reached the theoretical gross plastic moment capacity, with the exception of M5S0, which was detailed to fail in block shear.

As expected, since deformation/stress concentrated at the local block shear

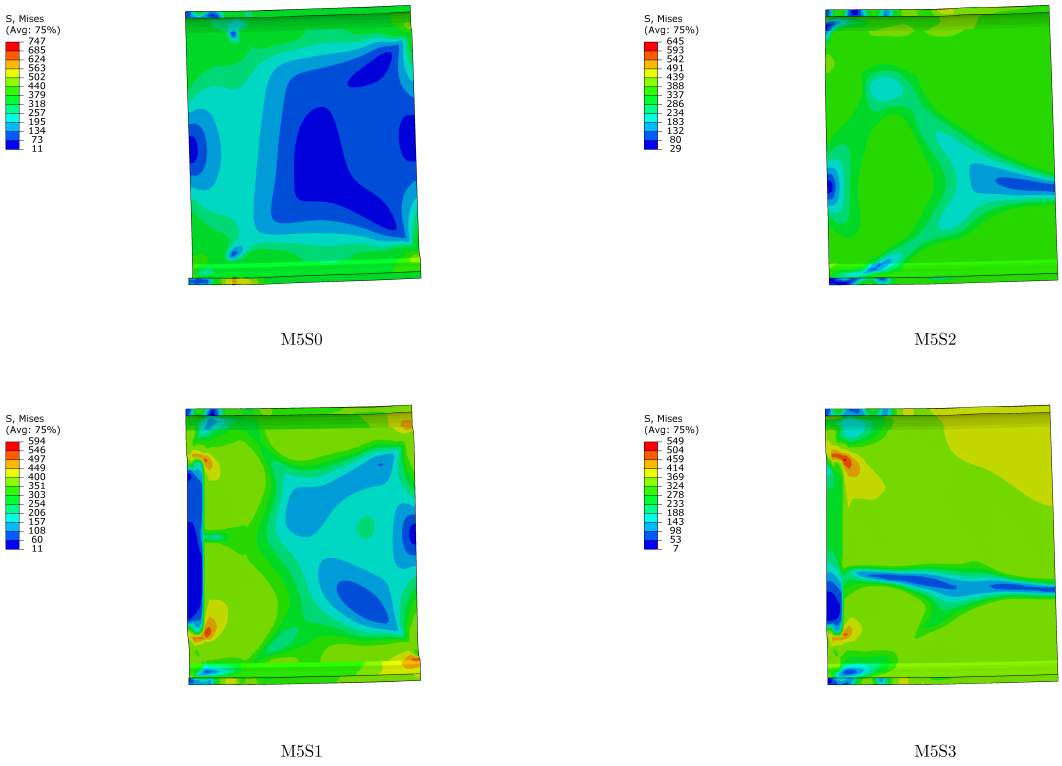

Figure A.3: Comparison of Von Mises stress distributions for the M5S series.

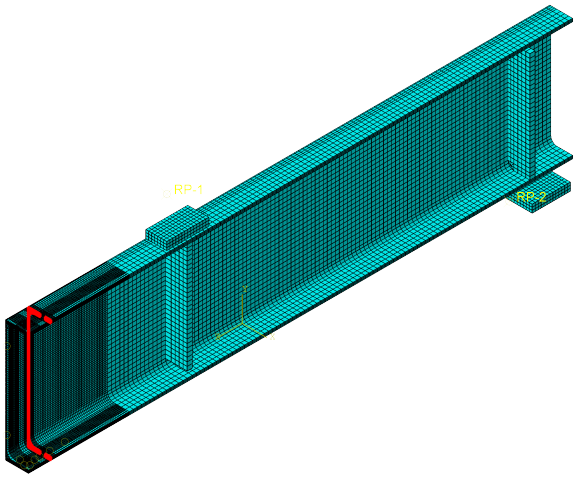

Figure A.4: Location of critical section.

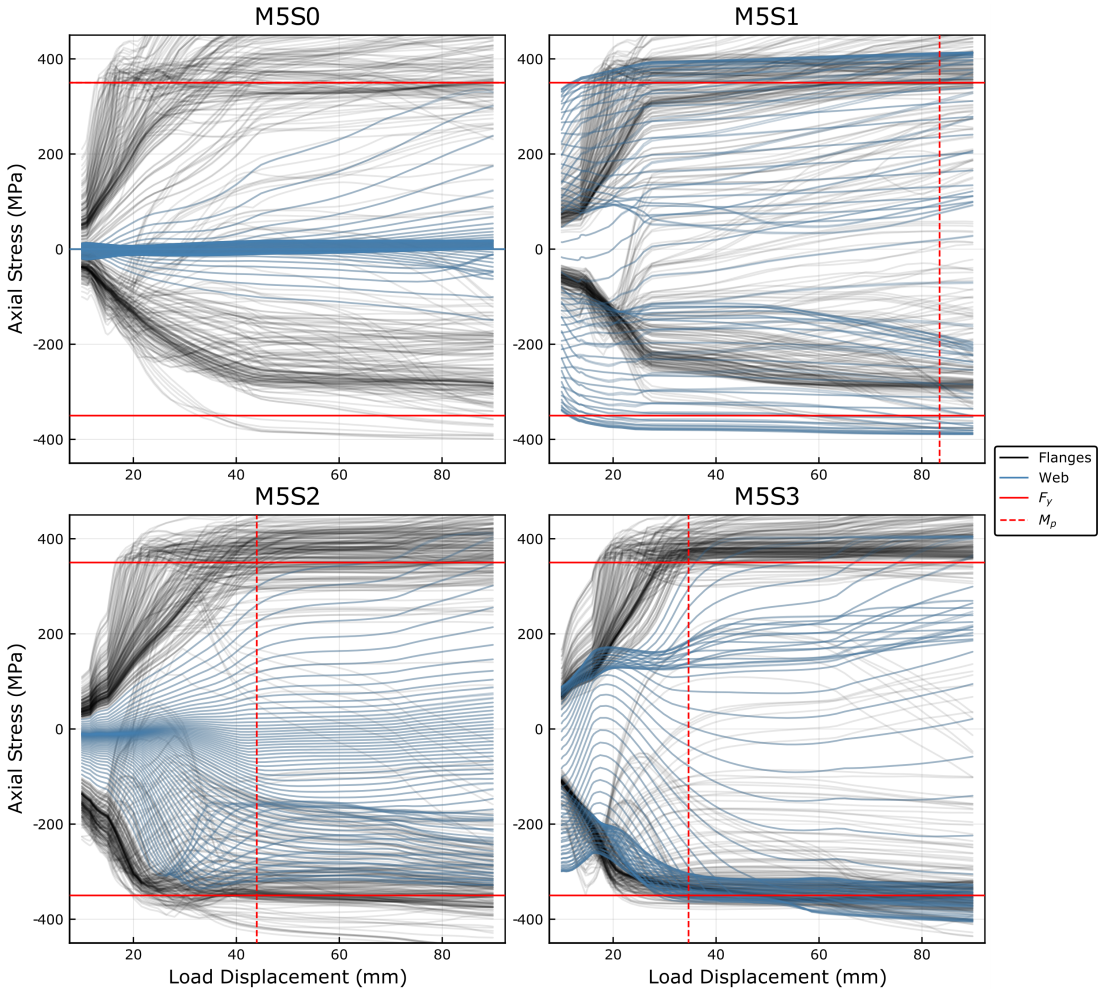

Figure A.5: Axial stress distribution across critical net section.

region for the M5S0 specimen, the elements along the web were at or near zero stress throughout the entire loading history. With the addition of a web splice in the M5S1 specimen, the web elements along the net critical section participated to the overall flexural resistance to a significantly higher degree. Although the M5S1 had an improved flexural resistance over the M5S0 specimen, significant deformation of the tension flange still existed, as noted by the asymmetric distribution of flange stresses; the M5S1 specimen was able to reach the gross plastic moment capacity, but only due to significant strain hardening of the tension flange.

A similar pattern was observed between the M5S2 (3 bolt rows, flange only

connection) and the M5S3 specimens (3 bolt rows, flange + web connections), where the inclusion of the web splice allowed a greater degree of participation of the web at the critical net section. It was noted that for the M5S2 and M5S3 specimens, the stress distribution of the web was not symmetric. Compressive web elements reached the yield strength to a higher degree than tensile web elements, suggesting that compressive web buckling could limit the actual resistance of the section in more realistic conditions. In general, however, the stress distribution along the web of the critical net section was not uniform, nor did it reach a stress state close to the ultimate strength as assumed by the Swanson Equation. This further confirmed that the assumed failure mechanism of the Swanson Equation was divorced from the true failure material behaviour for bolted W-sections under flexure.

Without further investigation, it is difficult to evaluate or recommend the Swanson Equation for general use when determining the flexural capacity of a reduced flange area W-section. On one hand, a wide range of sections with reduced flange areas are capable of reaching the overall gross plastic moment, as observed by the M1-M12 specimens modelled during this research project. The Swanson Equation, with the highest allowable flexural capacity for typical section-connection combinations, would allow for structural steel designers to maximize the performance of bolted W-sections. On the other hand, the true failure mechanism does not align with the assumed mechanism of the Swanson Equation, as observed by the M5S specimens. Whether the compromise between a reflective design equation and additional allowable flexural performance would provide real-life benefits while maintaining the existing levels of design safety should be better understood by additional research.

Appendix B

Code

designtools.jl

```
function fourpoint_xy(force, a, l, x, E, I)
delta = force .*  a ./ (6 .* E .* I)
.* (3 .* l .* a .- 3 .* a^2 .- x^2 )
return (delta ./ 1e6)[1] #mm
end

function fourpoint_yx(delta, a, l, x, E, I)
force = (6 .* delta .* E .* I)
./ (a .* (3 .* l .* a .- 3 .* a^2 .- x^2 ))

return (force .* 1e3)[1] #kN
end

function bearing_res(sec_props, l_bearing,
fy; E = 200e3, interior = true, phi_bi = 0.80, phi_be = 0.75)
#input: section, yield strength
#if interior = true, this is a load point on the
#INTERIOR of the beam
#if false, this is a member end bearing support
h = sec_props.d .- (2 .* sec_props.t_f) #mm, web height
w = sec_props.t_w #mm, web thickness
t = sec_props.t_f #mm, flange thickness

web_slenderness = h ./ w

if (web_slenderness .>= 1100/sqrt(fy))[1]
```

```
println("Web slenderness limit reached. Bearing stiffeners required.")
return
end

if interior
println("Interior Load:")
#interior bearing resistance
N = l_bearing .+ 10 .* t

br_1 = (phi_bi .* w .* N .* fy / 1e3)[1]
#kN, web local plastic buckling
br_2 = (phi_bi .* 1.45 .* w.^2 .* sqrt(fy * E) ./ 1e3)[1]
#kN, web overall buck

println("Web local buckling resistance: " * string(br_1) * " kN")
println("Web overall buckling resistance: " * string(br_2) * " kN")
return min(br_1, br_2)

else
println("Member end support:")
#beam end bearing resistance
N = l_bearing .+ 4 .* t
br_1 = (phi_be .* w .* N .* fy / 1e3)[1]
#kN, web local plastic buckling
br_2 = (phi_be .* 0.60 .* w.^2 .* sqrt(fy * E) ./ 1e3)[1]
#kN, web overall buck

println("Web local buckling resistance: " * string(br_1) * " kN")
println("Web overall buckling resistance: " * string(br_2) * " kN")
return min(br_1, br_2)
end
end

function comp_resistance(area, fy, ry, k, L; E = 200e3, phi = 0.90, n = 1.34)
lambda = k .* L ./ ry .* sqrt.(fy ./ pi^2 ./ E)

return (phi .* area .* fy .* (1 .+ lambda.^(2n)).^(-1 ./ n) ./ 1e3)[1]
end


function bearing_stiffener_res(sec_props, t_stiffener, d_stiffener,
```

```
fy; phi = 0.9, n_stiffeners = 1.0, k = 0.75, E = 200e3, interior = true)

#check stiffener dimension is within flange width:
d_max = (sec_props.b_f .- sec_props.t_w) ./ 2

if (d_stiffener .> d_max)[1]
println("Bearing stiffeners extend past flange.")
println("Max. stiffener depth = " * string(d_max) *" mm.")
return
end

#web height
h_w = sec_props.d .- (2 .* sec_props.t_f)

#slenderness limit check
stiff_slenderness = d_stiffener ./ t_stiffener
if (stiff_slenderness .>= (200 / sqrt(fy)))[1]
println("Stiffener too slender. Revise.")
return
end

#web area
if interior
b_web = 25 .* (sec_props.t_w) .- t_stiffener
a_web = 25 .* (sec_props.t_w).^2
else
b_web = 12 .* (sec_props.t_w) .- t_stiffener
a_web = 12 .* (sec_props.t_w).^2
end

#total effective area
a_total = a_web .+ (d_stiffener .* t_stiffener) .* 2 .* n_stiffeners

#moment of inertia
#stiffener
d_stiff = 2 .* d_stiffener .+ sec_props.t_w
b_stiff = t_stiffener

#web
d_web = sec_props.t_w
#b_Web is defined above
```

```
I = n_stiffeners .* (b_stiff .* d_stiff.^3) ./ 12 +
(b_web .* d_web.^3) ./ 12

#radius of gyration
r = sqrt.(I ./ a_total)

comp1 = comp_resistance(a_total, fy, r, k, h_w, phi = phi)

comp2 = 2 *  (1.5 * phi * d_stiffener * t_stiffener * fy / 1e3)

comp = min(comp1, comp2)

println("Bearing resistance: " * string(comp) * " kN")
return comp[1]
end

function init_plate_sizer(sec_props, m_p_nominal, fy_p)

#input the gross plastic moment of a section,
#returns the required exterior plate thickness to transfer the moment as
#a force couple.
#this function ignores the contribution of the interior plates.
typ_thickness = [6.35, 12.7, 16, 19, 20, 22,
22.2, 24, 25.4, 27, 28.6, 30, 31.8, 36, 38.1]


for thickness in typ_thickness
force = thickness .* sec_props.b_f .* fy_p ./ 1e3 #yield force

moment = force .* (sec_props.d .+ thickness) ./ 1e3 #kNm

if (moment .>= m_p_nominal)[1]
ratio = moment ./ m_p_nominal
println("Plate thickness of ",
thickness, "mm provides ",
ratio .* 100, "% of required gross plastic moment.")
return thickness[1]
break
end
end
```

```
println("Thickness must exceed 38.1mm.")
return
end

function init_plate_sizer2(sec_props, d_b, gauge, fy_beam, fy_plate, fu_plate;
tol = 0, n_rows = 2)

#input the gross plastic moment of a section,
#returns the required exterior plate thickness to transfer the moment as
#a force couple.

#Typical thicknesses of steel plates
typ_thickness = [6.35, 12.7, 16, 19, 20, 22,
22.2, 24, 25.4, 27, 28.6, 30, 31.8, 36, 38.1, 50.8]

#determine max gross capacity of beam section
m_plastic = plastic_moment(sec_props, fy_beam) #kNm

#force in flange required to be transmitted by plates
flange_force = moment2force(sec_props, m_plastic) #kN

#force is split in half between interior and exterior plates
plate_force = flange_force ./ 2 #kN

exterior_force = 2 .* plate_force
interior_force = plate_force

#design exterior plate
for thickness in typ_thickness
ext_gross = thickness .* sec_props.b_f #mm^2
ext_net = ext_gross .- ((d_b .+ tol) .* thickness) .* n_rows #mm^2

ext_gross_yield = ext_gross .* fy_plate ./ 1e3
ext_net_frac = ext_net .* fu_plate ./ 1e3

ext_critical = min(ext_gross_yield, ext_net_frac)

if (ext_critical .>= exterior_force)[1]
ratio = ext_critical ./ exterior_force .* 100
println("Exterior Plate Thickness of ", thickness, "mm provides ",
ratio, "% of required force.")
```

```
ext_thickness = thickness
break
end
end


#design interior plate
for thickness in typ_thickness
int_gross = thickness .* (sec_props.b_f ./ 2 .- sec_props.k_1)
int_net = int_gross .- ((d_b .+ tol) .* thickness) .* (n_rows ./ 2)

int_gross_yield = int_gross .* fy_plate ./ 1e3
int_net_frac = int_net .* fu_plate ./ 1e3

int_critical = min(int_gross_yield, int_net_frac)

if (int_critical .>= interior_force)[1]
ratio = int_critical ./ interior_force .* 100
println("Interior Plate Thickness of ", thickness, "mm provides ",
ratio, "% of required force.")
int_thickness = thickness
break
end
end


return ext_thickness[1], int_thickness[1]
end

function Vr_weld(sec_props, t_stiff, Xu, Fu, D, L; phi_w = 0.67)
#Defined Properties
t1 = t_stiff
t2 = max(t1, sec_props.t_w[1])
#Maximum Weld Size
if t1 <= 6
D_max = t1
else
D_max = t1 - 2
end
#minimum Weld Size
if t2 <= 12
```

```
D_min = 5
elseif 12 < t2 <= 20
D_min = 6
else
D_min = 8
end
#Minimum weld length
L_min = max(40, 4 * D)

#check limits

if D < D_min || D > D_max
println("Revise Weld Size")
return
end

if L < L_min
println("Increase weld length.")
return
end

#Weld Metal Fracture
Vr_weld =  0.67 * phi_w * 0.707 * D * L * Xu / 1e3

#Base Metal Fracture
Vr_base = 0.67 * phi_w * D * L * Fu / 1e3

return min(Vr_weld, Vr_base)
end

function weld_size_finder(P, sec_props, t_stiff, Xu, Fu, L; phi_w = 0.67)

D1 = P / (0.67 * phi_w * 0.707 * L * Xu / 1e3)
D2 = P / (0.67 * phi_w * L * Fu / 1e3)

D = max(D1, D2)

t1 = t_stiff
t2 = max(t1, sec_props.t_w[1])
#Maximum Weld Size
if t1 <= 6
```

```
D_max = t1
else
D_max = t1 - 2
end
#minimum Weld Size
if t2 <= 12
D_min = 5
elseif 12 < t2 <= 20
D_min = 6
else
D_min = 8
end
#Minimum weld length
L_min = max(40, 4 * D)

#check limits

if D < D_min
D = D_min
elseif D > D_max
D = D_max
end

if L < L_min
println("Increase weld length.")
return
end

println("Minimum Weld Size: " * string(D))
return Vr_weld(sec_props, t_stiff, Xu, Fu, D, L; phi_w = phi_w), D
end
```

exploretools.jl

```
using Plots
using DataFrames
using CSV
pyplot()
```

```
W_data = CSV.read("W.csv")

function name2data(section_name)
#input a section name as a string (eg. "W460X19"),
#returns all section properties of that section
#as a database to then be called

#out_frame is the 1 dimensional data frame for all section
#info for the section = section_name
out_frame = W_data[W_data[1:end, :name] .== section_name, :]

#first two columns are redundant and are removed for output
out_frame = out_frame[:, 3:end]

#Output relevant 1 dimensional dataframe
return out_frame
end

function plastic_moment(sec_props, yield_strength; phi = 1.0)
#input is one row dataframe of a given section + material yield strength
#returns the theoretical plastic moment capacity (Z x Fy)
return phi * (sec_props.Z_x  * yield_strength ./ 1e3)[1]
end

function yield_moment(sec_props, fy; phi = 1.0)
#returns the moment corresponding to the first instance where the
#extreme tension (and compression) fibres reach Fy

return (sec_props.S_x .* fy ./ 1e3)[1]
end

function net_plastic_modulus(sec_props, d_b, n_bolts; tol = 0)
#returns approximate (ignoring K-curve area) plastic modulus
#of a given section with reduced flange areas from bolt holes


hole_area = (d_b + tol) * sec_props.t_f[1]
centroid_distance = (sec_props.d[1] - sec_props.t_f[1]) / 2

z_negative = 2 * n_bolts * hole_area * centroid_distance
```

```
Z_final = sec_props.Z_x[1] * 1e3 - z_negative

return (Z_final ./ 1e3)
end

function netIx(sec_props, d_b; tol = 0, n_rows = 2)
#Calculating the net moment of Inertia due to bolt holes
#Via NEGATIVE areas of bolt holes & parallel axis theorem

gross_Ix = sec_props.I_x[1] * 1e6

d_centroid = (sec_props.d[1] - sec_props.t_f[1]) / 2
#Distance from center of section to center of flange

db = d_b + tol

A_bolt = db * sec_props.t_f[1]
bolt_Ix = db * sec_props.t_f[1]^3 / 12

bolt_reduction = 2 * n_rows * (bolt_Ix + A_bolt * d_centroid^2)

net_Ix = gross_Ix - bolt_reduction

return net_Ix
end

function netSx(sec_props, d_b; tol = 0, n_rows = 2)

y= sec_props.d[1] / 2

return netIx(sec_props, d_b; tol = tol, n_rows = n_rows) / y
end

function net_yield_moment(sec_props, d_b, fy;
tol = 0, phi = 1.0, n_rows = 2)
y = sec_props.d[1] / 2

net_sx = netIx(sec_props, d_b; tol = tol, n_rows = n_rows) / y

return phi * net_sx * fy / 1e6
end
```

```
function s16_14_1(sec_props, d_b, fy; disp = true,
n_rows = 2, tolerance = 0, phi = 1.0)
gross_flange_area = sec_props.b_f .* sec_props.t_f

area_loss = sec_props.t_f .* (d_b + tolerance) .* n_rows

net_area = gross_flange_area .- area_loss
ratio = (net_area ./ gross_flange_area)[1]
net_zx = net_plastic_modulus(sec_props, d_b,
n_rows; tol = tolerance)
net_plastic_moment = phi * net_zx .* fy ./ 1e3 #kNm
if (ratio .< 0.85)[1]
if disp
println("85% rule triggered. Net properties should be used.")
end
return true, ratio, net_zx, net_plastic_moment
else
if disp
println("85% rule not triggered. Gross section properties OK.")
end
return false, ratio, net_zx, net_plastic_moment
end
end

function edge_distance(sec_props, d_b, gauge)
#returns edge distance of given section + connection gauge
edge = (sec_props.b_f .- gauge) ./ 2
return edge[1]
end

function geo_limits(sec_props, d_b, n_bolts)
#where n_bolts is IN THE DIRECTION OF LOADING

pitch_min = 2.7 * d_b #mm

#minimum edge distances corresponding to bolt diameter
bolt_sizes = 25.4 .* [5/8 3/4 7/8 1 1.125 1.25] #mm
edge_limits = [28 32 38 44 51 57] #mm
idx = findfirst(x -> (x - d_b) >= 0, bolt_sizes)[2]
```

```
edge_min = edge_limits[idx]

#minimum end distance
if n_bolts > 2
end_min = edge_min
else
end_min = 1.5 * d_b
end


#Determine gauge limits (EXTREMELY CONSERATIVE DUE TO k_1)
gauge_min = 2 * (sec_props.k_1[1] + edge_min)

# println("Minimum values for [pitch edge end] distances (mm)")
return [pitch_min edge_min end_min]
end

function geo_comparison(design, minimums)
#input is: [PITCH EDGE END]
#compares design geometry to s16 limits

comp = design .> minimums #outputs array of booleans

pitch_check = comp[1]
edge_check = comp[2]
end_check = comp[3]

if all(value -> value == true, comp)
println("Bolt hole geometry limits satisfied. Design OK.")
return true
else
println("Bolt hole geometry limits not satisfied. Revise.")
println("Minimum [pitch edge end] = ",
minimums, " ; Design = ", design)
return false
end
end

function net_flange_area(sec_props, d_b;
n_rows = 2, tolerance = 0)
```

```
# define hole size
d = d_b + tolerance

#gross flange area
gross = sec_props.b_f .* sec_props.t_f #mm^2

#loss of area due to holes
loss = sec_props.t_f .* d .* n_rows #mm^2

return (gross .- loss)[1] #mm^2
end

function s16_block_strength(sec_props, d_b, fy, fu, end_dist,
pitch, gauge, n_bolts;
disp = true, phi_u = 1.0, ut = 1.0, tolerance = 0)

#d_b = bolt diameter
#fy, fu = material strengths
#end_dist = dist from end center of hole to free end of section
#edge_dist = dist from center of hole to section edge
#pitch = distance between bolts parallel to load
#gauge - distance between bolts perp. to load (across the web)
#n_bolts = number of bolts in one line

#define hole size
d = d_b .+ tolerance
#Determine connection length l_c
l_c = end_dist + pitch * (n_bolts -1)

#Edge fracture
net_fracture1 = (sec_props.b_f .- gauge .- d) .* sec_props.t_f
gross_shear1 = 2 * l_c .* sec_props.t_f

#Center fracture
net_fracture2 = (gauge .- d) .* sec_props.t_f #mm^2
gross_shear2 = 2 * l_c .* sec_props.t_f .+ l_c .* sec_props.t_w #mm^2

#gross shear strength
if fy > 460
shear_strength = fy
else
```

```
shear_strength = 0.5 * (fy + fu)
end

#Find forces for each component
tension1 = (ut * fu) .* net_fracture1 ./ 1e3
tension2 = (ut * fu) .* net_fracture2 ./ 1e3

shear1 = gross_shear1 .* shear_strength .* 0.6 ./ 1e3
shear2 = gross_shear2 .* shear_strength .* 0.6 ./ 1e3

block1 = tension1 .+ shear1
block2 = tension2 .+ shear2

#Return critical capacity
if (block1 .< block2)[1]
if disp
println("Edge block shear governs.")
end
return (phi_u .* block1)[1] #kN
else
if disp
println("Center block shear governs.")
end
return (phi_u .* block2)[1] #k
end
end

function s16_edgeblock(sec_props, d_b, fy, fu, end_dist,
pitch, gauge, n_bolts;
disp = true, phi_u = 1.0, ut = 1.0, tolerance = 0)

#d_b = bolt diameter
#fy, fu = material strengths
#end_dist = dist from end center of hole to free end of section
#edge_dist = dist from center of hole to section edge
#pitch = distance between bolts parallel to load
#gauge - distance between bolts perp. to load (across the web)
#n_bolts = number of bolts in one line

#define hole size
d = d_b .+ tolerance
```

```
#Determine connection length l_c
l_c = end_dist + pitch * (n_bolts -1)

#Edge fracture
net_fracture1 = (sec_props.b_f .- gauge .- d) .* sec_props.t_f
gross_shear1 = 2 * l_c .* sec_props.t_f

#gross shear strength
if fy > 460
shear_strength = fy
else
shear_strength = 0.5 * (fy + fu)
end

#Find forces for each component
tension1 = (ut * fu) .* net_fracture1 ./ 1e3

shear1 = gross_shear1 .* shear_strength .* 0.6 ./ 1e3

block1 = tension1 .+ shear1

return (phi_u .* block1)[1] #kN
end

function s16_complete(sec_props, d_b, fy, fu, end_dist,
pitch, n_bolts; n_rows = 2, phi_u = 1.0, ut = 1.0, tolerance = 0)

d = d_b .+ tolerance
#Determine connection length l_c
l_c = end_dist + pitch * (n_bolts -1)

#net fracture area
net_fracture = sec_props.t_f[1] * (sec_props.b_f[1] - n_rows * d)
#gross shear area
gross_shear = sec_props.t_w[1] * l_c

#gross shear strength
if fy > 460
shear_strength = fy
else
shear_strength = 0.5 * (fy + fu)
```

```
end

tension = (ut * fu) .* net_fracture ./ 1e3

shear = gross_shear .* shear_strength .* 0.6 ./ 1e3

block = tension .+ shear

return (phi_u .* block)[1] #kN
end

function s16_centerblock(sec_props, d_b, fy, fu, end_dist,
pitch, gauge, n_bolts;
disp = true, phi_u = 1.0, ut = 1.0, tolerance = 0)

#d_b = bolt diameter
#fy, fu = material strengths
#end_dist = dist from end center of hole to free end of section
#edge_dist = dist from center of hole to section edge
#pitch = distance between bolts parallel to load
#gauge - distance between bolts perp. to load (across the web)
#n_bolts = number of bolts in one line

#define hole size
d = d_b .+ tolerance
#Determine connection length l_c
l_c = end_dist + pitch * (n_bolts -1)

#Center fracture
net_fracture2 = (gauge .- d) .* sec_props.t_f #mm^2
gross_shear2 = 2 * l_c .* sec_props.t_f .+ l_c .* sec_props.t_w #mm^2

#gross shear strength
if fy > 460
shear_strength = fy
else
shear_strength = 0.5 * (fy + fu)
end

#Find forces for each component
tension2 = (ut * fu) .* net_fracture2 ./ 1e3
```

```
shear2 = gross_shear2 .* shear_strength .* 0.6 ./ 1e3

block2 = tension2 .+ shear2

return (phi_u .* block2)[1] #kN
end

function force2moment(sec_props, flange_force)
#flange force should be in kN
return (sec_props.d - sec_props.t_f)[1] .* flange_force[1] ./1e3 #kNm
end

function moment2force(sec_props, moment)
#moment in kNm
return ((moment .* 1e3) ./ (sec_props.d .- sec_props.t_f))[1] #kN
end

function net_moment_inertia(sec_props, d_b, n_bolts; tol = 0)
I_initial = sec_props.I_x .* 1e6 #mm^4

#Define hole size d
d = d_b .+ tol #mm
chr
#define the moment of inertia of the missing areas
I_bolt = d .* sec_props.t_f.^3 ./ 12 #mm^4
A_bolt = d .* sec_props.t_f #mm^2

# distance of hole areas to centroid of section
bolt_to_centroid = (sec_props.d .- sec_props.t_f) ./ 2

#Reduction of I_initial via parallel axis theorem
I_reduction = n_bolts .* (I_bolt .+ (A_bolt .* bolt_to_centroid.^2))

#Final net moment of inertia
I_final = I_initial .- I_reduction

return (I_final ./ 1e6)[1]
end

function section_overview(section_name, d_b, end_dist, fy, fu,
```

```
pitch, gauge, n_bolts;
phi = 1.0, phi_u = 1.0, tol = 0, disp_plots = true)
println("For " * section_name * ": ")
section = name2data(section_name)
#output theoretical full section moment resistance
mp_gross = plastic_moment(section, fy; phi = phi)
m_y = yield_moment(section, fy; phi = phi)

#check on 85% rule
redux, ratio, net_zx, net_plastic_moment =
s16_14_1(section, d_b, fy;
phi = phi, tolerance = tol)

#Theoretical net yield (elastic) moment
m_y_net = net_yield_moment(section, d_b, fy;
tol = tol, phi = phi)

#check geo limits
edge = edge_distance(section, d_b, gauge)
#array of relevant connection geometry
connex_geo = [pitch edge end_dist]
#array of minimum distances required by s16 standard
connex_limits = geo_limits(section, d_b, 2)
#evaluation of design and required connection‘ geometry
geo_pass = geo_comparison(connex_geo, connex_limits)

#moment resistances

#All block shear components
edgeblock = s16_edgeblock(section, d_b, fy,
fu, end_dist, pitch, gauge, n_bolts;
phi_u = phi_u, tolerance = tol)
edgeblock_moment = force2moment(section, edgeblock)

centerblock = s16_centerblock(section, d_b, fy,
fu, end_dist, pitch, gauge, n_bolts;
phi_u = phi_u, tolerance = tol)
centerblock_moment = force2moment(section, centerblock)

completeblock = s16_complete(section, d_b, fy,
fu, end_dist, pitch, n_bolts; phi_u = phi_u,
```

```
tolerance = tol)
completeblock_moment = force2moment(section,
completeblock)

#output results
connex_length = end_dist + pitch * (n_bolts - 1)


##CRITICAL LENGTH##

l_c_prime = lc_crit_finder(section, fy, fu, d_b, gauge;
tol = tol)

pitch_prime = (l_c_prime - end_dist) / (n_bolts - 1)

######
output_dataframe = DataFrame(Section = section_name,
BoltDiameter = d_b,
HoleTolerance = tol,
EndDistance = end_dist,
Pitch = pitch,
Gauge = gauge,
N_bolts = n_bolts,
ConnectionLength = connex_length,
CriticalLength = l_c_prime,
CriticalPitch = pitch_prime,
F_y = fy,
F_u = fu,
phi = phi,
phi_u = phi_u,
s16_14_1_trigger = redux,
NetZx = net_zx,
NetPlasticMoment = net_plastic_moment,
NetGrossRatio = ratio,
GrossPlasticMoment = mp_gross,
ElasticMoment = m_y,
NetElasticMoment = m_y_net,
CompleteBlockMoment = completeblock_moment,
EdgeBlockMoment = edgeblock_moment,
CenterBlockMoment = centerblock_moment)
```

```
#Bar plots for moments

#concatenate the different section moment capacities
moment_recap = vcat(output_dataframe.GrossPlasticMoment,
output_dataframe.NetPlasticMoment,
output_dataframe.ElasticMoment,
output_dataframe.NetElasticMoment,
output_dataframe.CompleteBlockMoment,
output_dataframe.EdgeBlockMoment,
output_dataframe.CenterBlockMoment)

#labels for each moment type
moment_names = ["Gross Plastic",
"Net Plastic",
"Elastic",
"Net Elastic",
"Complete Block",
"Edge Block",
"Center Block"]

#display plot
if disp_plots
sec_plot = bar(moment_names,moment_recap,
xrotation = 15,
ylabel = "Moment (kNm)",
title = "Section Moment Capacity Summary: " * section_name,
legend = false)

return sec_plot, output_dataframe
else
return output_dataframe
end
end

function max_pitch_finder(sec_props, db, fy, fu,
min_end, min_pitch, min_gauge, n_bolts;
factor = 1.0, tol = 0, disp = false)

global pitch_temp = min_pitch
global block_temp = 0
```

```
plastic_force = moment2force(sec_props,
plastic_moment(sec_props, fy))

while block_temp < factor * plastic_force
block_temp = s16_block_strength(sec_props,
db,
fy,
fu,
min_end,
pitch_temp,
min_gauge,
n_bolts;
disp = false)

pitch_temp += 5
end
return pitch_temp
end

function matrix_blockshear(sec_props, db, fy, fu,
endrange, pitchmatrix, gaugematrix, n_bolts, tol)

L = length(endrange)

main_matrix = Matrix[]

#For every valid value of the end distance,
#of pitch and gauge
for k = 1:L
matrix = [force2moment(sec_props,
s16_block_strength(sec_props, d_b, fy, fu, endrange[k],
pitchmatrix[i, j], gaugematrix[i, j],
n_bolts; tolerance = tol, disp = false))
for i = 1:L, j = 1:L]

push!(main_matrix, matrix)
end
return main_matrix
end

function target_moment_matrix(target, dim)
```

```
#given the target in kNm:

base = ones(dim, dim)

return base .* target
end

function edge_bs_matrix(sec_props, db, fy, fu,
endrange, pitchmatrix, gaugematrix, n_bolts;
phi_u = 1.0, tol = 0)

L = length(endrange)

main_matrix = Matrix[]

for k = 1:L
matrix = [force2moment(sec_props,
s16_edgeblock(sec_props, d_b, fy, fu, endrange[k],
pitchmatrix[i,j], gaugematrix[i,j],
n_bolts; phi_u = phi_u,
tolerance = tol, disp = false)) for i = 1:L, j = 1:L]

push!(main_matrix, matrix)
end
return main_matrix
end

function center_bs_matrix(sec_props, db, fy, fu,
endrange, pitchmatrix, gaugematrix, n_bolts;
phi_u = 1.0, tol = 0)

L = length(endrange)

main_matrix = Matrix[]

for k = 1:L
matrix = [force2moment(sec_props,
s16_centerblock(sec_props, d_b, fy, fu, endrange[k],
pitchmatrix[i,j], gaugematrix[i,j],
n_bolts; phi_u = phi_u, tolerance = tol,
disp = false)) for i = 1:L, j = 1:L]
```

```
push!(main_matrix, matrix)
end
return main_matrix
end

function complete_matrix(sec_props, db, fy, fu,
endrange, pitchmatrix, n_bolts; tol = 0)

L = length(endrange)

main_matrix = Matrix[]
for k = 1:L
matrix = [force2moment(sec_props,
s16_complete(sec_props, db, fy, fu, endrange[k],
pitchmatrix[i,j], n_bolts;
tolerance = tol)) for i = 1:L, j = 1:L]

push!(main_matrix, matrix)
end
return main_matrix
end

function critical_matrix(edge, center, net)

L = length(edge)

main_matrix = Matrix[]

for k = 1:L
matrix = [min(edge[k][i,j], center[k][i,j],
net[k][i,j]) for i = 1:L, j = 1:L]

push!(main_matrix, matrix)
end

return main_matrix
end

function geo_viewer(; section_name = "")
d = W_data.d
```

```
b = W_data.b_f
w = W_data.W

threed = scatter3d(d, b, w,
legend = false,
xlabel = "d (mm)",
ylabel = "b (mm)",
zlabel = "W (kg/m)",
color = :black,
camera = (10,10))

bw = scatter(b, w,
legend = false,
xlabel = "b (mm)",
ylabel = "W (kg/m)",
color = :black,
grid  = false)

dw = scatter(d, w,
legend = false,
xlabel = "d (mm)",
ylabel = "W (kg/m)",
color = :black,
grid = false)

bd = scatter(b, d,
legend = false,
xlabel = "b (mm)",
ylabel = "d (mm)",
color = :black,
grid = false)


if section_name != ""
sec = name2data(section_name)
sec_d = sec.d
sec_b = sec.b_f
sec_w = sec.W

scatter3d!(threed, [sec_d], [sec_b], [sec_w],
color = :red,
```

```
markersize = 10)

scatter!(bw, [sec_b], [sec_w],
color = :red,
markersize = 10)

scatter!(dw, [sec_d], [sec_w],
color = :red,
markersize = 10)

scatter!(bd, [sec_b], [sec_d],
color = :red,
markersize = 10)
end


twod = plot(dw, bw, layout = (1,2))

allthree = plot(threed, twod, layout = grid(2,1,
heights = [0.8, 0.2]), size = (800, 800))

fours = plot(bd, threed, dw, bw, layout = (2,2),
size = (1000,600))

return fours
end

function geo_viewer2(d, b, w; section_name = "")
d1 = W_data.d
b1 = W_data.b_f
w1 = W_data.W

threed = scatter3d(d1, b1, w1,
legend = false,
xlabel = "d (mm)",
ylabel = "b (mm)",
zlabel = "W (kg/m)",
color = :black,
camera = (10,10))

bw = scatter(b1, w1,
```

```
legend = false,
xlabel = "b (mm)",
ylabel = "W (kg/m)",
color = :black,
grid  = false)

dw = scatter(d1, w1,
legend = false,
xlabel = "d (mm)",
ylabel = "W (kg/m)",
color = :black,
grid = false)

bd = scatter(b1, d1,
legend = false,
xlabel = "b (mm)",
ylabel = "d (mm)",
color = :black,
grid = false)


scatter3d!(threed, d, b, w,
legend = false,
xlabel = "d (mm)",
ylabel = "b (mm)",
zlabel = "W (kg/m)",
color = :red,
markersize = 10,
camera = (10,10))

scatter!(bw, b, w,
legend = false,
xlabel = "b (mm)",
ylabel = "W (kg/m)",
color = :red,
markersize = 10,
grid  = false)

scatter!(dw, d, w,
legend = false,
xlabel = "d (mm)",
```

```
ylabel = "W (kg/m)",
color = :red,
markersize = 10,
grid = false)

scatter!(bd, b, d,
legend = false,
xlabel = "b (mm)",
ylabel = "d (mm)",
color = :red,
markersize = 10,
grid = false)


twod = plot(dw, bw, layout = (1,2))

allthree = plot(threed, twod, layout = grid(2,1,
heights = [0.8, 0.2]), size = (800, 800))

fours = plot(bd, threed, dw, bw,
layout = (2,2), size = (1000,600))

return fours
end

function lc_crit_finder(sec_props, fy, fu, d_b, gauge;
tol = 0, u_ebs = 1.0, u_cbs = 1.0)

#Given the section properties, bolt size, and gauge
#Returns the critical length (l_c') where the
#theoretical EBS and CBS failure modes are equal
tf = sec_props.t_f[1]
tw = sec_props.t_w[1]
bf = sec_props.b_f[1]
dg = gauge
db = d_b + tol

if fy > 460
fv = 0.6 * fy
else
fv = 0.6 * (fy + fu) / 2
```

```
end

return (fu * tf) / (fv * (2tf - tw)) *
(bf * (u_cbs - u_ebs)
+ db * (u_ebs - 2*u_cbs) + u_ebs * dg)
end

function lc_crit_finder2(tf, tw, bf, dg, db,
fy, fu, d_b, gauge;
tol = 0, u_ebs = 1.0, u_cbs = 1.0)

if fy > 460
fv = 0.6 * fy
else
fv = 0.6 * (fy + fu) / 2
end

return (fu * tf) / (fv * (2tf - tw)) *
(bf * (u_cbs - u_ebs)
+ db * (u_ebs - 2*u_cbs) + u_ebs * dg)
end


function separator(fy; fu_bolt = 1050)
db_store = 25.4 .* [1/2, 3/4, 7/8, 1]
s16_14_matrix = Vector[]
fit_check = Vector[]

#for a given bolt diameter
for db = 1:length(db_store)
#bolt diameter of current iteration
bolt_diameter = db_store[db]
Ab = bolt_diameter^2 / 4 * pi
Fub = Ab * fu_bolt

#store array for s16_14.1 check
checkstore = []
fitstore = []
#for each section in the W_data dataframe:
for i = 1:size(W_data, 1)
#current section of iteration
```

```
secprop = W_data[i, :]

flangeforce = moment2force(secprop,plastic_moment(secprop, fy))
n_bolts_raw = flangeforce * 1e3 / 2 /
(0.6 * Fub) / 2
n_bolts = 2 * ceil(n_bolts_raw / 2)

#see if s16_14.1 passes
check, netzx, netmp = s16_14_1(secprop, bolt_diameter,
fy; disp = false, tolerance = 2)
#collect pass/fail information
push!(checkstore, check)

#minimum connection limits
pitch_min, edge_min, end_min = geo_limits(secprop,
bolt_diameter, n_bolts) #pitch/edge/end
gauge_min = 2 * (secprop.k_1[1] + edge_min)

if (secprop.b_f[1] - gauge_min) / 2 < edge_min
fit = false
else
fit = true
end
push!(fitstore, fit)


end
push!(s16_14_matrix, checkstore)
push!(fit_check, fitstore)
end
return s16_14_matrix, fit_check
end


function platedesign(sec_props, d_b, fy, fu, n_bolts;
n_rows = 2, tol = 0, factor = 1.2)


maxmoment = plastic_moment(sec_props, fy)
```

```
F = moment2force(sec_props, maxmoment)
F_ext = factor * F / 2
F_int = factor * F / 4

#bank of minimum thickness values
t_ext_store = []
t_int_store = []

#First minimum thickness is that of Factor X flange thickness
t_min = sec_props.t_f[1] * factor

push!(t_ext_store, t_min)
push!(t_int_store, t_min)

#second minimum thickness is of gross yield of the platedesign
t_ext1 = F_ext * 1e3 / (sec_props.b_f[1] * fy)

b_int = (sec_props.b_f[1] - 2 * sec_props.k_1[1]) / 2
t_int1 = F_int * 1e3 / (b_int * fy)

push!(t_ext_store, t_ext1)
push!(t_int_store, t_int1)

#Third minimum is the bearing failure of the plate
t_ext2 = F_ext * 1e3 /
(3 * 0.8 * n_bolts * n_rows * d_b * fu)
t_int2 = F_int * 1e3 /
(3 * 0.8 * n_bolts * n_rows * d_b * fu)

push!(t_ext_store, t_ext2)
push!(t_int_store, t_int2)

#net section rupture
t_ext3 = F_ext * 1e3 /
(sec_props.b_f[1] - n_rows * (d_b + tol)) / fu
t_int3 = F_int * 1e3 /
(b_int - n_rows / 2 * (d_b + tol)) / fu

push!(t_ext_store, t_ext3)
push!(t_int_store, t_int3)
```

```
return maximum(t_ext_store), maximum(t_int_store)
end
```

analysistools.jl

```
using CSV
using DataFrames
using Statistics

##For analysis of output files from Abaqus FE Analysis

function reportparser(rpt_file::String,
data_row; allowable_missing = 0.05)

#Import the base file, with all its issues
init_import = CSV.read(rpt_file,
header = false,
datarow = data_row,
delim = ' ',
ignorerepeated = true,
silencewarnings = true)


third_import = second_import[mean.(ismissing,
eachrow(second_import)) .< allowable_missing, :]

last_import = third_import[:,2:end]

#return the final cleaned value
return last_import

end


function failpoint_EBS(df, fy, fu; failure = true,
gen = false, fv = 0)
```

```
if gen

if fv == 0
println("ERR: fv is set to 0 MPa.")
return
end

shearyield = findfirst(x -> x >= fv, df.EBSS_GEN)
fracture = findfirst(x -> x >= fu, df.EBSF_GEN)

out = [shearyield, fracture]

if any(x -> x == nothing, out)
println("EBS Failure does not occur.")
return false
else
if failure
return max(shearyield, fracture)
else
return shearyield, fracture
end
end
end



shearyield = findfirst(x -> x >= fy, df.EBSS)
fracture = findfirst(x -> x >= fu, df.EBSF)

out = [shearyield, fracture]

if any(x -> x == nothing, out)
println("EBS Failure does not occur.")
return false
else
if failure
return max(shearyield, fracture)
else
return shearyield, fracture
end
```

```
end


end

function failpoint_CBS(df, fy, fu;
failure = true, gen = false, fv = 0)

if gen

if fv == 0
println("ERR: fv is set to 0 MPa.")
return
end

shearyield = findfirst(x -> x >= fv,
df.CBSS_GEN)
fracture = findfirst(x -> x >= fu,
df.CBSF_GEN)

out = [shearyield, fracture]

if any(x -> x == nothing, out)
println("CBS Failure does not occur.")
return false
else
if failure
return max(shearyield, fracture)
else
return shearyield, fracture
end
end

end

shearyield = findfirst(x -> x >= fy, df.CBSS)
fracture = findfirst(x -> x >= fu, df.CBSF)

out = [shearyield, fracture]

if any(x -> x == nothing, out)
```

```
println("CBS Failure does not occur.")
return false
else
if failure
return max(shearyield, fracture)
else
return shearyield, fracture
end
end

end
```

Jupyter Sample

W610X101_A: Failure in Edge Block Shear

Initializing julia functions required for analysis and design.

In [1]:

```
include("exploretools.jl")
include("designtools.jl")
```

Out[1]:

```
weld_size_finder (generic function with 1 method)
```

In [2]:

```
m5_geo = geo_viewer(; section_name = "W610X101")
```

Out[2]:

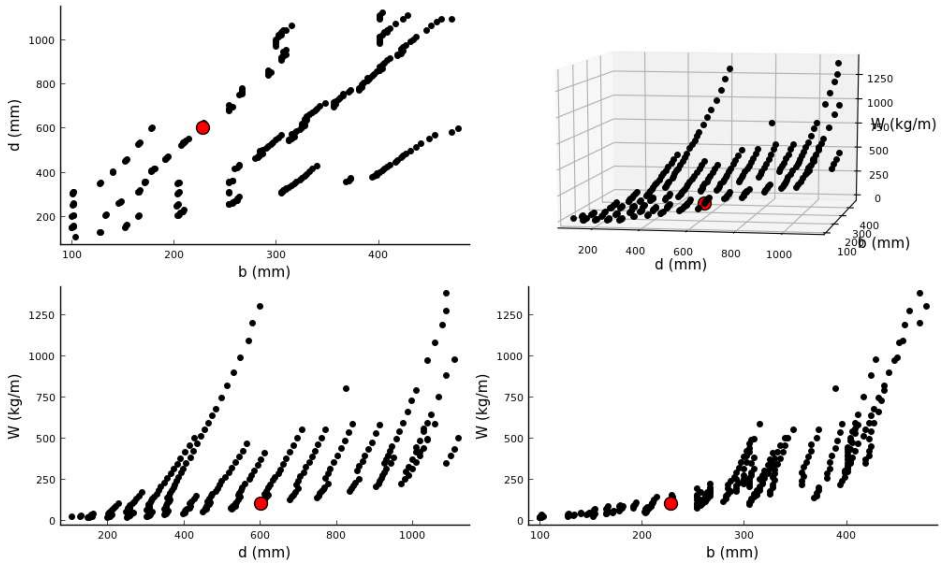

Initializing the section properties desired:

In [3]:

```
section = "W610X101"
sec_props = name2data(section)
```

Out[3]:

1 rows × 38 columns (omitted printing of 28 columns)

	W	A	d	d_det	b_f	b_fdet	t_w	t_wdet	t_wdet/2	t_f
	Float64	Int64	Int64	Int64	Int64	Int64	Float64	Float64	Float64	Float64
1	101.0	13000	602	603	228	229	10.5	11.1	6.35	14.9

Initializing connection details:

In [4]:

```
n_rows = 2
```

Out[4]:

```
2
```

Initializing material properties:

NOTE:

The true value of f_y is take from David Pizzuto's `T8` test specimen coupon data. However, the ultimate strength f_u is taken as the nominal value times the material factor r_y, since true engineering ultimate stress is difficult to derive from the *true* properties.

In [5]:

```
ry = 1.1
rt = 1.1

fy = 350 * ry #Mpa
fu = 460  #Mpa

fy_plate = fy #Mpa
fu_plate = fu #Mpa

fu_bolt = 1050 #Mpa
```

Out[5]:

```
1050
```

1: Maximum theoretical moment capacity

Determine the plastic moment and the elastic (just @ yield) moment of the section:

In [6]:

```
M_p = (plastic_moment(sec_props, fy))[1] #kNm
M_y = sec_props.S_x[1] * fy / 1e3 #kNm
```

Out[6]:

```
970.2000000000002
```

Design capacity

The detailing of the connection will be such that the moment end will fail at X% of M_p or M_y

In [7]:

```
X = 80 #%
M_des = X/100 * M_y
```

Out[7]:

```
776.1600000000002
```

Equivalent force in flange

The corresponding force in the flange with respect to M_{design} is determined:

In [8]:

```
F_des = moment2force(sec_props, M_des) #kN
```

Out[8]:

```
1322.0235053653555
```

2: Bolt Design

The effect of holes caused by bolt holes will be determined.

Bolt diameter + hole tolerance:

In [9]:

```
d_b = 25.4 * 7/8 #mm
tol = 2 #mm
```

Out[9]:

2

Effect on flange. Determine if the 85% rule clause will be triggered or not:

In [10]:

```
redux, ratio, Z_x_net, M_p_net = s16_14_1(sec_props, d_b, fy; tolerance = tol)

if M_p_net < M_des
    println("Warning: Net Plastic Moment less than design moment.")
end

A_flange_net = net_flange_area(sec_props, d_b; tolerance = tol)
```

```
85% rule triggered. Net properties should be used.
```

Out[10]:

2675.295

Determine number of bolts per row

Based on the shear strength of a single bolt, determine the required number of bolts.

Nominal strength of bolt, r_n is the minimum between the shank shear strength and the ultimate bearing resistance of the flange at the bolt hole:

In [11]:

```
A_b = (pi * d_b^2) / 4 #mm^2
F_nv = fu_bolt #Mpa
F_ub = fu #Mpa
t_f = sec_props.t_f[1] #mm

phi_b = 1.0

rn_1 = phi_b * 0.6 * F_nv * A_b / 1e3 #kN
rn_2 = 2.4 * F_ub * d_b * t_f / 1e3 #kN

rn = min(rn_1, rn_2)
```

Out[11]:

244.40718562093363

Determining the total number of bolts required per row:

Note that since inner splice plates will be used, the bolts will **not** be under single-shear loading. However, since the distance of the shear plane from the neutral axis will differ, the shear stresses in each shear plane should maybe not be considered even.

The value is rounded up to the nearest ***even*** integer.

In [12]:

```
shearplanes = 2
```

Out[12]:

2

In [13]:

```
n_bolts_tot = Int(ceil(F_des / rn / shearplanes))

n_bolts_float = n_bolts_tot / 2
n_bolts = 2 * ceil(n_bolts_tot / 2) / 2

if n_bolts < 2.0
    n_bolts = 2.0
end

n_bolts
```

Out[13]:

2.0

3: Connection Limits

The connection geometry limits as a function of the section geometry and the bolt size is determined:

S16-14 minimum limits:

The S16 sets minimum limits for pitch, edge, and end distances.

The minimum *gauge* is s.t. the bolt hole (including tolerance) does not encroach on the curved K-area of the section.

In [14]:

```
pitch_min, edge_min, end_min = geo_limits(sec_props, d_b, n_bolts) #pitch/edge/end

gauge_min = 2 * (sec_props.k_1[1] + edge_min)
gauge_max = sec_props.b_f[1] .- 2 .* edge_min

end_max = (12 .* sec_props.t_f)[1]
```

Out[14]:

```
178.8
```

For a more realistic maximum end distance, set a hard limit (~5 inches)

In [15]:

```
end_max = 5 * 25.4
```

Out[15]:

```
127.0
```

Verify the possibility of a center block shear failure mode:

In [16]:

```
maximum_edge = s16_edgeblock(sec_props, d_b, fy, fu, end_min, pitch_min, gauge_min, n_bolt
s; tolerance = tol)
minimum_center = s16_centerblock(sec_props, d_b, fy, fu, end_min, pitch_min, gauge_min, n_
bolts; tolerance = tol)

if maximum_edge < minimum_center
    println("Center Block Shear Impossible")
else
    println("Center Block Shear theoretically possible")
end
```

```
Center Block Shear Impossible
```

Determine if section is theoretically too narrow for *any* bolts:

In [17]:

```
if (sec_props.b_f[1] - gauge_min) / 2 < edge_min
    println("Section too narrow for bolts. Revise.")
else
    println("Flange width sufficient.")
end
```

```
Flange width sufficient.
```

Maximum pitch:

There is no set limit on the maximum pitch allowed for bolts. The maximum pitch is instead defined as the pitch at which the block shear resistance of the connection configuration matches that of the gross plastic moment (the theoretical highest moment possible in the beam).

In [18]:

```
max_pitch = max_pitch_finder(sec_props, d_b, fy, fu, end_min, pitch_min, gauge_min, n_bolt
s; tol = tol)
```

Out[18]:

```
175.0075
```

4: Connection Design

The three design variables for the connection are: bolt pitch, gauge, and end distance. The design space of these variables is first explored.

First, define `increment`, the resolution between data points in the design space (mm).

In [19]:

```
increment = 6.35 #mm (1/4 inch)
```

Out[19]:

```
6.35
```

The design space will be carried by plotting all possible combinations of pitch/gauge/end and evaluating the resulting block shear moment to the desired block shear moment capacity.

The design space is created by:

The number of dimensions is based on the maximum range difference in the three design variables.

In [20]:

```
pitch_dif = max_pitch - pitch_min
gauge_dif = gauge_max - gauge_min
end_dif = end_max - end_min

dif_max = max(pitch_dif, gauge_dif, end_dif)
dif_n = Int(ceil(dif_max / increment))
```

Out[20]:

```
19
```

Each design variable range is turned into a linear space vector:

In [21]:

```
pitchrange = collect(range(pitch_min, stop = max_pitch, length = dif_n))
gaugerange = collect(range(gauge_min, stop = gauge_max, length = dif_n))
endrange = collect(range(end_min, stop = end_max, length = dif_n))
```

Out[21]:

```
19-element Array{Float64,1}:
  33.3375
  38.54097222222222
  43.74444444444445
  48.947916666666664
  54.15138888888889
  59.35486111111111
  64.55833333333334
  69.76180555555555
  74.96527777777777
  80.16875
  85.37222222222222
  90.57569444444445
  95.77916666666667
 100.98263888888889
 106.18611111111112
 111.38958333333333
 116.59305555555555
 121.79652777777778
 127.0
```

The pitch and gauge vectors are turned to equivalent matrices:

In [22]:

```
pitch_matrix = repeat(reshape(pitchrange, 1, :), length(pitchrange), 1)
gauge_matrix = repeat(gaugerange, 1, length(pitchrange))
```

Out[22]:

```
19×19 Array{Float64,2}:
 149.0    149.0    149.0    149.0    …  149.0    149.0    149.0    149.0
 149.167  149.167  149.167  149.167     149.167  149.167  149.167  149.167
 149.333  149.333  149.333  149.333     149.333  149.333  149.333  149.333
 149.5    149.5    149.5    149.5       149.5    149.5    149.5    149.5
 149.667  149.667  149.667  149.667     149.667  149.667  149.667  149.667
 149.833  149.833  149.833  149.833  …  149.833  149.833  149.833  149.833
 150.0    150.0    150.0    150.0       150.0    150.0    150.0    150.0
 150.167  150.167  150.167  150.167     150.167  150.167  150.167  150.167
 150.333  150.333  150.333  150.333     150.333  150.333  150.333  150.333
 150.5    150.5    150.5    150.5       150.5    150.5    150.5    150.5
 150.667  150.667  150.667  150.667  …  150.667  150.667  150.667  150.667
 150.833  150.833  150.833  150.833     150.833  150.833  150.833  150.833
 151.0    151.0    151.0    151.0       151.0    151.0    151.0    151.0
 151.167  151.167  151.167  151.167     151.167  151.167  151.167  151.167
 151.333  151.333  151.333  151.333     151.333  151.333  151.333  151.333
 151.5    151.5    151.5    151.5    …  151.5    151.5    151.5    151.5
 151.667  151.667  151.667  151.667     151.667  151.667  151.667  151.667
 151.833  151.833  151.833  151.833     151.833  151.833  151.833  151.833
 152.0    152.0    152.0    152.0       152.0    152.0    152.0    152.0
```

Mapping Failure Modes

The 3 design failure modes: *Edge block shear, Center block shear,* and *Complete (Net) block shear* are determined.

In [23]:

```
edgebs_matrix = edge_bs_matrix(sec_props, d_b, fy, fu, endrange, pitch_matrix, gauge_matri
x, n_bolts; tol = tol)
centerbs_matrix = center_bs_matrix(sec_props, d_b, fy, fu, endrange, pitch_matrix, gauge_m
atrix, n_bolts; tol = tol)
cbs_matrix = complete_matrix(sec_props, d_b, fy, fu, endrange, pitch_matrix, n_bolts; tol
= tol)
```

Out[23]:

```
19-element Array{Array{T,2} where T,1}:
 [868.378 878.362 … 1038.11 1048.09; 868.378 878.362 … 1038.11 1048.09; … ; 8
68.378 878.362 … 1038.11 1048.09; 868.378 878.362 … 1038.11 1048.09]
 [876.509 886.493 … 1046.24 1056.22; 876.509 886.493 … 1046.24 1056.22; … ; 8
76.509 886.493 … 1046.24 1056.22; 876.509 886.493 … 1046.24 1056.22]
 [884.641 894.625 … 1054.37 1064.35; 884.641 894.625 … 1054.37 1064.35; … ; 8
84.641 894.625 … 1054.37 1064.35; 884.641 894.625 … 1054.37 1064.35]
 [892.772 902.756 … 1062.5 1072.48; 892.772 902.756 … 1062.5 1072.48; … ; 89
2.772 902.756 … 1062.5 1072.48; 892.772 902.756 … 1062.5 1072.48]
 [900.904 910.888 … 1070.63 1080.62; 900.904 910.888 … 1070.63 1080.62; … ; 9
00.904 910.888 … 1070.63 1080.62; 900.904 910.888 … 1070.63 1080.62]
 [909.035 919.019 … 1078.76 1088.75; 909.035 919.019 … 1078.76 1088.75; … ; 9
09.035 919.019 … 1078.76 1088.75; 909.035 919.019 … 1078.76 1088.75]
 [917.167 927.151 … 1086.89 1096.88; 917.167 927.151 … 1086.89 1096.88; … ; 9
17.167 927.151 … 1086.89 1096.88; 917.167 927.151 … 1086.89 1096.88]
 [925.298 935.282 … 1095.03 1105.01; 925.298 935.282 … 1095.03 1105.01; … ; 9
25.298 935.282 … 1095.03 1105.01; 925.298 935.282 … 1095.03 1105.01]
 [933.43 943.414 … 1103.16 1113.14; 933.43 943.414 … 1103.16 1113.14; … ; 93
3.43 943.414 … 1103.16 1113.14; 933.43 943.414 … 1103.16 1113.14]
 [941.562 951.546 … 1111.29 1121.27; 941.562 951.546 … 1111.29 1121.27; … ; 9
41.562 951.546 … 1111.29 1121.27; 941.562 951.546 … 1111.29 1121.27]
 [949.693 959.677 … 1119.42 1129.41; 949.693 959.677 … 1119.42 1129.41; … ; 9
49.693 959.677 … 1119.42 1129.41; 949.693 959.677 … 1119.42 1129.41]
 [957.825 967.809 … 1127.55 1137.54; 957.825 967.809 … 1127.55 1137.54; … ; 9
57.825 967.809 … 1127.55 1137.54; 957.825 967.809 … 1127.55 1137.54]
 [965.956 975.94 … 1135.68 1145.67; 965.956 975.94 … 1135.68 1145.67; … ; 96
5.956 975.94 … 1135.68 1145.67; 965.956 975.94 … 1135.68 1145.67]
 [974.088 984.072 … 1143.82 1153.8; 974.088 984.072 … 1143.82 1153.8; … ; 97
4.088 984.072 … 1143.82 1153.8; 974.088 984.072 … 1143.82 1153.8]
 [982.219 992.203 … 1151.95 1161.93; 982.219 992.203 … 1151.95 1161.93; … ; 9
82.219 992.203 … 1151.95 1161.93; 982.219 992.203 … 1151.95 1161.93]
 [990.351 1000.33 … 1160.08 1170.06; 990.351 1000.33 … 1160.08 1170.06; … ; 9
90.351 1000.33 … 1160.08 1170.06; 990.351 1000.33 … 1160.08 1170.06]
 [998.482 1008.47 … 1168.21 1178.19; 998.482 1008.47 … 1168.21 1178.19; … ; 9
98.482 1008.47 … 1168.21 1178.19; 998.482 1008.47 … 1168.21 1178.19]
 [1006.61 1016.6 … 1176.34 1186.33; 1006.61 1016.6 … 1176.34 1186.33; … ; 100
6.61 1016.6 … 1176.34 1186.33; 1006.61 1016.6 … 1176.34 1186.33]
 [1014.75 1024.73 … 1184.47 1194.46; 1014.75 1024.73 … 1184.47 1194.46; … ; 1
014.75 1024.73 … 1184.47 1194.46; 1014.75 1024.73 … 1184.47 1194.46]
```

`crit_matrix` For each combination of pitch, gauge, and end, the minimum value from the three matrices above is the critical failure mode of the connection geometry:

In [24]:

```
crit_matrix = critical_matrix(edgebs_matrix, centerbs_matrix, cbs_matrix)
```

Out[24]:

```
19-element Array{Array{T,2} where T,1}:
 [634.411 662.746 … 1038.11 1048.09; 633.74 662.076 … 1038.11 1048.09; … ; 62
3.01 651.345 … 1038.11 1048.09; 622.339 650.674 … 1038.11 1048.09]
 [657.489 685.824 … 1046.24 1056.22; 656.818 685.154 … 1046.24 1056.22; … ; 6
46.088 674.423 … 1046.24 1056.22; 645.417 673.753 … 1046.24 1056.22]
 [680.567 708.903 … 1054.37 1064.35; 679.896 708.232 … 1054.37 1064.35; … ; 6
69.166 697.501 … 1054.37 1064.35; 668.495 696.831 … 1054.37 1064.35]
 [703.645 731.981 … 1062.5 1072.48; 702.974 731.31 … 1062.5 1072.48; … ; 692.
244 720.579 … 1062.5 1072.48; 691.573 719.909 … 1062.5 1072.48]
 [726.723 755.059 … 1070.63 1080.62; 726.052 754.388 … 1070.63 1080.62; … ; 7
15.322 743.657 … 1070.63 1080.62; 714.651 742.987 … 1070.63 1080.62]
 [749.801 778.137 … 1078.76 1088.75; 749.131 777.466 … 1078.76 1088.75; … ; 7
38.4 766.735 … 1078.76 1088.75; 737.729 766.065 … 1078.76 1088.75]
 [772.879 801.215 … 1086.89 1096.88; 772.209 800.544 … 1086.89 1096.88; … ; 7
61.478 789.814 … 1086.89 1096.88; 760.807 789.143 … 1086.89 1096.88]
 [795.957 824.293 … 1095.03 1105.01; 795.287 823.622 … 1095.03 1105.01; … ; 7
84.556 812.892 … 1095.03 1105.01; 783.885 812.221 … 1095.03 1105.01]
 [819.035 847.371 … 1103.16 1113.14; 818.365 846.7 … 1103.16 1113.14; … ; 80
7.634 835.97 … 1103.16 1113.14; 806.963 835.299 … 1103.16 1113.14]
 [842.114 870.449 … 1111.29 1121.27; 841.443 869.778 … 1111.29 1121.27; … ; 8
30.712 859.048 … 1111.29 1121.27; 830.042 858.377 … 1111.29 1121.27]
 [865.192 893.527 … 1119.42 1129.41; 864.521 892.856 … 1119.42 1129.41; … ; 8
53.79 882.126 … 1119.42 1129.41; 853.12 881.455 … 1119.42 1129.41]
 [888.27 916.605 … 1127.55 1137.54; 887.599 915.935 … 1127.55 1137.54; … ; 87
6.868 905.204 … 1127.55 1137.54; 876.198 904.533 … 1127.55 1137.54]
 [911.348 939.683 … 1135.68 1145.67; 910.677 939.013 … 1135.68 1145.67; … ; 8
99.946 928.282 … 1135.68 1145.67; 899.276 927.611 … 1135.68 1145.67]
 [934.426 962.761 … 1143.82 1153.8; 933.755 962.091 … 1143.82 1153.8; … ; 92
3.025 951.36 … 1143.82 1153.8; 922.354 950.689 … 1143.82 1153.8]
 [957.504 985.839 … 1151.95 1161.93; 956.833 985.169 … 1151.95 1161.93; … ; 9
46.103 974.438 … 1151.95 1161.93; 945.432 973.767 … 1151.95 1161.93]
 [980.582 1000.33 … 1160.08 1170.06; 979.911 1000.33 … 1160.08 1170.06; … ; 9
69.181 997.516 … 1160.08 1170.06; 968.51 996.846 … 1160.08 1170.06]
 [998.482 1008.47 … 1168.21 1178.19; 998.482 1008.47 … 1168.21 1178.19; … ; 9
92.259 1008.47 … 1168.21 1178.19; 991.588 1008.47 … 1168.21 1178.19]
 [1006.61 1016.6 … 1176.34 1186.33; 1006.61 1016.6 … 1176.34 1186.33; … ; 100
6.61 1016.6 … 1176.34 1186.33; 1006.61 1016.6 … 1176.34 1186.33]
 [1014.75 1024.73 … 1184.47 1194.46; 1014.75 1024.73 … 1184.47 1194.46; … ; 1
014.75 1024.73 … 1184.47 1194.46; 1014.75 1024.73 … 1184.47 1194.46]
```

`blockshear_matrix` takes the minimum between the edge and center block modes for any given value of pitch, gauge.

Visualizing the Design Space

The **complete** design space of pitch/gauge/end is plotted.

Note: the Z-axis is *not* the end distance. The end distance, however is implicitly linked (linear) to the Z-axis for any given combination of pitch and gauge.

In [25]:

```
title = "Connection Geometry Design Space: " * section

fig1 = surface(pitch_matrix, gauge_matrix, crit_matrix,
    title = title,
    xlabel = "Pitch (mm)",
    ylabel = "Gauge (mm)",
    zlabel = "Critical Moment Capacity (kNm)",
    legend = false,
    #color = :viridis,
    alpha = 0.5,
    markersize = 2,
    size = (800,800))

#cgradients() #use this function to see color map libraries available
```

Out[25]:

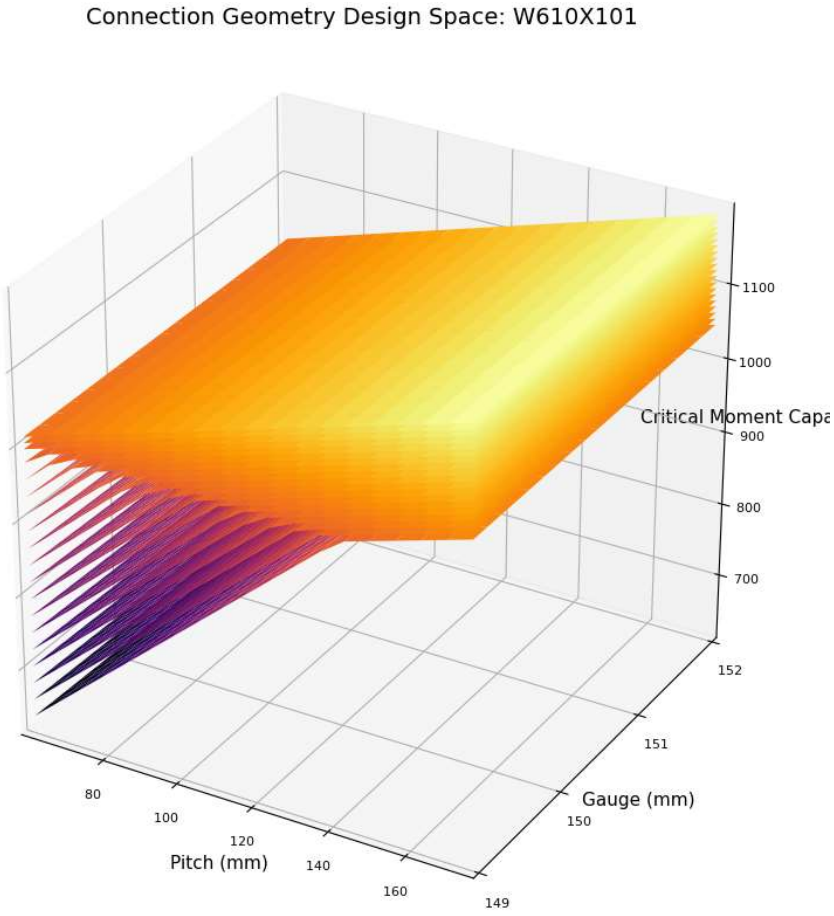
Connection Geometry Design Space: W610X101
Critical Moment Capa
1100
1000
900
800
700
80
100
120
140
160
Pitch (mm)
149
150
151
152
Gauge (mm)

Target Moment Values

The free design space is now compared to the target limits, namely the design space should consist only of combinations that incur a block shear moment capacity that is **LESS THAN**:

1. The Gross Plastic Moment M_p
2. The Elastic Moment M_y

and should approach:

1. The design target moment M_{des}

Define the moment capacity targets:

In [26]:

```
mdes_matrix = target_moment_matrix(M_des, length(endrange))
```

Out[26]:

```
19×19 Array{Float64,2}:
 776.16  776.16  776.16  776.16  776.16  …  776.16  776.16  776.16  776.16
 776.16  776.16  776.16  776.16  776.16     776.16  776.16  776.16  776.16
 776.16  776.16  776.16  776.16  776.16     776.16  776.16  776.16  776.16
 776.16  776.16  776.16  776.16  776.16     776.16  776.16  776.16  776.16
 776.16  776.16  776.16  776.16  776.16     776.16  776.16  776.16  776.16
 776.16  776.16  776.16  776.16  776.16  …  776.16  776.16  776.16  776.16
 776.16  776.16  776.16  776.16  776.16     776.16  776.16  776.16  776.16
 776.16  776.16  776.16  776.16  776.16     776.16  776.16  776.16  776.16
 776.16  776.16  776.16  776.16  776.16     776.16  776.16  776.16  776.16
 776.16  776.16  776.16  776.16  776.16     776.16  776.16  776.16  776.16
 776.16  776.16  776.16  776.16  776.16  …  776.16  776.16  776.16  776.16
 776.16  776.16  776.16  776.16  776.16     776.16  776.16  776.16  776.16
 776.16  776.16  776.16  776.16  776.16     776.16  776.16  776.16  776.16
 776.16  776.16  776.16  776.16  776.16     776.16  776.16  776.16  776.16
 776.16  776.16  776.16  776.16  776.16     776.16  776.16  776.16  776.16
 776.16  776.16  776.16  776.16  776.16  …  776.16  776.16  776.16  776.16
 776.16  776.16  776.16  776.16  776.16     776.16  776.16  776.16  776.16
 776.16  776.16  776.16  776.16  776.16     776.16  776.16  776.16  776.16
 776.16  776.16  776.16  776.16  776.16     776.16  776.16  776.16  776.16
```

In [27]:

```
surface!(pitch_matrix, gauge_matrix, mdes_matrix, color = :red)
```

Out[27]:

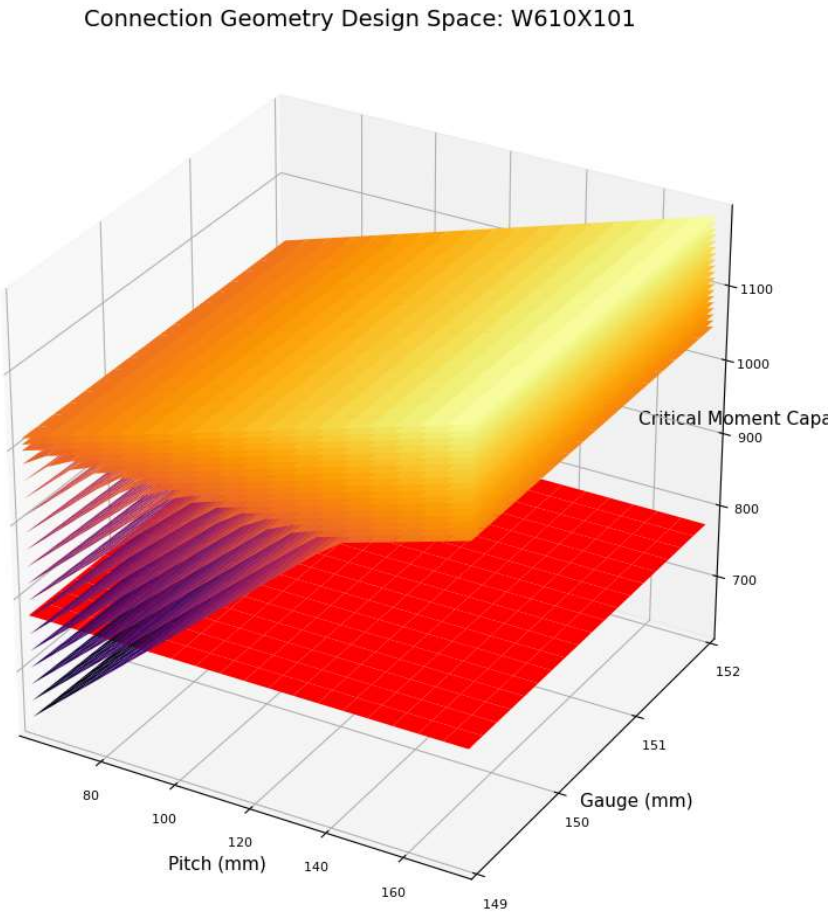

Extracting valid connection combinations

Find all combinations within X% of M_{des}

Narrow down the search results to combinations that are within a certain threshold of the target matrix.

In [28]:

```
pitch_close = Vector[]
gauge_close = Vector[]
block_close = Vector[]
end_close = []
X = 0.15 #IE 5% tolerance

for i = 1:dif_n
    idx = findall(x -> abs((x - M_des)) < X * M_des, crit_matrix[i])

    if size(pitch_matrix[idx])[1] != 0
        push!(pitch_close, pitch_matrix[idx])
        push!(gauge_close, gauge_matrix[idx])
        push!(block_close, crit_matrix[i][idx])
        push!(end_close, endrange[i])
    end

end
```

In [37]:

```
limit_x = (pitchrange[1], pitchrange[end])
limit_y = (gaugerange[1], gaugerange[end])

for i = 1:length(end_close)
    end_dist_simple = round(end_close[i], sigdigits = 3)
    title = "Target Combinations for " * section * "; End = " * string(end_dist_simple) *
"mm"
    display(scatter(pitch_close[i], gauge_close[i],
        xlabel = "Pitch (mm)",
        ylabel = "Gauge (mm)",
        xlims = limit_x,
        ylims = limit_y,
        title = title,
        legend = false))
end
```

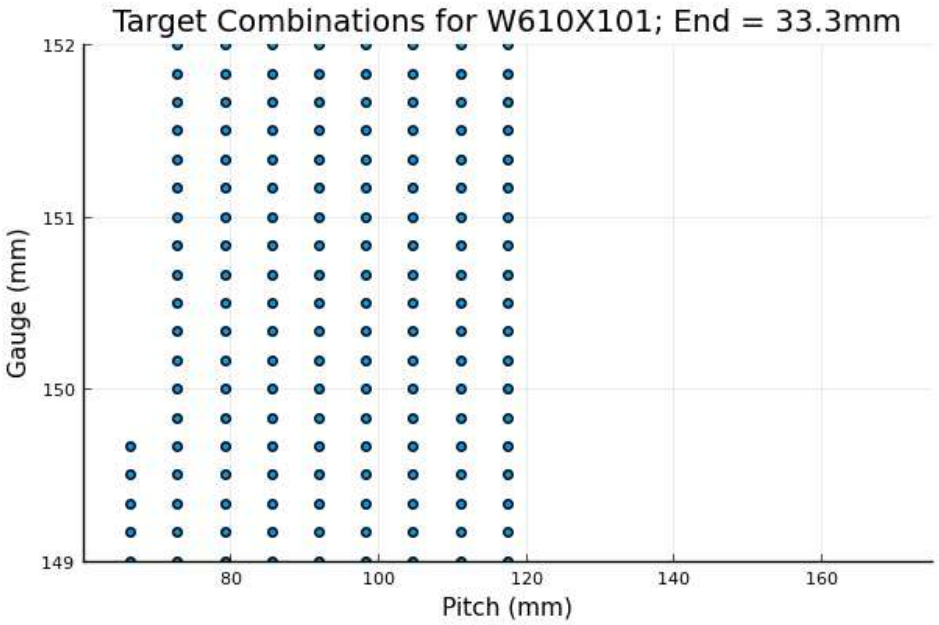
Target Combinations for W610X101; End = 33.3mm
Gauge (mm)
152
151
150
149
80
100
120
140
160
Pitch (mm)

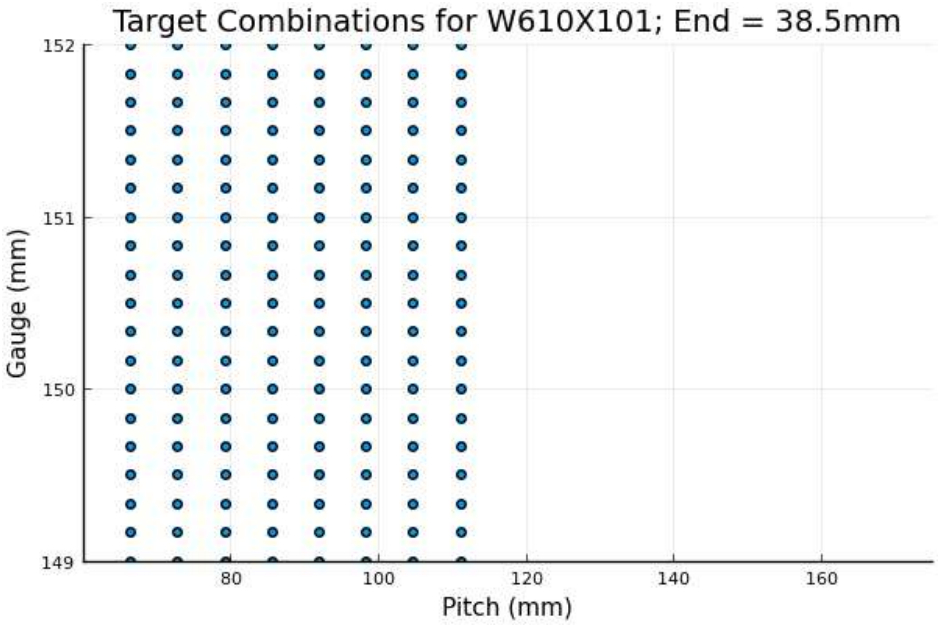
Target Combinations for W610X101; End = 38.5mm
Gauge (mm)
Pitch (mm)
152
151
150
149
80
100
120
140
160

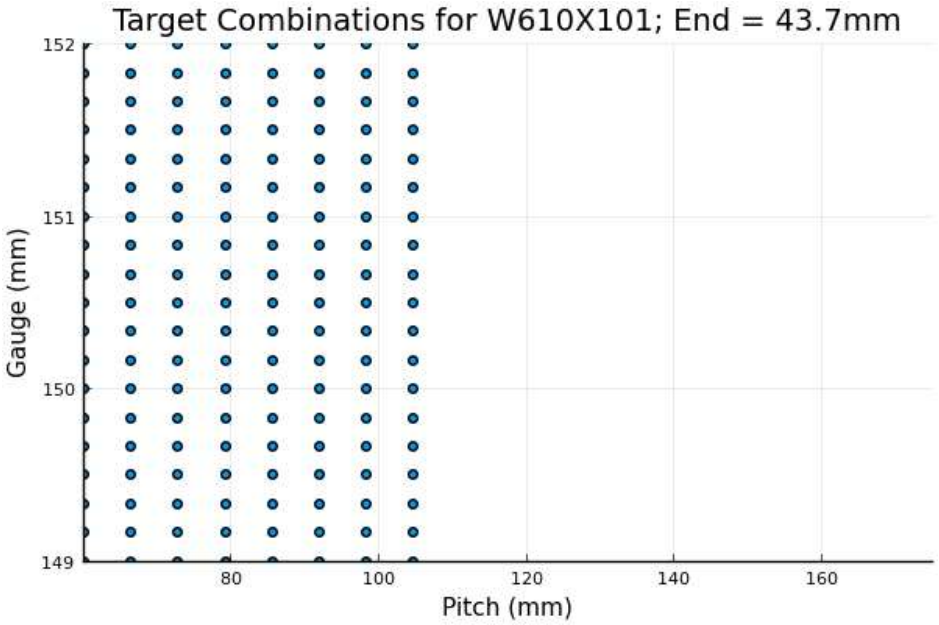
Target Combinations for W610X101; End = 43.7mm
Gauge (mm)
Pitch (mm)
152
151
150
149
80
100
120
140
160

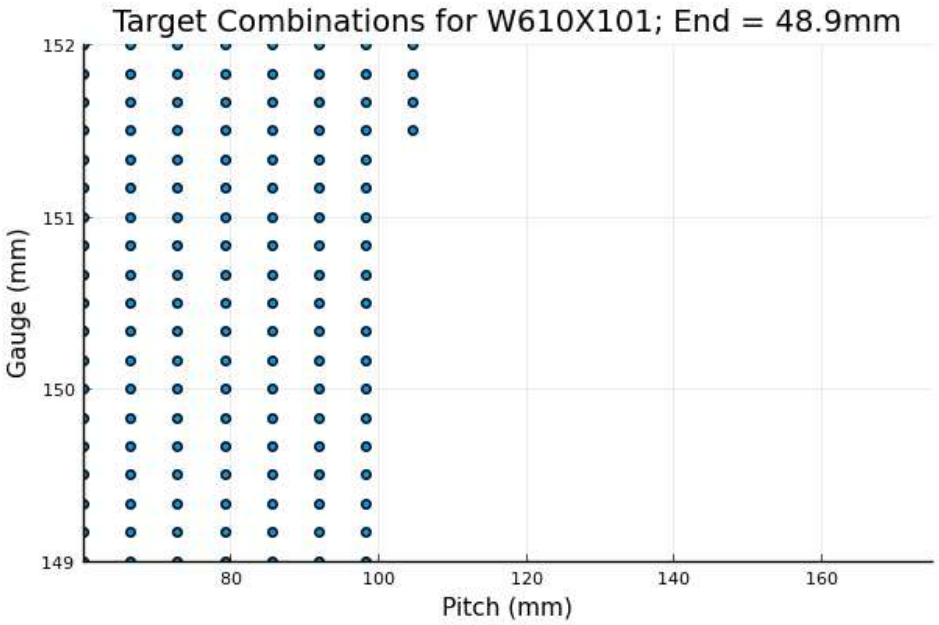
Target Combinations for W610X101; End = 48.9mm
Gauge (mm)
152
151
150
149
80
100
120
140
160
Pitch (mm)

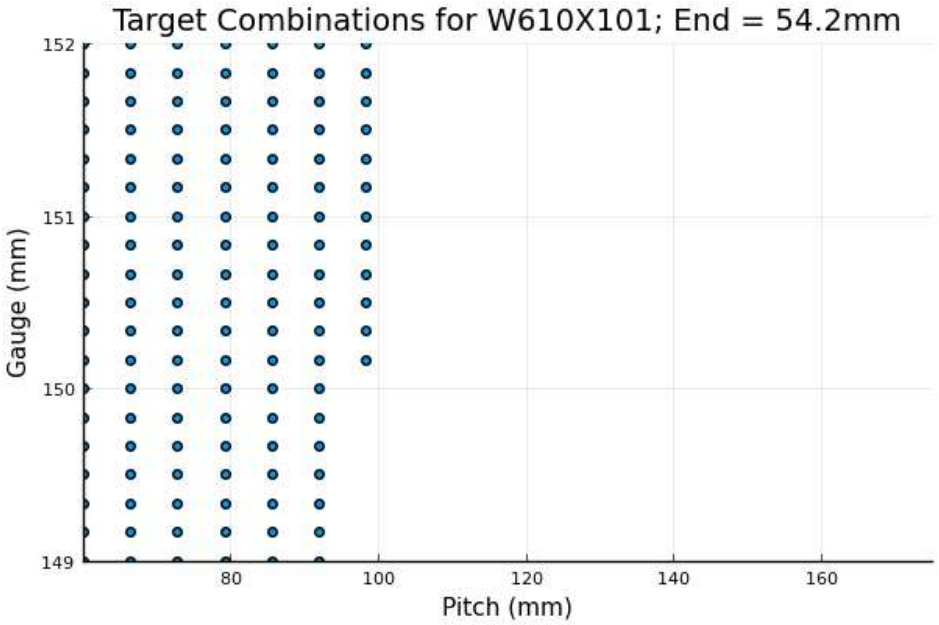
Target Combinations for W610X101; End = 54.2mm
Gauge (mm)
152
151
150
149
80
100
120
140
160
Pitch (mm)

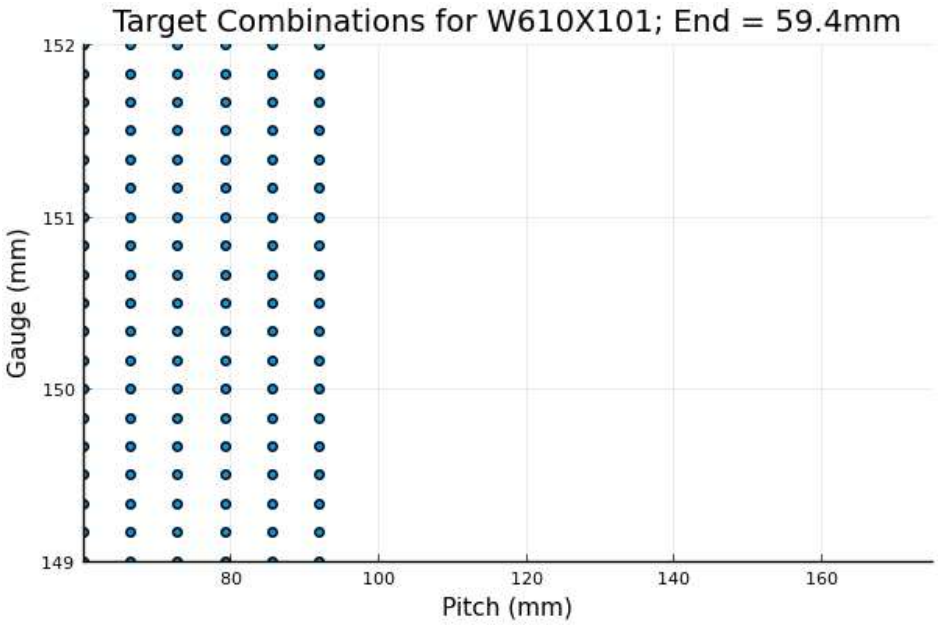
Target Combinations for W610X101; End = 59.4mm
Gauge (mm)
152
151
150
149
80
100
120
140
160
Pitch (mm)

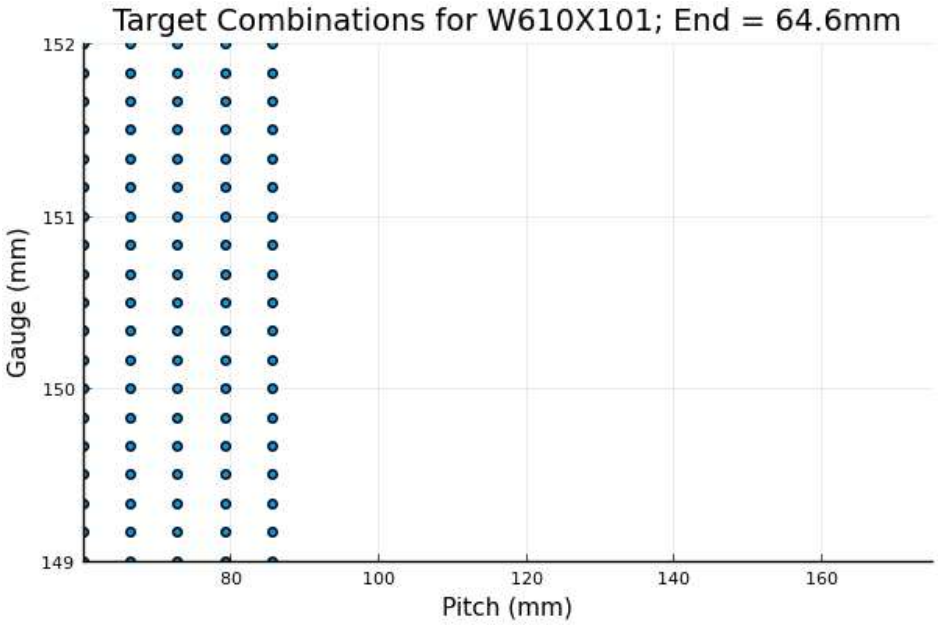
Target Combinations for W610X101; End = 64.6mm
Gauge (mm)
152
151
150
149
80
100
120
140
160
Pitch (mm)

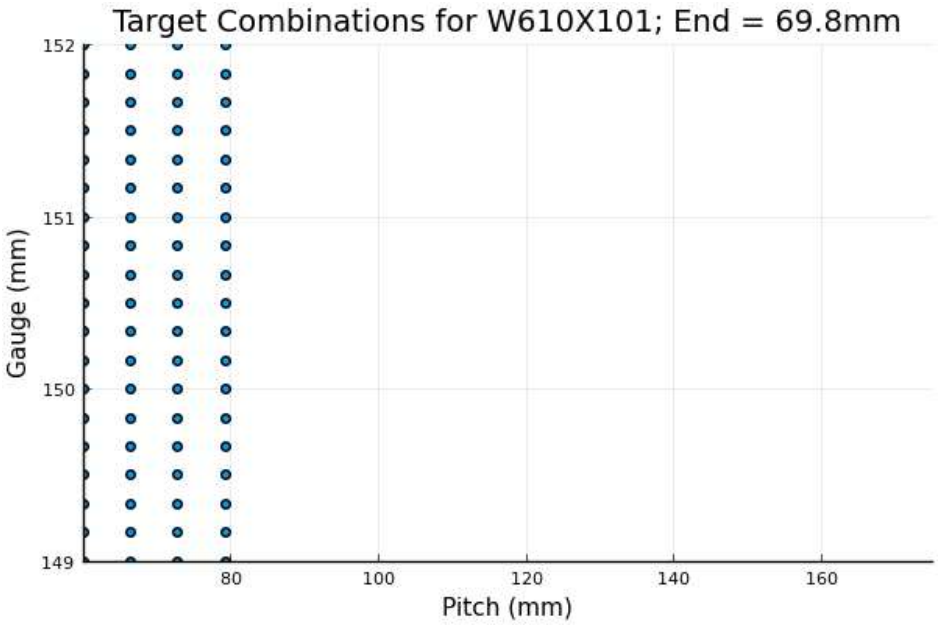
Target Combinations for W610X101; End = 69.8mm
Gauge (mm)
152
151
150
149
80
100
120
140
160
Pitch (mm)

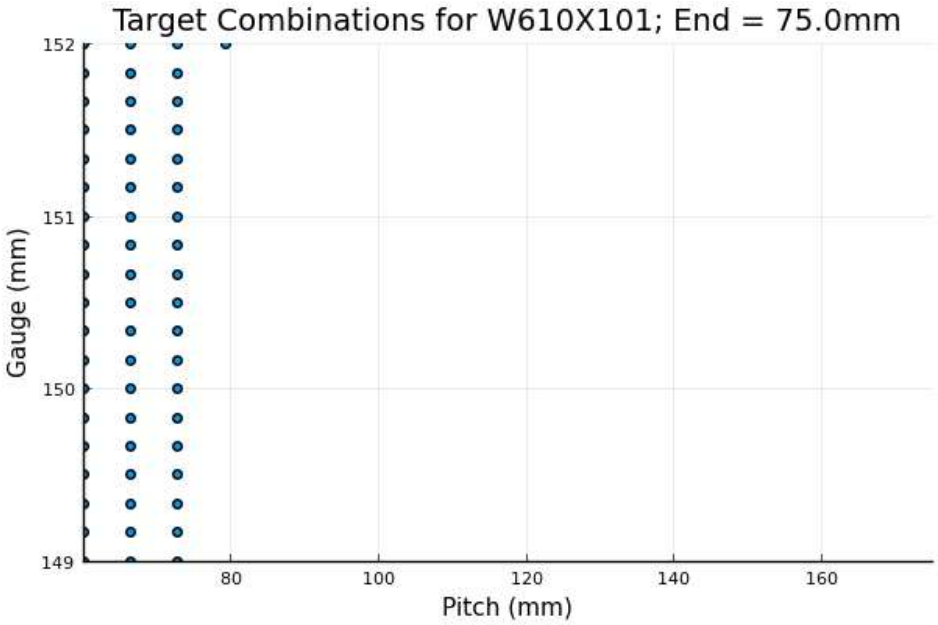
Target Combinations for W610X101; End = 75.0mm
Gauge (mm)
152
151
150
149
80
100
120
140
160
Pitch (mm)

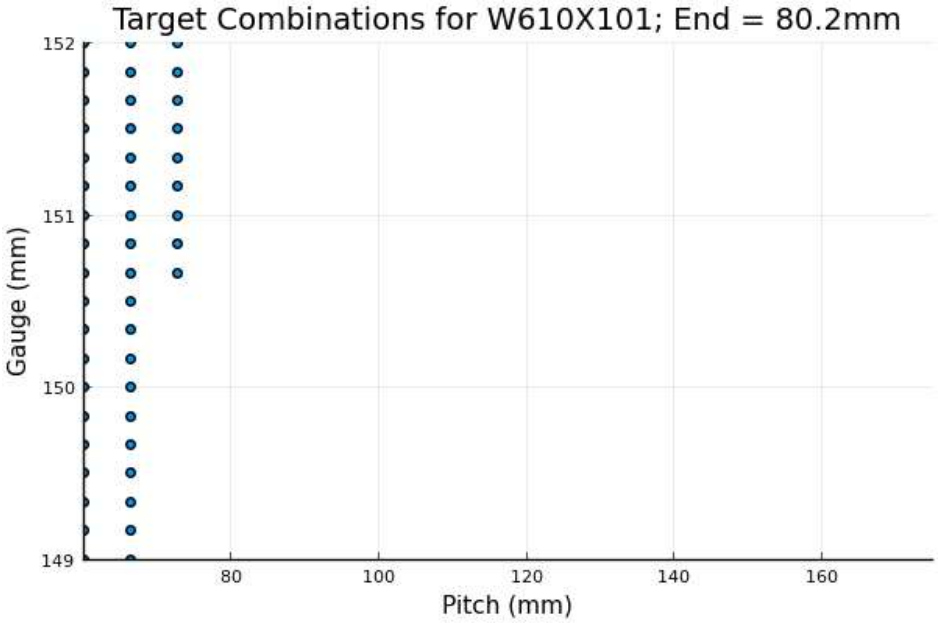
Target Combinations for W610X101; End = 80.2mm
Gauge (mm)
152
151
150
149
80
100
120
140
160
Pitch (mm)

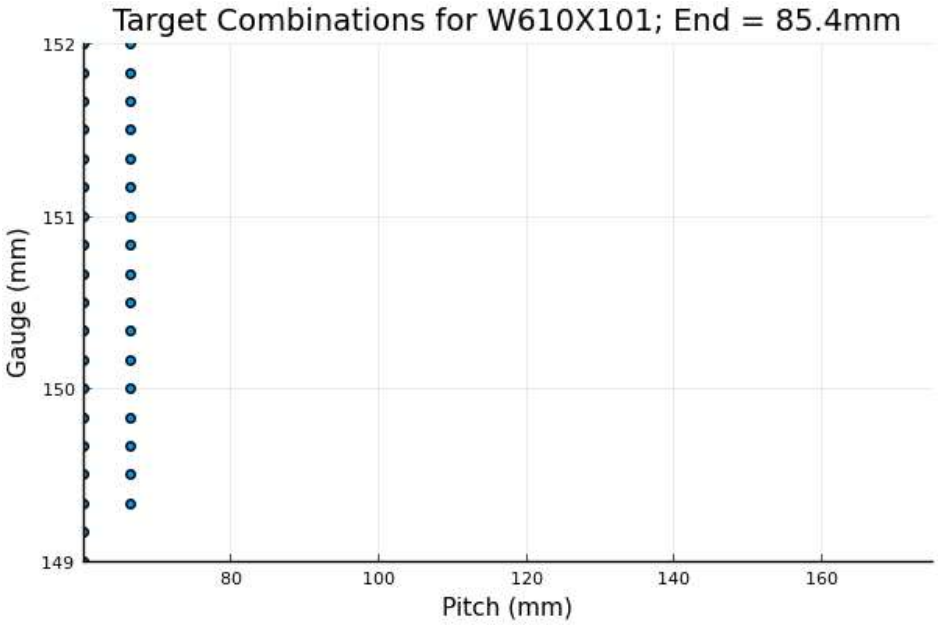
Target Combinations for W610X101; End = 85.4mm
Gauge (mm)
152
151
150
149
80
100
120
140
160
Pitch (mm)

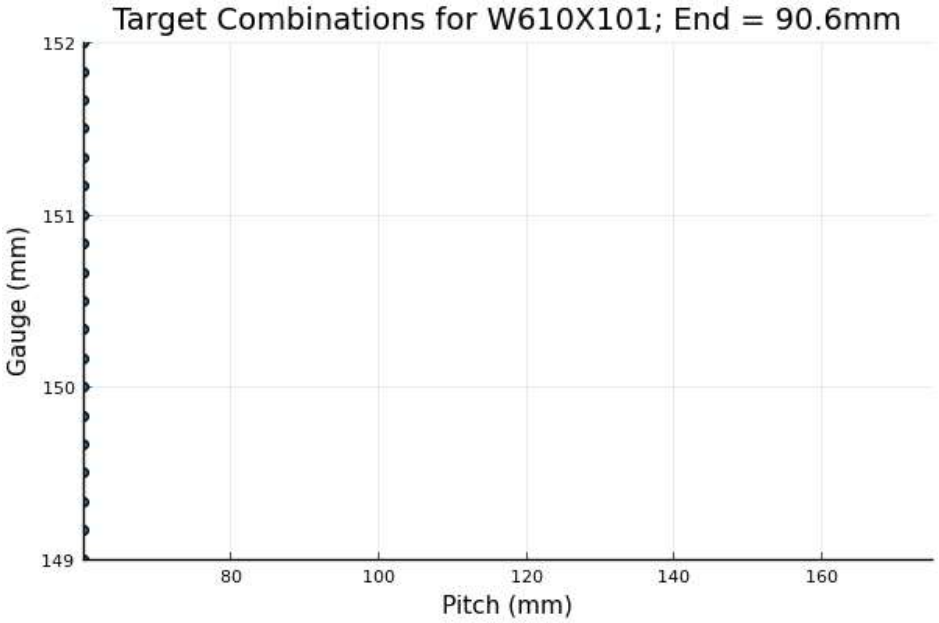
Target Combinations for W610X101; End = 90.6mm
Gauge (mm)
152
151
150
149
80
100
120
140
160
Pitch (mm)

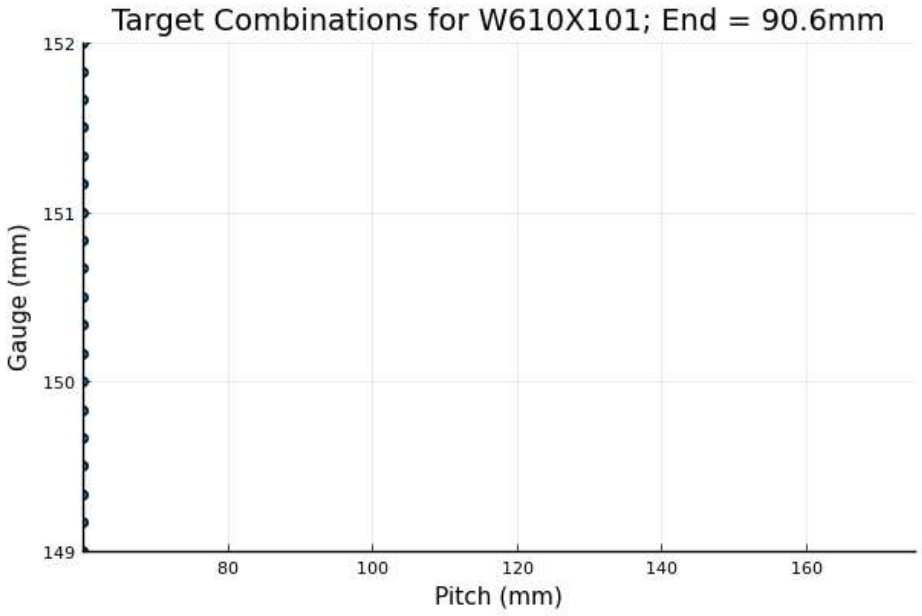
Target Combinations for W610X101; End = 90.6mm
Gauge (mm)
152
151
150
149
80
100
120
140
160
Pitch (mm)

In [42]:

```
i = 4
end_dist_simple = round(end_close[i], sigdigits = 3)
title = "Target Combinations for " * section * "; End = " * string(end_dist_simple) * "mm"
scatter(pitch_close[i], gauge_close[i],
    xlabel = "Pitch (mm)",
    ylabel = "Gauge (mm)",
    xlims = limit_x,
    ylims = limit_y,
    title = title,
    legend = false)
```

Out[42]:

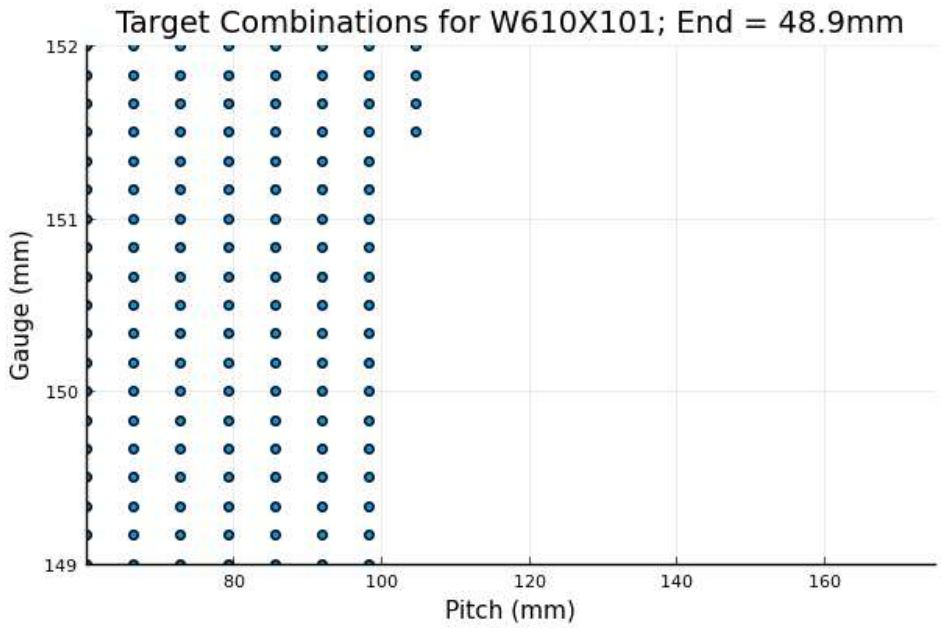

In [43]:

```
savefig("m5targetcombos.pdf")
```

Choose desired combination in Design Space for further analysis

The complete design space for the given section size + bolt number is determined. A definitive connection geometry should be determined for the design of the splice plates, and final verification of the connection.

Choose End, Pitch, Gauge based on allowable design space

In [30]:

```
end_distance = 35
pitch = 75
gauge = 145
```

Out[30]:

```
145
```

Overall connection design review:

Now that all required connection details are provided (number of bolts, pitch, gauge, end), an evaluation of the section can be made:

In [31]:

```
bar1, overview = section_overview(section, d_b, end_distance, fy, fu, pitch, gauge, n_bolt
s; tol = tol)
bar1
```

```
For W610X101:
85% rule triggered. Net properties should be used.
Bolt hole geometry limits satisfied. Design OK.
```

Out[31]:

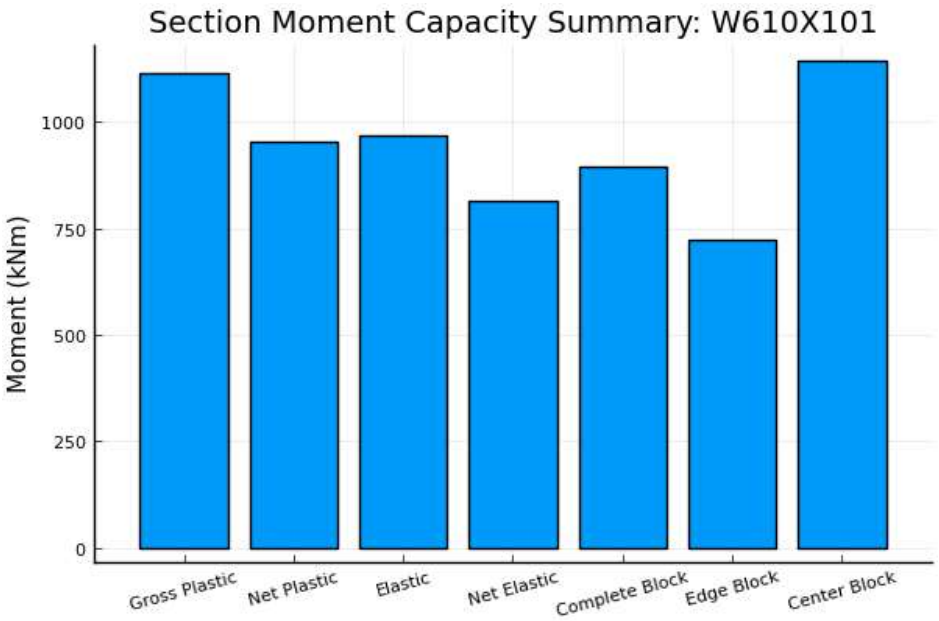

In [32]:

```
overview
```

Out[32]:

1 rows × 24 columns (omitted printing of 16 columns)

	Section	BoltDiameter	HoleTolerance	EndDistance	Pitch	Gauge	N_bolts	ConnectionLeng
	String	Float64	Int64	Int64	Int64	Int64	Float64	Float
1	W610X101	22.225	2	35	75	145	2.0	11(

Factored Resistances

In [35]:

```
bar2, overview_2 = section_overview(section, d_b, end_distance, fy, fu, pitch, gauge, n_bo
lts; tol = tol, phi = 0.9, phi_u = 0.75)
bar2
```

```
For W610X101:
85% rule triggered. Net properties should be used.
Bolt hole geometry limits satisfied. Design OK.
```

Out[35]:

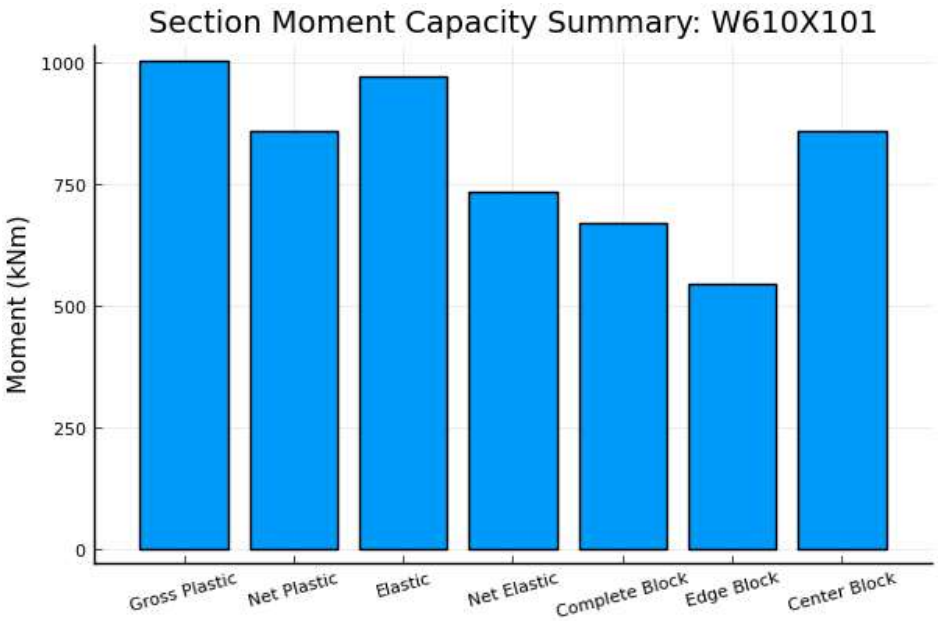

In [36]:

```
203e3 / (sec_props.t_f[1] * (sec_props.b_f[1] - gauge - d_b - tol) / 2)
```

Out[36]:

463.6039497686262